

**Modelling the Solids
Transport Phenomena Within
Flighted Rotary Dryers**

**Thesis submitted by
Andrew LEE, BE(Hons) QLD
in May 2008**

**for the degree of Doctor of Philosophy
in the School of Engineering
James Cook University**

Acknowledgements

I would like to acknowledge the invaluable assistance of many people and thank them for the help and support they have given me throughout the course of my thesis.

- Dr. Madoc Sheehan and Dr. Phil Schneider for their constant support and input. Without your patience and prodding, this would have taken far longer than it did.
- Dr. Paul Britton for his enthusiastic support and constant encouragement. Our conversations gave me an opportunity to sound out new ideas, and your help on experimental design was invaluable.
- Ms. Chrestella Wardjiman and Professor Martin Rhodes from Monash University, Australia, for their collaboration on modelling the gas-solids interactions in falling curtains of solids.
- Mr. Curt Arrowsmith, Mr. Stu Peterson and Mr Warren O'Donnell for their help with designing, building and testing the experimental apparatus used in this thesis. I am grateful that you could find the time in your busy schedules to construct this equipment for me.
- Mr. Clay Armstrong for setting up and programming the flight unloading apparatus and his help with designing the filter used in analysing the flight unloading experiments.
- Dr. Darren Stevens for providing an example of a CFD model for falling curtains of solids in a gas flow. That model provided me with the example I needed to learn how to use the software and develop my own model.

Finally, I would like to thank my family and friends for their ever present support during my time at university. Without them, I would not have been able to get through the tough times and finish my work.

Statement of Access

I, the undersigned, author of this work, understand that James Cook University will make this thesis available for use within the University Library and, via the Australian Digital Theses network, for use elsewhere.

I understand that, as an unpublished work, a thesis has significant protection under the Copyright Act and;

I do not wish to place any further restriction on access to this work.

30th July 2008

Andrew Lee

Declaration

I declare that this thesis is my own work and has not been submitted in any form for another degree or diploma at any university or other institution of tertiary education. Information derived from the published or unpublished work of others has been acknowledged in the text and a list of references is given.

30th July 2008

Andrew Lee

Table of Contents

1. INTRODUCTION.....	2
2. LITERATURE REVIEW.....	5
2.1. INTRODUCTION.....	5
2.2. PROPERTIES OF BULK SOLIDS	5
2.3. CHARACTERISATION OF SOLIDS TRANSPORT	8
2.3.1. <i>Experimental Methods</i>	10
2.3.1.1. Industrial Scale versus Pilot Scale	10
2.3.1.2. Measuring Dryer Holdup	11
2.3.1.3. Measuring the Residence Time Distribution.....	12
2.3.1.4. Dynamic Response Experiments.....	13
2.4. MODELLING APPROACHES	13
2.4.1. <i>Empirical Models</i>	14
2.4.2. <i>Mechanistic Models</i>	17
2.4.3. <i>Compartment Modelling</i>	21
2.4.3.1. Theory of Compartment Modelling	21
2.4.3.2. Compartment Models of Rotary Dryers.....	23
2.4.4. <i>Summary of Modelling Methods</i>	26
2.4.5. <i>Multi-Scale Modelling</i>	27
2.5. MODELLING OF FLIGHT HOLDUP.....	28
2.6. MODELLING OF KILNING BEDS	29
2.7. DRAG EFFECTS ON FALLING PARTICLES	30
2.7.1. <i>Integration of Drag Effects on Solids Transport</i>	31
2.8. SUMMARY OF LITERATURE REVIEW.....	33
3. DRYER MODEL DEVELOPMENT AND SIMULATION	35
3.1. A NUMERICAL APPROACH TO MODELLING A ROTARY DRYER	35
3.1.1. <i>Defining Dimensions</i>	35
3.1.2. <i>Model Development</i>	36
3.1.3. <i>Modes of Solids Transport</i>	37
3.1.4. <i>Describing the Behaviour of the Phases</i>	39
3.2. QUANTIFYING THE MODES OF SOLIDS TRANSPORT.....	40
3.2.1. <i>Form of the Solids Transport Equations</i>	41
3.2.2. <i>Effect of Dryer Loading on Flight Unloading</i>	41
3.2.3. <i>Passive Cycle Time</i>	42
3.2.4. <i>Active Cycle Time</i>	44
3.2.5. <i>Effects of Gas-Solids Interactions</i>	46
3.2.6. <i>Solids Transport via Kilning</i>	48
3.3. PROCESS SIMULATION USING GPROMS [®]	49
3.3.1. <i>Model Entities</i>	50

3.3.2. <i>Parameters and Variables</i>	51
3.3.3. <i>Process Entities</i>	52
3.3.4. <i>Estimation and Experiment Entities</i>	53
3.3.5. <i>Other Entity Types</i>	53
3.3.6. <i>Numerical Solvers in gPROMS[®]</i>	54
3.3.7. <i>Drawbacks to gPROMS[®]</i>	54
3.3.7.1. <i>Interfacing with Excel[®]</i>	55
3.4. MODEL IMPLEMENTATION USING GPROMS [®]	55
3.4.1. <i>Model Structure</i>	55
4. GEOMETRIC ANALYSIS OF AN UNLOADING FLIGHT.....	57
4.1. THE SOLIDS DYNAMIC ANGLE OF REPOSE	58
4.2. CALCULATION OF FLIGHT HOLDUP AND UNLOADING	58
4.2.1. <i>Non-Perpendicular Flights</i>	59
4.2.2. <i>Additional Geometric Definitions</i>	60
4.2.3. <i>Calculation of Maximum Flight Holdup</i>	62
4.2.3.1. Transition Points	65
4.2.3.2. Maximum Flight Holdup.....	72
First Unloading Phase, $\psi_1 \rightarrow \psi_2$	72
Second Unloading Phase, $\psi_2 \rightarrow \psi_3$	73
Third Unloading Phase, $\psi_3 \rightarrow \psi_4$	75
Fourth Unloading Phase, $\psi_4 \rightarrow \psi_5$	77
Effects of Serrated Flights	78
4.2.4. <i>Theoretical Unloading Profile</i>	79
4.2.5. <i>Comparison of Unloading Profile to Previous Literature</i>	81
4.2.6. <i>Limitations and Assumptions of the Geometry Model</i>	82
4.3. APPLYING THE GEOMETRIC MODEL TO SOLIDS TRANSPORT.....	82
4.4. EFFECTS OF DRYER LOADING ON SOLIDS TRANSPORT.....	83
4.4.1. <i>The Design Load</i>	85
4.4.2. <i>The Loading Factor</i>	87
4.5. IMPLEMENTING GEOMETRIC MODEL IN SOLIDS TRANSPORT MODEL.....	89
5. EXPERIMENTAL VALIDATION OF THE GEOMETRIC UNLOADING MODEL	92
5.1. FLIGHT UNLOADING APPARATUS.....	92
5.2. COMMISSIONING AND TESTING	95
5.2.1. <i>Levelling the Collection Tray</i>	96
5.2.2. <i>Influence of External Sources</i>	96
5.2.3. <i>Dynamic Effects</i>	99
5.2.4. <i>Centrifugal Effects</i>	100
5.2.5. <i>Surface Friction Effects</i>	101

5.2.6. <i>Camera Location</i>	102
5.3. EXPERIMENTAL METHODS	102
5.3.1. <i>Experimental Materials</i>	102
5.3.2. <i>Experimental Design</i>	106
5.3.3. <i>Experimental Procedures</i>	107
5.4. DATA ANALYSIS	109
5.4.1. <i>Image Analysis</i>	109
5.4.2. <i>Load Cell Data Analysis</i>	112
5.4.3. <i>Normalizing Time Values</i>	112
5.4.3.1. Solids Bulk Density	117
5.4.4. <i>Repeatability</i>	118
5.4.5. <i>Effects of Abrasive Surface</i>	122
5.5. VALIDATION OF GEOMETRIC UNLOADING MODEL.....	125
5.5.1. <i>Model Inputs</i>	125
5.5.2. <i>Measurement of the Dynamic Angle of Repose</i>	126
5.5.3. <i>Validation at Different Rotation Velocities</i>	129
5.5.4. <i>Validation with Different Flight Geometries</i>	137
5.5.5. <i>Validation with Different Solid Materials</i>	142
5.5.6. <i>Summary of Model Validation</i>	147
5.6. ANALYSIS OF PHOTOGRAPHIC DATA.....	148
5.6.1. <i>Curtain Thickness</i>	148
5.6.2. <i>Particle Velocity</i>	152
5.6.3. <i>Bulk Density of Moving Layer of Solids</i>	157
5.6.4. <i>Further Observations</i>	159
6. MODELLING GAS-SOLID INTERACTIONS IN ROTARY DRYERS.....	161
6.1. THE AXIAL PARTITIONING COEFFICIENTS	161
6.2. EXPERIMENTAL MEASUREMENT OF SINGLE PARTICLE DRAG COEFFICIENTS.....	161
6.2.1. <i>Theory</i>	163
6.2.2. <i>Experimental Method</i>	164
6.2.3. <i>Results</i>	166
6.2.4. <i>Discussion</i>	167
6.2.5. <i>Summary</i>	169
6.3. METHODS FOR MODELLING THE GAS-SOLIDS INTERACTIONS FOR THE FALLING CURTAIN	169
6.4. COMPUTATIONAL FLUID DYNAMICS (CFD) MODELLING	169
6.5. CFD MODELLING OF TURBULENT FLOWS.....	171
6.5.1. <i>RANS Equations</i>	172
6.5.2. <i>Eddy Viscosity Turbulence Models</i>	173
6.5.3. <i>Interphase Momentum Transfer</i>	175
6.6. VERIFICATION AND VALIDATION OF CFD TECHNIQUES.....	175
6.6.1. <i>Comparing CFD Simulations to Wind Tunnel Experiments</i>	176

6.6.1.1.	Model Structure and Conditions	176
6.6.1.2.	Comparison of Results	177
	Experiments with Air Flow.....	177
	Experiments with No Air flow.....	184
6.6.1.3.	Conclusions.....	185
6.7.	CFD SIMULATION OF THE FALLING CURTAIN OF SOLIDS	186
6.7.1.	<i>Single Curtain Studies</i>	186
6.7.1.1.	Mesh Dependency.....	188
6.7.1.2.	Simulation Results	188
6.7.1.3.	Summary of Single Curtain Simulations.....	195
6.7.2.	<i>Multiple Curtain Studies</i>	196
6.8.	CONCLUSIONS	203
7.	DRYER MODEL VERIFICATION AND VALIDATION	204
7.1.	PARAMETER ESTIMATION	204
7.1.1.	<i>Dryer Geometry and Material Properties</i>	206
7.1.1.1.	Flight Serrations.....	206
7.1.1.2.	Solids Density	207
7.1.1.3.	Solids Dynamic Angle of Repose	208
7.1.1.4.	Solids Moisture Content.....	208
7.1.2.	<i>Estimated Parameter Values</i>	209
7.2.	PHYSICAL REALISM OF RESULTS.....	211
7.2.1.	<i>Average Kilning Phase Velocity</i>	211
7.2.2.	<i>Trends in Estimated Parameter Values</i>	212
7.2.3.	<i>Discussion of Model Fit</i>	215
7.3.	ALTERNATIVE MODEL STRUCTURES	217
7.4.	RESPONSE TO OPERATING CONDITIONS	219
7.4.1.	<i>Response to Dynamic Angle of Repose</i>	220
7.4.2.	<i>Response to Dryer Feed Rate</i>	223
7.5.	EFFECT OF DESIGN LOAD	225
7.6.	DISCUSSION	226
8.	CONCLUSIONS AND RECOMMENDATIONS	228
8.1.	CONCLUSIONS	228
8.2.	RECOMMENDATIONS	230
9.	REFERENCES.....	233
10.	APPENDIX I – GPROMS® CODE.....	239
10.1.	PROCESS ENTITY.....	239
10.2.	MODEL ENTITIES.....	242
10.2.1.	<i>Active Phase</i>	242
10.2.2.	<i>Passive Phase</i>	243

10.2.3.	<i>Geometry Model</i>	244
10.2.4.	<i>Cell Model</i>	248
10.2.5.	<i>Outflow Model</i>	248
10.2.6.	<i>Dryer Model</i>	249
10.3.	PARAMETER ESTIMATION ENTITY.....	250
10.4.	EXPERIMENT ENTITY	251
11.	APPENDIX II - MATLAB[®] CODE.....	253
11.1.	FILTERING FLIGHT RIG DATA	253
11.2.	FITTING MODEL TO FLIGHT RIG DATA.....	254

List of Figures

FIGURE 1.1. SCHEMATIC OF A TYPICAL COUNTER-CURRENT ROTARY DRYER.....	2
FIGURE 1.2. CROSS SECTION OF AN OPERATING FLIGHTED ROTARY DRYER.....	3
FIGURE 1.3. LOAD CONDITIONS WITHIN A FLIGHTED ROTARY DRYER; A) UNDERLOADED, B) DESIGN LOADED AND C) OVERLOADED OPERATIONS.....	4
FIGURE 2.1. EXPERIMENTAL METHODS FOR DETERMINING THE ANGLE OF REPOSE (WOODCOCK AND MASON, 1987 ¹).....	7
FIGURE 2.2. RESIDENCE TIME DISTRIBUTION FOR INVICTA SUGAR MILL DRYER NUMBER 2 (MONRO ¹⁰). ..	10
FIGURE 2.3. MODIFIED CHOLETTE-CLOUTIER MODEL ³³	24
FIGURE 2.4. MODEL PROPOSED BY SCHNEIDER <i>ET AL.</i> ³⁵	25
FIGURE 2.5. MODEL PROPOSED BY SHEEHAN <i>ET AL.</i> ³⁸	26
FIGURE 2.6. DIAGRAM SHOWING FORCES ACTING ON A FALLING PARTICLE IN A MOVING AIR STREAM. ..	30
FIGURE 3.1. DIMENSIONS USED IN DEVELOPING THE MODEL.....	36
FIGURE 3.2. A SLICE OF A DRYER.	37
FIGURE 3.3. EXAMPLE OF THE AVERAGE PARTICLE FALL PATH.	38
FIGURE 3.4. MAXIMUM AXIAL ADVANCE COMPARED TO CELL LENGTH.....	38
FIGURE 3.5. ONE-DIMENSIONAL NUMERICAL MODEL.	39
FIGURE 3.6. AVERAGE ACTIVE AND PASSIVE CYCLE TIMES.	42
FIGURE 3.7. AVERAGE FALL POINT AND PASSIVE CYCLE ARC.....	43
FIGURE 3.8. AXIAL TRANSPORT PARTITION COEFFICIENTS.	47
FIGURE 3.9. DIAGRAM OF MODEL STRUCTURE.	56
FIGURE 4.1. A GENERIC STRAIGHT 2-SECTION FLIGHT.	59
FIGURE 4.2. GEOMETRIC VARIABLES FOR NON-PERPENDICULAR FLIGHTS.....	59
FIGURE 4.3. DEFINITION OF SOME GEOMETRIC VARIABLES.	61
FIGURE 4.4. CALCULATION OF ψ_{ft} AND R_F	62
FIGURE 4.5. DEFINITION OF A FULL FLIGHT.	63
FIGURE 4.6. OVERVIEW OF TRANSITION POINTS.	65
FIGURE 4.7. TRANSITION POINT 1 ψ_1	66
FIGURE 4.8. DETAIL OF LENGTHS AND ANGLES AT THE SECOND TRANSITION POINT.....	66
FIGURE 4.9. TRANSITION POINT 3, ψ_3	68
FIGURE 4.10. TRANSITION POINT 4, ψ_4	69
FIGURE 4.11. TRANSITION POINT 5, ψ_5	70
FIGURE 4.12. CROSS-SECTIONAL AREA OF FLIGHTED MATERIAL BETWEEN ψ_1 AND ψ_2	73
FIGURE 4.13. CROSS-SECTIONAL AREA OF FLIGHTED MATERIAL BETWEEN ψ_2 AND ψ_3	74
FIGURE 4.14. CROSS-SECTIONAL AREA OF FLIGHTED MATERIAL BETWEEN ψ_3 AND ψ_4	76

FIGURE 4.15. CROSS-SECTIONAL AREA OF FLIGHTED MATERIAL BETWEEN ψ_3 AND ψ_4 AT HIGHER ψ .	77
FIGURE 4.16. CROSS-SECTIONAL AREA OF FLIGHTED MATERIAL BETWEEN ψ_4 AND ψ_5	78
FIGURE 4.17. MAXIMUM FLIGHT HOLDUP PROFILE FOR INVICTA MILL DRYER NUMBER 2.....	80
FIGURE 4.18. FLIGHT DISCHARGE RATE PROFILE FOR INVICTA MILL DRYER NUMBER 2.....	80
FIGURE 4.19. RELATIONSHIP BETWEEN DRYER AND FLIGHT LOADING FACTORS FOR INVICTA DRYER NUMBER 2.....	88
FIGURE 4.20. GPROMS [®] MODEL STRUCTURE.	91
FIGURE 5.1. PHOTOGRAPH OF EXPERIMENTAL APPARATUS.	93
FIGURE 5.2. SCHEMATIC OF COLLECTION TRAY AND FLIGHT CROSS-SECTION (ALTERNATIVE DESIGN)...	94
FIGURE 5.3. FORCE DIAGRAM ON COLLECTION TRAY.	96
FIGURE 5.4. EXAMPLE OF RAW EXPERIMENTAL DATA (2 RPM).	97
FIGURE 5.5. DERIVATIVE OF EXAMPLE RAW EXPERIMENTAL DATA (2 RPM).	97
FIGURE 5.6. EXAMPLE OF EXPERIMENTAL DATA AFTER FILTERING (2 RPM).	98
FIGURE 5.7. DERIVATIVE OF EXAMPLE RAW EXPERIMENTAL DATA AFTER FILTERING (2 RPM).	99
FIGURE 5.8. EXAMPLE OF THE EFFECTS OF IMPACT FORCES ON ACCUMULATED MASS MEASUREMENT (FLIGHT DESIGN 3, FILTER SAND, 8 RPM).	100
FIGURE 5.9. PHOTOGRAPH OF TROMMEL APPARATUS IN OPERATION.....	104
FIGURE 5.10. MATERIAL PARTICLE SIZE DISTRIBUTION.....	105
FIGURE 5.11. INITIAL LOCATION OF FLIGHT.....	110
FIGURE 5.12. MEASURING ANGLE OF ROTATION FROM PHOTOGRAPHS.....	110
FIGURE 5.13. MEASURING MATERIAL ANGLE OF REPOSE.....	110
FIGURE 5.14. SCHEMATIC OF FLIGHT SHOWING CALCULATION OF ANGLE OF REPOSE FROM MEASUREMENTS.	111
FIGURE 5.15. MEASURING THE CURTAIN THICKNESS.....	111
FIGURE 5.16. HIGH-SPEED CAMERA IMAGES SHOWING A TRACKED PARTICLE (CIRCLED IN BLACK).	112
FIGURE 5.17. MEASURED MASS FLOW RATE PROFILE (1/2 SCALE FLIGHT, 2 RPM, FILTER SAND).....	113
FIGURE 5.18. EXAMPLE OF ALIGNMENT METHOD FOR EXPERIMENTAL DATA (ALTERNATIVE FLIGHT, FILTER SAND, 2 RPM).....	114
FIGURE 5.19. COMPARISON OF ACCUMULATED MASS DATA (ALTERNATIVE FLIGHT, FILTER SAND, 2 RPM).	115
FIGURE 5.20. COMPARISON OF ACCUMULATED MASS DATA WITH 95% CONFIDENCE INTERVAL (ALTERNATIVE FLIGHT, FILTER SAND, 2 RPM).	116
FIGURE 5.21. COMPARISON OF MASS FLOW RATE DATA WITH 95% CONFIDENCE INTERVAL (ALTERNATIVE FLIGHT, FILTER SAND, 2 RPM).	116
FIGURE 5.22. COMPARISON OF RESULTS USING CONSOLIDATED AND UNCONSOLIDATED BULK DENSITIES (ALTERNATIVE FLIGHT, RIVER SAND, 8 RPM).....	117
FIGURE 5.23. REPEATABILITY OF ACCUMULATED MASS DATA (ALTERNATIVE FLIGHT, FILTER SAND, 2 RPM).	118
FIGURE 5.24. REPEATABILITY OF MASS FLOW RATE DATA (ALTERNATIVE FLIGHT, FILTER SAND, 2 RPM).	119

FIGURE 5.25. REPEATABILITY OF ACCUMULATED MASS DATA (ALTERNATIVE FLIGHT, FILTER SAND, 8RPM).	119
FIGURE 5.26. REPEATABILITY OF MASS FLOW RATE DATA (ALTERNATIVE FLIGHT, FILTER SAND, 8 RPM).	120
FIGURE 5.27. REPEATABILITY OF ACCUMULATED MASS DATA (1/2 SCALE FLIGHT, FILTER SAND, 2 RPM).	121
FIGURE 5.28. REPEATABILITY OF ACCUMULATED MASS DATA (1/2 SCALE FLIGHT, FILTER SAND, 8 RPM).	121
FIGURE 5.29. REPEATABILITY OF ACCUMULATED MASS DATA (FULL SCALE FLIGHT, FILTER SAND, 2 RPM).	122
FIGURE 5.30. COMPARISON OF EXPERIMENTS WITH AND WITHOUT ABRASIVE SURFACE AT 1 RPM.	123
FIGURE 5.31. COMPARISON OF EXPERIMENTS WITH AND WITHOUT ABRASIVE SURFACE AT 2 RPM.	123
FIGURE 5.32. COMPARISON OF EXPERIMENTS WITH AND WITHOUT ABRASIVE SURFACE AT 4 RPM.	124
FIGURE 5.33. COMPARISON OF EXPERIMENTS WITH AND WITHOUT ABRASIVE SURFACE AT 8 RPM.	124
FIGURE 5.34. EXAMPLE OF ANGLE OF REPOSE MEASUREMENTS FROM EXPERIMENTS 5-8.	127
FIGURE 5.35. DYNAMIC ANGLE OF REPOSE AS A FUNCTION OF ROTATIONAL VELOCITY FROM EXPERIMENTS 5-8.	127
FIGURE 5.36. ACCUMULATED MASS DATA (ALTERNATIVE FLIGHT, FILTER SAND, 1 RPM).....	131
FIGURE 5.37. MASS FLOW RATE DATA (ALTERNATIVE FLIGHT, FILTER SAND, 1 RPM).....	131
FIGURE 5.38. ACCUMULATED MASS DATA (ALTERNATIVE FLIGHT, FILTER SAND, 2 RPM).....	132
FIGURE 5.39. MASS FLOW RATE DATA (ALTERNATIVE FLIGHT, FILTER SAND, 2 RPM).....	132
FIGURE 5.40. ACCUMULATED MASS DATA (ALTERNATIVE FLIGHT, FILTER SAND, 4 RPM).....	133
FIGURE 5.41. MASS FLOW RATE DATA (ALTERNATIVE FLIGHT, FILTER SAND, 4 RPM).....	133
FIGURE 5.42. ACCUMULATED MASS DATA (ALTERNATIVE FLIGHT, FILTER SAND, 8 RPM).....	134
FIGURE 5.43. MASS FLOW RATE DATA (ALTERNATIVE FLIGHT, FILTER SAND, 8 RPM).....	134
FIGURE 5.44. NORMALISED ACCUMULATED MASS PROFILES AT DIFFERENT ROTATIONAL SPEEDS (ALTERNATE FLIGHT, FILTER SAND).	135
FIGURE 5.45. NORMALISED MASS FLOW RATE PROFILES AT DIFFERENT ROTATIONAL SPEEDS (ALTERNATE FLIGHT, FILTER SAND).	136
FIGURE 5.46. ACCUMULATED MASS DATA (1/2 SCALE FLIGHT, FILTER SAND, 2 RPM).	138
FIGURE 5.47. MASS FLOW RATE DATA (1/2 SCALE FLIGHT, FILTER SAND, 2 RPM).	138
FIGURE 5.48. ACCUMULATED MASS DATA (1/2 SCALE FLIGHT, FILTER SAND, 8 RPM).	139
FIGURE 5.49. MASS FLOW RATE DATA (1/2 SCALE FLIGHT, FILTER SAND, 8 RPM).	139
FIGURE 5.50. ACCUMULATED MASS DATA (FULL SCALE FLIGHT, FILTER SAND, 2 RPM).	140
FIGURE 5.51. MASS FLOW RATE DATA (FULL SCALE FLIGHT, FILTER SAND, 2 RPM).	140
FIGURE 5.52. ACCUMULATED MASS DATA (FULL SCALE FLIGHT, FILTER SAND, 8 RPM).	141
FIGURE 5.53. MASS FLOW RATE DATA (FULL SCALE FLIGHT, FILTER SAND, 8 RPM).	141
FIGURE 5.54. ACCUMULATED MASS DATA (ALTERNATIVE FLIGHT, ZEOLITE, 2 RPM).	143
FIGURE 5.55. MASS FLOW RATE DATA (ALTERNATIVE FLIGHT, ZEOLITE, 2 RPM).	143
FIGURE 5.56. ACCUMULATED MASS DATA (ALTERNATIVE FLIGHT, RIVER SAND, 2 RPM).	144

FIGURE 5.57. MASS FLOW RATE DATA (ALTERNATIVE FLIGHT, RIVER SAND, 2 RPM).....	144
FIGURE 5.58. ACCUMULATED MASS DATA (ALTERNATIVE FLIGHT, ZEOLITE, 8 RPM).....	145
FIGURE 5.59. MASS FLOW RATE DATA (ALTERNATIVE FLIGHT, ZEOLITE, 8 RPM).....	145
FIGURE 5.60. ACCUMULATED MASS DATA (ALTERNATIVE FLIGHT, RIVER SAND, 8 RPM).....	146
FIGURE 5.61. MASS FLOW RATE DATA (ALTERNATIVE FLIGHT, RIVER SAND, 8 RPM).....	146
FIGURE 5.62. COMPARISON OF THE THICKNESS OF THE MOVING LAYER OF SOLIDS COMPARED TO THE UNLOADING PROFILE OF THE FLIGHT (ALTERNATE FLIGHT, FILTER SAND, 1 RPM).....	149
FIGURE 5.63. COMPARISON OF THE THICKNESS OF THE MOVING LAYER OF SOLIDS COMPARED TO THE UNLOADING PROFILE OF THE FLIGHT (ALTERNATIVE FLIGHT, FILTER SAND, 4 RPM).....	150
FIGURE 5.64. COMPARISON OF THE THICKNESS OF THE MOVING LAYER OF SOLIDS COMPARED TO THE UNLOADING PROFILE OF THE FLIGHT (ALTERNATIVE FLIGHT, FILTER SAND, 8 RPM).....	150
FIGURE 5.65. THICKNESS PROFILE AT INCREASING ROTATIONAL SPEEDS (ALTERNATIVE FLIGHT, FILTER SAND).....	151
FIGURE 5.66. AVERAGE CURTAIN THICKNESS AT INCREASING ROTATIONAL SPEEDS (ALTERNATIVE FLIGHT, FILTER SAND).....	152
FIGURE 5.67. COMPARISON OF THE VELOCITY OF THE MOVING LAYER OF SOLIDS COMPARED TO THE UNLOADING PROFILE OF THE FLIGHT (ALTERNATIVE FLIGHT, FILTER SAND, 1 RPM).....	153
FIGURE 5.68. COMPARISON OF THE VELOCITY OF THE MOVING LAYER OF SOLIDS COMPARED TO THE UNLOADING PROFILE OF THE FLIGHT (ALTERNATIVE FLIGHT, FILTER SAND, 4 RPM).....	153
FIGURE 5.69. COMPARISON OF THE VELOCITY OF THE MOVING LAYER OF SOLIDS COMPARED TO THE UNLOADING PROFILE OF THE FLIGHT (ALTERNATIVE FLIGHT, FILTER SAND, 8 RPM).....	154
FIGURE 5.70. PARTICLE VELOCITY PROFILE AT INCREASING ROTATIONAL SPEEDS (ALTERNATIVE FLIGHT, FILTER SAND).....	155
FIGURE 5.71. BULK DENSITY OF THE MOVING LAYER OF SOLIDS AT DIFFERENT ROTATIONAL VELOCITIES (ALTERNATIVE FLIGHT, FILTER SAND).....	158
FIGURE 5.72. HIGH-SPEED CAMERA IMAGES OF A FLIGHT DURING UNLOADING AT INTERVALS OF 0.016 SECONDS (ALTERNATIVE FLIGHT, RIVER SAND, 8 RPM).....	160
FIGURE 6.1. ELECTRON MICROSCOPE IMAGE OF RAW SUGAR CRYSTALS.....	162
FIGURE 6.2. IMAGE OF A FALLING SUGAR CRYSTAL.....	165
FIGURE 6.3. DRAG COEFFICIENT OF A FALLING SUGAR CRYSTAL.....	167
FIGURE 6.4. WIND TUNNEL APPARATUS USED BY WARDJIMAN <i>ET AL.</i> ⁶⁸	176
FIGURE 6.5. PARTICLE CURTAIN TRAJECTORIES FOR PARTICLE CURTAIN WITH INLET THICKNESS OF 2 CM, SOLID MASS FLOW RATE OF 0.040 KG/S, AND MEAN GAS VELOCITY OF 0.9 M/S (○ RUN 1, □ RUN 2, △ RUN 3, ● CFD MODEL) ⁶⁸	178
FIGURE 6.6. PARTICLE CURTAIN TRAJECTORIES FOR PARTICLE CURTAIN WITH INLET THICKNESS OF 10 CM, SOLID MASS FLOW RATE OF 0.040 KG/S, AND MEAN GAS VELOCITY OF 0.9 M/S (○ RUN 1, □ RUN 2, △ RUN 3, ● CFD MODEL) ⁶⁸	178
FIGURE 6.7. PARTICLE CURTAIN TRAJECTORIES FOR PARTICLE CURTAIN WITH INLET THICKNESS OF 2 CM, SOLID MASS FLOW RATE OF 0.040 KG/S, AND MEAN GAS VELOCITY OF 1.2 M/S (○ RUN 1, □ RUN 2, △ RUN 3, ● CFD MODEL) ⁶⁸	179

FIGURE 6.8. PARTICLE CURTAIN TRAJECTORIES FOR PARTICLE CURTAIN WITH INLET THICKNESS OF 10 CM, SOLID MASS FLOW RATE OF 0.040 KG/S, AND MEAN GAS VELOCITY OF 1.2 M/S (○ RUN 1, □ RUN 2, Δ RUN 3, ● CFD MODEL) ⁶⁸	179
FIGURE 6.9. PARTICLE CURTAIN TRAJECTORIES FOR PARTICLE CURTAIN WITH INLET THICKNESS OF 5 CM, SOLID MASS FLOW RATE OF 0.047 KG/S, AND MEAN GAS VELOCITY OF 0.9 M/S (○ RUN 1, □ RUN 2, Δ RUN 3, ● CFD MODEL) ⁶⁸	180
FIGURE 6.10. GAS VELOCITY PROFILE AT THE TRAILING EDGE FOR PARTICLE CURTAIN WITH INLET THICKNESS OF 2 CM, SOLID MASS FLOW RATE OF 0.040 KG/S, AND MEAN GAS VELOCITY OF 0.9 M/S (○ MEASURED, — CFD MODEL) ⁶⁸	181
FIGURE 6.11. GAS VELOCITY PROFILE AT THE TRAILING EDGE FOR PARTICLE CURTAIN WITH INLET THICKNESS OF 10 CM, SOLID MASS FLOW RATE OF 0.040 KG/S, AND MEAN GAS VELOCITY OF 0.9 M/S (○ MEASURED, — CFD MODEL) ⁶⁸	181
FIGURE 6.12. GAS VELOCITY PROFILE AT THE TRAILING EDGE FOR PARTICLE CURTAIN WITH INLET THICKNESS OF 2 CM, SOLID MASS FLOW RATE OF 0.040 KG/S, AND MEAN GAS VELOCITY OF 1.2 M/S (○ MEASURED, — CFD MODEL) ⁶⁸	182
FIGURE 6.13. GAS VELOCITY PROFILE AT THE TRAILING EDGE FOR PARTICLE CURTAIN WITH INLET THICKNESS OF 10 CM, SOLID MASS FLOW RATE OF 0.040 KG/S, AND MEAN GAS VELOCITY OF 1.2 M/S (○ MEASURED, — CFD MODEL) ⁶⁸	182
FIGURE 6.14. GAS VELOCITY PROFILE AT THE TRAILING EDGE FOR PARTICLE CURTAIN WITH INLET THICKNESS OF 5 CM, SOLID MASS FLOW RATE OF 0.031 KG/S, AND MEAN GAS VELOCITY OF 0.9 M/S (○ MEASURED, — CFD MODEL) ⁶⁸	183
FIGURE 6.15. GAS VELOCITY PROFILE AT THE TRAILING EDGE FOR PARTICLE CURTAIN WITH INLET THICKNESS OF 5 CM, SOLID MASS FLOW RATE OF 0.047 KG/S, AND MEAN GAS VELOCITY OF 0.9 M/S (○ MEASURED, — CFD MODEL) ⁶⁸	183
FIGURE 6.16. SIMULATED GAS VELOCITY PROFILE ALONG THE CENTRELINE OF THE TUNNEL (SOLIDS INLET 10CM, 0.070 KG/S AND INLET GAS VELOCITY 1.2 M/S) WITH CURTAIN BOUNDARIES SHOWN.	184
FIGURE 6.17. CURTAIN STRUCTURE WITH INLET THICKNESS OF 2CM AND MASS FLOWRATES OF 0.040 KG/S (.... CFD, ○ RUN 1, □ RUN 2, Δ RUN 3) ⁷⁰	185
FIGURE 6.18. CURTAIN STRUCTURE WITH INLET THICKNESS OF 8CM AND MASS FLOWRATES OF 0.040 KG/S (.... CFD, ○ RUN 1, □ RUN 2, Δ RUN 3) ⁷⁰	185
FIGURE 6.19. SOLID CURTAIN PROFILES USING DIFFERENT MESHS.....	188
FIGURE 6.20. SOLIDS CURTAIN PROFILE AT DIFFERENT GAS VELOCITIES.....	189
FIGURE 6.21. HORIZONTAL GAS VELOCITY COLOUR MAP AT 1 M ABOVE TUNNEL FLOOR (1 M/S INITIAL GAS VELOCITY, 0.5 M INLET, 5.18 KG/M.S SOLIDS FLOW RATE). UNITS ARE M/S.....	190
FIGURE 6.22. HORIZONTAL GAS VELOCITY COLOUR MAP AT 1 M ABOVE TUNNEL FLOOR (2 M/S INITIAL GAS VELOCITY, 0.5 M INLET, 5.18 KG/M.S SOLIDS FLOW RATE). UNITS ARE M/S.....	190
FIGURE 6.23. SOLIDS CURTAIN PROFILE AT DIFFERENT CURTAIN LENGTHS.....	192
FIGURE 6.24. HORIZONTAL GAS VELOCITY COLOUR MAP AT 0.5 M ABOVE TUNNEL FLOOR (1 M/S INITIAL GAS VELOCITY, 0.1 M INLET, 5.18 KG/M.S SOLIDS FLOW RATE). UNITS ARE M/S.....	192

FIGURE 6.25. SOLIDS CURTAIN PROFILE AT DIFFERENT MASS FLOW RATES.	193
FIGURE 6.26. SIMULATED CURTAIN DISPLACEMENT OVER 2 METRES AT DIFFERENT GAS VELOCITIES... ..	194
FIGURE 6.27. SIMULATED CURTAIN DISPLACEMENT OVER 2 METRES AT DIFFERENT MASS FLOW RATES.	194
.....	
FIGURE 6.28. SOLIDS VOLUME FRACTION COLOUR MAP AT 0.25 M ABOVE TUNNEL FLOOR WITH 50 MM	
CURTAIN SPACING.....	198
FIGURE 6.29. SOLIDS VOLUME FRACTION COLOUR MAP AT 0.25 M ABOVE TUNNEL FLOOR WITH 60 MM	
CURTAIN SPACING.....	198
FIGURE 6.30. SOLIDS VOLUME FRACTION COLOUR MAP AT 0.25 M ABOVE TUNNEL FLOOR WITH 70 MM	
CURTAIN SPACING.....	199
FIGURE 6.31. SOLIDS VOLUME FRACTION COLOUR MAP AT 0.25 M ABOVE TUNNEL FLOOR WITH 80 MM	
CURTAIN SPACING.....	199
FIGURE 6.32. HORIZONTAL GAS VELOCITY COLOUR MAP AT 0.25 M ABOVE TUNNEL FLOOR WITH 50 MM	
CURTAIN SPACING. UNITS ARE M/S.	200
FIGURE 6.33. HORIZONTAL GAS VELOCITY COLOUR MAP AT 0.25 M ABOVE TUNNEL FLOOR WITH 60 MM	
CURTAIN SPACING. UNITS ARE M/S.	200
FIGURE 6.34. HORIZONTAL GAS VELOCITY COLOUR MAP AT 0.25 M ABOVE TUNNEL FLOOR WITH 70 MM	
CURTAIN SPACING. UNITS ARE M/S.	201
FIGURE 6.35. HORIZONTAL GAS VELOCITY COLOUR MAP AT 0.25 M ABOVE TUNNEL FLOOR WITH 80 MM	
CURTAIN SPACING. UNITS ARE M/S.	201
FIGURE 6.36. PLOT OF CURTAIN PROFILES FOR DIFFERENT CURTAIN SPACINGS.	202
FIGURE 7.1. EXPERIMENTAL TRACER DATA FROM INVICTA MILL DRYER NUMBER 2 (MONRO ¹⁰)	204
FIGURE 7.2. PREDICTED RTD CURVES AT DIFFERENT VALUES OF N	210
FIGURE 7.3. ESTIMATED VALUES OF t_{kiln} AT DIFFERENT VALUES OF N	213
FIGURE 7.4. ESTIMATED VALUES OF C_B AT DIFFERENT VALUES OF N	214
FIGURE 7.5. ESTIMATED VALUES OF C_F^G AT DIFFERENT VALUES OF N	214
FIGURE 7.6. COMPARISON OF DIFFERENT MODEL STRUCTURES.	219
FIGURE 7.7. INTERNAL SOLIDS FLOWRATES VERSUS DYNAMIC ANGLE OF REPOSE.....	221
FIGURE 7.8. TOTAL PASSIVE HOLDUP VERSUS DRYER FEED RATE.....	224

List of Tables

TABLE 2.1. RELATIONSHIP BETWEEN ANGLE OF REPOSE AND FLOW PROPERTIES (WOODCOCK AND MASON, 1987 ¹).....	7
TABLE 4.1. GEOMETRY OF THE INVICTA SUGAR MILL DRYER NUMBER 2	71
TABLE 4.2. SUMMARY OF TRANSITION POINTS FOR INVICTA SUGAR MILL DRYER NUMBER 2	71
TABLE 5.1. DIMENSIONS OF EXPERIMENTAL FLIGHTS.....	94
TABLE 5.2. MEASURED SOLIDS PROPERTIES	104
TABLE 5.3. MATERIAL PARTICLE SIZE DISTRIBUTION.....	105
TABLE 5.4. LIST OF EXPERIMENTS AND CONDITIONS.....	107
TABLE 5.5. MEASURED MATERIAL ANGLES OF REPOSE (EXPERIMENT NUMBERS CORRESPOND WITH TABLE 5.4).	128
TABLE 5.6. MEASURED PARTICLE VELOCITIES (EXPERIMENT NUMBERS CORRESPOND WITH TABLE 5.4).	156
TABLE 6.1. SINGLE CURTAIN SIMULATION CONDITIONS	187
TABLE 6.2. MULTIPLE CURTAIN SIMULATION CONDITIONS.....	197
TABLE 7.1. BULK DENSITIES OF RAW SUGAR	207
TABLE 7.2. ESTIMATED PARAMETER VALUES.....	209
TABLE 7.3. COMPARISON OF MOMENTS OF THE RTD	211
TABLE 7.4. CALCULATED AVERAGE KILNING PHASE VELOCITY	212
TABLE 7.5. DEPENDENCE OF PREDICTED SOLIDS FLOWRATES VALUES ON N	215
TABLE 7.6. AFFECT OF SOLIDS DYNAMIC ANGLE OF REPOSE ON SOLIDS TRANSPORT MODEL.....	220
TABLE 7.7. DRYER HOLDUP AT DIFFERENT DYNAMIC ANGLES OF REPOSE.....	222
TABLE 7.8. RATIO OF ACTIVE TO PASSIVE MASSES FOR DIFFERENT DYNAMIC ANGLES OF REPOSE.....	222
TABLE 7.9. PASSIVE HOLDUP AND KILNING FLOWRATE AT DIFFERENT DRYER FEED RATES.....	223
TABLE 7.10. EFFECT OF INCREASING THE MODEL DESIGN LOAD ON HOLDUPS.....	225

List of Equations

EQUATION 2.1. RELATIONSHIP FOR THE KINETIC ANGLE OF REPOSE ⁴	8
EQUATION 2.2. CALCULATION OF THE MEAN RESIDENCE TIME.....	8
EQUATION 2.3. CALCULATION OF THE MEAN RESIDENCE TIME FROM NORMALISED TRACER CONCENTRATIONS.....	9
EQUATION 2.4. MILLER, SMITH AND SCHUETTE EQUATION ¹⁸	14
EQUATION 2.5. FRIEDMAN AND MARSHALL EQUATION ¹¹	15
EQUATION 2.6. ALTERNATE FORM OF THE FRIEDMAN AND MARSHALL EQUATION.	15
EQUATION 2.7. MODIFIED FRIEDMAN AND MARSHALL EQUATION ¹⁹	16
EQUATION 2.8. ALVAREZ AND SHENE EQUATION ²⁰	16
EQUATION 2.9. SCHOFIELD AND GLIKIN EQUATION ⁴	17
EQUATION 2.10. MATCHETT AND BAKER MODEL ²³	18
EQUATION 2.11. EXTENDED TANKS-IN-SERIES MODEL ²⁸	22
EQUATION 2.12. FLIGHT DISCHARGE RATE BASED ON CROSS-SECTIONAL AREA OF SOLIDS ¹⁵	29
EQUATION 2.13. SCHILLER-NAUMANN EQUATION ⁴⁴	32
EQUATION 2.14. VELOCITY CORRECTION FACTOR ²⁷	32
EQUATION 3.1. GENERAL EQUATION FOR THE RATE OF SOLIDS TRANSPORT.....	41
EQUATION 3.2. DEFINITION OF SOLIDS TRANSPORT INTO ACTIVE PHASE.	42
EQUATION 3.3. CALCULATION OF MASS AVERAGED FALL POINT.....	44
EQUATION 3.4. AVERAGE RESIDENCE TIME OF FLIGHTED SOLIDS.....	44
EQUATION 3.5. CALCULATION OF MASS AVERAGED FALL HEIGHT	45
EQUATION 3.6. CALCULATING MASS AVERAGED FALL TIME.	45
EQUATION 3.7. FORWARD AXIAL PARTITIONING COEFFICIENT WITH ZERO AIRFLOW.	45
EQUATION 3.8. DEFINITION OF FORWARD PARTITIONING COEFFICIENT.....	47
EQUATION 3.9. DEFINITION OF KILNING MASS.....	48
EQUATION 4.1. PERPENDICULAR FLIGHT BASE ANGLE.	60
EQUATION 4.2. PERPENDICULAR FLIGHT TIP ANGLE.....	60
EQUATION 4.3. PERPENDICULAR FLIGHT BASE LENGTH.....	60
EQUATION 4.4. PERPENDICULAR FLIGHT TIP LENGTH.....	60
EQUATION 4.5. CALCULATION OF THE ANGLE OF ROTATION BETWEEN TWO FLIGHTS.	62
EQUATION 4.6. CALCULATION OF THE FLIGHT TIP RADIUS.	62
EQUATION 4.7. CALCULATION OF FLIGHT TIP ANGLE.	62
EQUATION 4.8. MAXIMUM HOLDUP IN A FULL FLIGHT.....	64
EQUATION 4.9. CALCULATION OF THE FIRST TRANSITION POINT, ψ_1	65
EQUATION 4.10. CALCULATION OF THE SECOND TRANSITION POINT, ψ_2	67
EQUATION 4.11. CALCULATION OF THE THIRD TRANSITION POINT, ψ_3	68
EQUATION 4.12. CALCULATION OF THE FOURTH TRANSITION POINT, ψ_4	69

EQUATION 4.13. CALCULATION OF THE FIFTH TRANSITION POINT, ψ_5	69
EQUATION 4.14. CALCULATION OF THE MAXIMUM FLIGHT HOLDUP BETWEEN ψ_1 AND ψ_2	73
EQUATION 4.15. CALCULATION OF THE MAXIMUM FLIGHT HOLDUP BETWEEN ψ_2 AND ψ_3	75
EQUATION 4.16. CALCULATION OF THE MAXIMUM FLIGHT HOLDUP BETWEEN ψ_3 AND ψ_4	76
EQUATION 4.17. CALCULATION OF THE MAXIMUM FLIGHT HOLDUP BETWEEN ψ_4 AND ψ_5	78
EQUATION 4.18. CALCULATION OF AVERAGE FLIGHT-TIP LENGTH.....	79
EQUATION 4.19. PORTER'S ASSUMPTION ⁵⁴	85
EQUATION 4.20. DETERMINING THE DESIGN LOAD OF A DRYER.	86
EQUATION 4.21. DESIGN LOAD OF A ROTARY DRYER.	86
EQUATION 4.22. CALCULATING FLIGHT LOADING FACTOR.....	87
EQUATION 4.23. RELATIONSHIP BETWEEN FLIGHT AND DRYER LOADING FACTORS.....	88
EQUATION 4.24. CORRELATION FOR THE MASS-AVERAGED FALL HEIGHT $(R^2 = 0.997)$	89
EQUATION 4.25. CORRELATION FOR THE MASS-AVERAGED FALL TIME $(R^2 = 0.996)$	90
EQUATION 4.26. CORRELATION FOR THE MASS-AVERAGED FALL ANGLE.....	90
EQUATION 4.27. CORRELATION FOR THE DRYER DESIGN LOAD $(R^2 = 0.999)$	90
EQUATION 4.28. CORRELATION FOR THE FLIGHT LOADING FACTOR $(R^2 = 0.991)$	90
EQUATION 5.1. LOCATING THE CENTRE OF MASS.....	95
EQUATION 5.2. RELATIONSHIP FOR THE DYNAMIC ANGLE OF REPOSE (SCHOFIELD AND GLIKIN ⁴).....	101
EQUATION 5.3. CALCULATION OF PARTICLE DENSITY.....	103
EQUATION 5.4. RELATING MASS FLOW RATE TO MOVING LAYER DIMENSIONS.....	157
EQUATION 6.1. HAIDER AND LEVENSPIEL CORRELATION ⁵⁶	162
EQUATION 6.2. FORCE BALANCE ON A FALLING PARTICLE.	163
EQUATION 6.3. CALCULATION OF DRAG FORCES BASED ON A DRAG COEFFICIENT.	163
EQUATION 6.4. EQUATION FOR DETERMINING THE DRAG COEFFICIENT.....	164
EQUATION 6.5. GENERAL FORM OF DRAG COEFFICIENT CORRELATION.	164
EQUATION 6.6. MODIFIED SCHILLER-NAUMANN EQUATION.....	167
EQUATION 6.7. RANS CONTINUITY EQUATION.	172
EQUATION 6.8. RANS MOMENTUM EQUATION.	172
EQUATION 6.9. EDDY VISCOSITY MODEL FOR REYNOLDS STRESSES.....	173
EQUATION 6.10. MODIFIED RANS MOMENTUM EQUATION.....	174
EQUATION 6.11. $k - \varepsilon$ MODEL FOR TURBULENCE VISCOSITY.....	174
EQUATION 6.12. TURBULENCE KINETIC ENERGY EQUATION.....	174
EQUATION 6.13. TURBULENCE DISSIPATION RATE EQUATION.	174
EQUATION 6.14. TURBULENCE PRODUCTION DUE TO VISCOUS AND BUOYANT FORCES.	175
EQUATION 6.15. INTERPHASE MOMENTUM TRANSFER COEFFICIENT ⁶⁷	175
EQUATION 7.1. CALCULATION OF EFFECTIVE FLIGHT TIP LENGTH.....	207

EQUATION 7.2. RELATIONSHIP BETWEEN DYNAMIC ANGLE OF REPOSE AND SOLIDS MOISTURE CONTENT ⁷² .	208
.....	208
EQUATION 7.3. ASSUMED MOISTURE CONTENT FUNCTION.	208

Nomenclature

A	- Area (m^2)
C	- Concentration (mol/L)
C_B	- Backmixing Partitioning Coefficient
C_D	- Drag Coefficient
C_F^G	- Reduction in Forward Partitioning Coefficient due to Drag
C_F^0	- Forward Partitioning Coefficient with no Drag
C_R	- Undisplaced Partitioning Coefficient
c	- Curtain Thickness (m)
D	- Diameter (m)
d_{load}	- Dryer Loading Factor
d_p	- Particle Diameter (m)
\bar{d}^0	- Average Forward Step of Material with no Gas Flow (m)
E	- Normalised Concentration
F	- Solids Flow Rate (kg/s)
F_D	- Drag Force (N)
f_{load}	- Flight Loading Factor
G	- Gas Flow Rate (kg/s)
g	- Acceleration due to Gravity (m/s^2)
H	- Flight Holdup (kg)
h	- Height (m)
k	- Turbulence Kinetic Energy per unit Mass (m^2/s^2)
L	- Length of Dryer (m)
M	- Total Mass (kg)
m	- Mass (kg)
N	- Cell Number
N_F	- Number of Flight in Dryer
R	- Radius of Dryer (m)
R_F	- Radius of a Flight Tip (m)
r	- Solids Volume Fraction

Re	- Reynolds Number
s	- Slope of dryer (mm/m)
s_1	- Base Length of a Flight (m)
s_2	- Tip Length of a Flight (m)
t	- Time (s)
\bar{t}	- Average Time (s)
U	- Velocity (m/s)
\forall	- Volume (m^3)
v	- Solids Velocity (m/s)
w	- Solids Moisture content (kg/kg)
x	- Length (m)

Greek Symbols

α_1	- Attachment Angle of a Flight to the Wall of the Dryer (degrees)
α_2	- Tip Angle of a Two-Section Flight (degrees)
β	- Solids Partitioning Coefficient
ε	- Turbulence Dissipation Rate (m^2/s^3)
θ	- Inclination of Dryer (degrees)
μ	- Kinetic Coefficient of Friction
ρ	- Density (kg/m^3)
ρ_b	- Bulk Density (kg/m^3)
ρ_p	- Particle Density (kg/m^3)
τ	- Mean Residence Time (s)
ϕ	- Solids Angle of Repose (degrees)
ψ	- Angle of Rotation (degrees)
ψ_{fl}	- Angle of Rotation between Flights (degrees)
ψ_{ft}	- Angle of Rotation Described by a Flight Tip (degrees)
ω	- Angular Velocity (radians/sec)

Subscripts

- a - Active Phase
- des - Design Load Conditions
- k - Kilning Phase
- m - Mass Averaged
- p - Passive Phase
- s - Solids
- t - Total

Abstract

This thesis presents the development and testing of a solids transport model for flighted rotary dryers based on the physical and geometric properties of the system. Particular emphasis was placed on understanding the internal flows and phenomena. An introduction to flighted rotary dryers is given in Chapter 1, where the context and relevance of this research is outlined. Chapter 2 gives a review of literature pertaining to the modelling and analysis of solids transport in flighted rotary dryers.

Chapter 3 discusses the development of the solids transport model based on the physical behaviour of a flighted rotary dryer. The solids transport model was developed based on numerical methods, dividing the dryer into a number of discrete slices, and each slice was further separated into two discrete phases. One phase selected to represent the material contained in the flights and in the bottom of the drum, whilst the other phase was selected to represent the solids falling through the moving gas stream. The flow of solids between phases was based on the physical movement of solids that occurs within an actual dryer. The magnitude of these flows was described using solid residence times and partitioning coefficients.

The solids transport phenomena occurring in the two phases were described using the geometry of the dryer and the physical properties of the solids. Chapter 4 presents a model for the unloading profile of a generic unserrated, straight, two-section flight, which was developed based on geometric analysis of the holdup within a flight. This unloading profile was then used to calculate the average fall path of a solid particle within a dryer, and thus the time spent within each phase of the dryer. Using measurements from CSR Invicta Mill's raw sugar dryer number 2, the average fall time of a particle was found to be in the order of 0.9 seconds, and the average time a particle spent in the flights to be in the order of 9 seconds. These residence times were then used to govern the flow of solids within the overall solids transport model, and the methodology describes a generic approach to modelling flighted rotary dryers.

A flight unloading apparatus was used to validate the geometric flight unloading model, the methods and results of which are presented in Chapter 5. The apparatus consisted of a 1m length of a full scale industrial dryer flight, which was rotated at a

controlled rate, and the rate at which material was discharged recorded. Tests were conducted using three different flight geometries and three different solid materials at rotational speeds between 1 and 8 rpm. It was found that the geometric unloading model accurately represents the experimental unloading profiles across the full range of conditions tested. High-speed photography was used to observe the solid material during unloading, and to measure factors such as the cascading curtain thickness, surface particle velocity and dynamic angle of repose. It was found that the dynamic angle of repose of the solids was dependent on the rotational velocity of the apparatus and showed significant variability. Surface velocities were found to be in the order of 1 m/s and surface thickness was found to be closely linked to the unloading rate of the flight. The data from these experiments was used in simulating interactions between gas and solids in the falling curtain in the following chapter.

Study of the high-speed photographs and unloading profiles revealed that the unloading of the flight was discontinuous, even though the materials used were generally regarded as free flowing. Observation of both the unloading profile and the high-speed images showed the flight unloading in pulses, with periods of high flow, and periods where less material was unloaded. This resulted in a varying material surface within the flight, which contributed to the high variability in measurements of surface properties. The effects of flight serrations and the methodology of modelling air drag in particulate curtains was also described.

Chapter 6 presents a study on using computational fluid dynamics (CFD) to simulate the gas-solids interactions within a falling curtain of solids. Experimental results from wind tunnel experiments conducted at Monash University, Melbourne, were used to verify and validate the CFD model. The simulated results showed good agreement with the experimental data for solids displacement and velocity. Data from the flight unloading experiments were then used to simulate the behaviour of the falling curtains of solids that occur within a rotary dryer. Simulations with a single curtain showed that gas-solids interactions were minimal for the conditions studied, with solids only being displaced in the first 10-20cm of the falling curtain. Simulation using multiple curtains in close proximity (50-80mm apart) showed that channelling of the gas flow between the curtains was significant (increases in gas velocity of up to 25% were

observed), and resulted in greater displacement of the falling curtains. However, limits on computational requirements prevented further study of this phenomena.

Chapter 7 presents the validation of the solids transport model using experimental data from an industrial flighted rotary dryer. The geometric flight unloading model was integrated into the overall solids transport model for a rotary dryer, and experimental data from Invicta Sugar Mill's dryer number 2 was used to statistically determine the remaining model parameters to validate the model. For a model using 33 slices, the kilning phase residence time was estimated to be 7.7 seconds, with 54% of the falling solids undergoing backmixing. It was found that the solids transport model provided a good fit to the experimental data, however it was unable to match the extended tail of the experimental curve. It was found that the number of slices used in the model to represent the dryer had a minimal influence on the quality of the statistical fit to the experimental data. Due to the inability of the solids transport model to match the extended tail of the experimental RTD, alternative model structures were considered and studied. However, the alternative model structures considered showed similar or poorer fits to the experimental data, and techniques to enhance the fit are described.

Further study of the model predictions revealed an improbable amount of kilning material within the dryer, with less than 5% of the solids within the dryer present in the falling curtains of solids. This in turn resulted in large amount of solids undergoing kilning, resulting in kilning being the dominant mode of solids transport within the model. This is believed to be unrealistic, and emphasised the need to undertake further experimental research into kilning and holdup in flighted rotary dryers. Based on the observations made in this thesis, a number of recommendations are made for the further development of solids transport models for rotary dryers, and these are presented in Chapter 8.

Chapter 1

1. Introduction

Flighted rotary dryers are used extensively in a range of industries for the control of temperature and moisture content of free flowing, particulate solids such as grains, sugar and mineral ores. Dryers range from small bench scale apparatus in pharmaceutical manufacture up large, 30m long, 6m diameter industrial ore dryers. Rotary dryers are commonly used due to their simplicity, low operational costs and flexibility to handle a wide range of throughputs and difficult feedstocks. Due to their size, rotary dryers often represent a significant capital expenditure, thus it is necessary to have a good understanding of dryer operations in order to ensure that the unit meets the desired requirements.

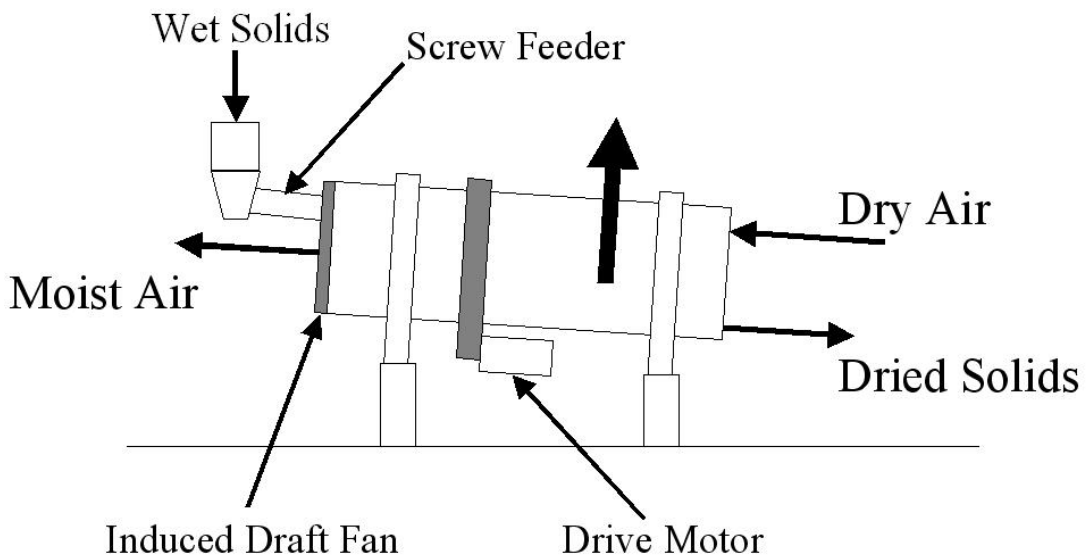


Figure 1.1. Schematic of a typical counter-current rotary dryer.

Many different types of flighted rotary dryers exist, including multi-pass units and units with centre fills. The simplest flighted rotary dryers consist of a rotating inclined drum with flights fitted to the internal walls. Moist solids are fed into the dryer at one end where it is collected in the flights of the dryer. These flights carry the solids into the upper half of the drum, where they are released in a continuous curtain across the

width of the dryer (see Figure 1.2). These particles fall under the influence of gravity and return to the floor of the dryer where they are collected once again by the flights. Axial transport of solids within the dryer is caused by the slope of the drum.

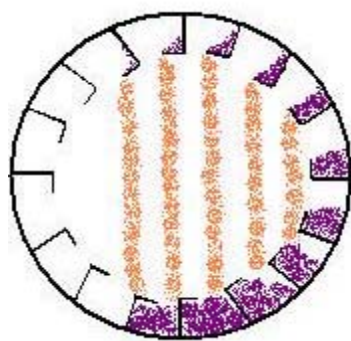


Figure 1.2. Cross section of an operating flighted rotary dryer.

Other types of rotary dryers may contain centre fills (a smaller shell in the centre of the drum), which may or may not have flights fitted to its external surface. In some cases this internal shell may be a flighted drum itself, with material travelling along this drum before being released into the outer drum, forming a multi-pass unit.

Drying gasses, commonly air or combustion gasses, are fed through the dryer either co- or counter-currently. These interact with the falling curtains of solids removing heat and moisture from the solids and creating drag forces that will influence the falling particles in the curtain, causing dispersion of the solids within the dryer.

Ideally, a rotary dryer would be operated such that every flight was filled to its capacity, allowing for the maximum amount of solids to be curtained at any point in time. In practice, however, rotary dryers are usually either underloaded, where there are insufficient solids to completely fill the flights, or overloaded, where there is more solids than the flights can carry. These concepts are illustrated in Figure 1.3. Underloaded conditions result in less solids entering the falling curtain, which leads to reduced drying time, while in overloaded conditions, the excess solids form a rolling bed on the floor of the dryer, which again limits the drying capacity of the dryer.

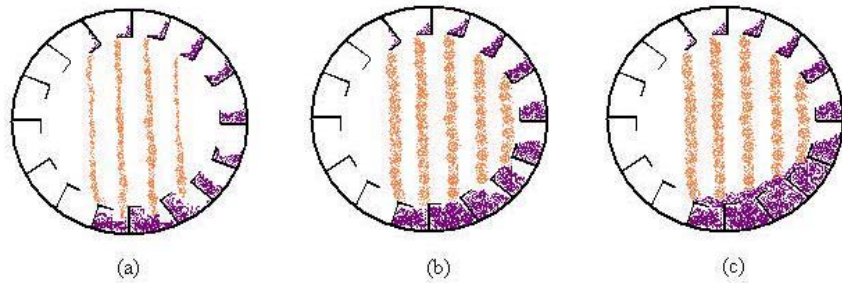


Figure 1.3. Load conditions within a flighted rotary dryer; a) underloaded, b) design loaded and c) overloaded operations.

Whilst flighted rotary dryers are widely used, their complex solids transport behaviour, and the difficulty of separating solids transport and heat and mass transfer phenomena within the dryer, has proved to be a significant stumbling block in the quest to understand their behaviour. Given the complex behaviour of flighted rotary dryers, and the lack of design and control procedures, there is a need for a model for flighted rotary dryers.

Despite the extensive use of rotary dryers in industrial applications for many years, a general model for a rotary dryer that is applicable to all dryer geometries and operating conditions has yet to be developed. A number of models have been developed for specific dryers and operating conditions, however these models are generally limited to a small range of conditions.

The aim of this thesis was to develop a solids transport model for a rotary dryer that could be applied to any sized dryer operating under any conditions. The following chapters discuss previous models for the solids transport in rotary dryers, and the development of a new solids transport model. The physical properties of the solids and geometry of the dryer were used to define the model parameters, and to allow the model to be fitted to any set of conditions and dryer dimensions. In order to validate the model, experimental data from an industrial flighted rotary dryer, located at CSR's Invicta Sugar Mill, was used.

Chapter 2

2. Literature Review

2.1. Introduction

A large amount of research has been devoted to studying and characterising the behaviour of rotary dryers. This literature review outlines the methods used to analyse the behaviour of rotary dryers and the various techniques that have been used to model various aspects of the operation of these units. Chapter 2.2 will discuss the importance of understanding the properties of the solid material in regards to the solids transport within a flighted rotary dryer. Chapter 2.3 will present the experimental methods for characterising the behaviour of flighted rotary dryers necessary for developing a useful model.

Chapter 2.4 will present a summary and discussion of the various approaches to modelling the solids transport occurring within flighted rotary dryers, highlighting the advantages and disadvantages of each. Chapters 2.5, 2.6 and 2.7 will discuss the modelling of the smaller scale solids transport phenomena that occur within a flighted rotary dryer, which contribute to the overall behaviour of the dryer and are important for developing an accurate model of the system.

2.2. Properties of Bulk Solids

To be able to understand a system involving the handling of bulk solids, it is important to understand the characteristics and behaviour of the bulk solids within the system. There are a number of properties of bulk solids that are important for understanding the behaviour of bulk solids, including voidage and bulk density, particle size and true density, particle shape, surface area and hardness, cohesion and adhesion, moisture content and safety hazards¹. All of these characteristics play an important role in the operation of rotary dryers, however the most significant of these are the bulk density of the solid, the cohesion and adhesion effects and the effect of moisture content on the solids.

The effects of cohesion and adhesion have a significant effect on the solids transport behaviour of a rotary dryer. This is most obviously evidenced by the angle of repose (ϕ_s) of the bulk solids. The static angle of repose of the solids represents the maximum angle of the free surface formed when the solids are poured into a heap. The angle thus formed is a property of the solid material, however this angle can be strongly affected by the condition of the material (e.g. moisture content) and the way in which the sloping surface is formed¹. For example, moisture content affects the adhesion between particles by adding surface tension effects which hold the particles together. This in turn increases the angle of repose of the solids as the additional adhesive forces help prevent the material surface from failing. Tegzes *et al.*² and Halsey and Levine³ both present experiments and discussion on the effects of thin liquid films (0 to 275 nm thick) on the angle of repose of granular media due to adhesive forces. Both articles identified three different regimes of behaviour in this range of film thickness, however in the case of rotary dryers, the film thickness is likely to be significantly larger due to the large amounts of moisture present in dryer feed stocks.

Many different methods have been developed for the measurement of the angle of repose for solids, the most common of which is the “poured” angle of repose¹, which is the angle between the surface of the material and the horizontal when the material is poured gently from a funnel onto a flat surface. Figure 2.1 shows a number of methods for determining the angle of repose for bulk solids (from Woodcock and Mason, 1987¹). The angle of repose for a solid can be used to give a qualitative guide to the flow properties of the bulk solids, as shown in Figure 2.1, however this approach should not be used as an accurate indication of flow characteristics¹.

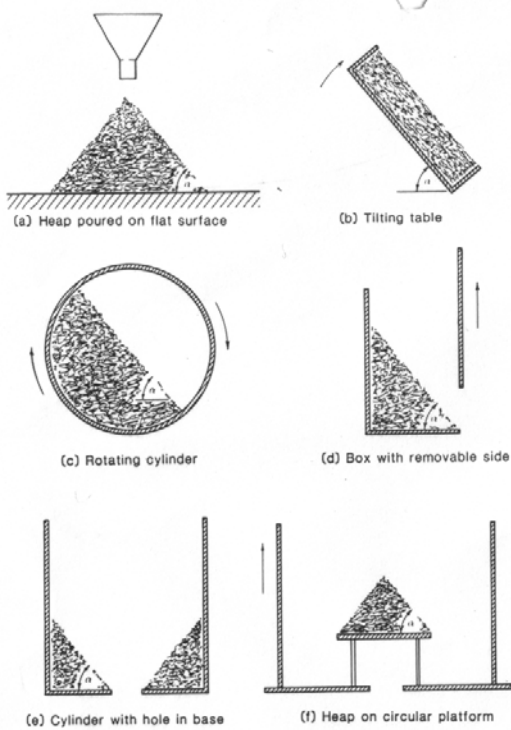


Figure 2.1. Experimental methods for determining the angle of repose (Woodcock and Mason, 1987¹).

Angle of Repose	Flow Characteristics
25-30°	Very free-flowing
30-38°	Free-flowing
38-45°	Fair flowing
45-55°	Cohesive
>55°	Very Cohesive

Table 2.1. Relationship between angle of repose and flow properties (Woodcock and Mason, 1987¹).

In rotary dryers however, the free surface of the solids is rarely static, as the material is constantly sliding off the face of the flight. In this case, rather than the static angle of repose, the slope of the surface is characterised by the kinetic angle of repose of the solid (ϕ). Schofield and Glikin⁴ derived a relationship for the kinetic angle of repose for particles in a flight, relating the kinetic angle of repose to the angular position of the flight around the drum, ψ , the diameter and rotational velocity of the drum, R and

ω respectively, and a property of the solid called the kinetic coefficient of friction, μ . The relationship is shown in Equation 2.1.

$$\phi = \tan^{-1} \left[\frac{\mu + \nu(\cos \psi - \sin \psi)}{1 - \nu(\mu \cos \psi + \sin \psi)} \right]$$

where $\nu = \frac{R\omega^2}{g}$

Equation 2.1. Relationship for the Kinetic Angle of Repose⁴.

Kelly⁵ developed an experimental method for measuring the kinetic angle of repose for a solid using a rotating drum. A number of cylinders with clear end caps were attached to the wall of the drum, each half filled with solids⁵, and the contents of the cylinders photographed as they rotated. These photographs were then used to measure the kinetic angle of repose of the solids, and hence the kinetic coefficient of friction.

2.3. Characterisation of Solids Transport

The first step in developing a model for any system is to gather experimental data that can be used to characterise the various aspects of the system that are to be considered. There are a number of approaches to characterising the solids transport behaviour of rotary dryers with varying degrees of difficulty and effectiveness.

The simplest method for gaining an understanding of the solids transport characteristics of a rotary dryer is the relationship between the feed rate, holdup and mean residence time of the dryer. The mean residence time for a unit describes the average time a particle spends within the unit, and is related to feed rate and holdup by Equation 2.2, where τ is the mean residence time, H is the holdup within the unit and F is the feed rate to the unit.

$$\tau = \frac{H}{F}$$

Equation 2.2. Calculation of the Mean Residence Time.

This method of characterising the solids transport behaviour of a dryer has the advantage of simplicity and is relatively easy to measure, however it does not give a lot of insight into the behaviour of the dryer. Most significantly, the mean residence time is only the average amount of time a particle spends within the dryer, and does not give any indication as to the dispersion of particles within the system.

A more useful method for characterising the solids transport behaviour of a system is to determine the residence time distribution (RTD) for the system, which describes the distribution of time particles spend within the dryer. Refer to Levenspiel⁶ for more information. The most common approach for determining the RTD is to add a tracer element to the feed stream to the dryer and to measure the concentration of the tracer element in the product stream. Using the concentration versus time data thus obtained, it is possible to develop the RTD for the dryer⁶ (see Figure 2.2). Using the RTD, it is then possible to calculate a number of statistical parameters which describe the shape of the distribution, including the mean residence time⁶ which is shown in Equation 2.3

where t represents time and $E(t) = \frac{C(t)}{\int_0^\infty C(t) dt}$ is the normalised tracer concentration ($C(t)$ is the tracer concentration at time t)⁶.

$$\tau = \frac{\int_0^\infty t \cdot C(t) dt}{\int_0^\infty C(t) dt} = \int_0^\infty t \cdot E(t) dt$$

Equation 2.3. Calculation of the Mean Residence Time from normalised tracer concentrations.

As can be seen from Figure 2.2 and other residence time distribution studies of rotary dryers⁷⁻⁹, there is significant dispersion of material within the dryer. The most significant features of the curve are the steep initial rise of the outlet concentration, as the front of tracer reaches the end of the dryer, and the extended tail of the distribution. These features indicate that there is little forward dispersion of the material, as the tracer material arrives in a concentrated front, and that there is no short-circuiting of material. However, the extended tail of the distribution indicates that there is significant backwards dispersion of material, presumed to be due to the effects of the counter-current airflow driving material back up the dryer.

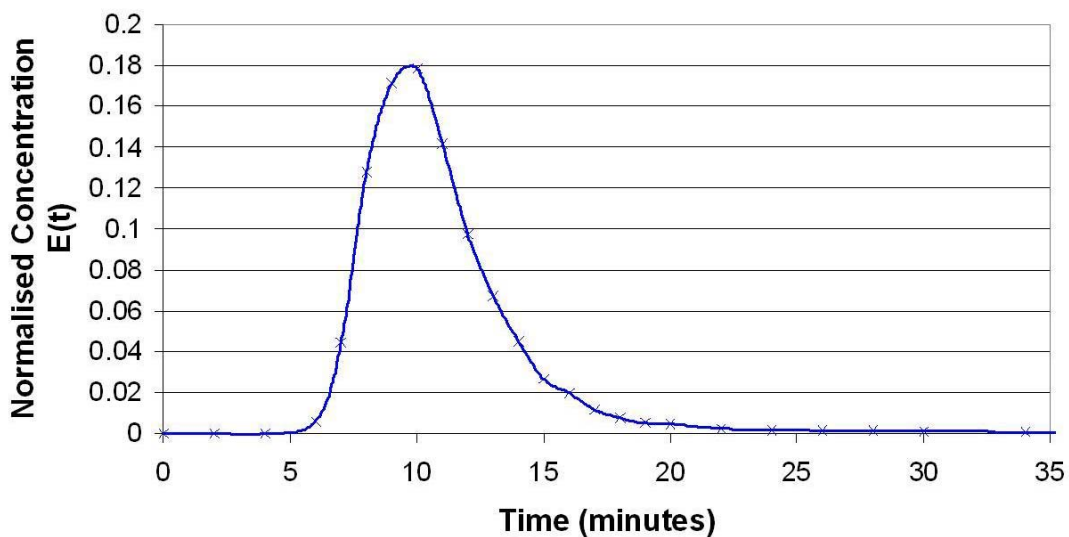


Figure 2.2. Residence time distribution for Invicta Sugar Mill dryer number 2 (Monro¹⁰).

2.3.1. Experimental Methods

Experiments form a significant part of any solids transport study, for without information on the systems behaviour it is difficult to gain any useful insight into unit operations. This section of the literature review will discuss the experimental methods used to measure the solids transport characteristics discussed in the previous section.

2.3.1.1. Industrial Scale versus Pilot Scale

Gathering useful data from industrial equipment can often be difficult, or even impossible, due to a number of reasons. Industrial operators are often unwilling to allow experiments to be conducted on their equipment due to problems such as productivity loss and changes in product composition. Additionally, industrial dryers are often difficult to control and lack instrumentation, making it difficult to accurately know the experimental conditions.

An alternative to conducting experiments on industrial dryers is to use pilot scale models of the system. This approach has the advantages of having complete and accurate control over all conditions affecting the dryer, and the freedom to make

changes as necessary. However, there are often problems with scaling the results of a pilot scale experiments to fit industrial scale systems.

2.3.1.2. Measuring Dryer Holdup

In almost every case, the feed rate of solids and gas to the dryer should be known with some accuracy when dealing with pilot-scale apparatus, however in industrial settings this may not be so easily determined. It is more difficult, however, to determine the mass holdup within a dryer, and a number of different methods have been developed in order to determine this. These include stopping the dryer and weighing the amount of material that remains within the dryer¹¹, stopping the feed to the dryer and weighing the material which subsequently leaves the dryer¹² and measuring the amount of power required to drive the dryer⁷. Given that these values can be measured, the mean residence time for the dryer can then be calculated. Inlet and outlet conditions are generally easy to obtain through sampling and simple instrumentation, although care must be taken to ensure that these samples are taken correctly.

Care must be taken to minimise measurement errors, as these can have a significant effect on the mass and energy balance used in modelling a dryer. Bazin *et al.*¹³ studied the propagation of random errors on the accuracy of mass and energy balance calculations for rotary dryers, as well as the effects of systematic errors. Measurements were taken from an industrial ore dryer and mass and energy balances were conducted and the predictions of these mass and energy balances studied to determine the effects of measurement errors. It was shown that small measurement errors were significantly amplified during the calculations¹³, and that many factors in dryer operations could lead to misleading instrumentation data. Bazin *et al.* specifically noted that thermocouple readings in the presence of radiation could deviate significantly from the actual temperature, and that infiltration of air from around the dryer seals could have a significant impact on the operation of a dryer¹³.

2.3.1.3. Measuring the Residence Time Distribution

Measuring the residence time distribution (RTD) of a dryer requires significantly more effort than measuring dryer holdup. In order to conduct a tracer study to determine the RTD for a dryer, a significant amount of preparation work is required, along with the time required to perform the experiment and analyse the results. Another problem associated with tracer studies on an industrial scale is the wariness of management at the idea of introducing a tracer material into their product. Levenspiel⁶ provides a good review of tracer studies and the analysis of tracer data and RTDs. A variety of tracer materials have been used to study the solids transport characteristics of rotary dryers. These include salts such as lithium chloride¹⁴, various forms of dyes¹⁵, glass beads¹⁵, radioactive materials¹⁶ and even moisture content⁸.

As stated by Levenspiel, experiments to determine the RTD can be carried out in two ways; pulse tests or step tests⁶. Pulse tests are the most commonly used as they require less tracer material and are simpler to conduct. The key criteria to a successful tracer study are;

1. There is limited dispersion between the injection point and the entrance to the system in question, and between the exit of the system and the sample point,
2. The system is operating at steady-state,
3. The tracer material does not affect the solids transport characteristics of the drying material.

It is necessary to determine an effective tracer material for use in the system in question, as poor choice of tracer can lead to poor results. Sheehan *et al.*¹⁴ compared the results of using a number of different tracers in an industrial sugar dryer. The tracers studied were lithium chloride, potassium chloride and water. It was shown that lithium chloride was a superior tracer in this situation, as the background levels of lithium in sugar are low, whilst both water and potassium have significant background concentrations¹⁴.

2.3.1.4. Dynamic Response Experiments

A simpler method for studying the solids transport characteristics of a system is to conduct step-change experiments on the system^{9, 10, 16, 17}. These experiments allow researchers to observe the dynamic response of the system, which can provide valuable information of the solids transport that occurs within the dryer. Whilst this information does not provide information on the RTD, when combined with tracer studies these experiments can be used to develop more realistic models for the system. Song *et al.*¹⁷ proposed a method for calculating the mean residence time of a system using step changes in feed rate, based on the similarities between a step change in the feed rate and a step tracer study. The results of this method were compared to data obtained from a tracer study on the same dryer, and were found to provide accurate and reproducible results¹⁷.

Dynamic experiments for characterising the solids transport in dryers offer significant advantages to tracer studies. Whereas tracer studies require large amounts of tracer material, and involve a large amount of preparation and testing, dynamic studies only require accurate measurement of inlet and outlet flow rates (which are generally required for tracer studies anyway). Also, dynamic studies can easily be conducted during start-up and shut-down procedures, meaning that they can be performed without affecting productivity. However, dynamic studies cannot provide the same level of information as tracer studies, meaning that if a detailed study of the dryer is required, it will probably be necessary to conduct tracer studies.

2.4. Modelling Approaches

As rotary dryers are used extensively in industrial applications, it is no surprise that a significant amount of research has gone into attempting to understand and to model the behaviour of these units. The main goals of these models have been to develop accurate predictions of the dryer holdup, mean residence time or RTD of the dryer. A wide range of approaches have been taken by various researchers in order to develop models for rotary dryers, ranging from simple correlations to complex mathematical and physical descriptions. These approaches can be grouped into four broad categories; empirical, mechanistic, statistical and dispersion based methods.

2.4.1. Empirical Models

The earliest methods used to model rotary drying operations were empirically based methods, using experimental data, often done on pilot scale dryers, to develop correlations between operating conditions and dryer design and the output of the dryer. A large number of these correlations have been developed over the years, many of which are still used industrially for the design and operation of dryers.

One of the earliest empirical correlation was developed by Miller, Smith and Schuette¹⁸, correlating the mean residence time, τ , with the geometry of the dryer as shown in Equation 2.4. Here L , D and s are the length, diameter and slope of the dryer respectively, ω is the rotational velocity of the dryer, ∇_{solids} is the volume of solids inside a flight, and k is a constant which depends on the number and shape of the dryer flights, and m is a constant which depends on gas flow. While this equation allows for predictions of the mean residence time within a dryer, the constants k and m must still be determined by fitting the model to experimental data from the specific dryer. This model also does not consider the effects of changing the solids or gas flow rates through the dryer.

$$\tau = \frac{kL}{sD\omega} + m\nabla_{solids}$$

Equation 2.4. Miller, Smith and Schuette Equation¹⁸.

Probably the most commonly used and cited empirical correlation is that of Friedman and Marshall¹¹ which correlates the total solids holdup in the dryer, M_T , with dryer geometry and operating conditions. Friedman and Marshall used a pilot scale rotary dyer to study the holdup of a range of materials under overloaded conditions. The Friedman and Marshall equation is shown in Equation 2.5, where F is the solids feed rate, G is the gas flow rate and K is an empirical constant. The \pm allows for co-current (-) and counter-current (+) airflow.

$$M_T = \frac{0.294LF}{s\omega^{0.9}D} \pm KG$$

Equation 2.5. Friedman and Marshall Equation¹¹.

The Friedman and Marshall equation is somewhat more useful than that of Miller *et al.*, as it allows for variations in the system with solids and gas feed rates, however it does not take into account the flight geometry of the system. The Friedman and Marshall equation can easily be rearranged in terms of mean residence time by dividing through by feed rate, which results in Equation 2.6, which is commonly reported in literature.

$$\tau = \frac{0.294L}{s\omega^{0.9}D} \pm K \frac{G}{F}$$

Equation 2.6. Alternate form of the Friedman and Marshall Equation.

More recently, the Friedman and Marshall equation was modified by Shahhosseini *et al.*¹⁹ to allow it to better represent a dynamic system. From Equation 2.6 it can be seen that if both the solids and gas feed rates are increased by proportional amounts ($\frac{G}{F}$ is constant), the Friedman and Marshall equation predicts that there will be no change to the mean residence time. In addition, the Friedman and Marshall equation predicts that solids feed rate has no effect on the mean residence time under zero gas flow rate conditions. Shahhosseini *et al.* introduced an additional term, γ , to account for variations in solids holdup under zero gas flow rate conditions¹⁹ and stated that $\frac{dM}{dt} = F_{in} - F$ and $F = \frac{M}{\tau}$, where M is the solids holdup in the dryer and F is the solids feed rate, resulting in Equation 2.7 where $\tan(\theta)$ is the slope of the dryer. Whilst this model addresses some of the shortcomings of the Friedman and Marshall model, it still does not consider the internal geometry of the dryer.

$$\tau = L \left[\frac{\alpha}{\tan(\theta)\omega^{0.9}D} + \frac{\beta(G + \gamma)}{D_p^{0.5}F} \right]$$

Equation 2.7. Modified Friedman and Marshall Equation¹⁹.

One of the most recent empirical models was developed by Alvarez and Shene²⁰ using a variety of materials in a pilot scale apparatus. From the experimental data, they developed Equation 2.8, where d_p is the average particle diameter, ρ is the density of the solids, s is the dryer slope and A_1 , A_2 , A_3 , A_4 , A_5 and A_6 are constants. The advantage of Equation 2.8 is that it allows for prediction of residence times for dryers with null slope and is applicable to a range of solid materials, however the large number of model parameters requires a significant amount of work in order to fit the model to a system.

$$\tau = \frac{A_1 d_p^{0.032} \rho^{0.956}}{F\omega(A_2 s + 1)} + \frac{A_3 d_p^{-0.065} \rho^{0.002}}{A_4 s + 1} - \frac{A_5 G^{0.5}}{A_6 s + 1}$$

Equation 2.8. Alvarez and Shene Equation²⁰.

Whilst empirical models are generally simple and easy to use, they are also limited in their applicability. In most cases, empirical correlations have been developed based on pilot scale experiments conducted over a limited range of dryer loadings and geometries. This leads to problems and errors when trying to apply these correlations to full-scale dryers and different loading conditions. In studies performed by Cao and Langrish²¹ and Renaud, Thibault and Trusiak²² it was shown that empirical models generally poorly predicted the mean residence time for a full scale dryer. Another weakness of empirical models is that they are quite often developed for only one feed material. There are some exceptions to this case, such as the Alvarez and Shene model²⁰, however most relationships given do not consider the effects of different feed materials.

2.4.2. Mechanistic Models

In order to address the limitations of empirical models, researchers^{4, 12, 23-26} began developing mechanistic type models, using physical and mathematical relationships to attempt to describe the solids transport within a dryer. These models generally take the form of equations relating the mean residence time of the dryer to various physical and geometric parameters, much like empirical models, however they generally include more complex relationships.

Schofield and Glikin⁴ developed a model for the mean residence time in a rotary dryer based on a “forward step” method. A physical analysis of the drag forces acting on falling particles in the falling curtain was used to calculate the average axial displacement of a particle in a single cascade (from when it leaves the flights to when it returns to the flights)⁴. Given this, and the length of the dryer, it is possible to determine the number of steps required for a particle to leave the dryer, and if the time taken for a fall is known, the mean residence time can also be calculated. This relationship is shown in Equation 2.9, where V is the superficial gas velocity in the dryer, h_{avg} and t are the average fall height and time of solid particles in the falling curtain respectively, ψ_{avg} is the average release point of the particles (measured from

the horizontal) and $K = \frac{1.5\phi \text{Re} \rho_{gas}}{d_p \rho_{solid}}$ represents the axial drag forces acting on the

particle due to the gas velocity. Schofield and Glikin determined the average fall time for a particle by multiplying the fall time at discrete points by the change in volume contained within a flight at these points, divided by the total volume discharged (i.e. a mass averaged fall time)⁴.

$$\tau = \frac{L}{h_{avg} \sin \theta - \frac{1}{2} KV^2 t^2} \left(t + \frac{\psi_{avg}}{180\omega} \right)$$

Equation 2.9. Schofield and Glikin Equation⁴.

Matchett and Baker^{12, 23} recognised that the solids transport within a dryer consisted of two phases; an “airborne phase” representing the solids in the falling curtain and a “dense phase” representing the solids in the flights of the dryer and rolling along the floor of the dryer. Whilst previous researchers had hinted at this dual nature of a dryer, most had assumed that the dryer could be accurately represented as a single-phase system, or had focused their attention on only one of the two phases²³. Matchett and Baker recognised that both phases had a significant impact on the solids transport, and that both needed to be treated individually. Utilising a range of physical and geometric relationships, Matchett and Baker proposed Equation 2.10²³, where t_a is the average time a solid particle spends in the airborne phase, v_s is the axial velocity of solids in the dense phase and α is a dimensionless parameter.

$$M_T = \frac{FL(2\omega t_a + 1)}{2\omega t_a \left(v_s + \frac{\alpha D \tan \theta}{2t_a} \right)}$$

Equation 2.10. Matchett and Baker Model²³.

Matchett and Baker validated their model using experimental data from two pilot scale dryers, achieving better than $\pm 20\%$ agreement between their experimental and predicted results¹². However, Matchett and Baker noted that the model did not consider the effects of drum geometry and number of flights on the solids transport in the dense phase, and that more information was required on the dense and airborne phase motions¹². Matchett and Sheikh²⁴ addressed some of these concerns, studying the effects of drum geometry and number of flights on the solids transport in the dense phase. Matchett and Sheikh proposed a number of modifications to the model of Matchett and Baker to account for the effects of drum geometry and number of flights, however they noted that their model lacked a mechanism for including variations in model parameters due to dryer throughput²⁴. Matchett and Sheikh also noted that the model assumed that the dryer holdup per unit length of flight was constant along the dryer, whilst evidence suggests that there is a material gradient along an inclined drum²⁴.

Following the lead of Matchett and Baker, Sherritt *et al.*²⁵ proposed another two-phase model for a rotary dryer based on the rate at which material is discharged from a flight. This model drew upon the work of a number of other researchers to develop a mechanistic representation of a dryer²⁵. The model was derived in general terms, relying on being able to mathematically describe the rate at which material was discharged from a flight as it traversed the drum, allowing the model to be applied to any dryer geometry. The performance of the model however was found to depend heavily on the drum configuration and loading conditions, with poor fits to the available data under certain circumstances²⁵. This was attributed to assumptions regarding the flow of material within non-discharging flights within the dryer.

Wang *et al.*²⁶ also developed a mechanistically based model for a rotary dryer using partial differential equations (PDEs) to describe the dynamic mass and energy balances present in the dryer. Mass and energy balances were developed for the dryer in the form of two-dimensional partial differential equations (time and axial position). Wang *et al.* used the Friedman and Marshall equation¹¹ to approximate the mean residence time for the dryer in order to solve the PDE system²⁶, whilst noting that the Friedman and Marshall equation did not account for flight geometry, and stated that further work would be required to improve this section of the model.

Studying the work of previous researchers, Wang *et al.*¹⁵ identified three key gaps in previous attempts to model rotary dryer. These were;

1. Lack of rigorous mathematical derivations in many papers. Wang *et al.* highlighted a shortfall in the geometric analysis of Sherritt *et al.*²⁷ and problems in discretising volume in some equations¹⁵. However, the most significant shortfall highlighted by Wang *et al.* was the use of average value approaches for falling particles (such as average fall time). This is obviously inadequate when dealing with systems with high dispersion around the mean¹⁵.
2. No model had been developed capable of handling arbitrary flight geometries¹⁵.

3. Researchers had studied particle transport and dryer dynamics separately¹⁵.

Addressing the gaps noted above, Wang *et al.*¹⁵ developed a model for the transport of solids through a rotary dryer based on analysing the rate at which solids were discharged from a flight. The model focussed on accurately measuring the rate at which solids were discharged from a flight, and used this to determine the axial velocity of the solids and the retention of solids within the airborne phase¹⁵. Wang *et al.* also modelled the dimensions and voidage of the solid curtain using an extreme value theory¹⁵. The results of this model were compared to experimental data from a pilot scale drying apparatus. Wang *et al.* reported that the simulated discharge rate deviated significantly from the observed experimental values, and thus the model accuracy could not be regarded as acceptable¹⁵. However, it was found that the simulated residence time for the pilot scale dryer was close to the observed experimental values (approximately 10% greater), and this difference was attributed to the effects of kilning and bouncing within the dryer, highlighting the significance of these modes of transport. Good agreement was also found between the simulated and observed curtain widths at a number of points in the dryer, which confirmed the validity of the extreme value method used by Wang *et al.*¹⁵. It was also observed that the particle density within the falling curtain was not constant, with the edges of the curtain having a lower particle density than the centre of the curtain¹⁵.

One common factor between many mechanistic and empirical type models is that they can generally only predict average, overall parameters, i.e. the total solids holdup or the mean residence time. This forces the assumption that all particles spend the same amount of time in the dryer, which is not the case as can be seen in typical RTDs (Figure 2.2). Additionally, the modelling of the overall behaviour of the dryer lumps all the material together, forcing the assumption that all material undergoes the same drying at all times. This is clearly not the case in a flighted rotary dryer, where the action of the flights periodically cascades the solids through the gas phase, promoting better heat and mass transfer. While this approach may be sufficient for developing control strategies or monitoring the operation of a dryer, this severely limits the accuracy of any heat and mass transfer correlations that may be applied to the model. There are some exceptions however, such as the model of Wang *et al.*²⁶.

2.4.3. Compartment Modelling

One approach used to overcome these limitations was to use compartment modelling techniques. This method assumes that the dryer can be divided into a number of discrete slices, and that each slice is then described using a combination of ideal reactors, with material flowing between slices. As each ideal reactor can be described using differential equations, this allows for a distribution of model parameters. A range of different compartment models have been developed in recent times using a wide range of approaches to simulate the solids transport in a dryer.

2.4.3.1. Theory of Compartment Modelling

Compartment modelling techniques draw strongly from conventional reactor design theory^{6, 28}. A number of different methods exist for modelling systems, including dispersion models, perfectly mixed vessels (CSTRs), plug flow reactors (PFRs), and laminar flow reactors. One of the most common methods used to model complex reactors, with a significant level of dispersion is to assume that the reactor can be modelled as a system of ideal reactors⁶.

The most common approach in compartment modelling is to use a Tanks-in-Series (TiS) model to represent the system. TiS models use a series of N CSTRs to represent the system in question^{6, 28}. This method is often chosen as it is the simplest method for modelling a system, both conceptually and computationally. TiS models have the advantage that development of the model is easy to follow, and do not require precise definition of the inlet and outlet boundary conditions²⁸. However, TiS models also have the drawback of requiring an integer value of N , which is a significant problem when N is small²⁸.

Two alternatives to the TiS type models are closed dispersion models and the Extended Tanks-in-Series (ETIS) model proposed by Martin²⁸. The closed dispersion model models the system using a dispersion coefficient and Fick's Laws of diffusion with bulk flow. Due to the need to solve partial differential equations, the closed dispersion model is often more computationally intensive than a TiS model, and it can

be shown that the closed dispersion model is equivalent to a TiS models when $N > 15$ ²⁸. Thus, the TiS model is generally simpler and less intensive to implement. The ETIS model (shown in Equation 2.11) is a generalisation of the TiS model which does not require an integer value for N , and given an integer value for N is identical to the equivalent TiS model²⁸.

$$E\left(\frac{t}{\tau}\right) = \frac{N^N}{\Gamma(N)} \left(\frac{t}{\tau}\right)^{N-1} e^{-N\theta}$$

Equation 2.11. Extended Tanks-in-Series Model²⁸.

One important fact to recognise about compartment based models, especially those that rely upon statistical fitting, is that there is no unique solution to fit the RTD for a given system. In most cases, there will be multiple solutions, often of widely differing structure, that can fit the RTD. In these situations, it is necessary to recognise that just because a model gives a good fit to the available data does not mean that it is representative of the system. Claudel *et al.*²⁹ present a good discussion of the difficulties in selecting a compartment-based model to represent a system. They recognise that consideration of the geometry and physical structure of the system is necessary in addition to RTD data in the development of compartment-based models²⁹. Claudel *et al.* also present a method for selecting model structures using possibility theory²⁹.

Martin²⁸ demonstrates how a basic analysis of the potential flows within a reactor can be used to aid the development of an effective compartment model for a complex reactor system. Martin demonstrated how individual flow phenomena within a reactor, such as inlet jets, short-circuiting flows and dead zones, could be represented by compartments and connected to give an accurate representation of the overall system²⁸. When linked with computational fluid dynamics, this has been termed the Network of Zones approach.

2.4.3.2. Compartment Models of Rotary Dryers

One of the simplest compartment models was reported by Kemp and Oakley³⁰ for use with dispersion type dryers. The model used a one dimensional incremental approach, dividing the dryer into a number of discrete slices along its length³⁰. The model treated solids transport as plug flow defined by a solids velocity, and contained equations for heat and mass transfer in each slice. The model required experimental data to determine a number of model parameters, however all these parameters had clear physical significance. Whilst the treatment of the solids transport in this model was rather rudimentary, this approach laid the foundations for the work that was to follow on compartment modelling of dryers.

Shahhosseini *et al.*³¹ developed a similar compartment model for a rotary dyer to that proposed by Kemp and Oakley. This model again treated the dryer as a number of discrete slices, with the mass flows in each slice defined using dynamic mass balances and the Modified Friedman and Marshall equation³¹. The parameters in the Modified Friedman and Marshall equation were calculated locally for each slice, rather than using global parameters as most previous models had. The model also used online data measurement to adaptively estimate model parameters, allowing for greater flexibility in the model³¹.

Didriksen³² proposed another model for an industrial beet pulp dryer based on mechanistic relationships. In this model, the dryer was again represented as a series of discrete slices, with the transport of solids between slices described using force balances on particles. Due to the mechanistic nature of the model, Didriksen noted that it would be possible to account for different residence times for different sized particles through the addition of extra force balances³².

Duchesne, Thibault and Bazin³³ studied the applicability of two different compartment type models for modelling a rotary dryer. The first model (Model A) was a simple tanks-in-series model, using single perfectly mixed tanks (CSTRs) in series to represent each slice of the dryer, while the second model (Model B), based on the work of Cholette and Cloutier³⁴, used pairs of perfectly mixed tanks which exchanged mass (see Figure 2.3) to represent each slice. Duchesne *et al.* proposed that

these pairs of tanks represent an “active phase” representing the falling curtain, wherein drying and axial transportation occurred, and a dead zone or “passive phase” representing solids contained within the flights of the dryer³³.

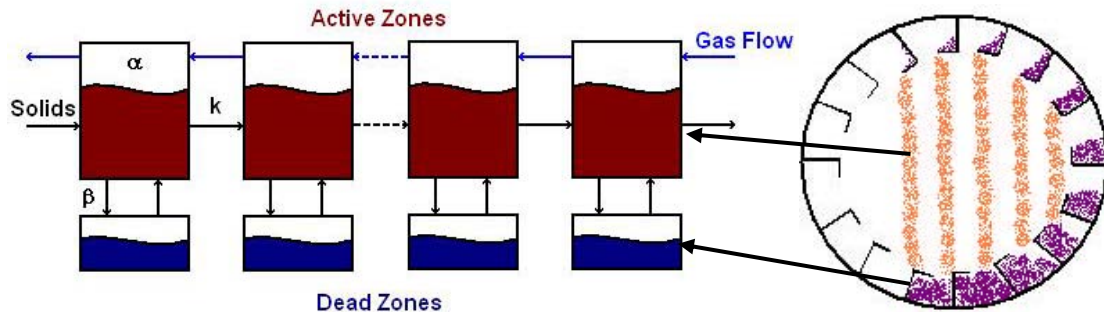


Figure 2.3. Modified Cholette-Cloutier Model³³.

Duchesne *et al.*³³ proposed that for Model B, axial transport of solids along the dryer was proportional to the bed mass gradient along the dryer, and that solids were partitioned between the active and dead phases according to two constants. Duchesne *et al.* then proceeded to compare the predictions of their models against experimental data³³ and concluded that Model A (CSTRs in series) was not capable of accurately reproducing the observed RTD, while Model B provided a good fit to the experimental data. Renaud *et al.*²² also compared the Modified Cholette-Cloutier model (Model B) against a number of empirical correlations using experimental data from an industrial ore dryer and concluded that the Modified Cholette-Cloutier model provided a good fit for the RTD.

In Australia, Monro¹⁰ studied the use of the Modified Cholette-Cloutier model for use with industrial sugar dryers. Comparing the predictions of the model with experimental tracer data from a full scale dryer¹⁴, Monro made a number of observations. Firstly, Monro identified that the model could not reproduce the initial sharp increase of the RTD, and also poorly reproduced the extended tail of the distribution¹⁰. Monro also noted that in order to fit the model to the data, an improbable bed depth profile needed to be assumed¹⁰. This is due to the proposed method of axial transport, where the axial transport rate is proportional to the bed depth gradient along the dryer, which implies that the bed depth must vary along the

length of the dryer. In practice, the bed depth within a rotary dryer is similar along its length, with the axial transportation of solids being due to the slope of the dryer.

Based on these observations, Schneider, Sheehan and Vigh³⁵ proposed a number of modifications to the model proposed by Duchesne *et al.*³³. In order to remedy the improbable bed depth profile, Schneider *et al.* proposed that the axial transport of solids occurred through the passive phase and was proportional to the mass holdup within a passive tank³⁵. It was also proposed that the exchange of mass between active and passive tanks be governed by the mass holdup in each phase³⁵, rather than be a direct partitioning of solids as proposed by Duchesne *et al.*³³ (see Figure 2.4). The accuracy of the model proposed by Schneider *et al.*³⁵ was studied by Schneider, Sheehan and Brown³⁶ based on the experimental data of Sheehan *et al.*¹⁴ using a numerical process modelling package (gPROMS^(R)). Schneider *et al.* reported that the modified model was capable of accurately reproducing the experimental RTD, however further work was required to improve and to properly validate the model. Lee *et al.*³⁷ continued the work of Schneider *et al.*³⁶, further optimising the model. Lee *et al.* also combined the Friedman and Marshall correlation with the model to account for variations in gas flow rate through the dryer and added an additional parameter to account for the effects of the kilning bed³⁷.

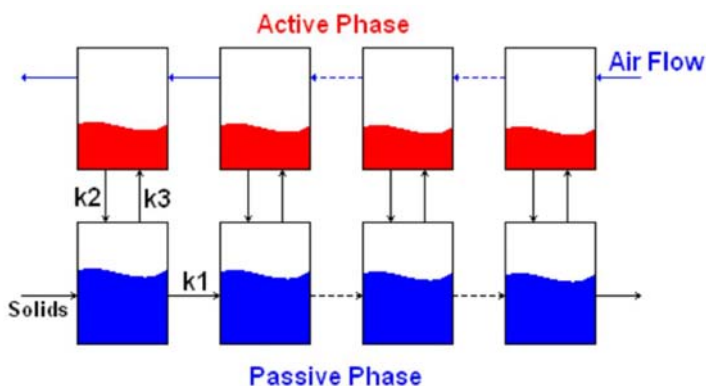


Figure 2.4. Model proposed by Schneider *et al.*³⁵

Whilst these models have been shown to provide accurate fits to the RTD, all are statistically based, and as such it is difficult to determine whether they actually provide a representation of the physical behaviour of the actual dryer. Sheehan *et al.*³⁸ studied the work of Lee *et al.*³⁷ and noted that the model predicted significantly lower

rates of solids transport between the active and passive phases than would be found in an actual dryer. In order to address this matter, Sheehan *et al.* proposed that all solids transport within the model could be described using geometric and mechanistic relationships³⁸, similar to the method proposed by Wang *et al.*¹⁵. In order to be able to reproduce the RTD using this modified model, a number of additional material flows were introduced, in order to better represent the physical behaviour of the model, as shown in Figure 2.5. Firstly, the axial flow of material was proposed to occur between active and passive cells of subsequent slices (flow 1 in Figure 2.5), representing the axial motion of falling solids due to the slope of the dryer. It was also proposed that material leaving the active phase would also be partitioned between the passive phase of the current slice (flow 2), and the previous active phase (flow 3) to represent back mixing of solids. The kilning flow proposed by Lee *et al.*³⁷ was retained (flow 4), as was the flow of material between the passive and active phases of each slice (flow 5) representing the release of solids into the falling curtain.

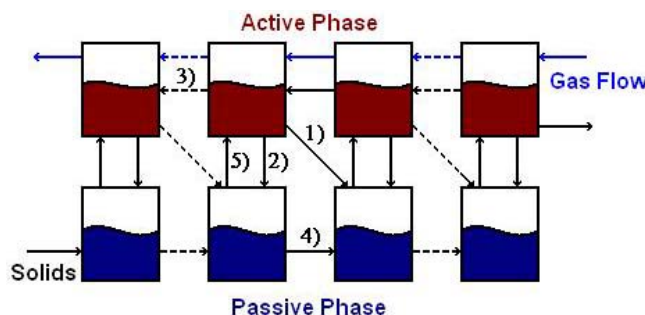


Figure 2.5. Model proposed by Sheehan *et al.*³⁸

Sheehan *et al.* reported that this model could also reproduce the experimentally observed RTD, however a number of parameters still required the development of a mechanistic description and were fitted statistically³⁸.

2.4.4. Summary of Modelling Methods

A number of different approaches have been taken to model the solids transport within rotary dryers, each with their own advantages and disadvantages. Empirical models are the simplest and easiest to use, however are generally very limited in

application. Mechanistic models are generally more complex, yet provide more general solutions, however often only provide overall predictions, forcing the assumption that all solids remain in the system for the same amount of time. Compartment type models can simulate the distribution of solids throughout the system, however to date have relied solely on statistical fitting of parameter values.

Each approach has advantages and disadvantages, yet it would be good to develop an approach that combines the advantages of each, without the disadvantages. The model of Sheehan *et al.*³⁸ demonstrated that it was possible to combine a compartment model structure with mechanistic descriptions of material flows to provide a model that could simulate the dispersion of solids without the need for statistical fitting of parameters.

2.4.5. Multi-Scale Modelling

In recent times, there has been a trend towards using multi-scale modelling techniques. Multi-scale models attempt to represent a system by studying the behaviour of the system at different scales^{39, 40}. Multiscale models are composite models composed of two or more submodels that describe phenomena at different scales³⁹. These “scales” represent different phenomena and are generally defined by a characteristic time or length of the objects and phenomena being represented³⁹. Examples of different scales that may be used within a model include inter-particle interactions, unit geometry and molecular level interaction to name but a few. More complex models exist which may use five or more levels of detail⁴⁰.

The use of multi-scale modelling allows researchers to attempt to build more accurate mechanistic representations of a system by building up the model in smaller stages. Each stage is in itself a mechanistic description of phenomena that occur within the system, which when linked together will hopefully provide an accurate representation of the whole. Multi-scale models can be constructed in four ways; bottom-up, top-down, concurrent and middle-out³⁹. Each method has advantages and disadvantages and will be better suited to some applications.

The model proposed by Sheehan *et al.*³⁸ is an example of top-down multi-scale modelling, where a large scale model of the system was constructed (compartment model) and then refined by adding smaller scale models, as discussed in the following sections.

2.5. Modelling of Flight Holdup

In order to better understand the solids transport occurring within a rotary dryer, a large amount of research has been focused on modelling the solids holdup profile within a flight as the flight travels around the circumference of the drum.

To be able to model the flight holdup and discharge, it is first necessary to determine how much solids can be contained within a flight at any time, and to understand the flow characteristics of the solids. The primary solids characteristic affecting this is the kinetic angle of repose of the solids in a flight. This determines the natural slope of the material surface that will be formed as the flight travels around the drum's circumference, and hence the amount of material that can be contained in a flight. This can then be used to study the unloading profile of the flight, which gives an insight into the interactions between drying gas and solids, and the heat and mass transfer phenomena. Using the equation derived by Schofield and Glikin⁴ for the kinetic angle of repose, Kelly⁵ developed a theoretical flight design which would create an even distribution of solids across the entire falling curtain, thus improving the efficiency of the dryer.

Revol, Briens and Chabagno⁴¹ further developed the previous work done in this field, developing correlations to determine the solids holdup in a flight with any number of segments. These correlations were then used to develop equations for the solids flux across the drum, and the power required to lift the solids and rotate the drum. The predictions of these equations were then compared to experimental data from a pilot scale apparatus⁴¹. Revol *et al.* reported that the correlations developed could accurately predict the power required to operate the dryer, however the predicted solids flux differed significantly from the observed flux⁴¹. This difference was attributed to the effects of the flight walls on the kinetic angle of repose⁴¹.

Wang *et al.*¹⁵ developed a model for the unloading of a two-section flight based on a geometric analysis of the material within the flight. Wang *et al.* calculated the cross-sectional area of solids contained within the flight and a function of flight location (ψ) and material angle of repose (ϕ). The cross-sectional area was then used to determine the discharge rate from the flight using Equation 2.12¹⁵. Wang *et al.* assumed that the material surface was defined by the material angle of repose and the flight tip, which neglects the presence of any material flowing over the flight tip. Attempts were made to compare the model to experimental data, however large amounts of error precluded making any conclusions.

$$F = -\rho_b \omega \frac{dA(\psi, \phi)}{d\psi}$$

Equation 2.12. Flight discharge rate based on cross-sectional area of solids¹⁵.

2.6. Modelling of Kilning Beds

One aspect of the solids transport occurring within rotary dryers that has not been considered in detail is the flow of solids within the kilning bed within an overloaded dryer. Some researchers, such as Friedman and Marshall¹¹ have developed empirical models of overloaded dryers, however, few have considered the mechanics of the kilning bed. A large amount of research, however, has gone into studying the solids transport in unflighted rotating drums. In these drums, solids are transported solely through the effects of kilning.

Jones *et al.*⁴² presented a preliminary study of the effects of lifters on the behaviour of a kilning bed using discrete element modelling (DEM) techniques. Jones *et al.* reported that the lifters had a significant effect on the behaviour of the kilning bed, with the simulations showing complex flow patterns and an increase in mixing within the bed⁴².

2.7. Drag Effects on Falling Particles

One of the most significant factors affecting the solids transport in rotary dryers is the effect of airflow on the falling particles in the dryer. As the particles are released from a flight, they enter the moving airstream, where they will be influenced by drag forces, as shown in Figure 2.6. The particle will experience drag forces due to the movement of the gas stream, as well as drag forces due to its vertical motion.

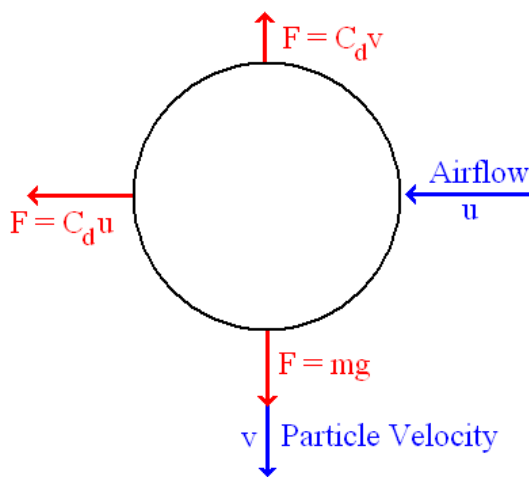


Figure 2.6. Diagram showing forces acting on a falling particle in a moving air stream.

In a flighted rotary dryer, particles are released in a relatively dense curtain, which will cause a significant resistance to airflow, which will result in a lower gas velocity within the curtain than in the bulk flow, as suggested by Kelly and O'Donnell²⁷. Additionally, in many industrial processes, there will be variation in particle sizes, which in turn leads to variations in the drag forces each particle will experience. Simply put, larger particles will be almost unaffected by the moving gas stream, while smaller particles will undergo significant displacement, or even entrainment in the gas stream. Finally, as the particles are released continuously across the dryer, some particles will fall further than others, and will thus be exposed to the effects of drag for longer periods, thus increasing the displacement of these particles. The combination of these effects results in both a back mixing of solids (in the case of a counter-current dryer), as well as a dispersion of particles due to the variations in magnitude and duration of these drag effects.

In order to be able to mechanistically account for the effects of the gas flow on the falling particles, it is necessary to develop a model for the drag forces acting on the particles. The earliest approaches to modelling solids transport, such as Friedman and Marshall¹¹ used a purely empirical approach, which although satisfactory in many cases, does not give any real insight into the phenomena occurring inside the dryer.

In general, drag forces acting on a particle are determined using a drag coefficient, C_d , using the equation $F_D = \frac{1}{2} \rho C_D A v^2$ where F_D is the drag force, ρ is the density of the fluid, A the cross sectional area of the particle facing the flow and v the velocity of the particle. Drag coefficients have been calculated for many different geometries and can be easily found in literature⁴³. Under most circumstances, it is found that the drag coefficient is not constant as the particle accelerates, thus most drag coefficients are expressed as functions of the Reynolds number⁴³, $Re = \frac{\rho v D}{\mu}$.

2.7.1. Integration of Drag Effects on Solids Transport

The first attempts to physically analyse the effects of drag forces on the particles in rotary dryers assumed that each particle could be treated separately as an isolated falling sphere using the Schiller-Naumann equation⁴⁴ (see Equation 2.13). The Schiller-Naumann equation was used to determine the change in the average distance a falling particle travels along the dryer during a single fall, and from that determine the average residence time of the solids^{4, 45}. This approach, however, was found to over predict the effects of drag by a significant factor. This was attributed to the particles falling in a curtain, thus most particles are shielded from the full effects of the gas stream, reducing the displacement of material. Due to this, it was proposed by Kelly and O'Donnell²⁷ that the gas stream velocity within the falling curtain of solid particles was lower than the average gas velocity, and thus that the gas velocity in the open channels was higher than the average gas velocity.

$$C_D = \frac{24}{Re} \left(1 + 0.15 Re^{0.687} \right)$$

Equation 2.13. Schiller-Naumann Equation⁴⁴.

An alternative approach to modelling the drag effects was proposed by Baker⁴⁵, who treated the falling curtain as a flat, double-sided plate. Baker compared the theoretical results of this approach and those of the Schiller-Naumann equation with experimental data⁴⁵. Baker reported that neither model could satisfactorily represent the observed data, with the mean residence time predictions from the isolated sphere model being 1 to 2 orders of magnitude greater than the experimental results⁴⁵. The results of the flat plate assumption were shown to underpredict the observed mean residence time, however the results were in much closer accord with the observed results than those of the isolated sphere model⁴⁵.

Sherritt⁴⁶ experimentally studied the effects of the rate of solids release, the bulk gas velocity and the fall height of material on the axial displacement of material. In these experiments, a variety of solids were cascaded through a wind tunnel and the axial distribution of particles measured using load cells²⁷. From these experimental results, Sherritt *et al.*²⁷ reported that the Schiller-Naumann equation with a single reduced gas velocity within the falling curtain could accurately predict the axial displacement of the solids. Using least squares regression, Sherritt *et al.* reported a correlation for a velocity correction factor, $c_v = \frac{U_c}{U_g}$ where U_c is the gas velocity in the material curtain and U_g is the bulk gas velocity, which is shown in Equation 2.14.

$$c_v = 1.546 h^{0.76} F_f^{-0.86} L^{-0.44}$$

Equation 2.14. Velocity correction factor²⁷.

Wardjiman *et al.*⁴⁷ also studied the interaction of gas and solids in a wind tunnel. In their experiments, a solids curtain was cascaded across the entire width of the experimental apparatus, and the falling curtain monitored using high-speed cameras⁴⁷. The results of these experiments were compared to theoretical predictions for the displacement of a single isolated particle⁴⁷. Wardjiman *et al.* reported that the leading

edge of the falling curtain was generally well represented by isolated spheres for all the studied solids flow rates. At relatively low solids mass flow rates, the isolated sphere model significantly under-predicted the displacement of the trailing edge of the curtain, however this improved with higher solids flow rates⁴⁷. This study does not directly apply to the solids curtains in a rotary dryer, as in this study, the gas flow was perpendicular to the face of the solids curtain, whereas in a dryer, the flow is parallel to the curtain face.

2.8. Summary of Literature Review

This literature review has highlighted the importance of understanding the bulk properties of the solids, and how these affect the solids transport within a dryer. Care must be taken to ensure the correct values of these parameters are known and used, otherwise a model cannot accurately represent the system.

Reviewing the different modelling techniques used, it is clear that each approach has its advantages and disadvantages. Empirical models are simple to use and develop, however they provide little insight into the behaviour of the system and are often limited to a small range of conditions. Mechanistic models allow for more detailed modelling of the system, allowing the model to be applied to a wider range of conditions. However, mechanistic models still suffer from the shortcoming of only providing an overall description of the system. Compartment models have the advantage of providing more detail of the internal behaviour of the dryer and can model dynamic responses, however often lack physical definition. This can be overcome by including physical and geometric models describing the solid flows within the model. Due to their ability to predict residence time distributions and solids transport at different points within the system, a compartment model was chosen for this thesis, using physical and geometric description of solid flows.

This review has shown that a number of researchers have demonstrated that geometric methods can be used to model the unloading of a flight. These methods will be used to develop a model for the unloading profile of the flight, and this information used to describe the solids transport occurring due to the action of the flights.

Little work has been done on kilning beds in flighted rotary dryers to date, and no models have been developed and validated for this mode of solids transport. Given the large amount of work required to study this, the scope of this thesis will be limited to the action of the flights, and kilning transport will be statistically estimated by comparison to experimental data.

The literature reviewed has demonstrated the importance of the gas-solids interactions in solids transport in flighted rotary dryers, and a wealth of information is available in this area. Current modelling approaches have been shown to be unsatisfactory in representing these interactions, so a different approach will be taken in this thesis. Computational fluid dynamics will be used to model the gas-solids interactions, and the results compared to experimental data.

3. Dryer Model Development and Simulation

3.1. A Numerical Approach to Modelling a Rotary Dryer

The compartment based approach to modelling rotary dyers, such as that used by Duchesne *et al.*³³, Schneider *et al.*³⁵ and Sheehan *et al.*³⁸, has been shown to provide accurate predictions of the solids transport in rotary dryers. However, this method relies upon the assumption that the dryer can be reasonably modelled as a series of interconnected tanks. Whilst this method has been shown to work in a number of situations, there do remain some questions as to the physical meaning of these models. In order to address this matter, a numerical approach similar to that used in finite element modelling was used to discretise the rotary dryer into slices. The solids transport within these slices and between neighbouring slices could then be studied to develop a model for the overall dryer.

3.1.1. Defining Dimensions

As a rotary dryer is a three-dimensional object, a comprehensive model of a dryer would need to be three-dimensional in order to capture the full detail of the solids transport. However, developing a full three-dimensional model of the solids transport within a dryer is a challenging task, and may not be necessary to provide accurate results.

At first glance, it may appear that a cylindrical coordinate system would be most applicable to a rotary dryer. However, as the vertical motion of falling particles is a significant factor in modelling the solids transport in a dryer, a Cartesian coordinate system will be used in this thesis. Figure 3.1 shows the coordinate system used in developing the model in this thesis. The x-coordinate is along the axis of the dryer, and thus describes the axial motion of solids. The y-coordinate is perpendicular to

this, and thus almost vertical (offset by the slope of the dryer, θ), and describes most of the vertical motion of the particles due to gravity. The z-coordinate is horizontal, such that flights in the upper section of the drum travel in the positive z-direction. This results in a left-handed coordinate system, which is tilted slightly from vertical, with the origin located at the centre of the upper end of the drum.

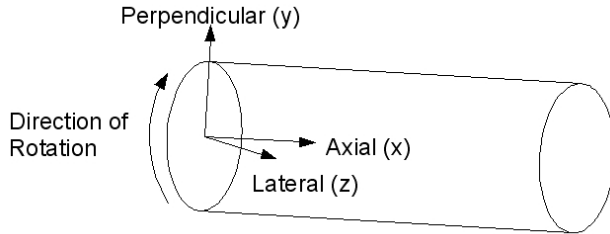


Figure 3.1. Dimensions used in developing the model.

Most, if not all models, for rotary dryers to date have only considered the x-coordinate of the dryer, dealing with the other two dimensions at a distance, if at all. The most common approach has been to use averages, such as the average fall time of particles, to account for the effects of the y- and z-coordinates. By utilising variables such as the average fall time and fall height of particles, the y-coordinate becomes unnecessary, and similarly, the need for the z-coordinate can be removed through averaging the gas-solids interactions across the drum.

3.1.2. Model Development

Consider a small element of a rotary dryer of length dL , such as that shown in Figure 3.2. Within this element there will be two phases of material; a passive phase containing the solids held within the flights of the dryer, and an active phase containing the falling material. Solids can be transported into and out of these phases in a number of ways, both between phases within the same element, and into neighbouring elements. For the passive phase, solids may enter either through kilning from the previous dryer element, or from the active phase as solids fall to the floor of the dryer. Solids may be transported out of the passive phase through discharge from the flights into the active phase or by kilning into the next dryer element.

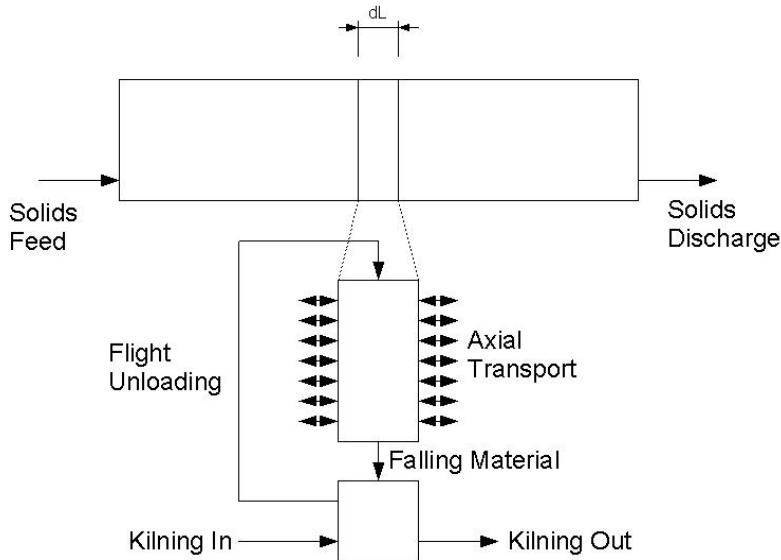


Figure 3.2. A slice of a dryer.

The active phase will receive solids from the passive phase through discharging flights and return them to the passive phase as they fall to the floor of the dryer. Solids will also be transported axially to the neighbouring dryer elements through effects such as the inclination of the dryer and gas-solids interactions.

3.1.3. Modes of Solids Transport

It can be easily appreciated that modelling the solids transport in three dimensions would be a complex and daunting task. More importantly, the computational requirements of such a model would probably exceed any benefit gained over a simpler one dimensional model similar to those already published.

To date, many researchers have addressed this by using the average fall path of a particle (see Figure 3.3). Using the average fall path of a particle, the time spent in the active phase can be calculated, as can the rate of axial advance of falling solids under the influence of gravity due to the slope of the dryer. Doing this eliminates the need to consider the y- and z-coordinates within the solids transport model (These will be considered in the smaller scale models, i.e. flight unloading). However, using the average fall path method assumes that all solids follow the same path, thus solids will remain within the same active phase for the duration of their fall.

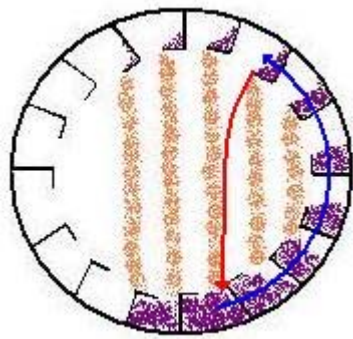


Figure 3.3. Example of the average particle fall path.

As a particle discharged from a flight in one dryer element may end up in the passive phase of another element due to axial transport, it is therefore necessary to distribute the discharge from the active phase to any passive phase that material could potentially be transported to. It is therefore necessary to determine how far material can be transported as it falls in the active phase. As each active phase must be connected by a solids transport flow to every potential receiving passive phase (and each flow requires another solids transport coefficient), this could result in a large number of criss-crossing solids transport streams. However, if the maximum distance solids can be transported axially is less than dL , then the furthest solids can be transported is into the neighbouring dryer element, as shown in Figure 3.4. This results in a model structure similar to the compartment models proposed by Schneider *et al.*³⁵, Lee *et al.*³⁷ and Sheehan *et al.*³⁸, which is shown in Figure 3.5.

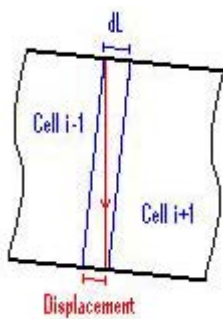


Figure 3.4. Maximum axial advance compared to cell length.

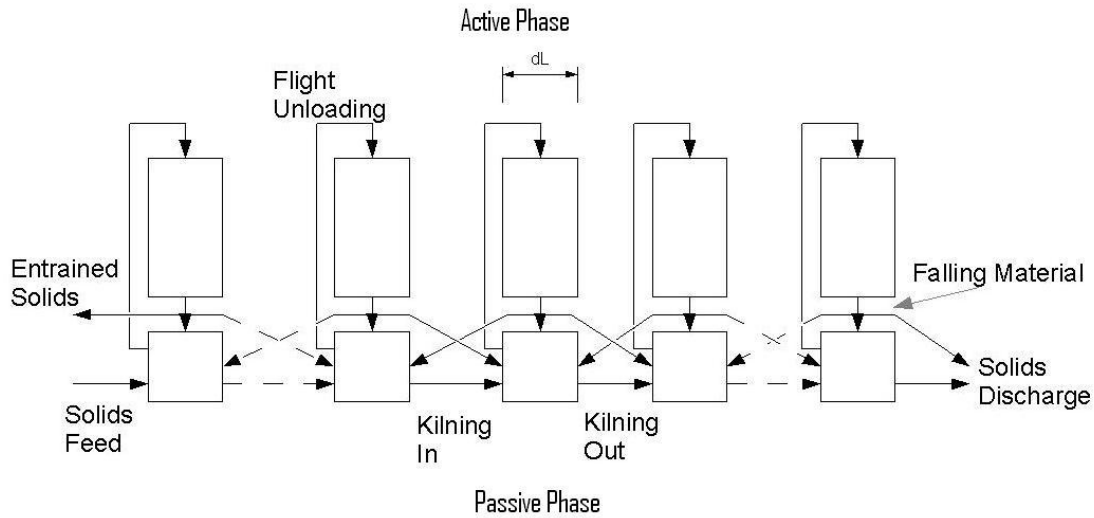


Figure 3.5. One-dimensional numerical model.

3.1.4. Describing the Behaviour of the Phases

It is also necessary to consider the internal behaviour of each element in the model, considering how the solid material moves through each different part of the dryer. Previous researchers, such as Duchesne *et al.*³³, Schneider *et al.*³⁵ and Sheehan *et al.*³⁸, assumed that both the active and passive phases within a rotary dryer could be adequately modelled as perfectly mixed tanks (i.e. that the solids within each phase were perfectly mixed). Lee *et al.*⁴⁸ highlighted the fact that this assumption is clearly not true for the active phase in a dryer, where there is no mixing of solids. Lee *et al.*⁴⁸ suggested that plug flow was a more appropriate assumption for the active phase, however upon comparison of the two types of models, Lee *et al.*⁴⁸ concluded that the results (i.e. RTDs) of the two models were the same. However, the computational demands of the model with plug flow were significantly greater than those of the model using only mixed flow.

Considering the numerical model developed above, the accuracy of these assumptions can be assessed. For the passive phase, if it is assumed that the heat and mass transfer occurring in this phase is negligible, then as the length of the element, dL , tends to zero then the variation in the solids properties will be negligible and the solids can be assumed to be homogeneous (perfect mixing). This will not occur in the current model, as dL is limited by the maximum forward step as discussed above, however, due to the complexity of the real system, it will be assumed to be an adequate

approximation. Thus, in this case a CSTR is suitable for modelling the passive phase. For the active phase however, it is obvious that the properties of the solids will change as they fall, due to heat and mass transfer, as was highlighted by Lee *et al.*⁴⁸. In the limit as dL tends to zero, the axial variation between neighbouring active phases becomes negligible, but the variation in the other dimensions remains significant.

Fortunately, within a single active phase, the temperature and moisture properties of the solids have little to no impact on the solids transport as the fall rate of the particles is solely dependent on drag forces (which are governed primarily by particle size). Whilst moisture content can have a significant effect on the way in which solids are released from the flights (e.g. clumping of cohesive solids), these only affect the initial release of the solids. That is, once the solids have been released into the active phase, changing the moisture content has no significant effect on the way the particle falls until it returns to the passive phase. Thus, in terms of solids transport the active phase can be sufficiently modelled as homogeneous in a one-dimensional model. It must be noted however, that this is not true when modelling the heat and mass transfer operations in the active phase as these are dependent on the temperature and moisture properties, thus the assumption of homogeneity is not applicable in these situations.

Based on these assumptions, each phase in the model can be described using simple dynamic mass balances, i.e. $\frac{dm}{dt} = F_{in} - F_{out}$. This allows the prediction of dynamic responses to changes in operating conditions, if the mass flow rates into and out off each phase are known.

3.2. Quantifying the Modes of Solids Transport

Defining the model structure and the modes of solids transport is only half the problem, as it is still necessary to quantify the solids transport that occurs. Sheehan *et al.*³⁸ proposed that all modes of solids transport that occur within a rotary dryer could be quantified based on physical and mathematical relationships.

3.2.1. Form of the Solids Transport Equations

Generally, previous researchers using compartment type models for rotary dryers (Duchesne *et al.*³³, Schneider *et al.*³⁵, Lee *et al.*³⁷, and Sheehan *et al.*³⁸) have assumed that the solids transport out of a compartment is proportional to the mass contained within that compartment, i.e. $F = kM$ where F and M are the flowrate from and holdup within the compartment respectively, and k is the solids transport coefficient, a constant. This can be rearranged to show that $k = \frac{F}{M} = \frac{1}{\tau}$ where τ is the residence time of the solids in the compartment, giving Equation 3.1.

$$F = \frac{M}{\tau}$$

Equation 3.1. General equation for the rate of solids transport.

3.2.2. Effect of Dryer Loading on Flight Unloading

Lee *et al.*⁴⁹ highlighted the fact that the transport of solids from the passive phase into the active phase is limited by the maximum amount of material that can be contained in the flight. As the loading of a dryer is increased, there comes a point where a flight entering the upper half of the drum cannot contain anymore solids, which is referred to as the design load point. Any increase in dryer loading beyond this point cannot be contained in the flight and lifted into the upper half of the drum to be released into the active phase, and will remain in the bottom of the drum as a bed of solids.

This means that the transport of solids into the active phase must be limited once the design load point is reached. By defining $M_{p,des}$ as the mass contained in the passive phase at the design load point, the transport into the active phase can be defined using the conditional equations given in Equation 3.2. The definition of $M_{p,des}$ will be discussed in Chapter 4.4.

$$F_{p \rightarrow a} = \frac{M_p}{\bar{\tau}_p} \quad M_p < M_{p,des}$$

$$F_{p \rightarrow a} = \frac{M_{p,des}}{\bar{\tau}_p} \quad M_p > M_{p,des}$$

Equation 3.2. Definition of solids transport into active phase.

3.2.3. Passive Cycle Time

Using the average fall path approach discussed earlier, it can be seen that there will be a corresponding average time spent within the passive phase. This will be defined by the time taken for a flight to travel between the point where a particle enters the passive phase, and the point where it is once again discharged into the active phase, as shown in Figure 3.6.

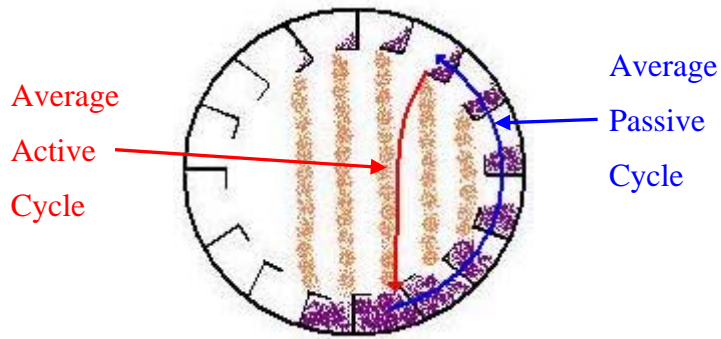


Figure 3.6. Average active and passive cycle times.

The first step in determining the average cycle path of a particle is to determine the point at which the particle leaves the flight. The most common approach to this has been to use a mass averaged method, using Equation 3.3. Here, $\bar{\psi}_m$ is the mass averaged fall point, ψ is the angle of rotation of the flight, H is the mass contained in the flight as a function of ψ and H_0 is the mass contained within the flight at a given starting point (generally as the flight passes into the upper half of the drum as shown in Figure 3.7). The following chapter will discuss the calculation of H and H_0 .

Next, it is necessary to determine where the material returns to the passive phase ($\bar{\psi}_r$). Calculation of the average point at which material returns to the drum is dependent upon a number of factors, including the velocity of material as it leaves the flight tip and drag effects in the active phase. Assuming the horizontal movement of solids in the active phase is negligible, the average point at which material returns to the drum will be vertically opposite the mass averaged release point, i.e. $\bar{\psi}_r = 180^\circ - \bar{\psi}_m$. In most dryers there will be noticeable horizontal movement of solids due to the velocity of the flight during unloading and the velocity of the solids as they leave the tip of the flight. However, this requires significantly more calculation, as drag forces must be accounted for, for a relatively small increase in accuracy (<10%). Knowing the angular velocity of the drum, the average residence time of the solids in the flights (passive cycle time) is given by Equation 3.4, where ω is measured in degrees/sec.

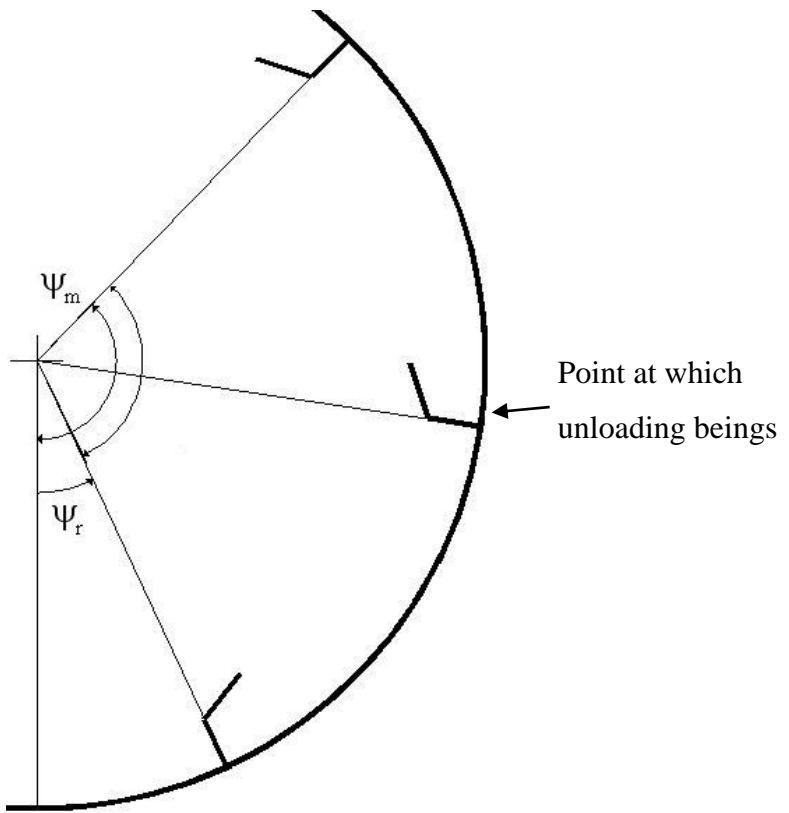


Figure 3.7. Average fall point and passive cycle arc.

$$\bar{\psi}_m = \frac{\int_0^{H_0} \psi dH}{H_0}$$

Equation 3.3. Calculation of Mass Averaged Fall Point.

$$\bar{\tau}_{\text{flight}} = \frac{2\bar{\psi}_m - 180^0}{\omega}$$

Equation 3.4. Average residence time of flighted solids.

This gives the average residence time of material within the passive phase, thus the rate of solids transport out of the passive phase due to the action of the flights is given

by $F_{p \rightarrow a} = \frac{M_p}{\bar{\tau}_{\text{flight}}}.$

For an underloaded dryer, where there are not enough solids to completely fill the flights, flights will not begin unloading until they are in the upper section of the drum (beyond the normal starting point). In these situations, dH in Equation 3.3 will be equal to zero up until the point where the flights begin to unload. Thus, $\bar{\psi}_m$, and hence $\bar{\tau}_{\text{flight}}$, are affected by flight loading. This will be discussed further in Chapter 4.

3.2.4. Active Cycle Time

The average residence time of the solids material in the active phase will equal the average fall time of a solid particle. Using the average fall point and the initial velocity of the solids, the equations of motion can be used to calculate the fall height and time of the solids.

Again assuming the particles have negligible initial velocity, and drag is also negligible, the average fall height can be calculated via simple geometry to give Equation 3.5. Then, using the equations of motion, the mass averaged fall time can be calculated as shown in Equation 3.6. Equation 3.5 also assumes that the particle is

returned to the passive phase as it passes the radius of the flight tip at the bottom of the dryer. This is reasonable, as any remaining fall height before the solids lands in the flight will be small. However, in dryers with significant kilning beds, the fall height may in fact be less than this, as the kilning bed may cover the flights in some cases. In these situations, the falling solids will return to the bed before they reach the flight tip radius.

$$\bar{h}_m = \frac{R_F}{\cos(\theta)} \left[1 + \sin \left(\frac{\int_0^{H_0} \psi dH}{H_0} \right) \right]$$

Equation 3.5. Calculation of Mass Averaged Fall Height

$$\bar{t}_m = \sqrt{\frac{2\bar{h}_m}{g}}$$

Equation 3.6. Calculating mass averaged fall time.

Additionally, whilst the material falls in the active phase, it also travels axially along the dryer due to the inclination of the drum. Based on the geometry of the dryer and the average fall height, it is possible to calculate the average axial transport of solids under conditions of zero airflow. Using the mass-averaged fall height of the material, \bar{h}_m , and the inclination of the dryer, θ , the average axial displacement under zero airflow conditions (\bar{d}^0) can be found using $\bar{d}^0 = \bar{h}_m \sin \theta$. This can then be used to determine the fraction of falling material that leaves a cell (i) in the compartment model and enters the next cell ($i+1$) by comparing the average displacement to the length of a cell (dL), as shown in Equation 3.7.

$$C_F^0 = \frac{\bar{d}^0}{dL} = \frac{\bar{h}_m \sin \theta}{(L/N)}$$

Equation 3.7. Forward Axial Partitioning Coefficient with Zero Airflow.

3.2.5. Effects of Gas-Solids Interactions

As was discussed in Chapter 2, a number of researchers have studied the effects of the gas-solids interactions in the active phase on the solids transport operations within a rotary dryer. Obviously, the moving stream of drying gasses will result in a displacement of the falling solids due to drag effects.

The most significant effect of the gas solids interactions is the axial displacement of solids due to drag forces, and previous research has demonstrated that the gas-solids interactions within a rotary dryer are complicated. Simplifications of the system, such as the extremes of assuming isolated spherical particles (maximum drag) or flat-plate behaviour (minimum drag) (Baker⁴⁵), are generally insufficient.

As an alternative to a rigorous fluid dynamic model, Sheehan *et al.*³⁸ proposed that the effects of the gas-solids interactions be modelled using empirically fitted partitioning coefficients, representing the total falling fraction of material being distributed into different solid flows (i.e. forwards, backwards and vertical), as shown in Figure 3.8. Thus, the amount of material flowing in each direction will be equal to the partitioning coefficient multiplied by the total flow leaving the active phase, i.e. $F_x = C_x F_a$. Given that the total flow leaving the active phase is split between the three

solids flows, i.e. $F_a = \frac{M}{\bar{t}_m} = C_F F_a + C_R F_a + C_B F_a$, it can be seen that $C_F + C_R + C_B = 1$.

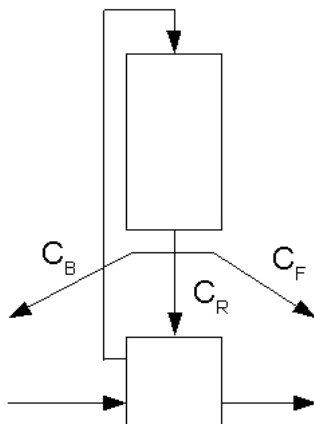


Figure 3.8. Axial transport partition coefficients.

The type of airflow used within the dryer (i.e. co- or counter-current airflow) has a significant impact on the partitioning coefficients. If the dryer is operated co-currently, then no material will be transported backwards along the dryer, as the gas-solids interactions will increase the forward displacement of solids. In a counter-current dryer however, there will be backmixing of solids due to gas-solids interactions, and the forward displacement of solids will be decreased. From Equation 3.7 the value of C_F under zero airflow is known, thus Sheehan *et al.*³⁸ proposed that the forward partitioning coefficient could be defined as shown in Equation 3.8, where C_F^G is the change in C_F^0 due to the gas-solids interactions.

$$C_F = C_F^0 C_F^G$$

Equation 3.8. Definition of Forward Partitioning Coefficient.

For their publication, Sheehan *et al.*³⁸ used statistical fitting to determine the partitioning coefficients for their model, however they suggested that, in future, mechanistic means could be used to calculate these values.

The other effect of the gas-solids interactions is the change in the fall height of the material, and thus the fall time. As material falls in the active phase, the axial displacement of the solids due to gas-solids interactions will result in a change in the distance the material falls. For example, if material is displaced forward along the dryer, the particles will have further to fall due to the drum floor sloping downwards

towards the discharge end. However, due to the small slope of the dryer (θ is generally less than 4°), a significant axial displacement would be necessary to cause a significant change in the fall height of the particles, thus this change can generally be neglected (for example, with a 4° inclination, a 1 m axial displacement of solids results in a 0.07 m increase in fall height).

3.2.6. Solids Transport via Kilning

The final mode of solids transport within a rotary dryer is via kilning of solids along the bottom of the dryer, and within the flights. In the past, researchers have studied either underloaded dryers, where it is assumed that there is no kilning, or overloaded dryers where kilning is significant. Few researchers have developed models applicable in both regimes.

Lee *et al.*⁴⁹ and Sheehan *et al.*³⁸ assumed that kilning could be represented in a similar fashion to the other modes of solids transport, using a kilning phase and solids transport coefficient. The kilning phase is modelled as an extension of the passive phase, and assumed to exist only in overloaded dryers, i.e. when $M_p > M_{p,des}$ (see Chapter 4.4 for the definition of $M_{p,des}$). Under these circumstances, the total mass in the passive phase is divided into flighted mass, which is fixed at $M_{p,des}$, and a kilning mass (M_k) as shown in Equation 3.9.

$$M_p = M_{p,des} + M_k$$

Equation 3.9. Definition of kilning mass.

As kilning occurs due to the slope of the dryer, all material within the passive phase will undergo some degree of kilning transport, including the material within the flights. Thus, the solids transport due to kilning can then be calculated in the same

way as for the other solids flows, such that $F_k = \frac{M_p}{\tau_k}$. However, τ_k may be a function of dryer loading, with higher levels of loading experiencing greater kilning flows, due

to the presence of a kilning bed, thus reducing τ_k (greater kilning means a lower residence time).

3.3. Process Simulation using gPROMS[®]

Simulation of the various models used in this thesis was done using the gPROMS[®] (General PROcess Modelling System) numerical modelling package produced by Process Systems Enterprise Limited. gPROMS[®] is a numerical modelling package designed specifically for use with process systems involving systems of algebraic, differential and partial differential equations, and is optimised for these systems. The gPROMS[®] code used for this thesis is reproduced in Chapter 10, and will be referenced in this section as examples.

gPROMS[®] uses a modular structure for the development of process models, with models consisting of a number of different types of entities including model, process, estimation and experimental entities. Model entities represent the inner working of the process, and can be built in a single entity or in a modular form. Process entities provide the operating conditions for the system, such as initial conditions, control parameters and other solver information. Estimation and experiment entities are used for parameter estimation and optimisation procedures, with the estimation entity containing the guesses and solution parameters for the procedure and the experiment entity containing the experimental data. Flows of materials (or data) between model entities are represented using “streams”, which simply carry values (or information) from one model to another.

The modular nature of coding in gPROMS[®] has a number of advantages. Firstly, each submodel can be modified to test different types of models with little to no effect on the rest of the model, and addition of other submodels (for example a kilning phase) is easy. The modular nature also means it is very easy to change the number of slices used to model the dryer, as it is only necessary to change one number in the overall model, rather than significantly modifying the model structure.

A more detailed description of the modelling process using gPROMS[®] and the structure on individual entities will be given in the following sections. The gPROMS user guides^{50, 51} also provide good descriptions of the modelling process and a number of useful examples.

3.3.1. Model Entities

Each model entity contains the equations that govern the behaviour of the model, as well as the structure of the streams that connect the model to other models. In the case of models containing partial differential equations (PDEs), the model entity also contains information on the solution method for the PDEs. Examples of Model Entities used in this thesis can be found in Chapter 10.2.

Model entities are laid out in a number of sections, each detailing a separate aspect of the model. The sections used in the simulation of the three compartment models were Parameter, Distribution Domain, Unit, Variable, Stream, Set, Boundary and Equation, and these sections are discussed below.

The Parameter section lists any global parameters that are referred to in the models (see next section for the definition of model parameters) that have been defined in the Process entity. The Distribution Domain section defines any domains required for distributed variable and PDEs in the model and gives the upper and lower limits on this domain. The Unit section defines any submodels that will be used within the current model and gives these models an identifying name that will be used within the model equations. Units can either be singular, or an array of units. The Variable section lays out all the variables that will be used within the model, including both controlled and process variables.

The Stream section of the model defines any Streams (i.e. material or data flows) entering or leaving the model entity, and states the variables that are contained within the Stream.

The Set section of the model entity defines the approximation method to be used for any distribution domains used in the model. This includes the method of approximation for the derivatives (e.g. forward difference method), the order of the solution (first, second order derivatives, etc.) and the number of solution points to use in the approximation.

The Equation section of the model entity contains all the equations that make up the model. These may be algebraic, differential (w.r.t. time) or PDEs. These equations do not have to be laid out in a specific format, as gPROMS® is designed to solve simultaneous equations (i.e. equations do not have to take the form $x = f(\dots)$).

3.3.2. Parameters and Variables

There are a number of different types of parameters and variables that are used in gPROMS® to represent different aspects of the operation. Parameters are globally defined values that do not change during the simulation of the process. Parameters are defined as being either Real numbers, Integers or Logical values, which limits the value that these can take. Parameters may also be defined as arrays of values.

Variables in gPROMS® can be grouped into two types; controlled variables which are defined by the process entity and describe variables that can be directly controlled, or process variables which can vary as the simulation proceeds. All variables in gPROMS® are defined using a unit type which are defined by the user in the Variable Type entities section. Variable types are used to define units for the variable and to ensure that the correct variable type is being used in Stream definitions in the models.

Variables may also be defined as arrays of values, or as a distributed variable for use in PDEs. Distributed variables are variables that vary continuously along a defined domain (e.g. velocity along a fall path) and use Distribution Domains described in the relevant section of the gPROMS® model.

3.3.3. Process Entities

Process entities contain information of the operating procedure and solution methods for the overall model. Similar to model entities, process entities are also divided into a number of sections. The sections used in the simulation of the compartment models were Unit, Parameter, Monitor, Set, Assign, Initial, SolutionParameters and Schedule. The Process Entity used in this thesis is shown in Chapter 10.1.

The Unit section defines the model entities that will be used in the process. Units can either be singular, or an array of units. The Parameter section defines all the parameters that will be used in the process and the Monitor section list all the variables that are to be monitored during the simulation.

The Set section assigns values to all the parameters defined in the parameter section and the Assign section assigns values to all the controlled variables in the process. Any variable given a value in the Assign section will not vary during the simulation unless it is reassigned a value in the Schedule section.

The Initial section specifies initial values for process variables in the process. It is important to note here that this section controls the degrees of freedom of the process. It is necessary for there to be zero degrees of freedom in the process, otherwise the simulation will not run.

The SolutionParameter section defines any solution procedures that are desired. This includes defining which numerical solver the simulation should use (if undefined gPROMS® will use the default solvers), any output channels to use (for example results can be output to Excel®) and the reporting interval to be used in reporting results (i.e. the time interval between each reported value for a variable).

Finally, the Schedule section defines the process to be simulated. This section allows the user to specify changes to controlled variables at specified time intervals, or to implement trigger conditions to trigger changes in control variables (e.g. a control system).

3.3.4. Estimation and Experiment Entities

One feature of using gPROMS[®] is the ability to statistically determine values for parameters in the model by fitting the model to experimental data. To do this, gPROMS[®] uses Estimation and Experiment entities⁵¹. In order to perform a parameter estimation, the parameter(s) to be estimated must be defined as variable in the model (this is because parameters in the model have a fixed value and can not be changed). The Parameter Estimation and Experiment Entities used in this thesis are shown in Chapters 10.3 and 10.4 respectively.

The Estimation entity defines which variables (parameters) are to be estimated and gives upper and lower limits for the estimation and an initial guess for each variable. The Estimation entity also defines the measured variable used in the Experiment entity, the estimation method to be used along with any solution parameters and the name of the Experiment entity to be used in the estimation procedure.

Experiment entities contain the experimental data in the form of a time value and a process variable value (the process variable used is defined within the entity as well). In addition to this, the Experiment entity describes how the controlled variable (e.g. the tracer concentration in the feed for a tracer experiment) changes during the experiment (e.g. for a pulse tracer experiment the tracer concentration will initially be zero, before being briefly increased as the tracer pulse is added at a given time, before returning to zero).

3.3.5. Other Entity Types

There exist a number of other less important entity types that have been mentioned above, such as Stream and Variable Type entities. These entities are relatively simple and are part of the mechanics of the gPROMS[®] system and thus will not be dealt with in detail. There are also a number of entity types that were not used in this thesis, and these are not included in this discussion.

3.3.6. Numerical Solvers in gPROMS[®]

gPROMS[®] provides a number of different inbuilt numerical solvers for linear, non-linear and differential-algebraic equations, as well as the facility to include custom built solvers. Details on the different solvers and their applicability is given in the gPROMS[®] Introductory User Guide⁵⁰.

From Parameter Estimation experiments, gPROMS[®] has a single inbuilt solver routine based on the maximum likelihood approach⁵¹. gPROMS[®] allows the user to specify several different statistical variance models for the experimental data used in the process. The options available are Constant Variance, Constant Relative Variance and Heteroscedastic models, and each are discussed briefly below. For more details see the gPROMS[®] Advanced Users Guide⁵¹.

A Constant Variance model is used for data where the variance (standard deviation squared) of the data is constant for the entire experiment, i.e. the absolute measurement error is constant. A Constant Relative Variance model is used where the magnitude of the error is dependent on the magnitude of the measured (or predicted) value, i.e. a constant relative measurement (or predicted) error. Heteroscedastic models are used if the measured (or predicted) values have different variances. It is important to specify the variance model as accurately as possible, as it can have a significant effect on the final result⁵¹.

3.3.7. Drawbacks to gPROMS[®]

Whilst gPROMS[®] is specifically designed for use in solving process based models, and provides an excellent system for the solution of many simple process problems, it lacks a number of features which are available in more conventional programming languages. Due to its nature as a simultaneous equation solver, gPROMS[®] has difficulty implementing many iterative solution methods that are trivial to implement in general programming languages. One simple example of this is the common $a = f(a)$ type iterative solution using a FOR, WHILE or IF loop. As gPROMS[®]

solves all equations simultaneously, these types of iterative solutions must be modified, otherwise the problem becomes unsolvable (as the value of a depends upon itself). It is possible to solve these types of iterative solutions in gPROMS[®] using arrays of values (i.e. $a_i = f(a_{i-1})$) however this requires additional computing resources and can rapidly become complicated.

3.3.7.1. Interfacing with Excel[®]

Another feature in the gPROMS[®] package is the ability to interface with a number of external software packages and programmes, such as Excel[®] and Fortran and C⁺⁺ programmes. This allows more difficult programming tasks, such as iterative calculations, to be outsourced to packages better suited to solving them. gPROMS[®] refers to these external programmes as Foreign Objects, which are called as part of the Process Entity. Once a Foreign Object is set up, the Model entities can pass values to or collect values from the Foreign Object freely.

It was found that Excel[®] could successfully be used to implement the geometry model and interface with the gPROMS[®] model. However, as each slice of the dryer needed to gather individual data from the geometry model, the number of Foreign Object calls that were required was significant. Due to this, the amount of processor time required to run a simulation was high, and it was eventually decided that a simpler approach would provide adequate results for significantly less simulation time. Due to this, the iterative geometric model was replaced by a correlation between the geometric values and the required outputs (see equations in Chapter 4.5 for examples of correlations used).

3.4. Model Implementation using gPROMS[®]

3.4.1. Model Structure

gPROMS[®] models is well suited to the implementation of compartment type models due to its modular structure. In this thesis, each compartment type (passive phase and active phase) was modelled as a separate model entity in gPROMS[®]. This allowed for

the equations governing each phase to be easily located and changed without affecting the rest of the model. Each slice of the dryer was then modelled using a separate model entity which combined the submodels (active and passive phase) as shown in Figure 3.9. The entire dryer was then modelled by connecting a number of slice models in series.

Figure 3.9 shows the different sub-models (Active Phase, Passive Phase and Dryer Slice) with streams connecting these components. The blue lines represent streams of material flowing between model components. It can be seen that multiple slice models can be connected in series by connecting the outlet streams of one slice model to the input streams of the next.

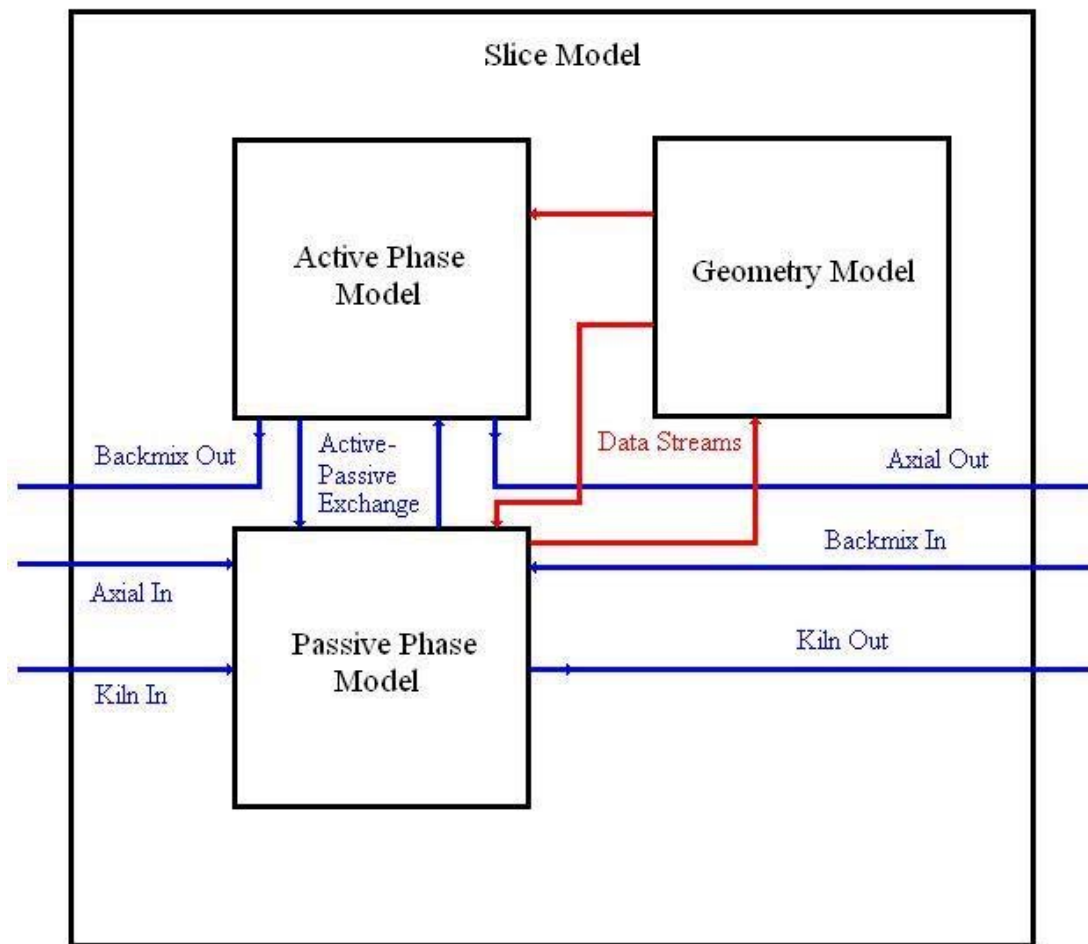


Figure 3.9. Diagram of Model Structure.

Chapter 4

4. Geometric Analysis of an Unloading Flight

Most models developed for rotary dryers developed to date have relied on empirical methods. This is especially true of compartment type models, and the models of Duchesne *et al.*³³, Schneider *et al.*³⁶ and Lee *et al.*³⁷ all used statistical fitting of experimental data to determine values for the solids transport coefficients in their models. Whilst these methods have shown the ability to reproduce the experimental data for which they were derived, the high degrees of freedom involved in these models means that these models may only provide an artificial fit to the data. In these cases, there is little to no physical meaning assigned to the parameter values.

As was reported by Sheehan *et al.*³⁸, the values for the solids transport coefficients reported by Lee *et al.*³⁷ for a rotary sugar dryer bore little resemblance to the expected physical system. For example, the values reported by Lee *et al.* suggested that the material in the active phase was being turned over 25.4 times per hour, or every 142 seconds³⁷. When one considers that it takes only a few seconds for material to fall the height of the dryer and that most dryers rotate approximately every 20 seconds, it becomes apparent that the turnover of the active phase should be far greater. To address this, Sheehan *et al.*³⁸ used the concept of using the geometry of the dryer and physical characteristics of the solids material to control the parameter values in the model, giving more physical relevancy to the model.

As was discussed in Chapter 3, the average residence times of both the active and passive phases can be related to the average fall path of the solids. This method hinges on knowing the average fall point of the solids, as shown in Equation 3.3. However, in order to find the average fall point, the unloading profile of a flight must be determined.

4.1. The Solids Dynamic Angle of Repose

It must also be noted that the dynamic angle of repose and cohesiveness are dependent on properties such as moisture content, which is of critical importance in drying operations. In many materials, increasing the moisture content of a solid will result in an increase in the cohesiveness and dynamic angle of repose^{2, 3}. Thus, in a rotary dryer, where the primary purpose of the unit is to remove moisture from the solids, the dynamic angle of repose will vary along the length of the dryer as moisture is removed. This will result in changes in variables such as fall height, fall time and design load with changing moisture content. Thus, it is necessary to define local values for these variables at each point along the dryer (each slice), rather than global values for the entire unit. Therefore, the geometric flight unloading model developed in this chapter needs to be implemented independently for each slice in the dryer.

4.2. Calculation of Flight Holdup and Unloading

In an unloading flight, the solids material is assumed to form a moving surface of material with a characteristic slope, described by the dynamic angle of repose of the solids. As was demonstrated by Wang *et al.*¹⁵ it is possible to calculate the theoretical amount of material contained within a flight from the cross-sectional area of the material (looking along the x-coordinate). For example, in a generic two-section flight with straight edges and no serrations, the material should form a cross-section such as that shown in Figure 4.1. To characterise a two-section flight the lengths of the two sections of the flight (s_1 and s_2), the angle at which the flight is attached to the wall (α_1) and the angle of the flight tip (α_2) need to be known. Material will be held up in the flight such that the slope of the material surface will begin at the tip of the flight and have an inclination of the dynamic angle of repose of the material (ϕ). Given this information, the cross-sectional area of the solid material can be calculated, and thus the mass contained within the flight.

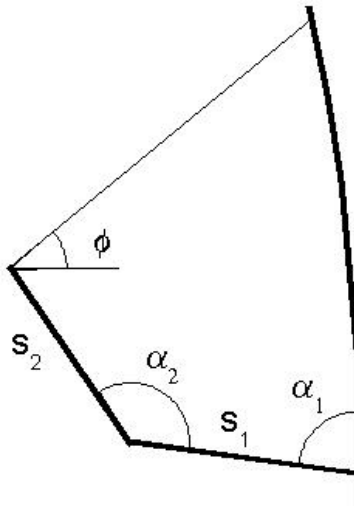


Figure 4.1. A generic straight 2-section flight.

4.2.1. Non-Perpendicular Flights

Whilst in many cases flights are attached perpendicularly to the walls of the dryer (i.e. $\alpha_1 = 90^\circ$), this is not always the case. In these cases, it is much easier to perform the geometric analysis assuming a similar flight which is attached perpendicularly, and then accounting for the difference by removing the shaded area shown in Figure 4.2. Here, s'_1 , s'_2 , α'_1 and α'_2 represent the dimensions of the perpendicular flight.

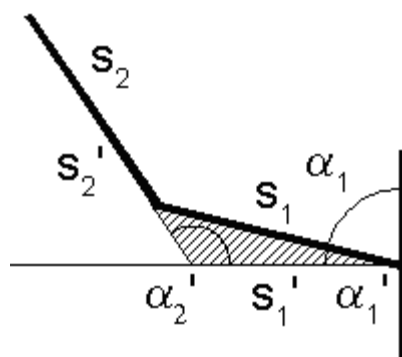


Figure 4.2. Geometric variables for non-perpendicular flights.

From Figure 4.2, it can be seen that α'_1 is the complement of α_1 , as shown in Equation 4.1. From the sum of the internal angles of a triangle, it can be seen that

$180^0 = \alpha'_1 + \alpha'_2 + \alpha_{2,\text{sup}}$ where $\alpha_{2,\text{sup}} = 180 - \alpha_2$ is the supplementary angle of α_2 , thus α'_2 can be calculated as shown in Equation 4.2. From this, s'_1 and s'_2 can be found

using the sine rule as $\frac{s_1}{\sin(\alpha'_2)} = \frac{s'_1}{\sin(180 - \alpha_2)} = \frac{(s'_2 - s_2)}{\sin(\alpha'_1)}$. This results in Equation

4.3 and Equation 4.4.

$$\alpha'_1 = 90^0 - \alpha_1$$

Equation 4.1. Perpendicular flight base angle.

$$\alpha'_2 = \alpha_2 - \alpha'_1$$

Equation 4.2. Perpendicular flight tip angle.

$$s'_1 = \frac{s_1 \sin(180 - \alpha_2)}{\sin(\alpha'_2)}$$

Equation 4.3. Perpendicular flight base length.

$$s'_2 = \frac{s_1 \sin(\alpha'_1)}{\sin(\alpha'_2)} + s_2$$

Equation 4.4. Perpendicular flight tip length.

It should be noted that when $\alpha_1 = 90^0$, these values simplify to their unprimed equivalents.

4.2.2. Additional Geometric Definitions

In addition to the geometry of the flights themselves, there are a number of other geometric variables that need to be defined regarding to the relationship of the flights to each other and the dryer as a whole. The most important of these is the definition of angle of rotation, ψ . In this work, angle of rotation is measured from the bottom of the drum in the direction of rotation, as shown in Figure 4.3. Also shown in Figure 4.3

is R_F representing the radius of a circle running through the tip of each flight, ψ_f representing the angle of rotation between two neighbouring flights and ψ_{ft} representing the angle of rotation between where the flight joins the wall of the drum and a line from the centre of the drum to the flight tip.

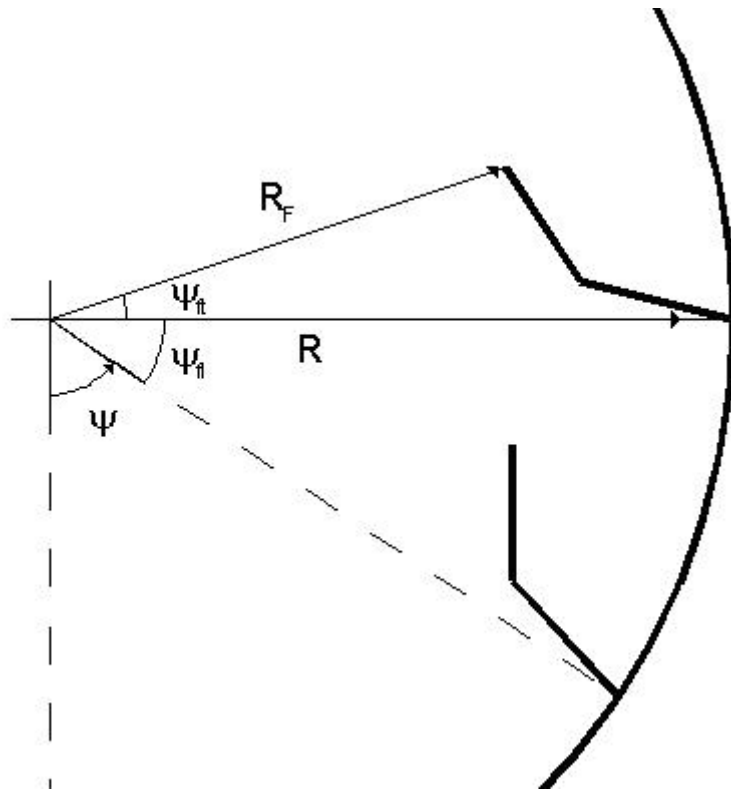


Figure 4.3. Definition of some geometric variables.

ψ_f can be calculated simply by dividing a full rotation by the number of flights in the dryer, N_F , as shown in Equation 4.5. ψ_{ft} and R_F can now be calculated using the cosine and sine rules as shown in Figure 4.4, where $\alpha_2'_{\text{sup}} = 180 - \alpha_2'$ is the supplementary angle of α_2' . Using the cosine rule, R_F can be calculated from R , s_1' , s_2' and α_2' as shown in Equation 4.6, and then the sine rule can be used to calculate ψ_{ft} as shown in Equation 4.7.

$$\psi_{ft} = \frac{360}{N_F}$$

Equation 4.5. Calculation of the angle of rotation between two flights.

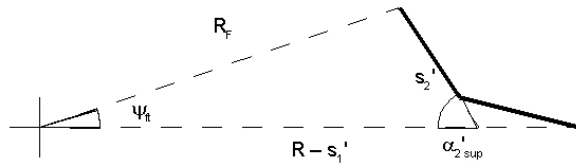


Figure 4.4. Calculation of ψ_{ft} and R_f .

$$R_f^2 = (R - s_1')^2 + s_2'^2 - 2(R - s_1')s_2' \cos(180 - \alpha_2')$$

Equation 4.6. Calculation of the flight tip radius.

$$\psi_{ft} = \sin^{-1} \left[\frac{s_2' \sin(180 - \alpha_2')}{R_f} \right]$$

Equation 4.7. Calculation of flight tip angle.

4.2.3. Calculation of Maximum Flight Holdup

As a flight rotates around the circumference of the drum it will gather and release material depending on where it is located in the drum and the loading of the flight (whether there is sufficient material to completely fill the flight or not). In terms of the solids transport occurring within a dryer, the most important period during the rotation of a flight is whilst the flight is unloading material in the upper portion of the drum, from $\psi + \psi_{ft} = 90^\circ$ to the point when the last solids leave the flight. It is during this period that the flight will discharge solids into the active phase, which is where most of the solids transport, and heat and mass transfer, occurs.

In order to determine the unloading profile of a flight, and to thus calculate the mass averaged fall height, it is necessary to know the maximum possible holdup within a

flight as it progresses around the circumference of the drum. Assuming the flighted material is always at its dynamic angle of repose, as the flight rotates the amount of mass that can be contained within the flight will decrease. Eventually, the flight will reach a point where there is more mass within the flight than it can contain. This mass must then be discharged from the flight.

Considering a flight as it travels around the circumference of the drum from $\psi = 0^0$ for a full rotation, a number of phases of flight loading become apparent. Initially, at $\psi = 0^0$, the flight may be buried under a kilning bed of material, thus it is necessary to define what material is contained within the flight, and what constitutes the kilning bed. As the material surface is assumed to be straight in unloading flights, the maximum holdup within a flight at $\psi = 0^0$ will be defined as the shaded area shown in Figure 4.5. This is defined as the maximum amount of material that can ever be contained within a flight (note that this is different to the design load of the dryer).

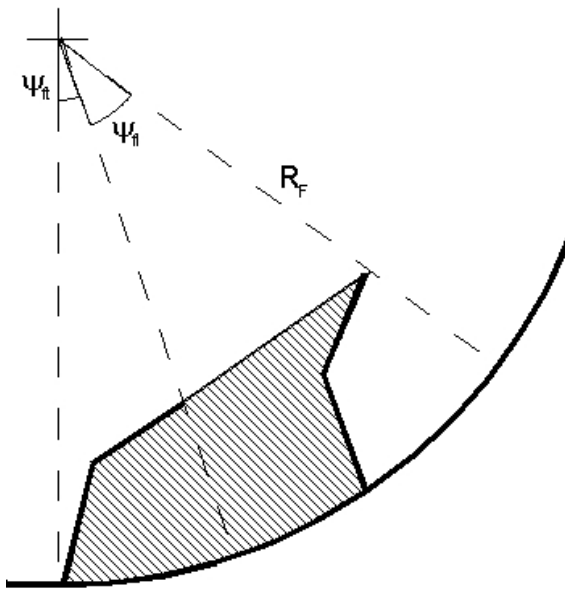


Figure 4.5. Definition of a full flight.

The mass holdup within a flight can be calculated using $H = \text{Area} \times \text{Length} \times \rho_b$, thus the cross-sectional area needs to be calculated. Looking at Figure 4.5, the cross-sectional area of the solid material (given by the shaded area) can be calculated as the area of the sector bounded by the two radial lines passing through the flight tips minus the area of the triangle bounded by the two lines and the material surface. The shaded

area not included in this sector is accounted for by the area of the next flight included in the sector.

The angle between the two lines passing through the flight tips of the two flights can be seen to be ψ_{fl} , thus the area of the sector is $A_{sec} = \frac{\pi}{180} \frac{R^2}{2} \psi_{fl}$ where ψ_{fl} is measured in degrees, and the area of the triangular section can be shown to be $A_{tri} = 0.5R_F^2 \sin(\psi_{fl})$. Thus, the maximum holdup within a flight can be calculated as shown in Equation 4.8.

$$H_{full} = \rho_{bulk} L \left[\frac{\pi}{180} \frac{R^2}{2} \psi_{fl} - \frac{R_F^2}{2} \sin(\psi_{fl}) \right]$$

Equation 4.8. Maximum holdup in a full flight.

Referring to Figure 4.6, as the flight travels around the circumference of the drum, the material surface will travel down the back of the next flight (I→II), then around the wall of the drum (II→III), and eventually along the base of the current flight (III→IV). As the material surface passes reaches each segment junction (such as the point where the flight bends (II)), there will be a discontinuity in the unloading profiles. Each phase in the unloading profile requires a different set of equations to determine the cross-sectional area of the solids, thus it is important to define the transition points between phases. Figure 4.6 shows the five transitions points, which will be discussed in more detail in the next section. Some of these transition points will occur in the lower section of the drum ($\psi < 90^\circ$) for most dryers where the flights do not unload into the active phase. However, the calculation of the mass contained within a flight may have uses in modelling the solids transport due to kilning, and for completeness all phases of unloading will be considered here.

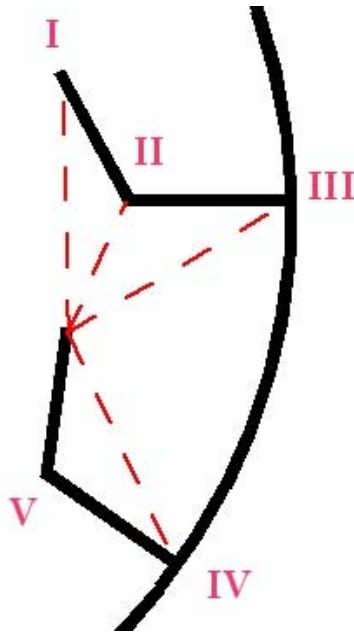


Figure 4.6. Overview of transition points.

4.2.3.1. Transition Points

Initially, as the flight rotates no material will be discharged from the flight until it reaches a point where the material will begin to flow. This will occur when the inclination of the line connecting the two flight tips (and hence the material surface) reaches the dynamic angle of repose of the solid material, ϕ , as shown in Figure 4.7. From Figure 4.7, using the sum of the internal angles of an isosceles triangle, $180^\circ = \psi_{fl} + 2\beta$, and it can also be seen that $180^\circ = \phi + \beta + \gamma$. Finally, again using the sum of the internal angles of a triangle, $180^\circ = (\psi_1 + \psi_{ft}) + \gamma + 90^\circ$. Thus, combining these three equations gives the equation for determining the first transition point, ψ_1 , as shown in Equation 4.9.

$$\psi_1 = \phi - \frac{\psi_{fl}}{2} - \psi_{ft}$$

Equation 4.9. Calculation of the first transition point, ψ_1 .

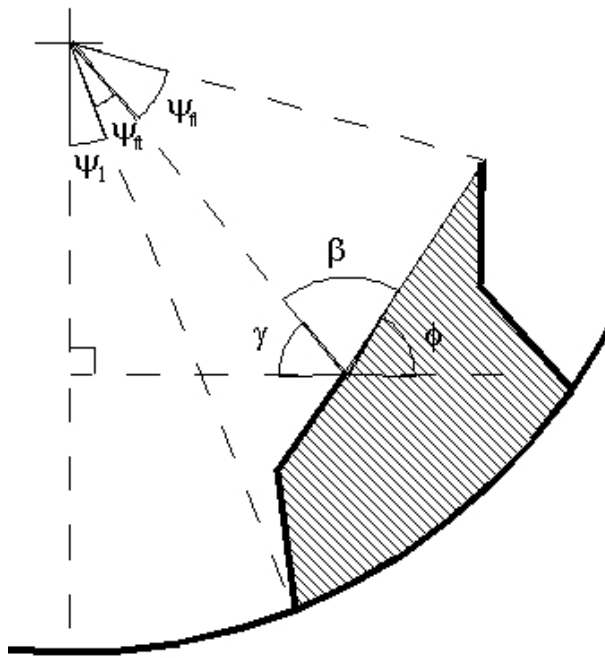


Figure 4.7. Transition point 1 ψ_1 .

The second transition point occurs when the material surface reaches the bend in the flight, as shown in Figure 4.8. The transition point, ψ_2 can be seen to be $\psi_2 = 90^\circ - \psi_{ft} - \varepsilon$ using the sum of the internal angles of a triangle.

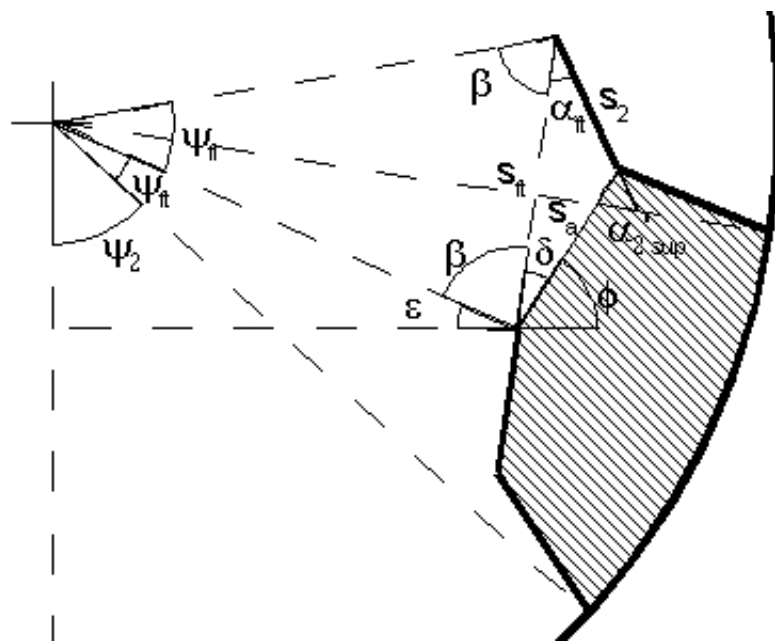


Figure 4.8. Detail of lengths and angles at the second transition point.

In order to calculate ε , it is first necessary to calculate the length along the material surface between the flight tip and where the radial line to the base of the next flight intersects it. The full length of the material surface, c , can be calculated from the length of the chord connecting the two flight tips, s_{ft} , and s_2 (see Figure 4.8). It can

be seen that $s_{ft} = 2R_F \sin\left(\frac{\psi_{fl}}{2}\right)$ where s_{ft} is the length of the chord connecting two

flight tips, and using the sum of the internal angles of a triangle $180^0 = \psi_{ft} + (\beta + \alpha_{ft}) + \alpha'_{sup}$ where α_{ft} is the angle between s_2 and s_{ft} . Using the

sum of the internal angles of an isosceles triangle, $\beta = 90^0 - \frac{\psi_{fl}}{2}$, thus

$\gamma = \alpha'_{sup} + \psi_{ft} - \frac{\psi_{fl}}{2} - 90^0$. Using the cosine rule gives $s_a^2 = s_2^2 + s_{ft}^2 - 2s_2s_{ft} \cos(\alpha_{ft})$,

and using the sine rule $\frac{\sin(\delta)}{s_2} = \frac{\sin(\alpha_{ft})}{s_a}$. Finally, $180^0 = \phi + \beta + \delta + \varepsilon$, which gives

$$\varepsilon = \phi - \frac{\psi_{fl}}{2} + \sin^{-1}\left(\frac{s_2 \sin(\alpha_{ft})}{\sqrt{s_2^2 + s_{ft}^2 - 2s_2s_{ft} \cos(\alpha_{ft})}}\right) - 90^0 \text{ which results in Equation 4.10.}$$

$$\psi_2 = \phi - \psi_{ft} - \frac{\psi_{fl}}{2} + \sin^{-1}\left(\frac{s_2 \sin(\alpha_{ft})}{s_a}\right)$$

Equation 4.10. Calculation of the second transition point, ψ_2 .

As the flight continues to unload, the material surface will eventually reach the base of the flight, as shown in Figure 4.9, and the next phase of unloading will begin. It can be seen from Figure 4.9 that $\beta = \psi_{fl} - \psi_{ft}$, and using the cosine rule, the length of the

material surface can be found to be $c = \sqrt{R^2 + R_F^2 - 2RR_F \cos(\psi_{fl} - \psi_{ft})}$. This length

can then be used with the sine rule to find $\frac{\sin \gamma}{R_F} = \frac{\sin(\psi_{fl} - \psi_{ft})}{c}$, then using the sum

of the internal angles of a triangle $\psi_{fl} + \gamma + \delta = 180^0$. Combining these equations with

$\psi_3 + \varepsilon + 90^0 = 180^0$ and $\delta + \varepsilon + \phi = 180^0$ gives Equation 4.11.

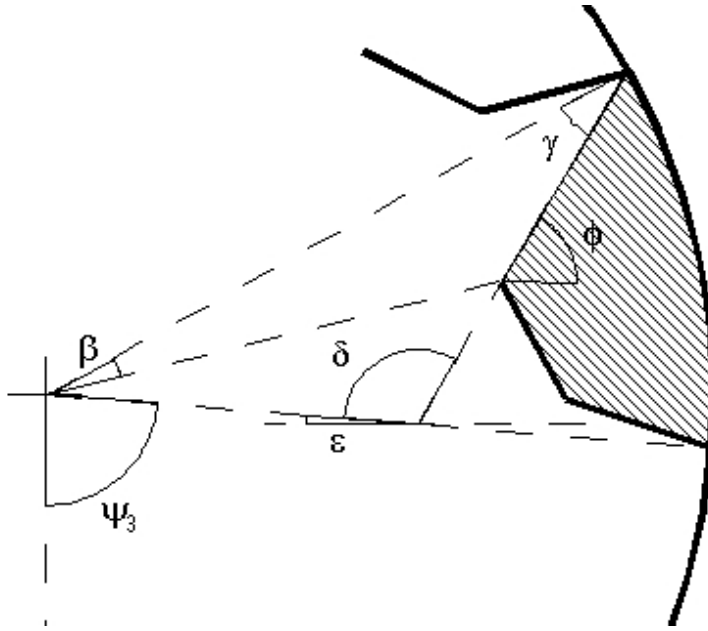


Figure 4.9. Transition point 3, ψ_3 .

$$\psi_3 = 90^\circ + \phi - \psi_{fl} - \sin^{-1} \left(\frac{R_F \sin(\psi_{fl} - \psi_{ft})}{\sqrt{R^2 + R_F^2 - 2RR_F \cos(\psi_{fl} - \psi_{ft})}} \right)$$

Equation 4.11. Calculation of the third transition point, ψ_3 .

The next phase of flight unloading occurs when the material surface reaches the base of the current flight, as shown in Figure 4.10. The length of the material surface can be found using the cosine rule to give $b^2 = s_1^2 + s_2^2 - 2s_1s_2 \cos(\alpha_2)$, and using the sine rule, it can be shown that $\beta = \text{asin}\left(\frac{s_2 \sin(\alpha_2)}{b}\right)$. From the sum of the internal angles of a triangle, $180^\circ = \phi + (\alpha'_1 + \beta) + \gamma$, and it can be shown that $180^\circ = \gamma + (\psi_4 - 90^\circ)$, thus ψ_4 can be calculated as shown in Equation 4.12.

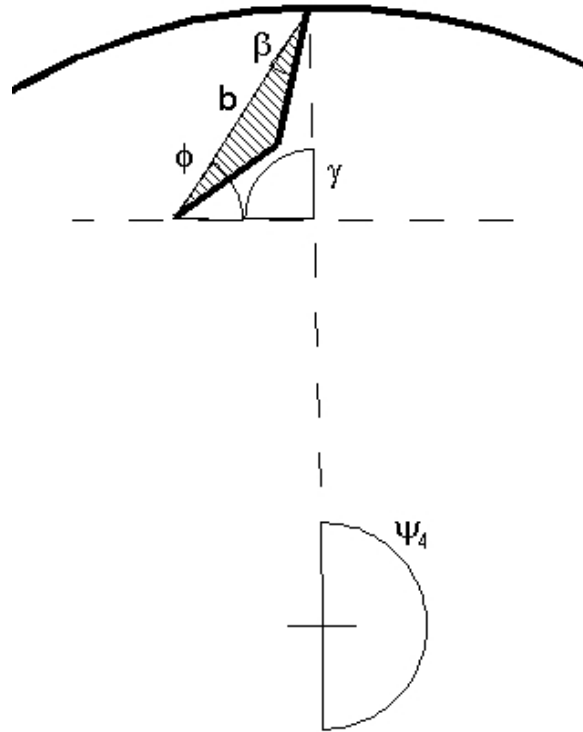


Figure 4.10. Transition point 4, ψ_4 .

$$\psi_4 = 90^\circ + \phi + \alpha'_1 + \sin^{-1} \left(\frac{s_2 \sin(\alpha_2)}{\sqrt{s_1^2 + s_2^2 - 2s_1 s_2 \cos(\alpha_2)}} \right)$$

Equation 4.12. Calculation of the fourth transition point, ψ_4 .

Finally, as the flight continues to unload it will eventually reach the point where the flight cannot contain any solids. This will occur when the inclination of the flight tip relative to the horizontal is equal to the solids dynamic angle of repose, as shown in Figure 4.11. As can be seen, from the sum of the internal angles of a triangle, $180^\circ = \phi + \alpha'_{2\text{ sup}} + \beta$, and $180^\circ = \beta + (\psi_5 - 90^\circ)$, ψ_5 can be calculated as shown in Equation 4.13.

$$\psi_5 = 90^\circ + \phi + \alpha'_{2\text{ sup}}$$

Equation 4.13. Calculation of the fifth transition point, ψ_5 .

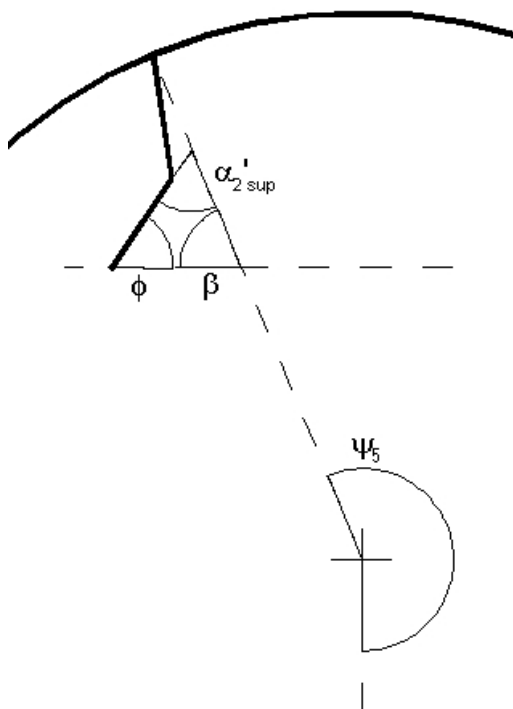


Figure 4.11. Transition point 5, ψ_5 .

Table 4.1 shows the geometry of the flights used in the Invicta Mill Dryer Number 2 (an industrial raw sugar dryer), and Table 4.2 shows the calculated transition points for solids angles of repose of $\phi = 30^\circ$ and $\phi = 60^\circ$. The dimensions of the flights and dryer are also given in Table 4.1. As can be seen, the transition points are linearly related to the dynamic angle of repose, that is, for an increase in 1° in the dynamic angle of repose of the solids, the transition points will shift 1° of rotation around the circumference of the drum. It can also be seen that for both cases given here, the first two transition points occur before the flight reaches the horizontal position (90°), where it begins unloading into the active phase. Any unloading occurring before $\psi = 90^\circ$ only results in material rolling into another flight. Thus, for the case given here, the first two phases of flight unloading have no effect on the solids transport into the active phase.

D	5 m
s ₁	0.195 m
s ₂	0.183 m
α ₁	90 ⁰
α ₂	117 ⁰
N _f	28 flights

Table 4.1. Geometry of the Invicta Sugar Mill dryer number 2.

Transition Point	ϕ = 30 ⁰	ϕ = 60 ⁰
ψ ₁	19.4 ⁰	49.4 ⁰
ψ ₂	34.1 ⁰	64.1 ⁰
ψ ₃	58.7 ⁰	88.7 ⁰
ψ ₄	150.4 ⁰	180.4 ⁰
ψ ₅	183.0 ⁰	213.0 ⁰

Table 4.2. Summary of transition points for Invicta Sugar Mill dryer number 2.

Studying the equations for the transition points, it can be seen that the two most significant factors in the location of the early transition points is the solids dynamic angle of repose and the flight spacing. It has already been noted that the location of the transition points is linearly related to the dynamic angle of repose, and it can be determined that increasing the flight spacing decreases the angular location ($ψ$) of the transition points. Thus, as most material have angles of repose $ϕ < 60^0$, for a dryer with a comparable or lower density of flights around the circumference of the drum it can be generalised that the first two phases of flight unloading have no impact on the solids transport into the active phase in most cases.

4.2.3.2. Maximum Flight Holdup

As was discussed in Chapter 4.2.3, the maximum amount of material that can be contained within a flight can be calculated from the cross-sectional area of the material contained within the flight using the equation $H = A \times L \times \rho_b$. It has already been defined that the maximum mass of solids that can be contained within a flight can be calculated using Equation 4.8, and it is logical that an empty flight can contain no solids.

Initially, as the flight travels around the drum, no material will be discharged from the flight until it reaches the first transition point, ψ_1 , thus for $\psi \leq \psi_1$, the maximum flight holdup is described by Equation 4.8.

First Unloading Phase, $\psi_1 \rightarrow \psi_2$

Once the flight reaches ψ_1 , solids will begin to discharge from the flight as it continues to travel around the drum. Between the first and second transition points, the cross-sectional area of the solid material will be similar to that shown in Figure 4.12. The simplest approach to calculating the cross-sectional area of the solids in this phase of unloading is to determine the difference in cross-sectional area compared to a full flight. From Figure 4.12 it can be seen that the difference in cross-sectional area is a triangle area described by the material surface and chord connecting the two flight tips. Focussing on the flight tip, it can be seen that $180^\circ = \phi + \beta + \gamma + \delta$, and from the sum of the internal angles of a triangle $180^\circ = (\psi + \psi_{ft}) + \beta + 90^\circ$. It can also be seen

that $\gamma = 90^\circ - \frac{\psi_{ft}}{2}$, thus $\delta = \psi + \psi_{ft} + \frac{\psi_{ft}}{2} - \phi$. Using the sine rule and the sum of the

internal angles of a triangle $\frac{b}{\sin(\delta)} = \frac{s_{ft}}{\sin(180^\circ - \alpha_{ft} - \delta)}$, and the area of the triangle

is $A_t = \frac{1}{2} s_{ft} (b \sin(\alpha_{ft}))$. Combining this with the holdup within a full flight, Equation

4.8, gives Equation 4.14, the maximum flight holdup during this phase of unloading.

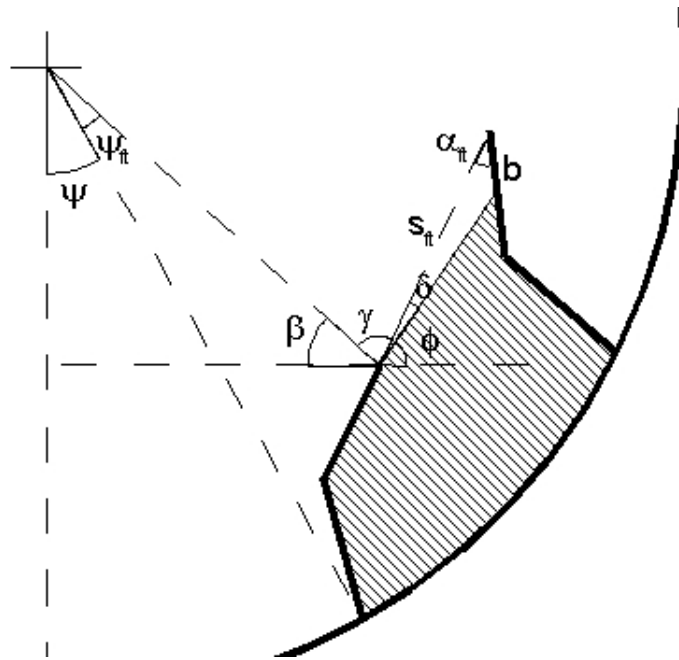


Figure 4.12. Cross-sectional area of flighted material between ψ_1 and ψ_2 .

$$H_{1-2} = H_{\text{full}} - \rho_{\text{bulk}} L \frac{s_{ft}^2}{2} \left(\frac{\sin\left(\psi + \psi_{ft} + \frac{\psi_{fl}}{2} - \phi\right)}{\sin\left(180^\circ - \alpha_{ft} - \psi - \psi_{ft} - \frac{\psi_{fl}}{2} + \phi\right)} \sin(\alpha_{ft}) \right)$$

Equation 4.14. Calculation of the maximum flight holdup between ψ_1 and ψ_2 .

Second Unloading Phase, $\psi_2 \rightarrow \psi_3$

Figure 4.13 shows the cross-sectional area of a flight during the second phase of unloading, whilst the material surface progresses down the base of the next flight. Again, the simplest method for calculating the maximum flight holdup is to calculate the difference in cross-sectional area between the current position and a full flight. Firstly, the triangle defined by $s_2-s_{ft}-b$ can be seen to have an area of $A_{t1} = \frac{1}{2} s_2 s_{ft} \sin(\alpha_{ft})$ and the second triangle an area of $A_{t2} = \frac{s_a^2}{2} \frac{\sin(\varepsilon) \sin(\zeta)}{\sin(180^\circ - \varepsilon - \zeta)}$. It

can be seen that $180^0 = \beta + \gamma + \alpha_a + \varepsilon + \phi$ where $180^0 = (\psi + \psi_{ft}) + \beta + 90^0$ and

$\gamma = 90^0 - \frac{\psi_{fl}}{2}$ as before. Using the sine rule, $\frac{\sin(\alpha_a)}{s_2} = \frac{\sin(\alpha_{ft})}{s_a}$ and it can be seen

that $360^0 = \alpha_2 + \zeta + (180^0 - \alpha_{ft} - \alpha_a)$. It can also be seen using the cosine rule that

$s_a^2 = s_2^2 + s_{ft}^2 - 2s_2s_{ft} \cos(\alpha_{ft})$. Thus, combining the above equations allows ε and

ζ to be calculated, yielding $\varepsilon = \psi + \psi_{ft} + \frac{\psi_{fl}}{2} - \alpha_a - \phi$, and $\zeta = 180^0 + \alpha_{ft} + \alpha_a - \alpha_2$.

Thus, the area of the second triangle is

$$A_{t2} = \frac{s_a^2}{2} \frac{\sin\left(\psi + \psi_{ft} + \frac{\psi_{fl}}{2} - \alpha_a - \phi\right) \sin(180^0 + \alpha_{ft} + \alpha_a - \alpha_2)}{\sin\left(\phi + \alpha_2 - \psi - \psi_{ft} - \frac{\psi_{fl}}{2} - \alpha_{ft}\right)}. \quad \text{Thus, the cross-}$$

sectional area of the material within a flight between ψ_2 and ψ_3 can be calculated as shown in Equation 4.15.

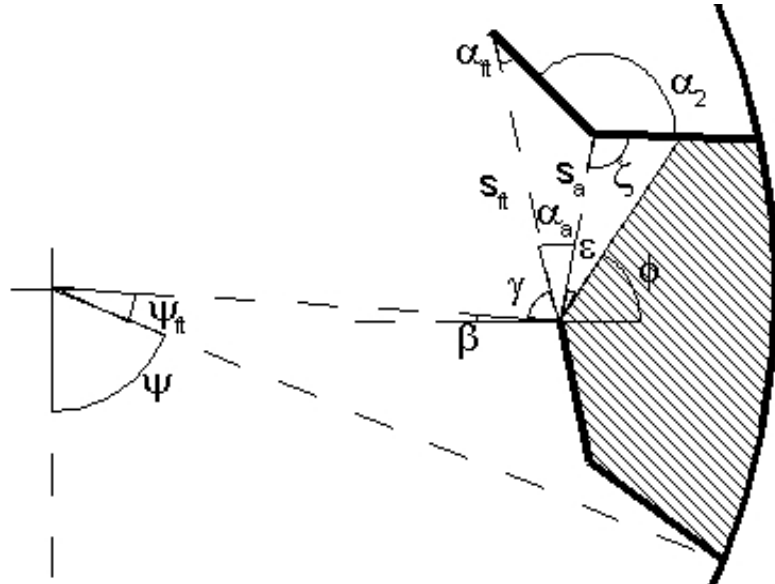


Figure 4.13. Cross-sectional area of flighted material between ψ_2 and ψ_3 .

$$H_{2-3} = H_{\text{full}} - \frac{\rho_{\text{bulk}} L}{2} \left(s_2 s_{ft} \sin(\alpha_{ft}) + s_a^2 \frac{\sin\left(\psi + \psi_{ft} + \frac{\psi_{fl}}{2} - \alpha_a - \phi\right) \sin\left(180^\circ + \alpha_{ft} + \alpha_a - \alpha_2\right)}{\sin\left(\phi + \alpha_2 - \psi - \psi_{ft} - \frac{\psi_{fl}}{2} - \alpha_{ft}\right)} \right)$$

Equation 4.15. Calculation of the maximum flight holdup between ψ_2 and ψ_3 .

Third Unloading Phase, $\psi_3 \rightarrow \psi_4$

Figure 4.14 shows the cross-sectional area of the solids during the third phase of unloading. The best approach to calculating the cross-sectional area of material within the flight is to calculate the area of the sector defined by the angle $\psi_{ft} + \beta$, and subtracting the area of the three triangles shown in Figure 4.14. Angle β can be calculated by first looking in detail at the angles formed at the flight tip in Figure 4.14. It can be seen that $\gamma = \psi_{ft} + (\psi - 90^\circ)$ as γ is congruent to the inclination of the radial line to the flight tip, and thus using the sine rule $\frac{\sin(180^\circ - \beta - (\gamma + \phi'))}{R_F} = \frac{\sin(\gamma + \phi')}{R}$, which results in the following equation,

$$\beta = \phi - \psi_{ft} - \psi + 90^\circ - \sin^{-1} \left[\frac{R_F}{R} \sin(\psi_{ft} + \psi + 90^\circ - \phi) \right].$$

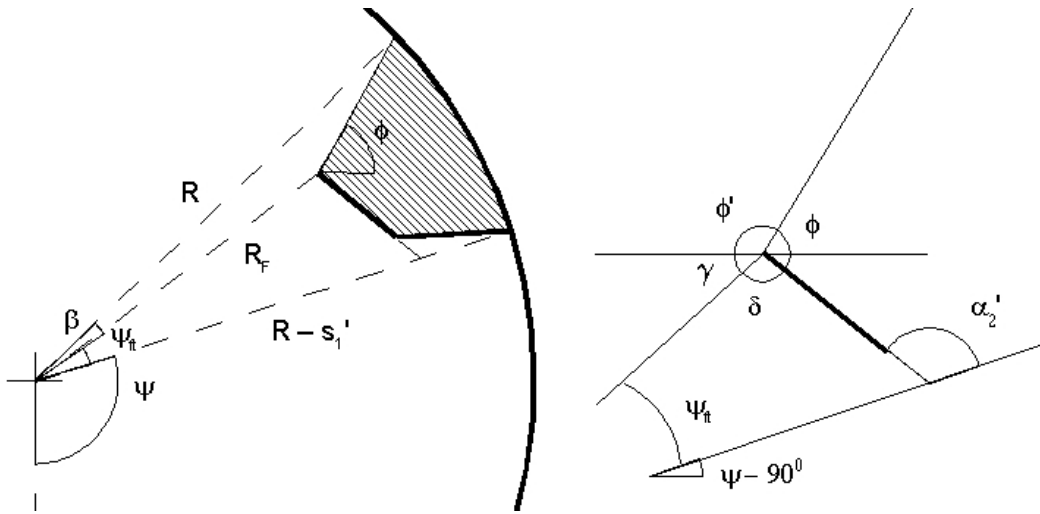


Figure 4.14. Cross-sectional area of flighted material between ψ_3 and ψ_4 .

Now that β is known, the area of the sector is given by

$$A_{\text{sec}} = \frac{R^2}{2} \left(\phi - \psi + 90^\circ - \sin^{-1} \left[\frac{R_F}{R} \sin(\psi_{ft} + \psi + 90^\circ - \phi) \right] \right) \frac{\pi}{180^\circ} \quad \text{where all angles are}$$

measured in degrees. The area of the triangle described by the angle ψ_{ft} and the flight tip can be found to be $A_{t1} = \frac{1}{2} (R - s_1') (s_2' \sin(\alpha_2))$ and the area of the triangle defined by angle β and the material surface is $A_{t2} = \frac{R}{2} (R_F \sin(\beta))$. Finally, the small triangle to account for non-perpendicular flights has an area $A_{t3} = \frac{s_1'}{2} (s_1' \sin(\alpha_1'))$. Upon combining these four areas, the maximum solids holdup of the material can be found using Equation 4.16.

$$\begin{aligned} H_{3-4} = & \frac{\rho_{\text{bulk}} L}{2} \left[R^2 \left(\phi - \psi + 90^\circ - \sin^{-1} \left[\frac{R_F}{R} \sin(\psi_{ft} + \psi + 90^\circ - \phi) \right] \right) \frac{\pi}{180^\circ} \right. \\ & - RR_F \sin \left(\phi - \psi_{ft} - \psi + 90^\circ - \sin^{-1} \left[\frac{R_F}{R} \sin(\psi_{ft} + \psi + 90^\circ - \phi) \right] \right) \\ & \left. - (R - s_1') (s_2' \sin(\alpha_2)) - s_1 (s_1' \sin(\alpha_1')) \right] \end{aligned}$$

Equation 4.16. Calculation of the maximum flight holdup between ψ_3 and ψ_4 .

It may appear at first glance that this equation will only apply up until $\beta = 0$ and the material surface lies along a radial line drawn through the flight tip. However, as the flight continues to rotate, β becomes negative, resulting in the area $A_{t2} = \frac{R}{2}(R_F \sin(\beta))$ becoming negative, as shown in Figure 4.15. As can be seen, using the area of the sector $\psi_f + \beta$ neglects part of the flighted material. This area represents part of the area $A_{t2} = \frac{R}{2}(R_F \sin(\beta))$, which being negative, increases the total cross-sectional area. Referring to Figure 4.15, the remaining portion of A_{t2} offsets the extra area of $A_{t1} = \frac{1}{2}(R - s_1')(s_2' \sin(\alpha_2))$ which is still being subtracted from the area of the sector, thus Equation 4.16 still holds.

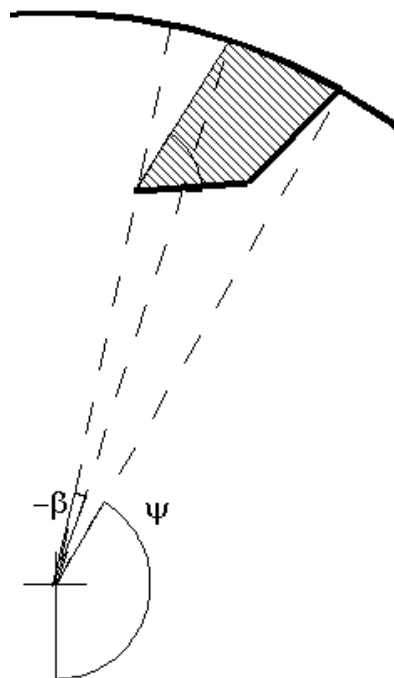


Figure 4.15. Cross-sectional area of flighted material between ψ_3 and ψ_4 at higher ψ .

Fourth Unloading Phase, $\psi_4 \rightarrow \psi_5$

During the final phases of unloading, the material cross-section will be similar to that shown in Figure 4.16. It can be seen that $180^\circ = \beta + (\psi - 90^\circ)$, and from the sum of

the internal angles of a triangle, $180^0 = \alpha'_{2\text{sup}} + \beta + (\phi - \gamma)$, thus $\gamma = \alpha'_{2\text{sup}} - \psi + \phi + 90^0$. Then, using the sine rule $\frac{b}{\sin(\alpha_2)} = \frac{s_2}{\sin(180^0 - \alpha_2 - \gamma)}$, and the maximum holdup of material can be found as shown in Equation 4.17.

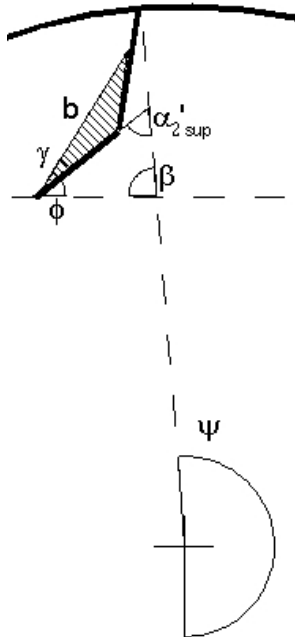


Figure 4.16. Cross-sectional area of flighted material between ψ_4 and ψ_5 .

$$H_{4-5} = \frac{\rho_{\text{bulk}} L}{2} s_2^2 \frac{\sin(\alpha_2) \sin(\alpha'_{2\text{sup}} - \psi + \phi + 90^0)}{\sin(90^0 - \alpha_2 - \alpha'_{2\text{sup}} + \psi - \phi)}$$

Equation 4.17. Calculation of the maximum flight holdup between ψ_4 and ψ_5 .

Effects of Serrated Flights

The method described above can be extended to any flight geometry, although more complex designs will require more involved calculations. For single section flights, i.e. where $s_2 = 0$, the equations developed above are applicable by setting s_2 to zero. Accounting for serrated flights is more difficult, as the material surface will not be a two dimensional plane, making calculation of maximum flight holdup more

complicated. Some researchers have proposed using an area averaged flight tip length (Sheehan⁵²) where it is assumed that a serrated flight behaves the same way as an unserrated flight with the same surface area, as shown in Equation 4.18 for triangular serrations. \bar{s}_2 is the average flight tip length, and s_w , s_d and s_N are the width depth and number of serrations per metre respectively.

$$\begin{aligned}\bar{s}_2 L &= s_2 L - \frac{L}{2} s_w s_d s_N \\ \bar{s}_2 &= s_2 - \frac{1}{2} s_w s_d s_N\end{aligned}$$

Equation 4.18. Calculation of average flight-tip length.

For testing of the geometric flight unloading model developed above, unserrated flights will be used, so this will not be an issue. However, most industrial dryers use serrated flights, thus when applying the unloading model to systems with serrated flights, Equation 4.18 hold.

4.2.4. Theoretical Unloading Profile

Using the equations derived above, the maximum holdup within a flight can be calculated at any point around the circumference of a dryer, and from this the discharge rate at any point can also be calculated as $F = \frac{dH}{dt} = \omega \frac{dH}{d\psi}$ where F is the rate at which solids are discharged from the flight and ω is the angular velocity of the flight. Using Invicta Mill Dryer Number 2, as shown in Table 4.1 (which has serrated flights), as an example gives the maximum holdup profile shown in Figure 4.17. Differentiating this (using a first-order central difference method) to find the discharge profile gives Figure 4.18.

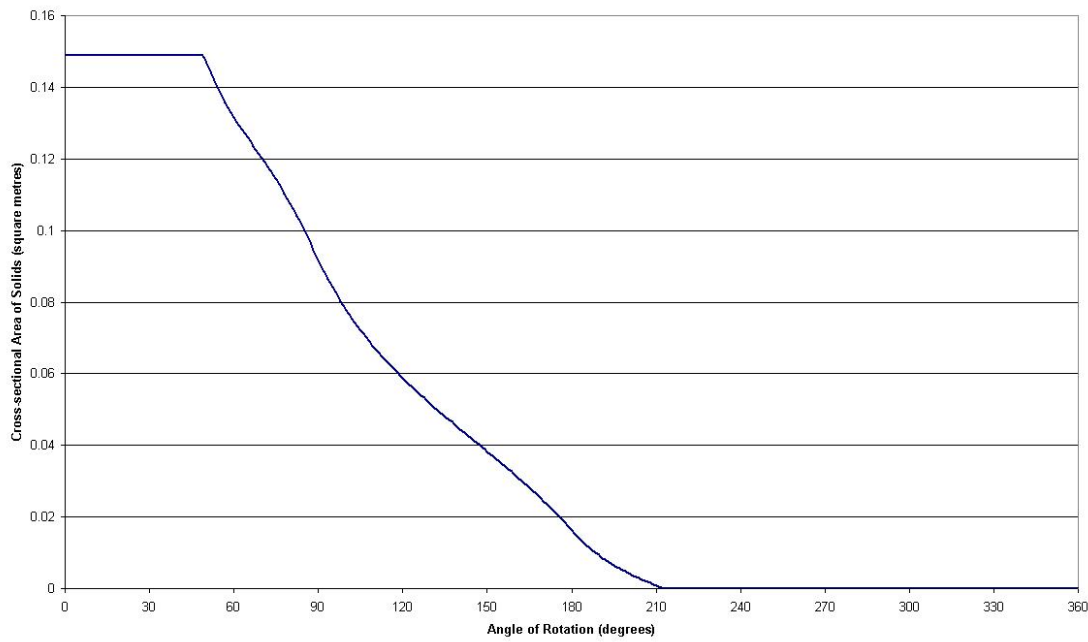


Figure 4.17. Maximum flight holdup profile for Invicta Mill Dryer Number 2.

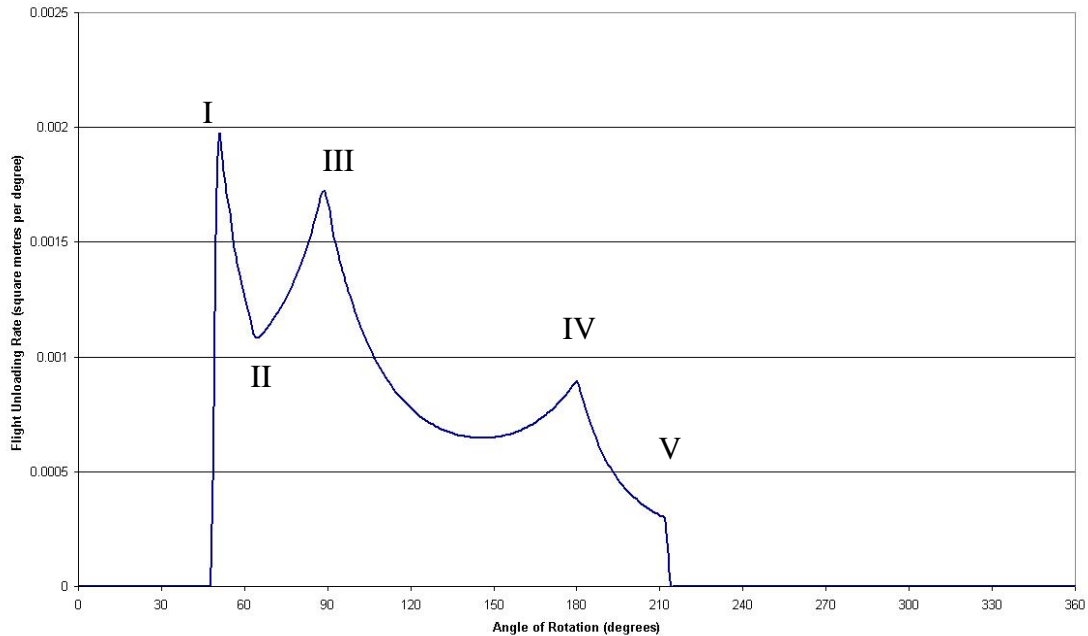


Figure 4.18. Flight discharge rate profile for Invicta Mill Dryer Number 2.

From Figure 4.18, the different phases of unloading can be clearly identified by the sharp changes in the unloading rate (indicated by the numbers I to V). Looking at the period where the flight is unloading material into the active phase ($90^\circ < \psi < \psi_5$), it can be seen in Figure 4.17 that most of the unloading occurs in the period between ψ_3

and ψ_4 . It can also be seen in Figure 4.18 that the unloading of material is biased towards the side of the dryer (90° to 120° rotation), where the fall height is small. A smaller portion of the material is discharged in the central part of the dryer where the fall time is highest, which results in lower fall times, and hence less opportunity for gas-solids contact. For comparison, see Kelly⁵ for examples of different unloading profiles.

It should be noted that for this analysis only the unloading of the flight has been considered. Thus, the amount of mass contained within the flight after unloading is finished remains at zero. However, this will not be the case, as the flights will begin to collect solids as they travel around the bottom of the dryer. As the purpose of this analysis was to study the discharge of the solids into the active phase, this aspect of the flight action has been neglected.

4.2.5. Comparison of Unloading Profile to Previous Literature

A number of previous authors have studied the discharge profile of a flight in a rotary dryer fitted with straight two-section flights. Schofield and Glikin published a theoretical analysis of a flight unloading profile for a two-section flight in an industrial fertilizer dryer⁴, which agrees well with the unloading profile developed above. Revol *et al.* also used a similar geometric method for flights with an arbitrary number of sections and compared their model to experimental data from a pilot scale dryer with three section flights⁴¹. Their model predicted a similarly shaped curve to that predicted by the model above, however they found that the experimental curve was more uniform than the prediction of their model, with the features of the theoretical curve being smoothed within the dryer⁴¹. Experiments were conducted in order to validate the model for the flight unloading profile, and these are discussed in Chapter 5.

4.2.6. Limitations and Assumptions of the Geometry Model

The geometric model for the unloading profile of a flight is dependent upon a number of assumptions, which are addressed in this section. Firstly, it is assumed that the forces holding the bulk material into the flight exceed the internal forces of the bulk solids, and thus that material will flow off the surface of the material, rather than the material moving as a bulk. This is especially true for the last phase of unloading (between ψ_4 and ψ_5) where the bulk solids are held in the flight by friction between the solids and the flight surface alone. If the internal forces are stronger than the retaining forces, the material will move as a bulk solid and fall off the flight tip together, rather than continuously flowing over the flight tip. This effect has been observed in experimental studies which will be discussed in Chapter 5.

It is also assumed that the material is free flowing, and that it will begin to flow continuously as soon as the inclination of the material surface reaches the materials dynamic angle of repose. If this is not the case and the material is cohesive, then the material will be discharged in clumps as the bulk material undergo failure and break away from the bulk.

It is also assumed that the material's dynamic angle of repose adequately describes the behaviour of the material within the flight, and that the inclination of the material surface will always be described by this.

4.3. Applying the Geometric Model to Solids Transport

The geometric unloading profile developed above now relates flight holdup to flight location, i.e. $H = f(\psi)$. This can now be used in Equation 3.3 to calculate the mass averaged fall point, and thus the residence times of the active and passive phases. For the example of the Invicta Mill Dryer Number 2, the geometric unloading model predicts a mass averaged fall point of $\bar{\psi} = 201.6^\circ$, resulting in a fall height $\bar{h}_m = 4.164$ m. This gives residence times of $\bar{t}_a = 0.824$ s for the active phase and for the passive phase $\bar{t}_p = 12.403$ s.

4.4. Effects of Dryer Loading on Solids Transport

The effects of dryer loading, or the amount of material within the dryer, upon the solids transport occurring within a dryer have long been a focus of research. It has often been highlighted by researchers that most models are only applicable across a small range of operating conditions where the model was developed and tested. One of the goals of the model proposed by Sheehan *et al.*³⁸ was to develop a model that would be applicable across the entire spectrum of rotary dryer operations, i.e. both under- and over-loaded dryers.

The most well-known and studied effect of dryer loading is the phenomena of kilning. When the amount of material contained within a dryer becomes more than can be contained within the flights and falling curtain, a rolling bed of solids begins to form on the floor of the drum. Due to the inclination and rotation of the dryer, this bed of solids undergoes a kilning motion, resulting in the axial transport of solids along the dryer. Whilst this phenomenon has been well documented in unflighted rotary kilns⁵³, there is limited literature available on a detailed study of kilning in flighted rotary dryers⁴².

Most researchers have taken an empirical approach to modelling kilning, especially in the field of compartment modelling, where kilning flow has been treated in the same way as other solid flows, i.e. that kilning flow is proportional to the mass of the kilning bed. In their paper, Sheehan *et al.*³⁸ presented a basic relationship for the kilning flow based on the rotational velocity of the drum and the size of the bed, however this relationship was not validated.

The other key effect of dryer loading is its impact on the unloading behaviour of the flights. In a drum that is at or beyond the design load point, there is sufficient material available for the flights to be full at $\psi + \psi_{fr} = 90^{\circ}$, and thus the flight will unload across the maximum width of the dryer (as governed by the dynamic angle of repose). In order to account for these effects, it is necessary to determine the amount of

material contained in a flight at $\psi + \psi_{ft} = 90^0$ (H_0), which can then be used to determine the point at which the flights begin to unload.

In a dryer below the design load point, there is insufficient material available to fill the flights at $\psi + \psi_{ft} = 90^0$, thus the flight will begin unloading somewhere beyond $\psi + \psi_{ft} = 90^0$. In this case, up until the point where the flight begins unloading, dH is equal to zero, which results in an increase in the mass averaged fall height, time and release point. It should also be noted that for underloaded flight $H_0 < H_{0,design}$. This has a significant impact of the solids transport phenomena occurring in an underloaded drum, as much of the solids transport is dependent upon these values.

For a design- or over-loaded flight, $H_0 = H_{0,design}$ and the values of \bar{h}_m , \bar{t}_m and $\bar{\psi}_m$ are equal to their values at the design load point. This is because the flights are at their maximum capacity at the design load, and thus any additional dryer loading has no effect on the unloading of the flights. For an underloaded dryer, the amount of material contained within a flight at $\psi + \psi_{ft} = 90^0$ can be defined as $H_0 = f_{load} \times H_{0,des}$ where f_{load} is the flight loading factor, and represents what fraction of the design flight load (H_0) the flight contains at $\psi + \psi_{ft} = 90^0$. Thus, f_{load} will range between 0 for a dryer in which the flights are completely empty and 1 for a dryer operating at or beyond its design point.

Thus, the necessary steps in accounting for loading effects on the solids transport are;

1. identify the design load of the dryer by relating $H_{0,des}$ to the holdup within the passive phase at this point, $M_{p,des}$, and
2. develop a relationship between f_{load} and the holdup within the passive phase, M_p .

4.4.1. The Design Load

Determining the design load of a dryer is critical to accurately modelling the solids transport behaviour of the system. The design load of a dryer is generally defined as being the total holdup within a dryer at which a loaded flight with its flight tip located at the horizontal ($\psi + \psi_{ft} = 90^\circ$) is completely filled with solids. However, relating the maximum holdup within a flight at $\psi + \psi_{ft} = 90^\circ$ to the total holdup within the dryer is not necessarily easy. One commonly cited approach is the use of the assumption of Porter⁵⁴ who proposed that the design load of a dryer is equal to the amount of material required to completely fill half of the flights within the dryer, as shown in Equation 4.19.

$$M_{des} = \frac{N_f H_{0,design}}{2}$$

Equation 4.19. Porter's Assumption⁵⁴.

Consider a flighted rotary dryer with an even number of flights (N_f) of known geometry operating at design load and steady-state. Looking at the dryer when one flight (referred to here as N_0) is located at $\psi + \psi_{ft} = 90^\circ$, it is possible to determine the amount of material contained within the passive phase of the dryer. It is known that N_0 is fully loaded due to the design load condition, thus the holdup in N_0 is $H_{0,design}$. From the geometric calculations derived in Chapter 4.2.3, the holdup in any

flight in the upper section of the drum $\left(N_1 \text{ to } N_{\frac{N_f}{2}-1} \right)$ can be calculated and it can be

seen that the flight at $\psi + \psi_{ft} = 270^\circ$ must be empty.

It can be seen that the amount of material discharged as a flight moves between two points (e.g. N_1 to N_2) is equal to the difference in the holdup between those two flights (i.e. $H_1 - H_2$). Assuming that material falls vertically, this material must eventually be collected by a flight vertically opposite the point of discharge, thus for

steady-state operation, a flight in the lower section of the drum must hold the same amount of material as a flight vertically opposite it. Thus, a design-loaded dryer (and an underloaded dryer) will have vertically symmetrical holdup within the flights. Thus, the total passive phase holdup in a design-loaded drum can be found using Equation 4.20.

$$M_{p,des} = H_{0,design} + 2 \sum_{i=1}^{\frac{N_f}{2}-1} H_i$$

Equation 4.20. Determining the design load of a dryer.

The holdup in any flight, H_i , can be shown to be equal to the maximum holdup of a flight at $\psi + \psi_{ft} = 90^0$ minus the amount of material discharged, i.e.

$$H_i = H_{0,des} - \int_{90^0 - \psi_{ft}}^{\psi_i} dH .$$

Combining this with Equation 4.20 and simplifying gives

$$\begin{aligned} M_{p,des} &= H_{0,des} + 2 \sum_{i=1}^{\frac{N_f}{2}-1} \left(H_{0,des} - \int_{90^0 - \psi_{ft}}^{\psi_i} dH \right) \\ &= H_{0,des} \times N_f - 2 \sum_{i=1}^{\frac{N_f}{2}-1} \int_{90^0 - \psi_{ft}}^{\psi_i} dH \end{aligned}$$

Equation 4.21. Design load of a rotary dryer.

Using the Invicta Mill Dryer Number 2 as an example, Porter's assumption (Equation 4.19) predicts a dryer design load of 13 109 kg, whilst Equation 4.21 predicts a design load of 8 479 kg, a 35% difference. Porter's assumption, however, is an approximation based on the assumption that each pair of flights (one in the upper half of the dryer and one in the lower half of the dryer) have a full flight load (measured at $\psi + \psi_{ft} = 90^0$) between them⁵⁴. This assumption is clearly different from the assumption of vertical symmetry used in the geometric model. In order to determine which model, if either, is most accurate, experimental studies of the design load in a flighted rotary dryer are needed.

4.4.2. The Loading Factor

As the amount of material contained in the flights decreases (i.e. as f_{load} decreases), the point at which material begins to be discharged from the flights will move further around the circumference of the drum. Thus, it is necessary to determine the relationship between f_{load} (the flight loading factor) and $\bar{\psi}_r$ (the average particle release point). Thus, a method for determining f_{load} from the conditions within the dryer is necessary. At first, it might seem that f_{load} can be simply calculated as the fractional loading of the overall dryer (i.e. $f_{\text{load}} = \frac{M_p}{M_{p,\text{des}}}$), however it will be shown in this section that this is not correct.

Let the dryer loading factor, d_{load} , be defined as the fraction of the design load currently contained within the dryer (or dryer element), i.e. $d_{\text{load}} = \frac{M_p}{M_{p,\text{des}}}$. Note that this is different to the flight loading factor, f_{load} , which is defined based on the loading within a single flight. As such, $d_{\text{load}} = 1$ when the holdup in the dryer is equal to or greater than the design load of the dryer, $M_p \geq M_{p,\text{des}}$, as at or above the design load, flights passing $\psi = 90^\circ$ are at the maximum flight holdup.

Using a similar method as that used to calculate the design load for a dryer in reverse, it is possible to determine f_{load} for any given d_{load} for a dryer. By setting d_{load} , the passive holdup is known, and Equation 4.22 can be solved for f_{load} , noting that H_i may be less than the maximum flight holdup for the angle of rotation for some flights.

$$d_{\text{load}} \times M_{p,\text{des}} = f_{\text{load}} \times H_{0,\text{des}} + 2 \sum_{i=1}^{\frac{N_f}{2}-1} H_i$$

Equation 4.22. Calculating flight loading factor.

Figure 4.19 shows the relationship between the dryer loading factor (d_{load}) and the flight loading factor (f_{load}) for Invicta Mill Dryer Number 2. As can be seen $f_{load} \neq d_{load}$, and the relationship is strongly non-linear. Equation 4.23 gives a sixth order polynomial fit to the data ($r^2 = 0.9986$), relating f_{load} to d_{load} , and hence to the holdup in the passive phase (M_p). It must be noted that this correlation is only applicable for $0 \leq d_{load} \leq 1$, and that for $d_{load} > 1$, $f_{load} = 1$ (a flight can never exceed its design load, whilst the dryer as a whole can). This relationship was used in the solids transport model for the Invicta Mill Dryer Number 2 to calculate f_{load} based on the dryer holdup.

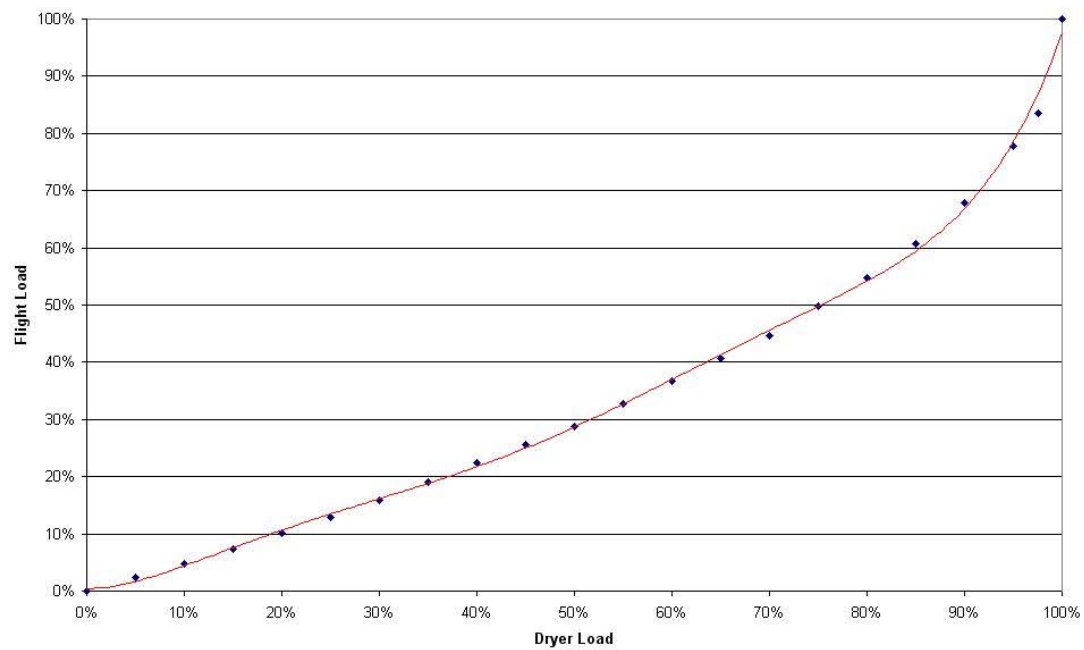


Figure 4.19. Relationship between dryer and flight loading factors for Invicta Dryer Number 2.

$$f_{load} = 4.5 \times 10^{-3} - 0.141 \times 10^{-2} d_{load} + 6.50 d_{load}^2 - 30.1 d_{load}^3 + 65.1 d_{load}^4 - 65.0 d_{load}^5 + 24.4 d_{load}^6$$

Equation 4.23. Relationship between flight and dryer loading factors.

4.5. Implementing Geometric Model in Solids Transport Model

Whilst the model developed in this chapter provides a means for calculating the solids transport coefficients required for the solids transport model, the implementation of the full geometric unloading model would be extremely computationally intensive. The geometric flight unloading model would need to be implemented for each differential slice of the dryer in the solids transport model, and recalculated at every time-step to account for changes in material properties (i.e. dynamic angle of repose). Given the number of cells used in most models (30 to 50), and the small time-steps employed, this rapidly adds up to a very large number of calculations.

Additionally, the software used in the implementation of the solids transport model (gPROMS[®]) is unsuited to iterative calculations within a single time step (see Chapter 3.3). gPROMS[®] does have facilities for calling external software routines, however there is a significant computational overhead associated with this, and does not relieve the necessity for running the geometric model for every cell in the model each time step.

To keep the calculation time of the model to manageable levels, the geometric model was implemented in Microsoft Excel[®] for a range of angles of repose and levels of flight loading (f_{load}), and linear regression methods used to determine correlations between these variables and the mass-averaged parameters (see Equations 4.24 to 4.26). Correlations were also developed for the dryer design load as a function of angle of repose, and to relate the flight loading factor (f_{load}) to the dryer loading factor (d_{load}) and the angle of repose, as shown in Equations 4.27 and 4.28.

$$\begin{aligned}\bar{h}_m \approx & 1.80 + 0.052\phi - 6.29 \times 10^{-4} \phi^2 + 6.32 \times 10^{-8} \phi^3 + 1.22 f_{load} + 2.17 f_{load}^2 - 1.22 f_{load}^3 \\ & + 0.01\phi f_{load} - 0.03\phi f_{load}^2 + 6.47 \times 10^{-4} \phi^2 f_{load} - 5.92 \times 10^{-4} \phi^2 f_{load}^2\end{aligned}$$

Equation 4.24. Correlation for the mass-averaged fall height ($R^2 = 0.997$).

$$\begin{aligned}\bar{t}_m \cong & 0.650 + 4.67 \times 10^{-3} \phi - 8.34 \times 10^{-5} \phi^2 + 1.10 \times 10^{-7} \phi^3 + 0.401 f_{load} - 0.106 f_{load}^2 - 0.012 f_{load}^3 \\ & + 2.75 \times 10^{-3} \phi f_{load} - 1.22 \times 10^{-3} \phi f_{load}^2 + 1.13 \times 10^{-4} \phi^2 f_{load} - 9.33 \times 10^{-5} \phi^2 f_{load}^2\end{aligned}$$

Equation 4.25. Correlation for the mass-averaged fall time ($R^2 = 0.996$).

$$\bar{\psi}_m \cong \sin^{-1} \left(\frac{\bar{h}_m}{2R_f} \right) + \frac{\pi}{2}$$

Equation 4.26. Correlation for the mass-averaged fall angle.

$$\begin{aligned}m_{p,des} = & \frac{\rho_b L}{N} \left(-2.31 + 0.34\phi - 0.018\phi^2 + 5.37 \times 10^{-4} \phi^3 \right. \\ & \left. - 8.64 \times 10^{-6} \phi^4 + 7.33 \times 10^{-8} \phi^5 - 2.55 \times 10^{-10} \phi^6 \right)\end{aligned}$$

Equation 4.27. Correlation for the dryer design load ($R^2 = 0.999$).

$$\begin{aligned}f_{load} = & -4.50 \times 10^{-2} - 9.97 \times 10^{-4} \phi + 2.73 \times 10^{-5} \phi^2 - 1.21 \times 10^{-7} \phi^3 + 1.84 d_{load} - 1.84 d_{load}^2 \\ & + 1.68 d_{load}^3 + 6.18 \times 10^{-3} \phi d_{load} - 6.06 \times 10^{-3} \phi d_{load}^2 - 1.41 \times 10^{-3} \phi^2 d_{load} + 1.21 \times 10^{-4} \phi^2 d_{load}^2\end{aligned}$$

Equation 4.28. Correlation for the flight loading factor ($R^2 = 0.991$).

The geometric unloading model was implemented as a separate submodel in gPROMS® as shown in Figure 4.20. The necessary input data (dryer loading (d_{load}) and solids moisture content (used to calculate the dynamic angle of repose of the solids)) were passed from the passive phase to the geometry model, where the above equations were used to calculate the mass averaged conditions, and thus the residence times of the active and passive phases. These values were then passed to the relevant submodels to model the solids transport.

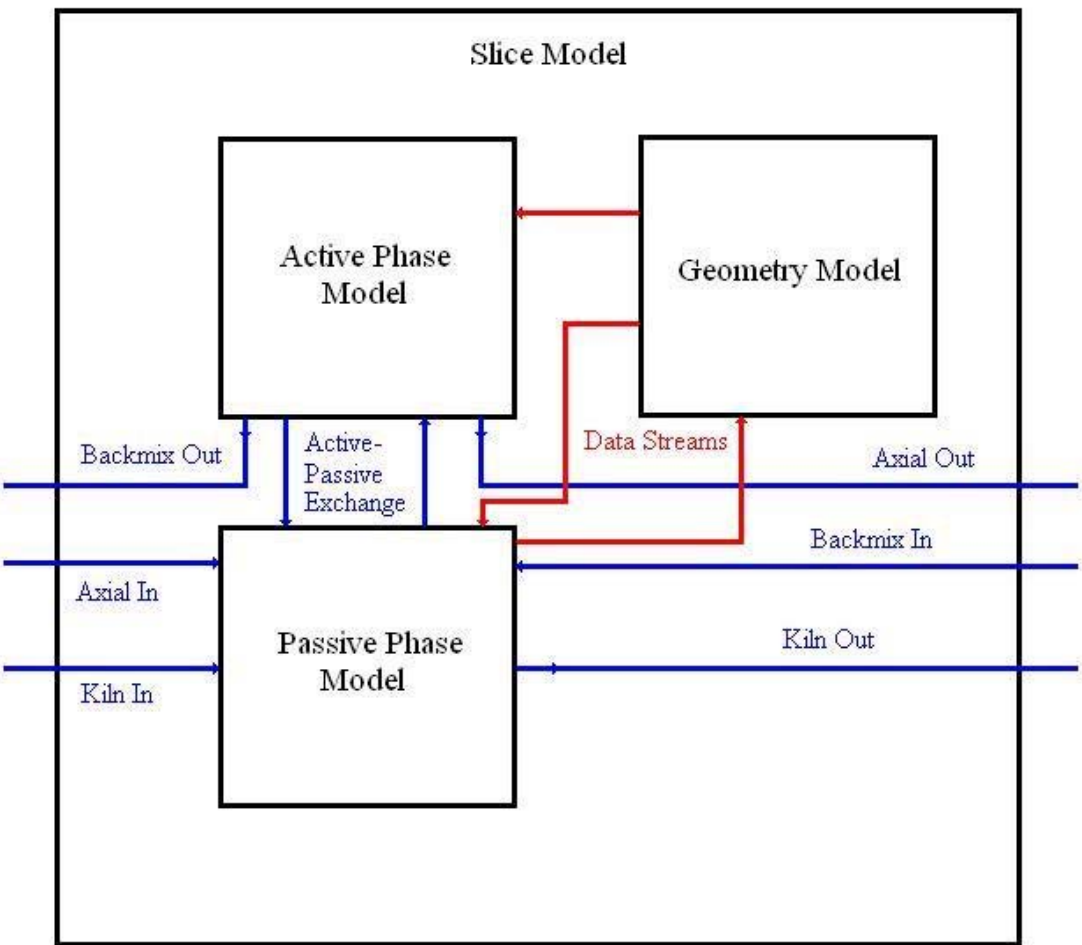


Figure 4.20. gPROMS[®] model structure.

Chapter 5

5. Experimental Validation of the Geometric Unloading Model

In order to validate the geometric unloading model for a flight developed in the previous chapter, it is necessary to measure either the mass flux leaving a flight or the mass contained within the flight as it rotates. From the available literature, two different methods have been used to experimentally evaluate the unloading profile of dryer flights to date. Hodgson and Keast⁵⁵ physically measured the mass flux at specific locations across the horizontal axis of the dryer in order to measure the unloading profile. Other researchers, such as Kelly⁵ and Revol *et al.*⁴¹ photographed the cross-section of flights at various locations around the circumference of a dryer and calculated the amount of mass contained in the flight at each point. Whilst both these methods have provided useful data on the unloading profile of the flight, it would be preferable to be able to directly measure the mass flow leaving the flight for an individual flight in isolation.

5.1. Flight Unloading Apparatus

In order to study the unloading profile of a single flight, an experimental apparatus was designed and commissioned at James Cook University in order to simulate the behaviour of a flight within a dryer. The apparatus consisted of a single flight that could be rotated at a controlled rate (rpm), allowing the flight to unload in controlled circumstances. The material discharged from the flight was collected in a tray mounted on load cells, allowing the amount of mass discharged over time to be measured directly.

The apparatus was designed to fit a 1 metre long section of a full-scale industrial dryer flight that could then be tipped and unloaded at a controlled rate. In order to achieve this, a horizontal shaft (1.5m long) to which the flight could be bolted was attached to a SEW-Eurodrive stepper motor. Bolting the flight to the drive shaft

allowed for rapid and easy swapping of different flight designs on the apparatus. The use of a stepper motor allowed for accurate control over the rotational velocity of the flight and repeatable start and finish points for unloading experiments. The drive shaft also included room to attach a camera mount, to allow filming of the flight as it unloaded.

In order to measure the discharge profile of the flight, an aluminium collection tray was placed below the drive shaft, mounted on four 50kg Button Type load cells (Precision Transducers SG-LPX-50) connected to four custom made amplifiers. The load cells were mounted in the four corners of the collection tray, and the height of each cell could be adjusted in order to balance the tray. The load cells allow continuous measurement of the mass of solids collected in the tray as the flight unloads, thus allowing the unloading profile to be calculated. Data from the load cells was collected using a computer running LabView® at a frequency of 0.01 seconds (100 Hz). Figure 5.1 shows a photograph of the experimental apparatus and Figure 5.2 shows a schematic of the tray and flight cross-section.



Figure 5.1. Photograph of experimental apparatus.

Three different sized flights were constructed for the apparatus to provide a range of different unloading profiles. The first flight design was a full-scale section of flight similar to that used in CSR's Invicta Sugar Mill Dryer Number 2 whilst the second was a geometrically scaled-down version of the same flight (half size). The third

flight design was of intermediate size, and had a different shape to allow studies on how flight dimensions affect unloading (referred to as Alternative). No flights were serrated. The two larger flights (Full Scale and Alternative) were fitted with clear viewing windows in one end to allow filming of the cross-section of the unloading flight. Testing of the apparatus was performed using the Half Scale flight, and the dimensions of all the flights are shown in Table 5.1.

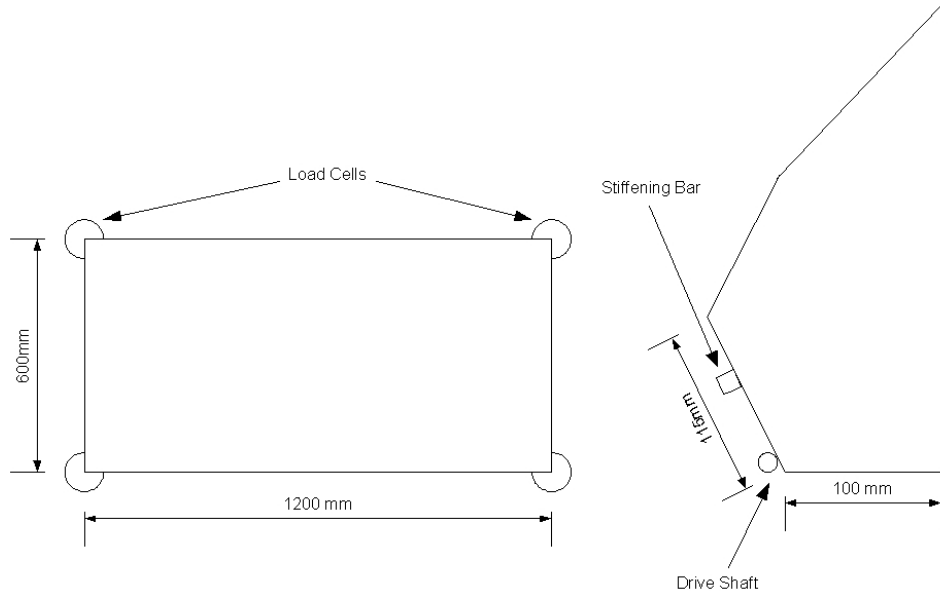


Figure 5.2. Schematic of collection tray and flight cross-section (Alternative design).

	Full Scale	½ Scale	Alternative
Flight Base Length, s_1	200 mm	100 mm	150 mm
Flight Tip Length, s_2	220 mm	110 mm	180 mm
Flight Base Angle, α_1	90°	90°	90°
Flight Tip Angle, α_2	117°	117°	100°
Length of Flight Section	1 m	1 m	1 m
Radius of Curvature	2.5 m	1.25 m	No Curve

Table 5.1. Dimensions of experimental flights.

5.2. Commissioning and Testing

Each of the load cells was individually tested and calibrated before being installed on the apparatus. The load cells were initially tested and calibrated using the School of Engineering's Instron testing machine. The load cell amplifiers were adjusted so that the output to the computer would be approximately 4.8 V at the load cells maximum load (50 kg). The load cells were later recalibrated in situ using known masses and the calibration data entered into LabView®. LabView® was also used to calculate the location of the centre of mass within the collection tray based on the readings of the four load cells (see Figure 5.2) as discussed below.

Looking in two-dimensions (see Figure 5.3), and assuming that the force due to the weight of the solids and the tray is exerted at the centre of mass of the system (a point source), a moment will be exerted at the two ends of the tray where it is supported by the load cells. These moments will be equal to the force exerted at each end multiplied by the distance to the centre of mass, $M_a = F_a x_a$ where M_a is the moment exerted, F_a is the force exerted on the load cells (the sum of the two load cells at each end) and x_a is the distance to the centre of mass. As this is a static system, the sum of the moments must be zero, thus $F_a x_a = F_b x_b$, where $x_a + x_b = l$ is the total length of the tray. Combining these equations gives Equation 5.2, which allows the calculation of x_a , i.e. the distance the centre of mass lies from one end of the tray. This can be performed for both dimensions of the tray to find the location of the centre of mass.

$$x_a = \frac{l}{\left(\frac{F_a}{F_b} - 1 \right)}$$

Equation 5.1. Locating the Centre of Mass.

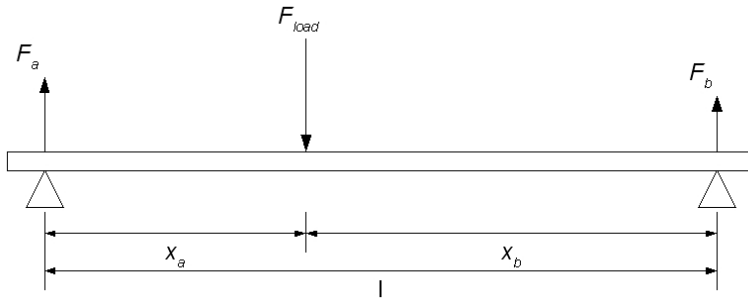


Figure 5.3. Force diagram on collection tray.

5.2.1. Levelling the Collection Tray

The first problem encountered with the apparatus involved levelling the apparatus so that the load was distributed evenly across the four load cells (i.e. the centre of mass was in the geometric centre of the tray). It was found that the apparatus was very sensitive to the levelling of the collection tray, with only small adjustments in the height of each load cell having a significant impact on the readings of the cells. It was also found that moving the apparatus could have a large effect on the load cell readings due to variations in the height of the floor, thus it was necessary to level the tray each time the apparatus was moved. Levelling of the tray with an empty tray was achieved by adjusting the height of each of the four load cells until the readings on each cell were the same. The heights of the load cells were adjusted using a pair of nuts on each of the four mounting screws in the bottom of the load cell.

5.2.2. Influence of External Sources

During initial testing it rapidly became apparent that the load cells were highly susceptible to background noise and interference from external sources. Figure 5.4 shows the readings from a load cell for an experiment using the Alternative flight design and filter sand at 2 rpm. The effects of background noise can be seen in the variation in the data. This becomes more apparent when plotting the derivative of the data (i.e. the mass flow rate entering the collection tray), as can be seen in Figure 5.5.

The mass flow rate was calculated from the accumulated mass data using a first-order central difference method.

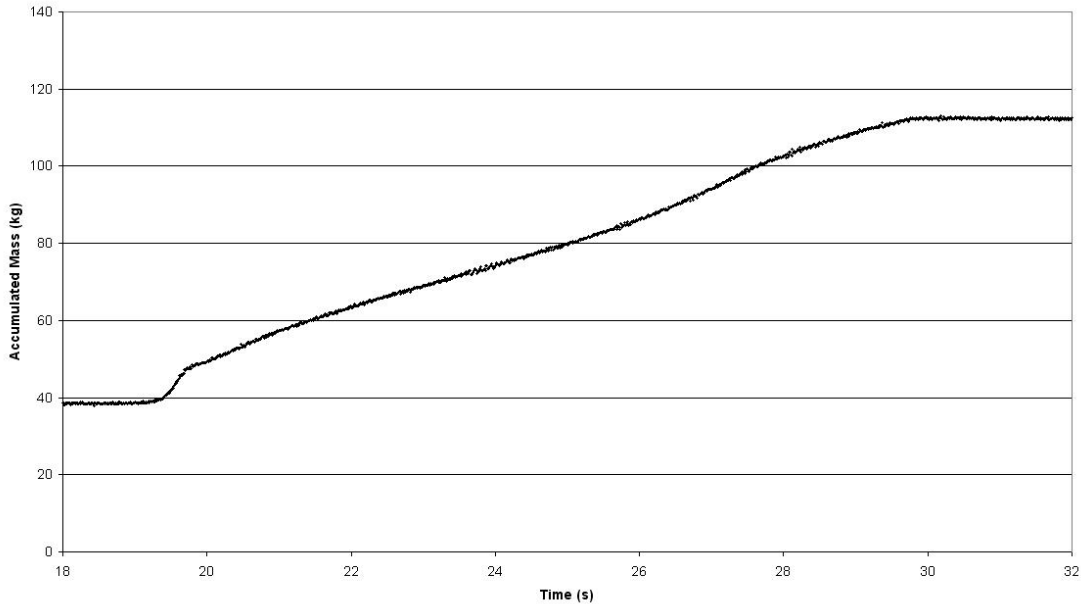


Figure 5.4. Example of raw experimental data (2 rpm).

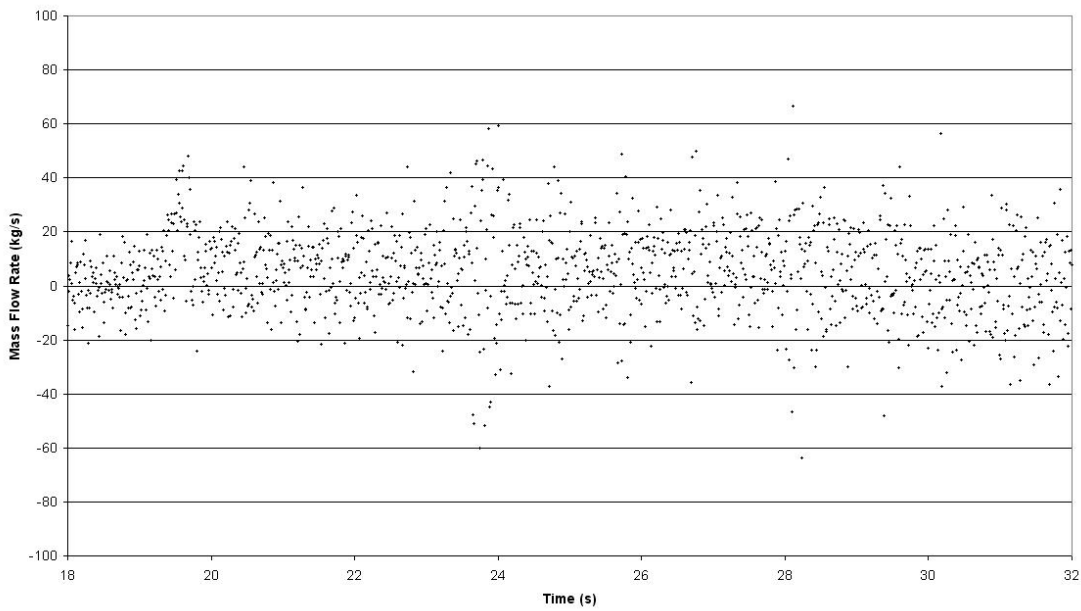


Figure 5.5. Derivative of example raw experimental data (2 rpm).

The main sources of noise within the system were believed to be due to the motor and drive shaft, which are mounted on the same frame as the load cells, thus transmitting the vibration of the motor to the load cells. To remedy this, a Finite Impulse Response (FIR) filter was implemented using Matlab[®] to remove the noise from the data. The filter used was a 200th order FIR filter with a cut-off frequency of 3 Hz, which, when applied to the data in Figure 5.4, gives the results shown in Figure 5.6 and Figure 5.7. The cut-off frequency of 3 Hz was chosen to be as low as possible without affecting the actual data, whilst removing as much noise as possible. As can be seen in the differentiated data after filtering (Figure 5.7) compared to Figure 5.5, the FIR filter used significantly reduced the noise present in the experimental results.

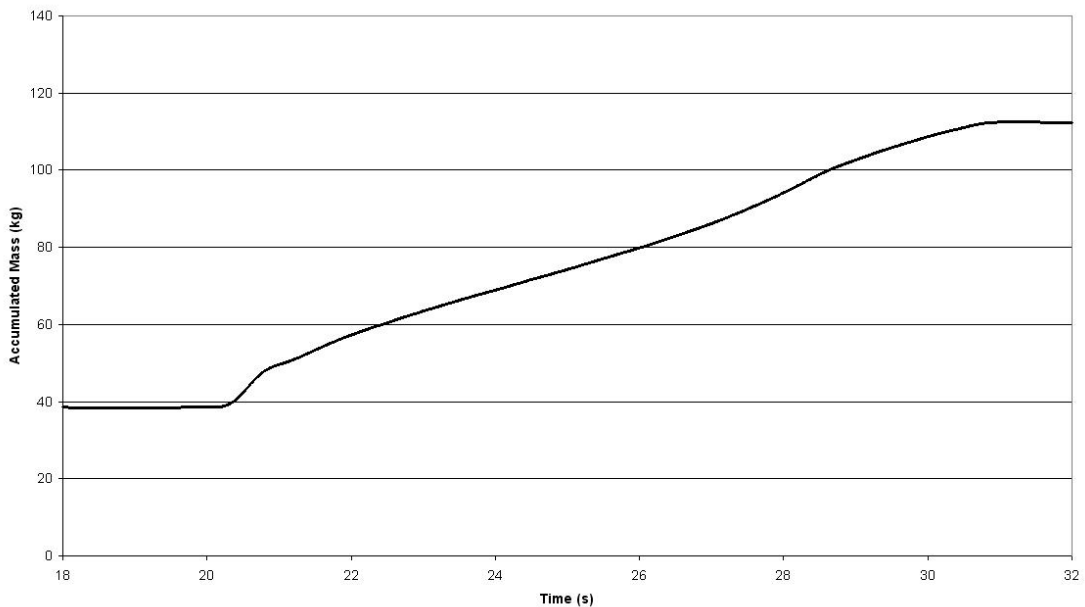


Figure 5.6. Example of experimental data after filtering (2 rpm).

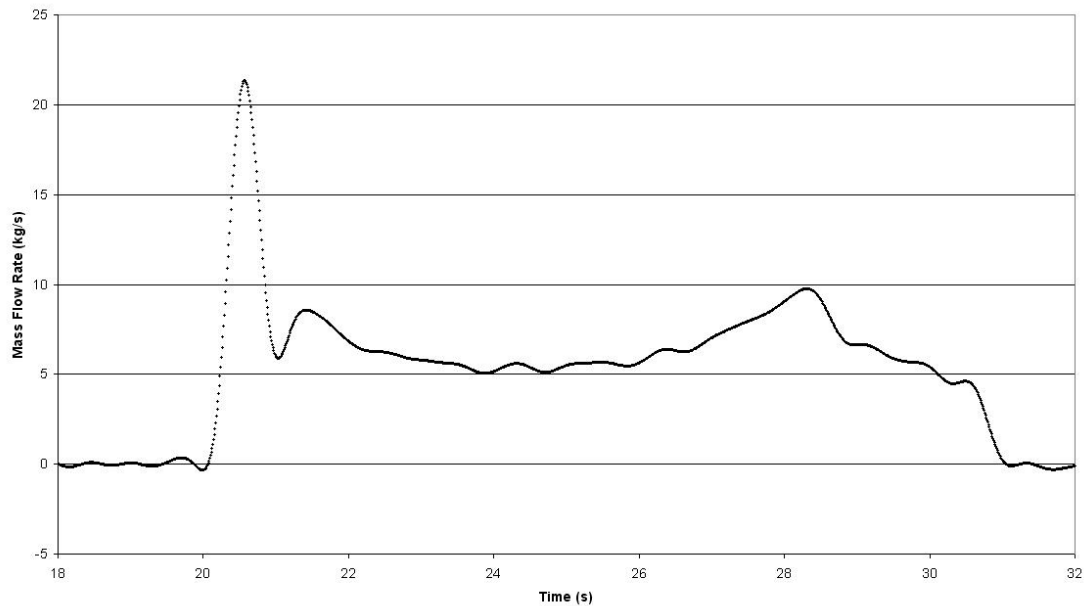


Figure 5.7. Derivative of example raw experimental data after filtering (2 rpm).

It was also noted during testing that other external effects, such as a breeze within the laboratory seemed to influence the results, thus care was taken to minimise external sources influencing the results. In addition, the collection tray was preloaded with an evenly distributed mass of solids (approximately 30kg) to help reduce vibration.

5.2.3. Dynamic Effects

As the rotational velocity (rpm) of the apparatus was increased, it was observed that the load cell readings reach a peak, before decreasing noticeably to their final total mass (see highlighted point in Figure 5.8). This would appear to suggest that the mass in the tray decreases after the flight has finished unloading, which is not physically possible. It is assumed that this peak is due to impact forces from the falling material being detected by the load cells, and increasing the force expected from the static mass in the tray. A number of methods were attempted in order to minimize this effect by cushioning the falling material as it hits the tray. These include increasing the initial mass within the tray, placing a layer of open-cell foam in the bottom of the tray, and placing a layer of closed-cell foam over this, however none of these methods successfully removed this effect. Analytical methods were also attempted to model

the effects of impact forces, however estimation of the model parameters (specifically the duration of impact for a particle) was found to be impossibly arduous.

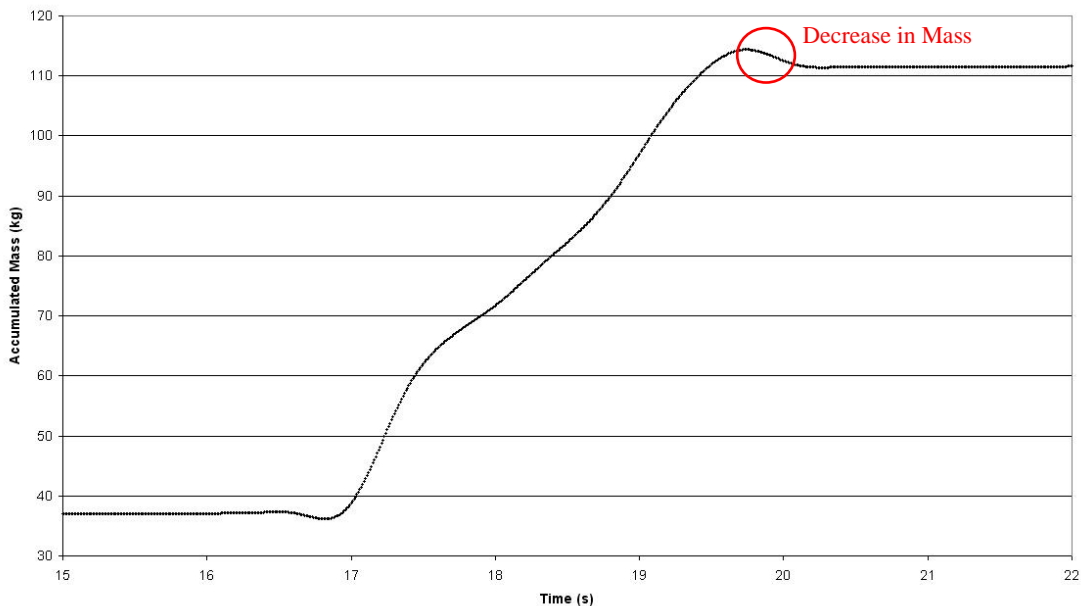


**Figure 5.8. Example of the effects of impact forces on accumulated mass measurement
(Flight design 3, filter sand, 8 rpm).**

Further testing of the apparatus using accelerometers to measure dynamic effects is planned, however upon comparison with modelled data, it was observed that this effect was restricted only to the very final section of the unloading profile. Thus, impact forces were not accounted for in this thesis.

5.2.4. Centrifugal Effects

One concern with the design of the flight unloading apparatus is that the flight rotates closely around the drive shaft, whilst in an actual dryer, the flight would describe a much larger arc. Due to this, the centripetal forces affecting the material in the experimental apparatus are less than they would be in an actual dryer ($11\times$ less using the full scale flight). Thus, the forces holding material within the flight will be less, possibly resulting in a different dynamic angle of repose for the solids in the experimental apparatus as compared to the same material in an actual dryer. This would result in a different unloading profile to that seen in an actual dryer. Schofield

and Glikin⁴ developed a relationship for the dynamic angle of repose of a solid within a flight as a function of the solid coefficient of friction (μ) and the angular velocity (ω), radius (r), length of flight tip (l) and location of a flight (θ) as shown in Equation 5.2.

$$\tan \phi = \frac{\mu - r \frac{\omega^2}{g} (\cos \theta - \mu \sin \theta)}{1 - r \frac{\omega^2}{g} (\sin \theta - \mu \cos \theta)}$$

Equation 5.2. Relationship for the dynamic angle of repose (Schofield and Glikin⁴)

For the case of the flight unloading apparatus, the length ($r-l$) is replaced by the distance from the drive shaft to the flight tip. Given that this distance is small, the centripetal forces occurring within the flight unloading apparatus should be small, thus Equation 5.2 can be approximated as $\tan \phi = \mu$. Thus, the dynamic angle of repose of the solids within the flight unloading apparatus should be solely determined by the coefficient of friction, and thus be approximately constant.

5.2.5. Surface Friction Effects

In the later stages of unloading (primarily between transition points IV and V), it was observed that the material in the flight began to move as a bulk, rather than flowing off the end of the flight. This was attributed to the forces acting on the bulk exceeding the friction between the solids and the flight surface. This phenomenon was not considered in the geometric unloading model, and would be unlikely to occur in an industrial dryer due to flight coating. Thus, in order to replicate the conditions for which the geometric model was developed, the surface of the flight tip was covered with an abrasive surface (sand paper) to increase friction between the surface and the solids. Covering the flight tip with this material was observed to prevent the bulk movement of solids during unloading. Whilst this may not accurately represent the true flight surface in an industrial dryer, it should be noted that many industrial dryer flights become coated in a layer of solids material that may have a similar effect

(especially in the case of sticky materials such as sugar). All observed flights in industrial dryers have been extensively coated with solids.

5.2.6. Camera Location

A high-speed camera (see Chapter 5.1 for details) was mounted on the drive shaft of the apparatus, allowing it to travel with the flight as it rotated and observe the cross-sectional area of the solids in the flight. However, this means that the camera was observing the material in contact with the end wall of the flight, and thus the behaviour of the solids would have been influenced by friction with the wall. However, as the end walls of the flights were made from Perspex, the friction between the particles and the wall would be less than the friction between particles, minimising the effect of the wall.

5.3. Experimental Methods

The flight unloading apparatus allows the unloading profile of a flight to be easily studied in isolation, and allows for easy testing using different flights, materials and rotational speeds. In the following section, the materials and experimental methods used to validate the geometric flight unloading model are presented.

5.3.1. Experimental Materials

Three granular solid materials were used in the experiments using the flight unloading apparatus. These were a Grade 7 filter sand, a zeolite filter medium (Olson's Zeolite Pool Filtration Medium) and a fine river sand. Before the materials were used in the flight unloading apparatus, the particle size distribution, particle density, bulk density (both consolidated and unconsolidated) and the static and dynamic angles of repose of each material were measured. The particle size distribution was measured using dry sieving. Particle density was calculated by taking a sample of material of known mass, and adding water to make up the mixture (water and solids) to a given volume.

The mass of the combined solids and water was then measured and used to calculate the particle density as shown below.

Let V_T , V_s and V_w be the volume of the total mixture, solids and water respectively, m_s and m_w be the mass of solids and water and ρ_s and ρ_w be the density of solids and water respectively. Then,

$$\begin{aligned} V_T &= V_s + V_w \\ &= \frac{m_s}{\rho_s} + \frac{m_w}{\rho_w} \\ &= \frac{m_s}{\rho_s} + \frac{m_T - m_s}{\rho_w} \\ \frac{m_s}{\rho_s} &= V_T - \frac{m_T - m_s}{\rho_w} \end{aligned}$$

Rearranging gives:

$$\rho_s = \frac{m_s}{V_T - \frac{m_T - m_s}{\rho_w}}$$

Equation 5.3. Calculation of particle density.

The unconsolidated solids bulk density was measured by loosely filling a container of known volume with solids and weighing the sample. When compared to the results obtained from the flight unloading apparatus, it was observed that the solids bulk densities within the flight were consolidated within the flight (see Chapter 5.4.3.1 for an example). The consolidated solids bulk density was determined by filling a container of know volume with solids and tapping the side of the container to consolidate the solids. The container was then topped up with more solids and tapped again until no more consolidation occurred. The sample was then weighed in order to determine the consolidated bulk density. The dynamic angle of repose was measured by placing a sample of the material in a horizontal rotating cylinder (trommel), and photographing the slope of the material surface at two different rotational speeds (1 and 2 rpm) (see Figure 5.9). The images were then analysed using ImageJ software (<http://rsb.info.nih.gov/ij/>) to measure the angle of repose. The static angle of repose was measured using the same apparatus by stopping the rotating cylinder and

measuring the slope of the material surface at rest. The measured solids properties are shown below in Table 5.2. The errors given for densities are standard probable errors based on measurement uncertainty, whilst the errors on the angles of repose are 95% confidence intervals.

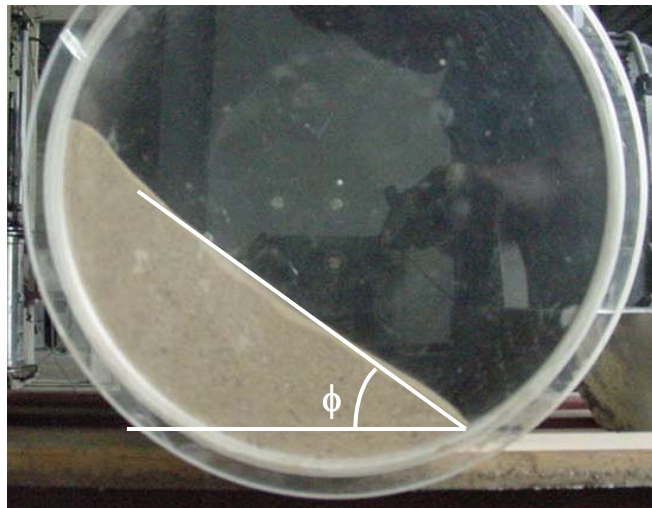


Figure 5.9. Photograph of trommel apparatus in operation.

Material	Particle Density (kg/m ³)	Bulk Density (Unconsolidated) (kg/m ³)	Bulk Density (Consolidated) (kg/m ³)	Static Angle of Repose	Dynamic Angle of Repose
Filter Sand	2530±60	1306±0.04	1474±0.04	34±1°	35±2°
Zeolite	2200±60	1075±0.03	1246±0.04	36±2°	38±2°
River Sand	2580±70	1299±0.04	1483±0.04	34±1°	33±2°

Table 5.2. Measured solids properties.

The particle size distribution for each material is given in Table 5.3 in terms of the percentage of material passing a given sieve size. Figure 5.10 shows the cumulative particle size distribution for the different materials derived from these results.

Sieve Size (micron)	wt% Material Passing Sieve Size		
	Filter Sand	Zeolite	Fine Sand
2000	100.00 %	100.00 %	100.00 %
1180	99.75 %	37.08 %	97.83 %
600	10.61 %	2.25 %	96.34 %
425	0.59 %	0.46 %	93.76 %
300	0.10 %	0.24 %	73.46 %
150	0.03 %	0.14 %	15.39 %
75	0.00 %	0.05 %	1.22 %

Table 5.3. Material particle size distribution.

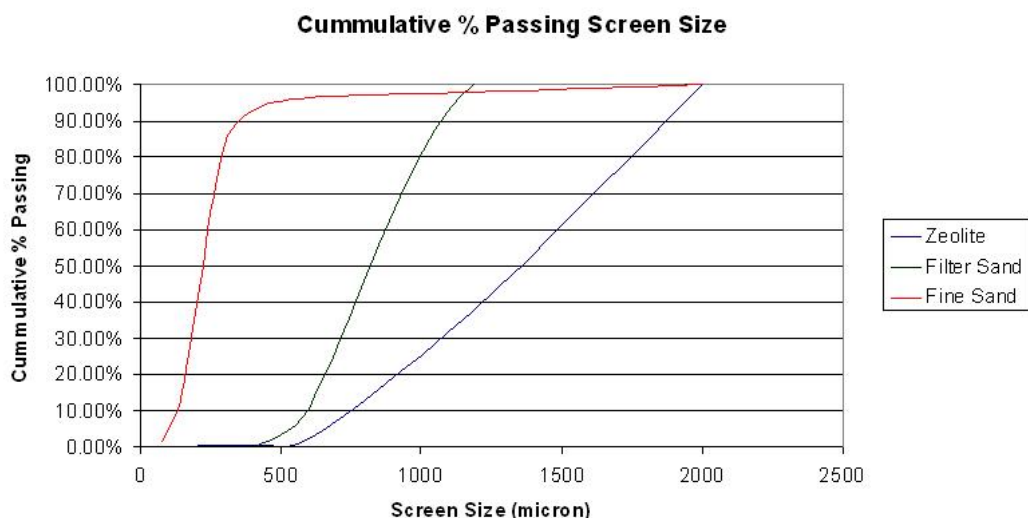


Figure 5.10. Material particle size distribution.

From Figure 5.10 it can be seen that the three materials have significantly different particle size distributions. The fine river sand shows a very tight range of particle sizes, with most particles having sizes between 150 and 300 microns. The other materials show broader particle size distributions and larger particle sizes. Comparing the values in Table 5.2, it can be seen that the properties of the fine river sand and the filter sand are very similar, whilst the zeolite material shows a lower density than the

two sands. Whilst some variation can be seen in the measured angles of repose, the amount of error present in these measurements precludes any meaningful comparison.

5.3.2. Experimental Design

In order to fully validate the geometric unloading model for a flight, it was necessary to demonstrate that the model could accurately predict the unloading profile of any two-stage flight under any operating conditions. Three flights of different geometry were tested, and three different solid materials were employed to test the effects of solids properties on the unloading. The only operating condition that effects the unloading of flights is the rate of rotation of the dryer, so tests were conducted at four different speeds of rotation to study this effect.

As discussed in Chapter 5.2.5, an abrasive surface was placed on the flight tip in order to prevent bulk motion of solids in the later stages of unloading. In order to study the effects of this bulk motion of solids, and additional set experiments were conducted without the abrasive surface on the flight tip.

Given the large number of variables involved, and the aim being to validate the model rather than determine the effects of variables, a full factorial experiment was deemed to be unnecessary. The final set of experiments is given below in Table 5.4, along with the conditions of that experiment (a * indicates experiments without the abrasive surface in place). In order to test repeatability, repeats of experiments 6, 8, 9, 10, 11 and 12 were conducted. All experiments were filmed using high-speed photography.

Experiment	Flight	Material	Speed (rpm)
1	Alternative*	Filter Sand	1
2	Alternative*	Filter Sand	2
3	Alternative*	Filter Sand	4
4	Alternative*	Filter Sand	8
5	Alternative	Filter Sand	1
6	Alternative	Filter Sand	2
7	Alternative	Filter Sand	4
8	Alternative	Filter Sand	8
9	½ Scale	Filter Sand	2
10	½ Scale	Filter Sand	8
11	Full Scale	Filter Sand	2
12	Full Scale	Filter Sand	8
13	Alternative	Zeolite	2
14	Alternative	Zeolite	8
15	Alternative	River Sand	2
16	Alternative	River Sand	8

Table 5.4. List of experiments and conditions.

5.3.3. Experimental Procedures

In order to ensure safety and consistency between runs, a standard procedure was developed for conducting the flight unloading experiments. The procedure for completing an experiment is given below.

1. The flight was filled with solid material using a bucket, and the material surface levelled using a ruler run along the tip and back edge of the flight*.

* For the experiments using the largest flight design (Full Scale), it was found that the flight could hold more mass than the load cells could measure. In this situation, the

2. The safety cage was closed and locked and the rotational speed of the unloading apparatus was set.
3. The spotlights (for the high-speed camera) were turned on and the high-speed camera alignment and settings were checked.
4. The load cell data acquisition programme was started.
5. The high-speed camera was triggered to start filming.
6. The unloading apparatus was turned on and allowed to completely unload.
7. After the apparatus had completed unloading, the load cell data acquisition was stopped.
8. After the camera had finished filming, the camera was set to download the captured images to the computer.
9. The spotlights were turned off.
10. The apparatus was returned to its starting position.
11. The safety cage was unlocked and opened.
12. Solid material was returned to the flight from the collection tray, ready for the next experiment.

flight was loaded with as much material as possible, rather than being filled completely.

5.4. Data Analysis

In order to be able to compare the data from the high-speed camera, load cells and geometric unloading model, a significant amount of data analysis was required. The images from the high-speed camera were analysed to obtain quantitative data for the variables of interest (angle of repose, curtain thickness and particle velocity). The data from the load cells was filtered to remove background noise and to calculate the mass flow rate. The two sets of data were then aligned to a normalized time in order to compare the results to the model predictions. This was done by determining the start time of the experiment in both sets of data and defining this as time zero, as discussed in the following sections.

5.4.1. Image Analysis

The images captured from the high-speed camera were analysed manually using the freely available software ImageJ. The images were used to calculate the angle of repose of the solids, the thickness of the layer of solid material as it left the flight tip and the velocity of the solid particles as they left the flight as a function of angle of rotation. The camera was set to operate at 125 frames per second with a shutter speed of $1025\mu\text{s}$, and the images were taken at a resolution of 800×600 pixels.

The angle of rotation of the flight at the beginning of the experiment (ψ_0 , the angle between the base of the flight and a vertical line drawn downwards as shown in Figure 5.11) was determined by measuring the angle between the flight tip and a known horizontal beam (refer to Figure 5.12). From there, the angle of rotation (ψ) could be calculated for any frame based on the speed of rotation. Once the angle of rotation was calculated, the angle of repose of the material (ϕ) in each frame could be calculated by measuring the angle between the material surface and the flight tip (ζ) (see Figure 5.13). The angle the material surface makes relative to the base of the flight can be shown to be $\zeta - (180^\circ - \alpha_2)$ using internal angles (see Figure 5.14), and

the angle of the base of the flight to the horizontal is $\psi + 90^\circ$, thus the material angle of repose can be found to be $\phi = \zeta + \psi + \alpha_2 - 270^\circ$.

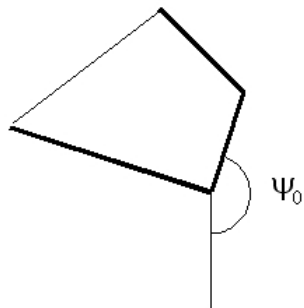


Figure 5.11. Initial location of flight.

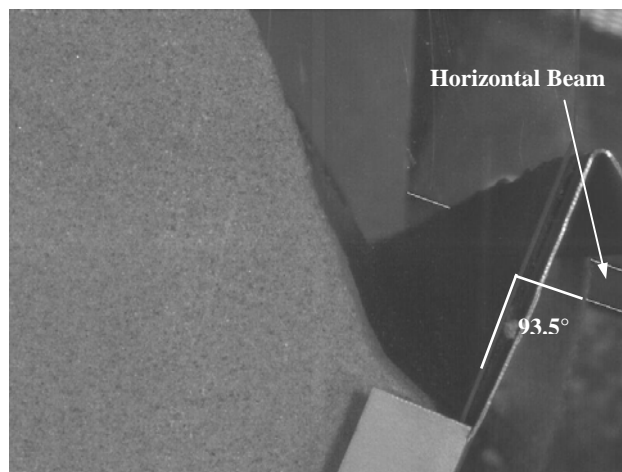


Figure 5.12. Measuring angle of rotation from photographs.

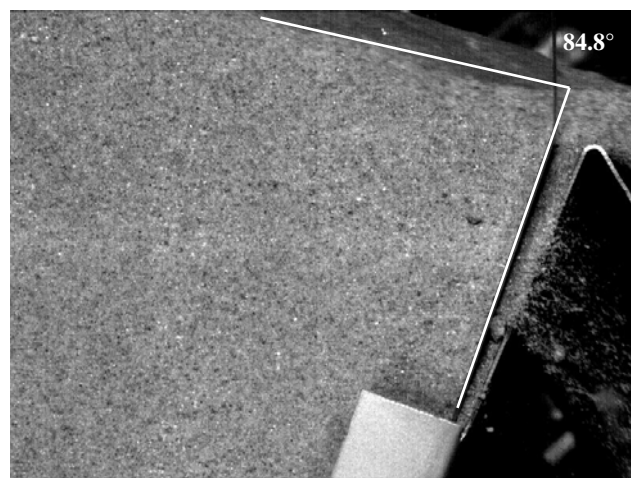


Figure 5.13. Measuring material angle of repose.

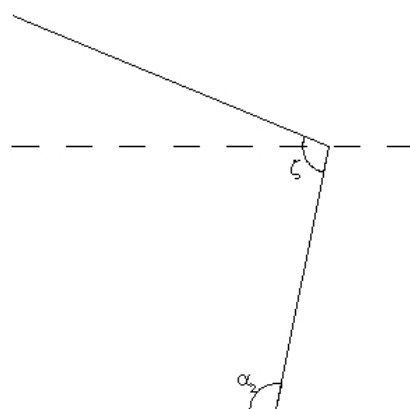


Figure 5.14. Schematic of flight showing calculation of angle of repose from measurements.

The thickness of the material curtain (c) flowing off the flight tip was calculated by measuring the distance from the flight tip to the material surface in pixels from the photographs. This thickness was then converted into millimetres by measuring a known length in the photograph (the distance from the flight tip to the support frame) in pixels and scaling the result (see Figure 5.15). The velocity or particles leaving the tip of the flight were calculated by tracking individual particles between frames, as shown in Figure 5.16. By measuring the location of a particle in two frames, the displacement of the particle can be calculated, and hence the velocity.



Figure 5.15. Measuring the curtain thickness.

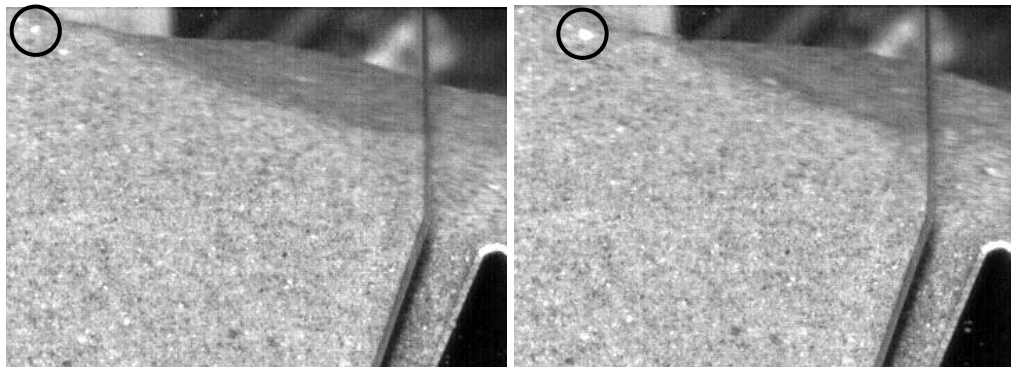


Figure 5.16. High-speed camera images showing a tracked particle (circled in black).

5.4.2. Load Cell Data Analysis

The load cell data acquired from the experiments consisted of readings from each individual load cell at intervals of 0.01 seconds. In order to analyse the results of each experiment, the individual load cell readings were first summed to give a total mass reading for the entire tray and the initial mass in the tray subtracted. The accumulated mass versus time data was then filtered using the FIR filter discussed in Chapter 5.2.2 using Matlab[®]. The filtered data was then differentiated using a central difference method (gradient function in Matlab[®]) to calculate the mass flow rate at each point. The Matlab[®] code used can be found in Chapter 11.1.

5.4.3. Normalizing Time Values

In order to compare the data from the load cells, high-speed photography and geometric unloading model, all the results needed to be adjusted to a normalized time. As both the geometric unloading model and high-speed photography data contained angle of rotation data, these were easily aligned. The load cell data however was measured independently of the angle of rotation, thus a method was needed to align this data with the rest. The geometry model described in Chapter 4 was implemented directly in Matlab[®] and was used to calculate the total discharged mass and mass flow rate from the flight. The average experimentally measured angle of repose (calculated from the high-speed camera images) was used as an input to the geometric unloading

model. Full Matlab[®] code for fitting the experimental data to the geometric unloading model can be found in Chapter 11.2.

In order to compare the experimental results and the predictions of the geometric unloading model it was necessary to align the two sets of data to a common time basis. The photographic data from the high-speed camera could be used to determine the point at which the flight began unloading, which was defined as time zero, and the rotational location of the flight at this point. This could then be used as the start point for the geometric unloading model which could then be used to align experimental load cell data. To do this, it was necessary to choose an easily identifiable point in the unloading profile that could be used to align the experimental and predicted unloading curves. The three most easily identifiable points, shown in Figure 5.17, are the start and finish of the unloading profile, and the intermediate peak in the mass flow rate profile.

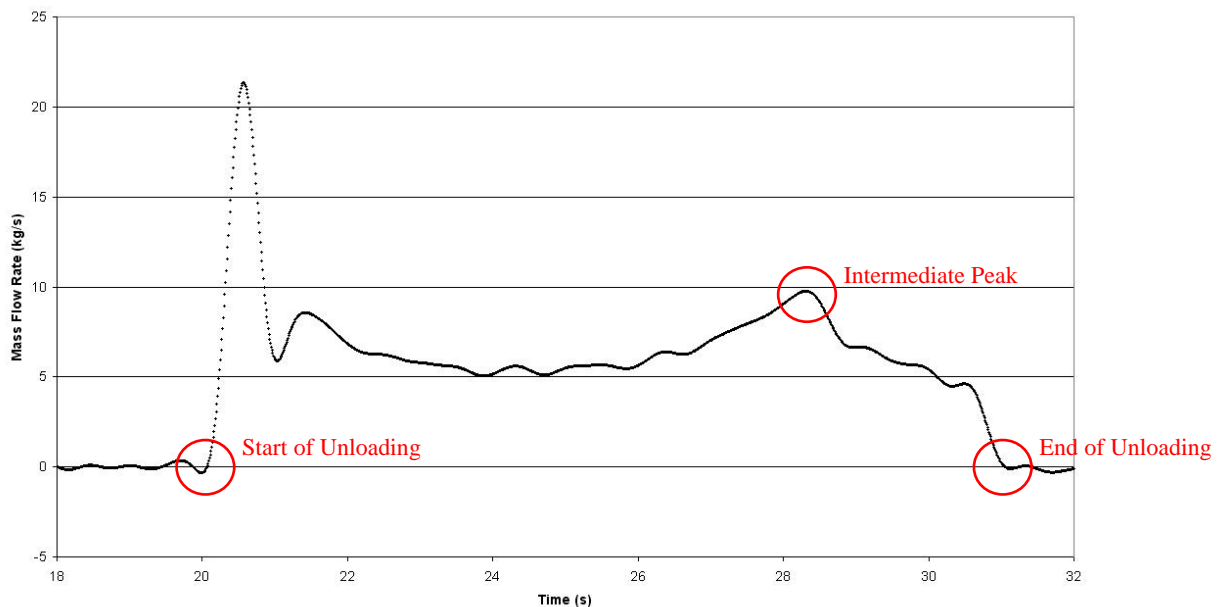


Figure 5.17. Measured mass flow rate profile (1/2 scale flight, 2 rpm, filter sand).

The best option for aligning the profiles was considered to be the point where the flight unloading apparatus first begins to discharge mass, as this point is independent of experimentally measured variables such as material angle of repose. This point corresponds to the point in the load cell data where mass first begins to enter the

collection tray. This point was identified as being the point where the derivative of the load cell data (i.e. the mass flow rate) became greater than 0. An example of the results of this alignment method is shown in Figure 5.18 for an experiment using the alternative flight design and filter sand at 2 rpm.

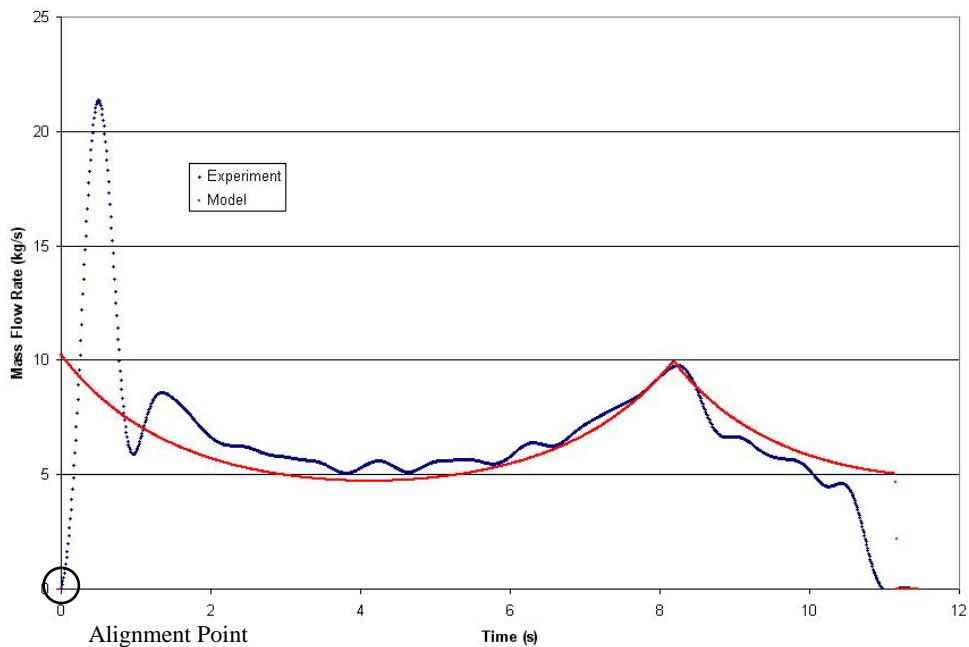


Figure 5.18. Example of alignment method for experimental data (Alternative Flight, Filter Sand, 2 rpm).

Figure 5.18 shows that this alignment method provides a good match between the experimental mass flow rate and model data. Figure 5.19 shows the comparison of the accumulated mass data for the same experiment. It can be seen here that the comparison between the model and experimental results for the accumulated mass is not as good as for the mass flow rate. It can be seen that the model appears to predict an accumulated mass at time zero, which would appear to be unusual. This is due to the definition of time zero being the point where the experimental data begins to increase. However, it can be seen that when the flight begins to unload, it does so with a sudden discharge of mass, rather than the smooth unloading curve predicted by the model. Thus, in order for the model to fit the experimental data, the start point for the simulated unloading profile must be offset to before time zero, resulting in the predicted accumulated mass at time zero.

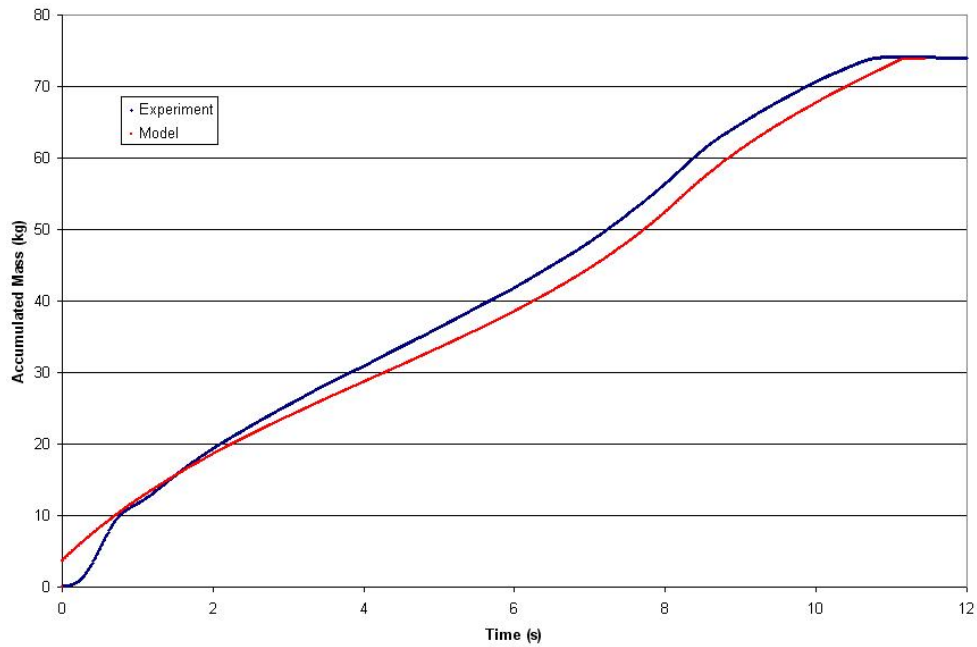


Figure 5.19. Comparison of accumulated mass data (Alternative Flight, Filter Sand, 2 rpm).

This deviation is probably due to errors in the material dynamic angle of repose used in the geometric unloading model. The value used in the model was the average of the angle of repose measured using the high-speed camera, thus is subject to error (a 95% confidence interval of $39.6^\circ \pm 3.4^\circ$ for this example). In order to assess the effects of this error, the standard deviation of the measured angle of repose data used to assess the variability in the geometry model predictions of the total mass and unloading profiles (± 2 standard deviations gives the 95% confidence interval). An example of these results is shown in Figure 5.20 and Figure 5.21. For this example, it can be seen from Figure 5.20 that the experimental accumulated mass data is very close to the 95% confidence interval boundary across the entire experiment.

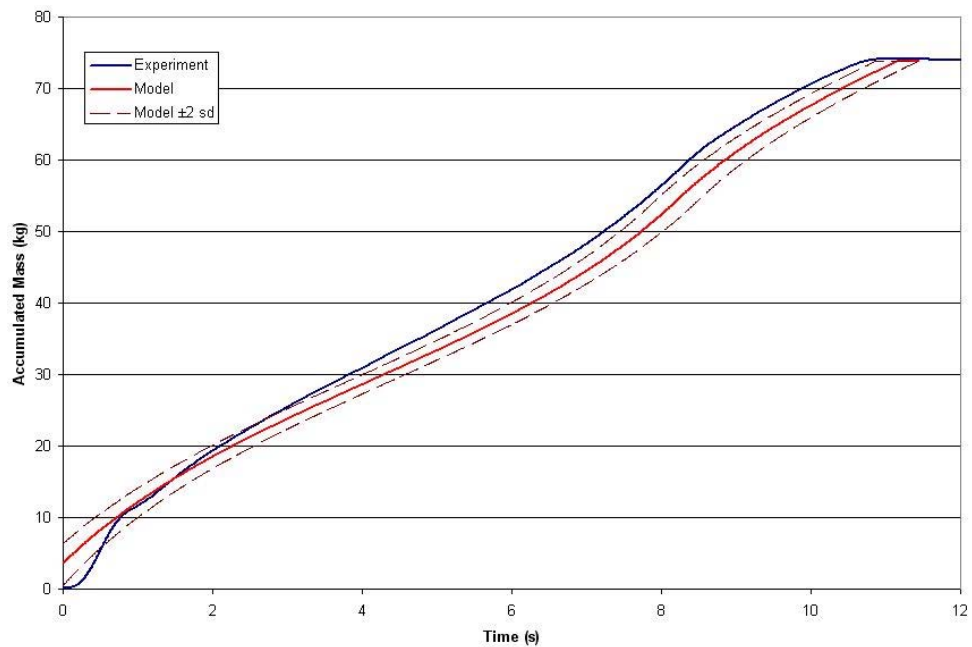


Figure 5.20. Comparison of accumulated mass data with 95% confidence interval (Alternative Flight, Filter Sand, 2 rpm).

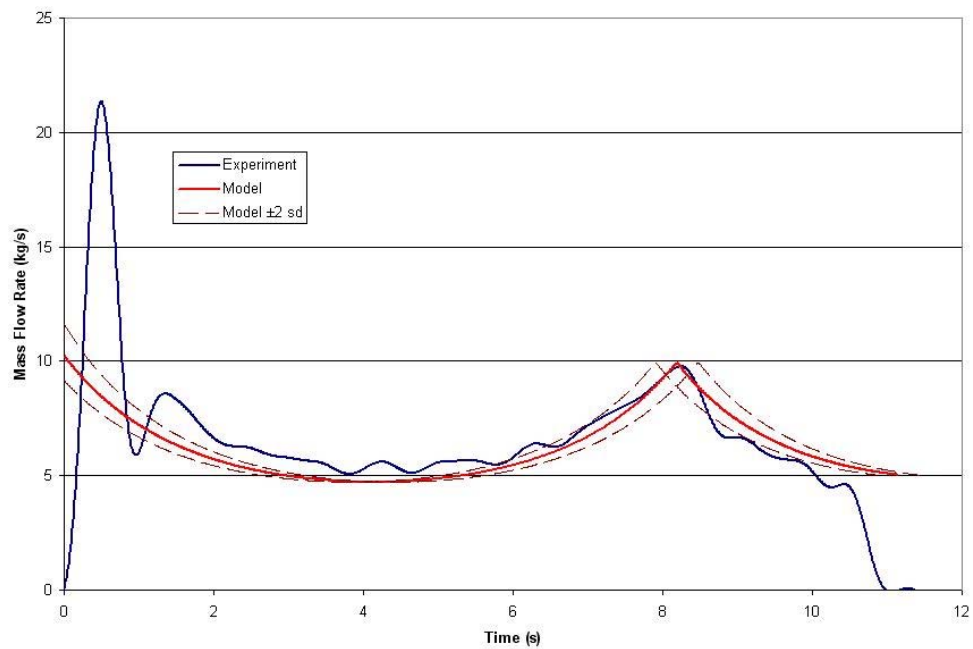


Figure 5.21. Comparison of mass flow rate data with 95% confidence interval (Alternative Flight, Filter Sand, 2 rpm).

5.4.3.1. Solids Bulk Density

Initially, the experimentally measured unconsolidated bulk density of the solids was used in the geometry model, however, it was found that bulk densities of approximately 200 kg/m^3 greater than the measured value gave a better fit to the experimental results (see for example Figure 5.22). Experiments to determine the consolidated bulk density of the solids were conducted (see Chapter 5.3.1), and it was found that this provided a much better fit to the experimental data, accounting for the required 200 kg/m^3 increase in bulk density observed. For example, using the alternative flight with fine river sand at 8 rpm, it can be seen that the experimentally measured unconsolidated bulk density of 1299 kg/m^3 provides a very poor fit to the experimental results, while the higher consolidated bulk density of 1480 kg/m^3 provides a much better fit to the data. This is believed to be due to the solids consolidating within the flight due to both the loading of the flight and vibration before unloading commences.

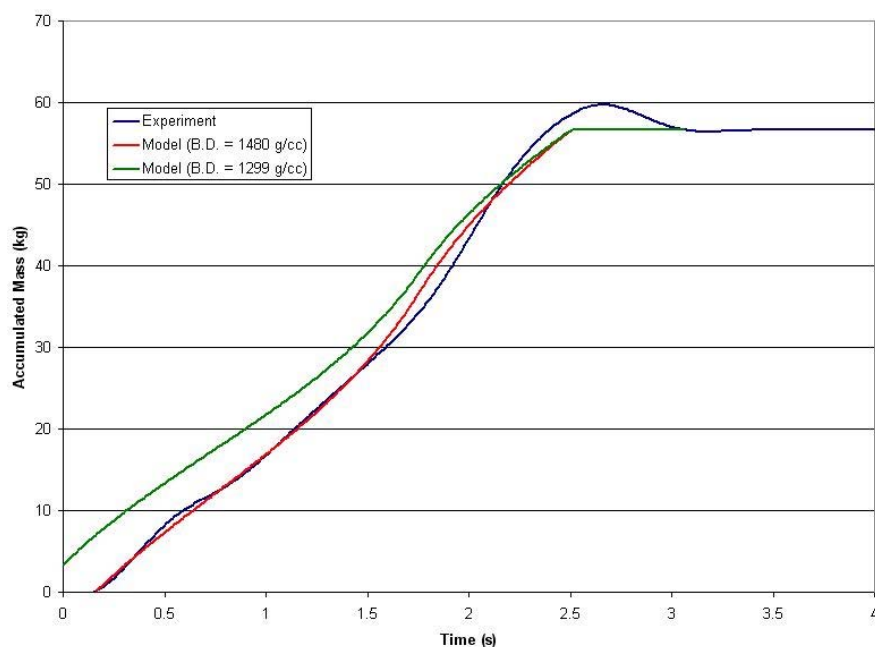


Figure 5.22. Comparison of results using consolidated and unconsolidated bulk densities (Alternative Flight, River Sand, 8 rpm).

5.4.4. Repeatability

In order to test the repeatability of the experimental results, a number of repeat experiments were performed. Repeat experiments were performed for each flight geometry at 2 and 8 rpm, giving a total of six sets of conditions for which repeats were performed. Figures 5.23 and 5.24 show the comparison of the two repeat experiments for flight design 3 using filter sand at 2 rpm, whilst Figures 5.25 and 5.26 show the comparison for the same flight and material at 8 rpm.

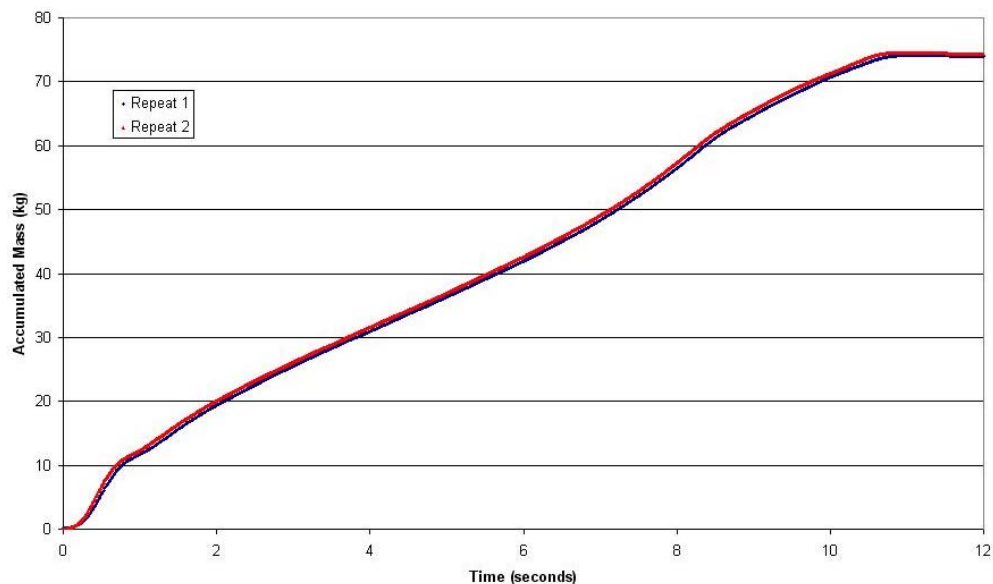


Figure 5.23. Repeatability of accumulated mass data (Alternative Flight, Filter Sand, 2 rpm).

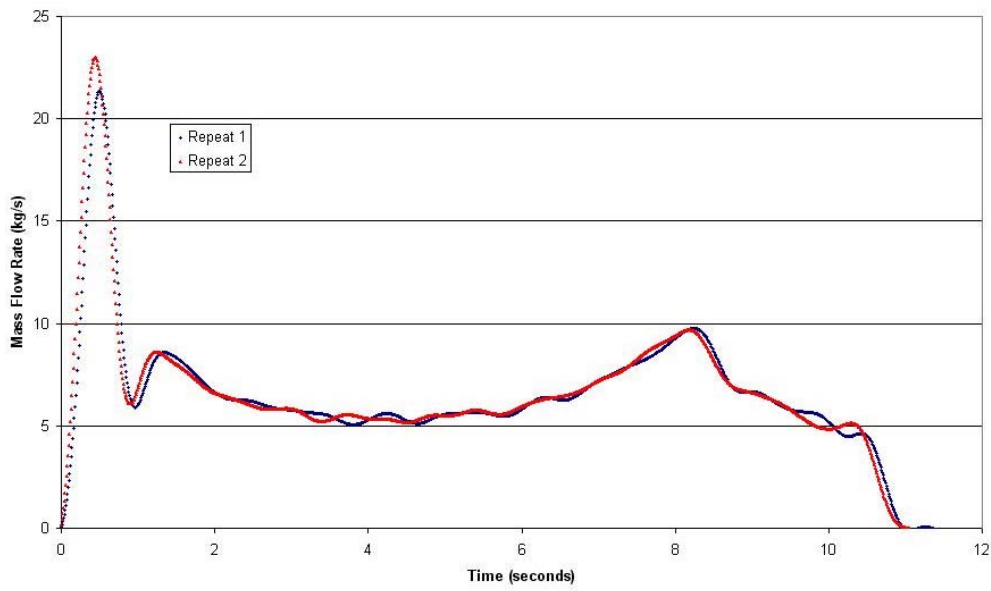


Figure 5.24. Repeatability of mass flow rate data (Alternative Flight, Filter Sand, 2 rpm).

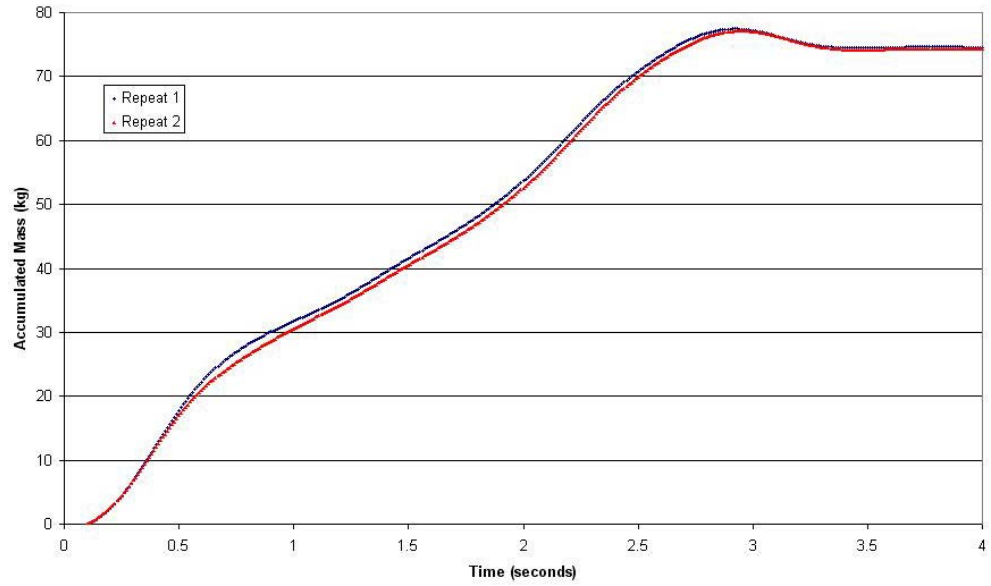


Figure 5.25. Repeatability of accumulated mass data (Alternative Flight, Filter Sand, 8 rpm).

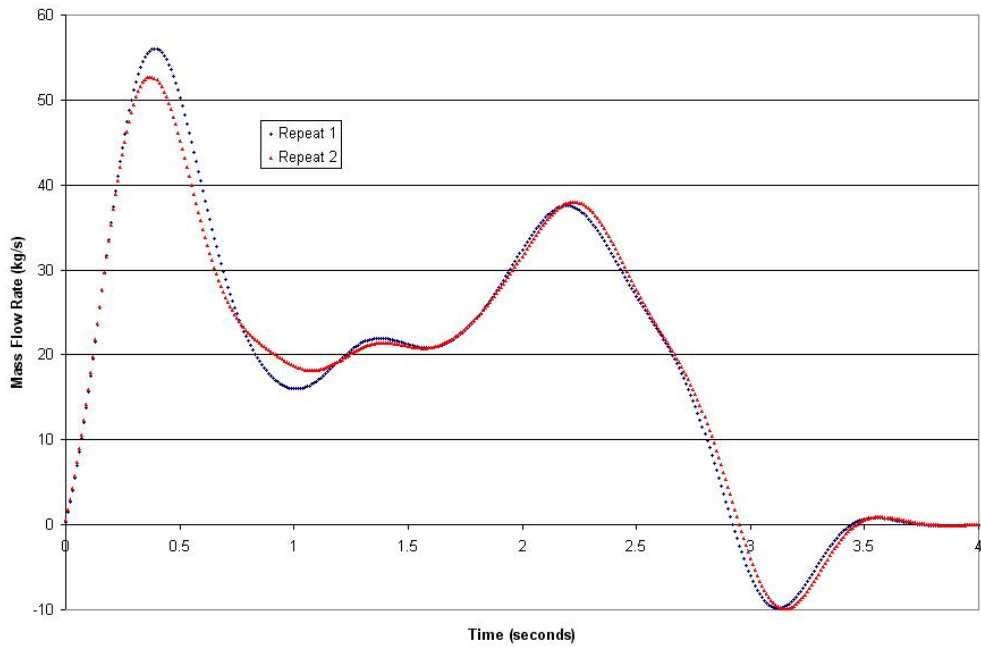


Figure 5.26. Repeatability of mass flow rate data (Alternative Flight, Filter Sand, 8 rpm).

As can be seen from Figures 5.23 to 5.24, there is extremely good repeatability in the experimental data for these conditions. There are some minor variations between experiments observable in Figure 5.26, however, in general the experiments are almost identical. A similar degree of repeatability was observed in the other repeated experiments, as shown in Figures 5.27 to 5.29.

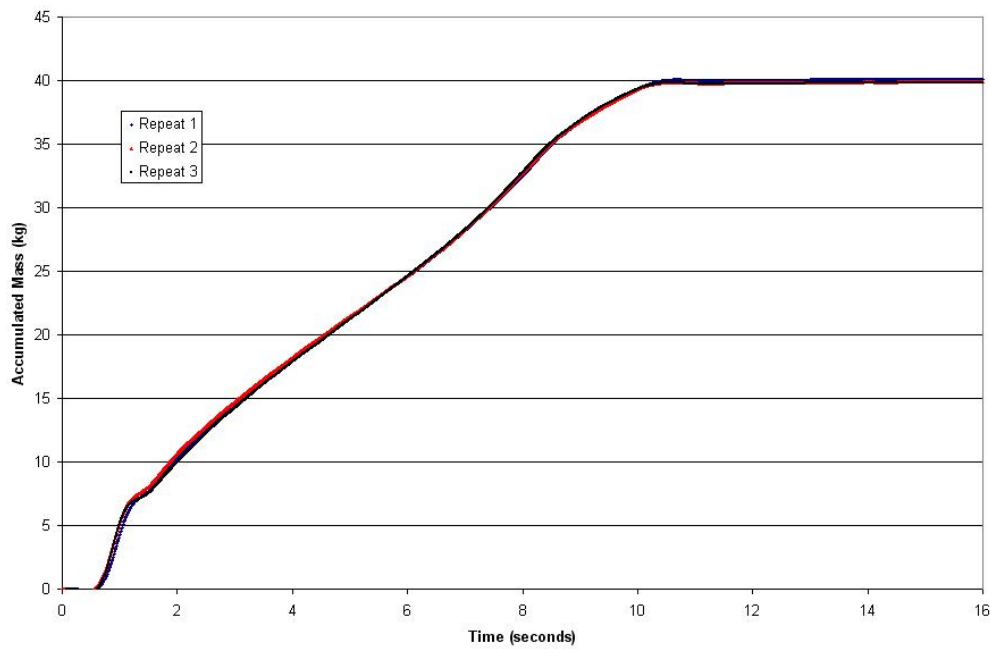


Figure 5.27. Repeatability of accumulated mass data (1/2 Scale Flight, Filter Sand, 2 rpm).

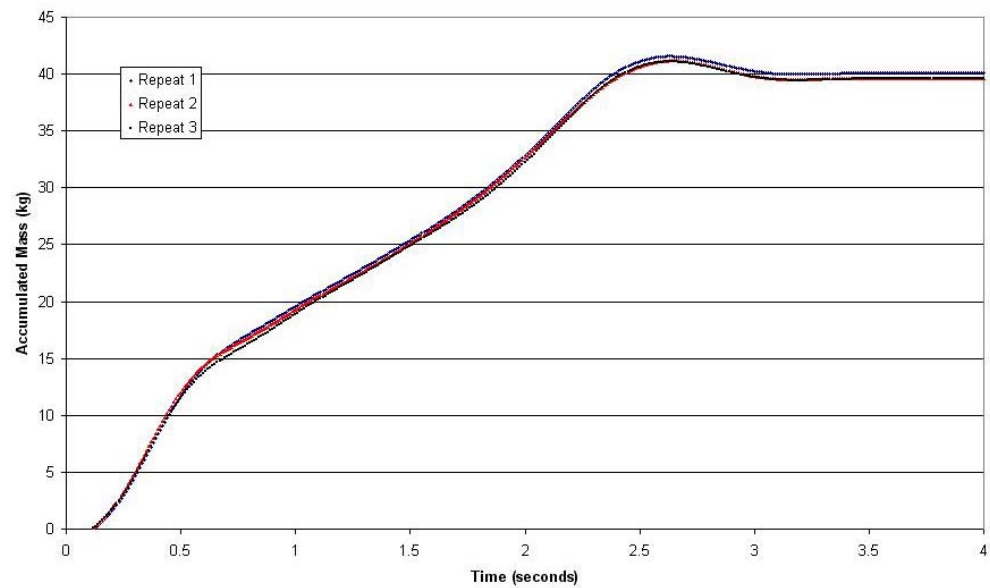


Figure 5.28. Repeatability of accumulated mass data (1/2 Scale Flight, Filter Sand, 8 rpm).

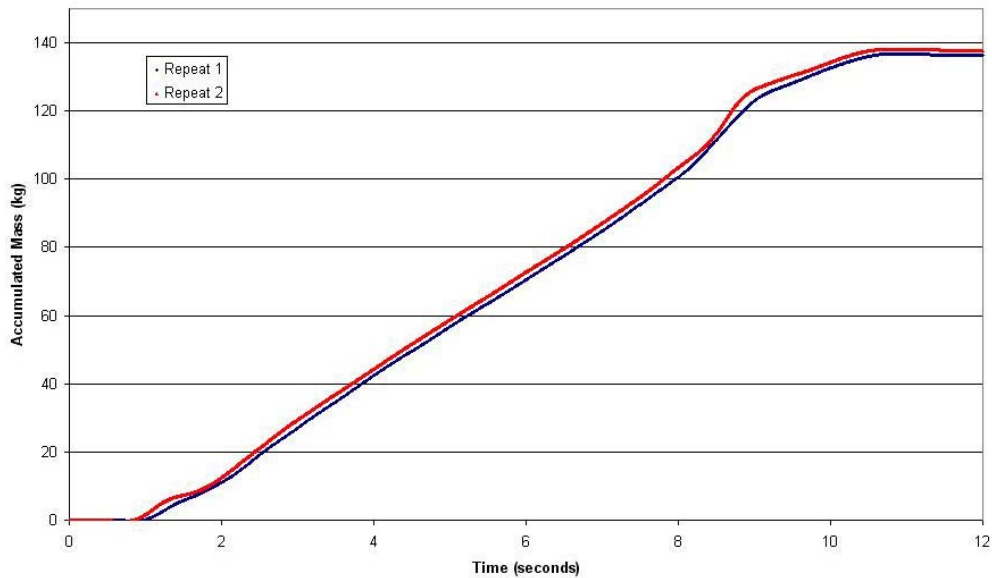


Figure 5.29. Repeatability of accumulated mass data (Full Scale Flight, Filter Sand, 2 rpm).

5.4.5. Effects of Abrasive Surface

As was discussed in Chapters 5.2.5 and 5.3.2, an abrasive material was attached to the surface of the flight tip for most experiments in order to prevent the bulk motion of solids. In order to study the effects of the bulk motion of the solids during flight unloading, a number of experiments were conducted with and without the abrasive surface in order to compare the results. Figures 5.30 to 5.33 show the comparison between the experiments conducted using the alternative flight design and filter sand with and without the abrasive material at 1, 2, 4 and 8 rpm respectively.

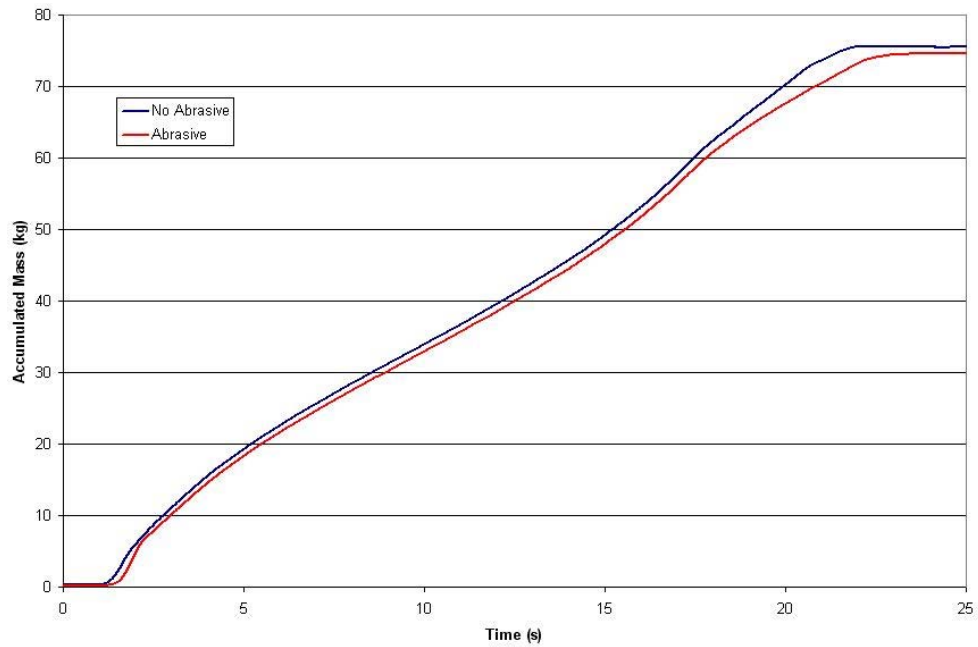


Figure 5.30. Comparison of experiments with and without abrasive surface at 1 rpm.

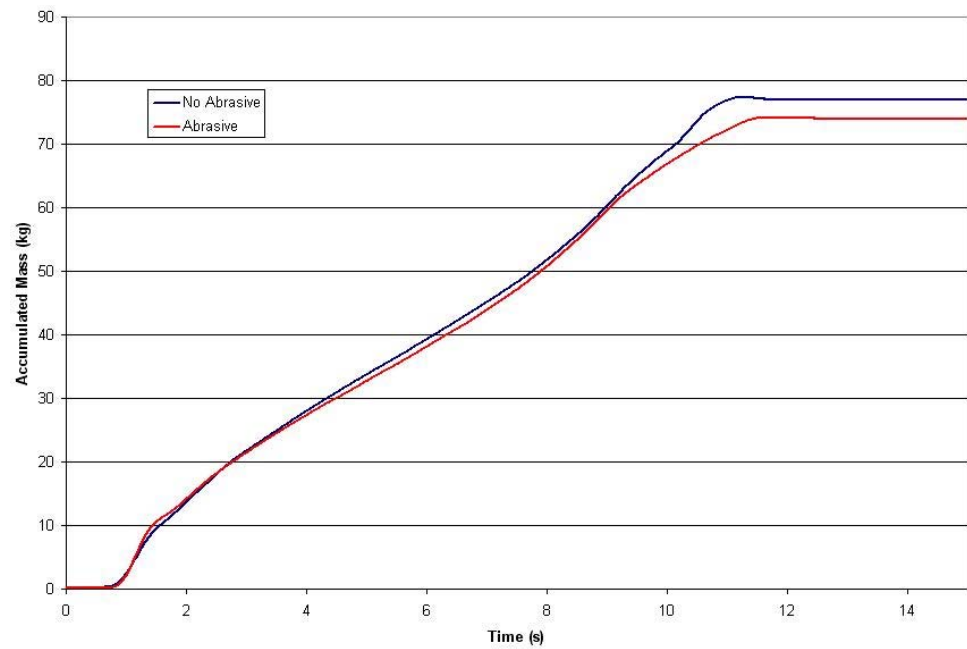


Figure 5.31. Comparison of experiments with and without abrasive surface at 2 rpm.

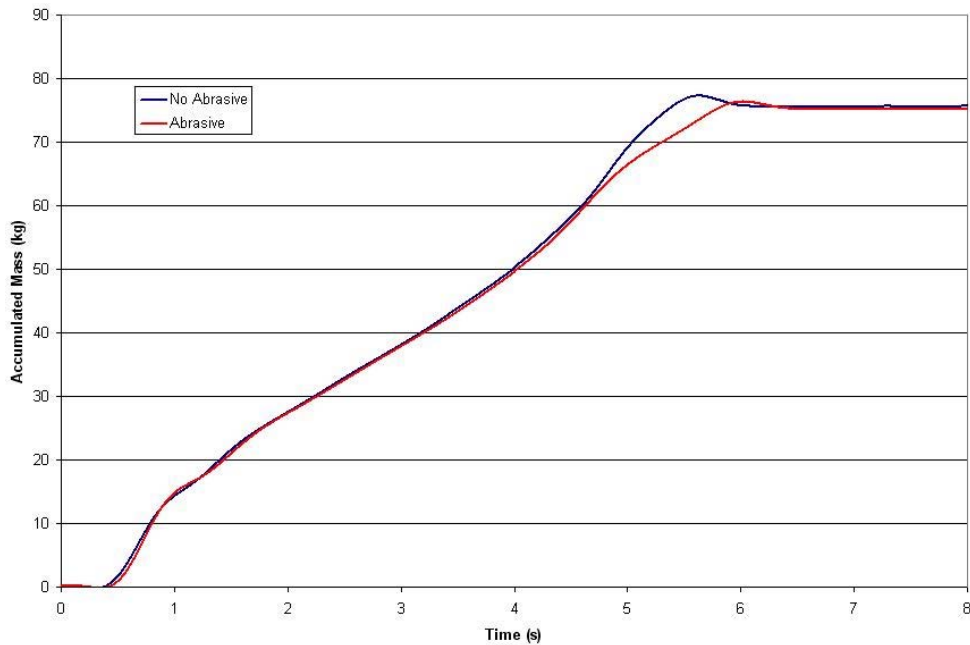


Figure 5.32. Comparison of experiments with and without abrasive surface at 4 rpm.

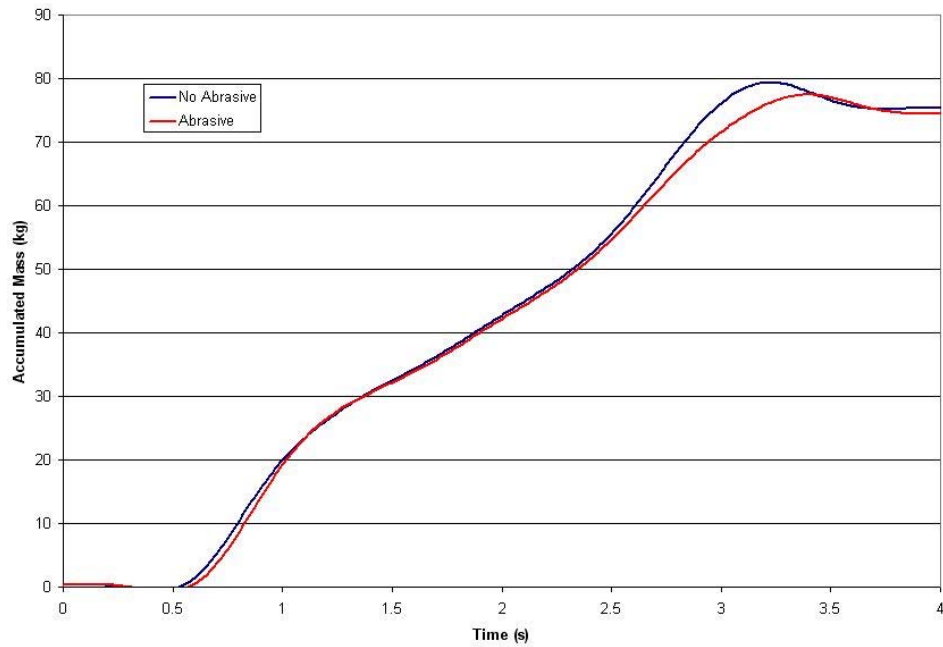


Figure 5.33. Comparison of experiments with and without abrasive surface at 8 rpm.

It can be seen that the abrasive surface has no effect on the early part of the unloading cycle, as is to be expected. However, in the later stages of unloading, where friction between the flight tip and the material is responsible for retaining material in the

flight, it can be seen that the flights with the abrasive surface retain the solid material for longer. This effect is more noticeable at higher rotational speeds.

The relationship between rotational speed and dynamic effects is also clearly illustrated in Figures 5.30 to 5.33. It can be clearly seen that as the rotational speed is increased, the overshoot at the top of the unloading curve due to impact forces also increases.

5.5. Validation of Geometric Unloading Model

Once the methods for data analysis had been developed and tested, the results of the experiments discussed in Chapter 5.3.2 could be used to test the geometric flight unloading model.

5.5.1. Model Inputs

The geometric flight unloading model requires a number of inputs in order to predict the unloading profile of a flight. Firstly, the model requires a full description of the flight geometry, including length of the flight section and the radius of curvature of the drum. Secondly, the rotational velocity is required to determine the speed of the flight and the rate at which material will be discharged. Finally, the model also requires two material properties; the bulk density of the solid material in the flight and the dynamic angle of repose of the material.

For the experiments conducted to validate the geometric unloading model, the flight geometry is known from the choice of flight design, and the rotational velocity is set using the stepper motor. The bulk density of material within the flight is assumed to be the consolidated bulk density of the material (see Chapter 5.4.3.1), and the dynamic angle of repose of the material is calculated from analysis of the high-speed camera images. Thus, all the required inputs for the geometric unloading model are defined.

5.5.2. Measurement of the Dynamic Angle of Repose

As discussed in Chapter 5.4.1, the high-speed camera images were used to measure the dynamic angle of repose of the material in the flight during the experiments. Figure 5.34 shows the dynamic angle of repose measurements from four experiments (Alternative Flight design using filter sand at 1, 2, 4 and 8 rpm respectively). Plotting the average dynamic angle of repose versus rotational velocity, as shown in Figure 5.35, it can be observed that the dynamic angle of repose appears to increase linearly with rotational velocity for these experiments. This trend is only apparent for these four experiments however, with other experiments showing dynamic angles of repose that do not follow this trend (see Table 5.5), thus this trend may be meaningless.

In measuring the dynamic angle of repose of the solids, it was found that the material surface in the flight was often not straight. This contradicts the assumption that the material surface in the flight is described solely by the dynamic angle of repose. This also made accurate measurement of the dynamic angle of repose difficult, as the material surface did not have a single characteristic slope.

It can also be seen from Figure 5.34 that the dynamic angle of repose shows some variation as the flight unloads, however it appears approximately constant for most of the experiment. Given the variability of the results, and the difficulty in accurately measuring the dynamic angle of repose from the high-speed camera images, it cannot be determined if these are real effects or simply the result of errors. It can also be seen that in some experiments there is significant variation in the dynamic angle of repose in the early stages of unloading. This may be due to the transition between a static material and unloading.

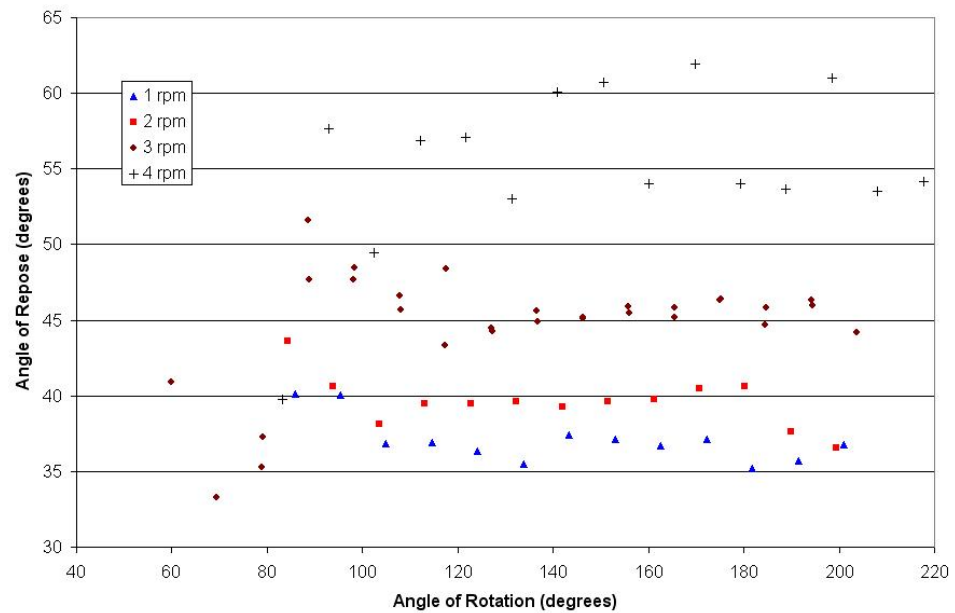


Figure 5.34. Example of angle of repose measurements from Experiments 5-8.

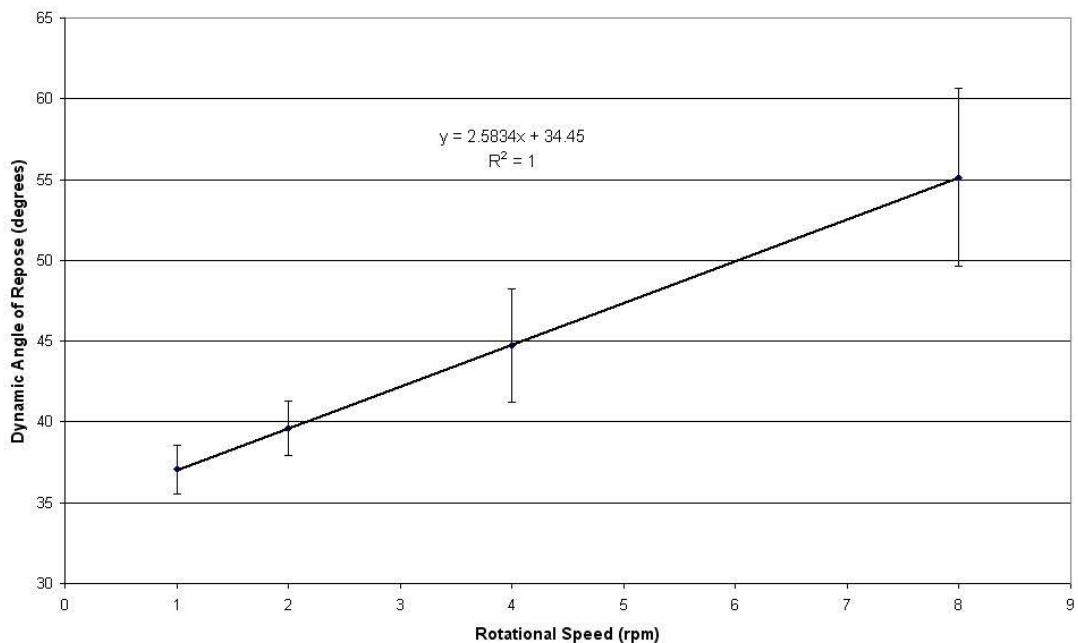


Figure 5.35. Dynamic angle of repose as a function of rotational velocity from Experiments 5-8.

Table 5.5 shows a summary of the average measured angle of repose for all experiments, along with the standard deviation in the measured angles (approximately 30 images were analysed for each experiment). It can be seen that there is significant variation in the average angle of repose measured, and that in some cases there is

significant variability in the results (indicated by a high standard deviation). This degree of variation was not observed in the experiments using the trommel apparatus (see Chapter 5.3.1), and suggests that the material surface does not have a single characteristic angle of repose. This will be discussed further in Chapter 5.6.4.

A general trend of increasing standard deviation with increasing rotational speed can be observed across most of the experiments, suggesting that the error is influenced by the rotational speed. The experiment numbers in Table 5.5 correspond to the experimental conditions listed in Table 5.4.

Experiment	Rotational Speed (rpm)	Mean Angle of Repose	St. Dev. Of Angle of Repose
1	1	40.0°	2.0°
2	2	39.1°	3.4°
3	4	74.0°	2.7°
4	8	53.8°	5.4°
5	1	37.1°	1.5°
6	2	39.6°	1.7°
6 repeat	2	39.9°	3.2°
7	4	44.7°	3.5°
8	8	55.1°	5.5°
8 repeat	8	55.1°	10.4°
9	2	46.5°	6.1°
10	4	53.7°	6.9°
11	2	52.7°	7.1°
12	4	47.8°	5.5°
13	2	43.7°	2.2°
14	4	55.5°	8.2°
15	2	41.4°	4.4°
16	4	47.2°	13.5°

Table 5.5. Measured material angles of repose (experiment numbers correspond with Table 5.4).

5.5.3. Validation at Different Rotation Velocities

The first parameter to be studied experimentally was the rotational velocity of the flight. A set of experiments was conducted at four different rotational velocities (1, 2, 4 and 8 rpm) using the same flight design and solid material (Alternative Flight design and filter sand). Figures 5.36 to 5.43 show the experimentally measured accumulated mass and mass flow rate results for these experiments compared to the predictions of the geometric flight unloading model.

As can be seen from Figures 5.36 to 5.43, the fit between the model and the experimental data is fairly good, given the variability in the measurement of the dynamic angle of repose. For all the experiments, the measured accumulated mass is very close to the predicted 95% confidence interval (based on the standard deviation of the measured dynamic angle of repose), and in many cases lies within the 95% confidence interval. The small deviations observed may in part be attributed to errors in determining the starting point of the experiment used to align the experimental data with the model (see Chapter 5.4.3). The measured mass flow rate data matches very well with the model predictions, with the results of three of the four experiments falling well within the 95% confidence interval, and the fourth experiment lying just outside the 95% confidence interval (see Figure 5.37).

It can be seen that the model predictions for the accumulated mass show a very similarly shaped curve to the experimentally measured mass in the later parts of the experiments, however there are some significant differences in the early stages of the unloading profile. The most significant deviation occurs at the very beginning of the unloading profile, where it can be seen that the experimentally measured accumulated mass results show a sharp increase in mass, whilst the model predictions show a smooth curve. This is attributed to the experimental flight starting in an underloaded state, thus needing to rotate until it reaches the point where it is fully loaded and solids begin to discharge. However, it is believed that the material remains stationary in the flight until a point beyond where the material undergoes bulk failure at the surface, causing a large mass of material to be suddenly discharged. This may be due to the time required for the material surface to begin flowing over the flight tip. It can

be seen that this effect is most pronounced at lower rotational velocities, which is probably due to slower movement of the flight allowing more time for the material to begin moving within the flight. At higher rotational velocities, the faster flight movement forces the initial unloading to occur much more rapidly, allowing the material flow to stabilise more quickly.

This effect can also be seen in the mass flow rate comparisons, where the experimental results show a very large initial spike in mass flow rate that is not represented in the model predictions. However, in most cases, the model and experimental results rapidly converge, and from there on show similar trends.

The influence of the dynamic effects discussed in Chapter 5.2.3 can also be seen in the later stages of the unloading profiles, although these are most significant in the experiments conducted at 4 and 8 rpm (see Figures 5.40 to 5.43). In these experiments, it can be seen in the later stages of unloading that the experimentally measured accumulated mass results begin to increase faster than predicted by the model, eventually rising beyond the final mass before then decreasing back to the final state. This is most evident in Figure 5.42, where the experimental results can be seen to closely follow the experimental predictions until close to the end of the unloading profile, where they begin to diverge. This divergence is small however.

Studying the fit of the model to the experimental results shown in Figures 5.36 and 5.37, it can be seen that the fit is not as good as can be seen in the other experiments. In most of the experiments, it can be seen that the model predictions agree well with the peak corresponding to the fourth transition point. However, in Figures 5.36 and 5.37, it can be seen that the peak of the experimental data occurs after the predicted range of the peak from the model. This is probably due to errors in determining the initial point in the experiment for aligning the curves (i.e. the point where the derivative of the load cell data begins to increase).

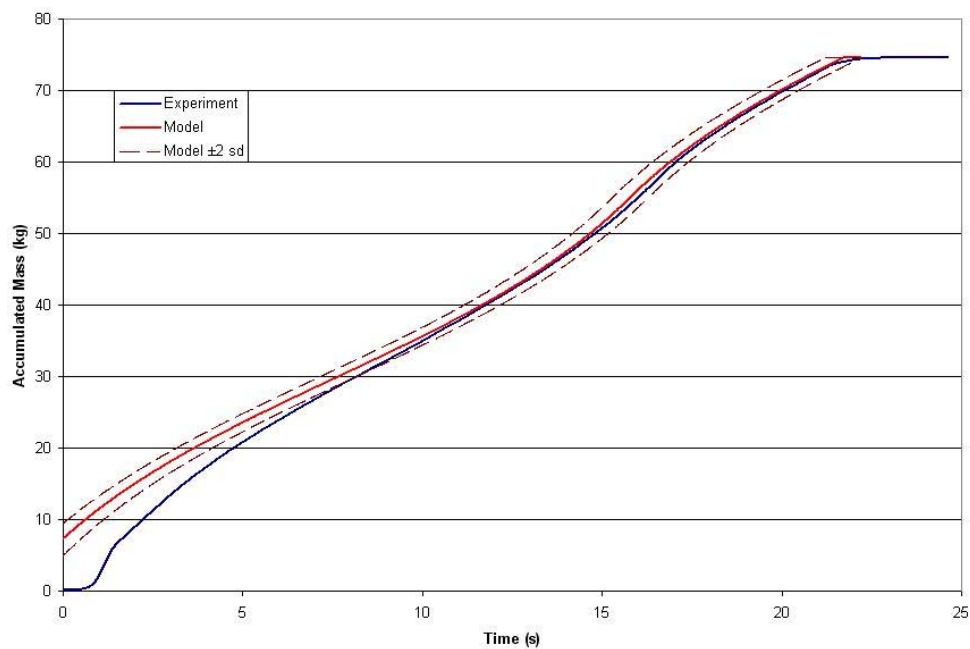


Figure 5.36. Accumulated mass data (Alternative Flight, Filter Sand, 1 rpm).

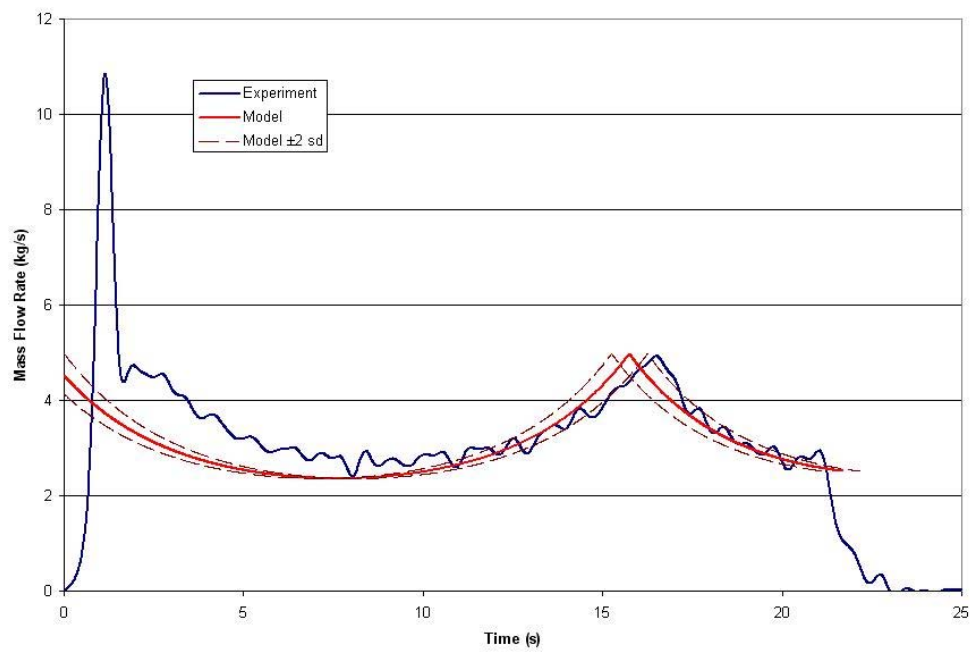


Figure 5.37. Mass flow rate data (Alternative Flight, Filter Sand, 1 rpm).

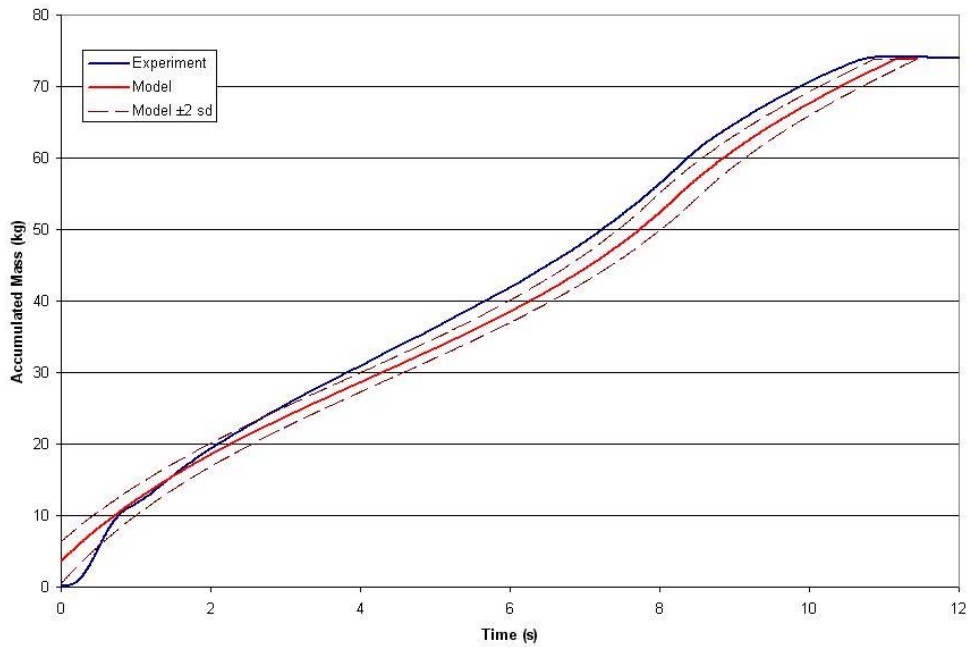


Figure 5.38. Accumulated mass data (Alternative Flight, Filter Sand, 2 rpm).

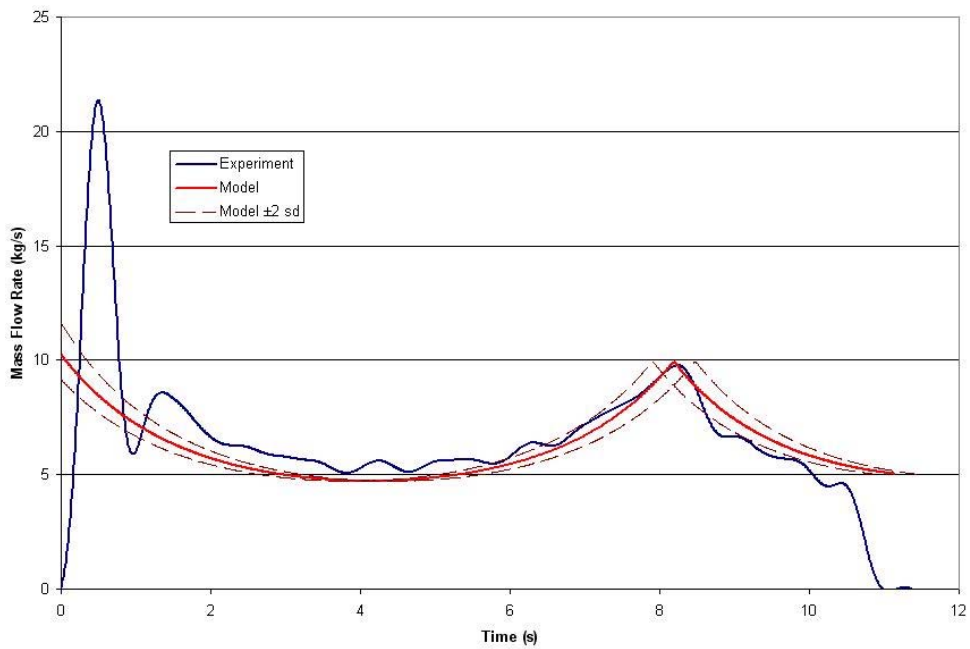


Figure 5.39. Mass flow rate data (Alternative Flight, Filter Sand, 2 rpm).

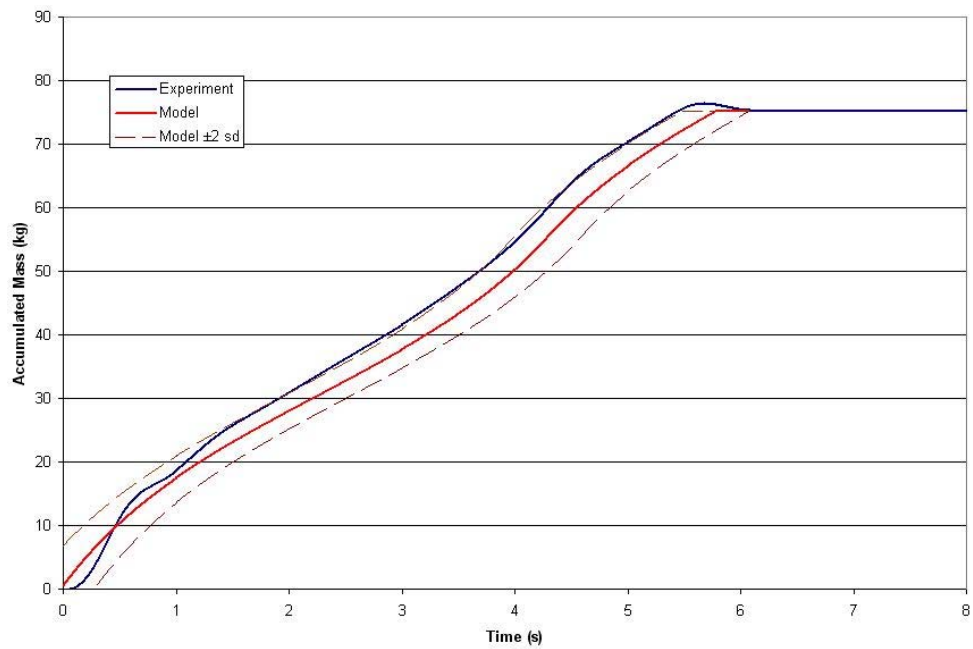


Figure 5.40. Accumulated mass data (Alternative Flight, Filter Sand, 4 rpm).

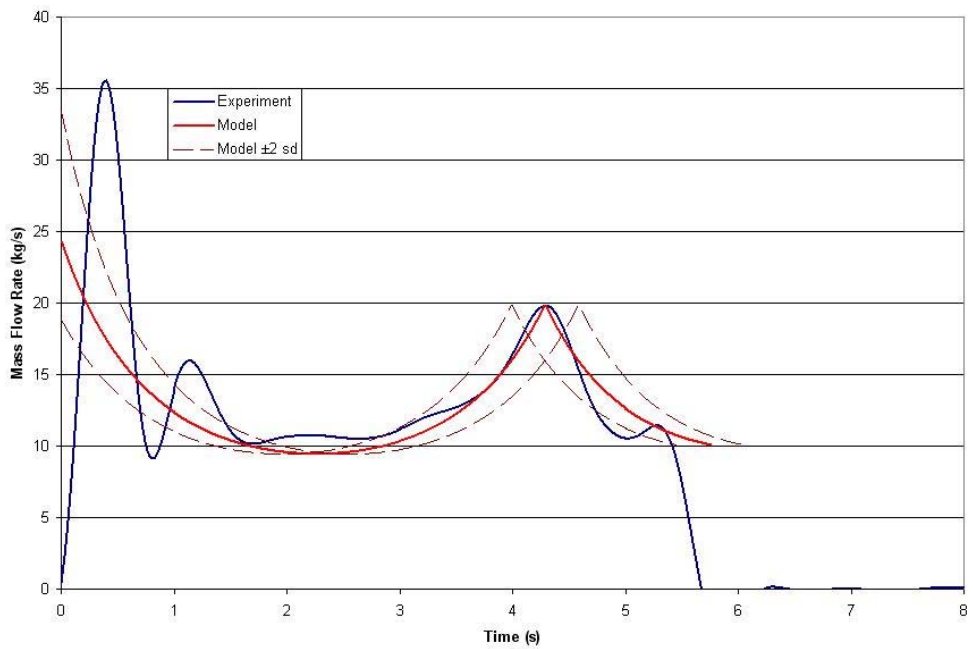


Figure 5.41. Mass flow rate data (Alternative Flight, Filter Sand, 4 rpm).

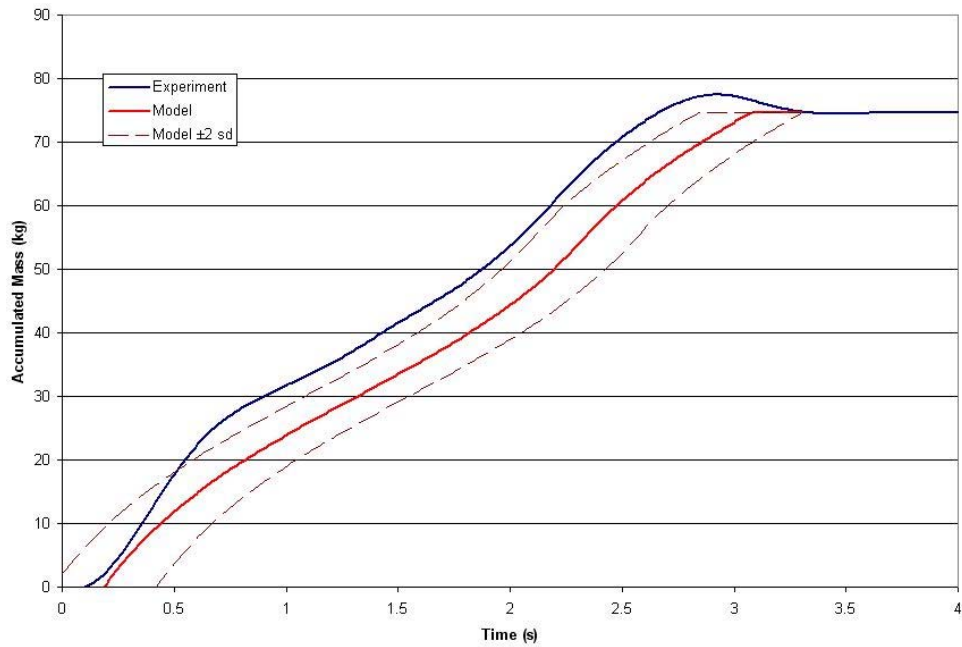


Figure 5.42. Accumulated mass data (Alternative Flight, Filter Sand, 8 rpm).

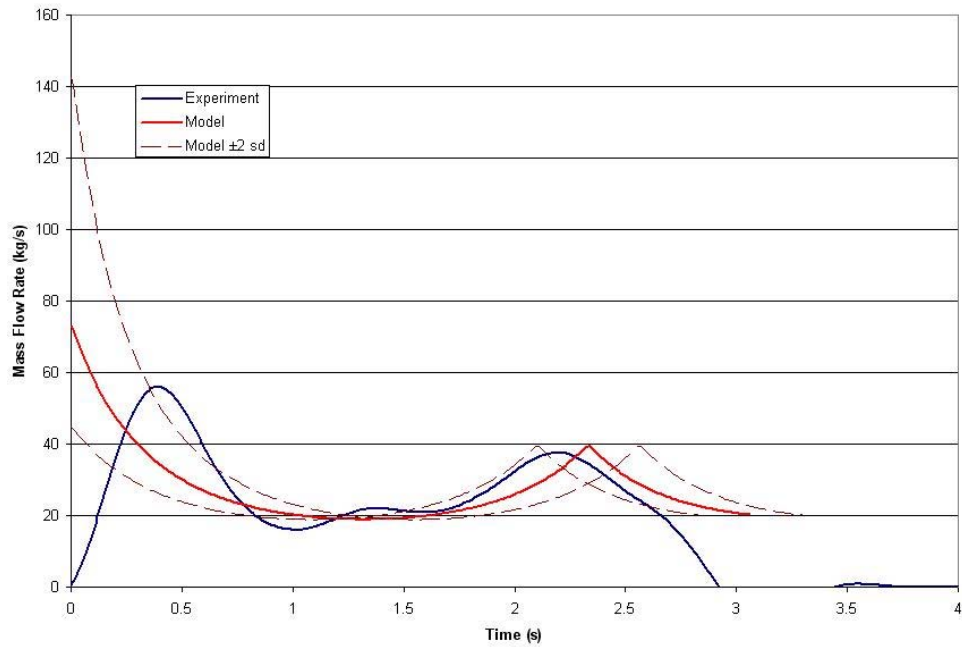


Figure 5.43. Mass flow rate data (Alternative Flight, Filter Sand, 8 rpm).

The results of these experiments can be compared to each other by normalising the experimental data. For the accumulated mass data, this is done by dividing the measured accumulated mass by the total accumulated mass (to give a fraction of the

total accumulated mass), and the mass flow rates can be compared by dividing the flow rate by the rotational speed (rad/s) to give an angular mass flow rate (kg/radian). This can then be plotted against the rotation of the flight (time divided by the rotational speed of the flight). Figure 5.44 shows the normalised accumulated mass profiles for the four experiments conducted using the Alternative flight and filter sand. As can be seen, the profiles are very similar across the range of rotational speeds, indicating the rotational speed has little effect on the unloading profile in this case. The normalised mass flow rate results are shown in Figure 5.45, and it can be seen that aside for noise in the results, the unloading profiles are very similar, with the peaks associated with the fourth transition point all falling close together. It can be seen that the peak tends to occur later (greater angle of rotation) at higher rotational speeds, suggesting that the angle of repose increases with rotational speed. This reinforces the observations made in Chapter 5.5.2 and demonstrates how the angle of repose impacts the unloading profile.

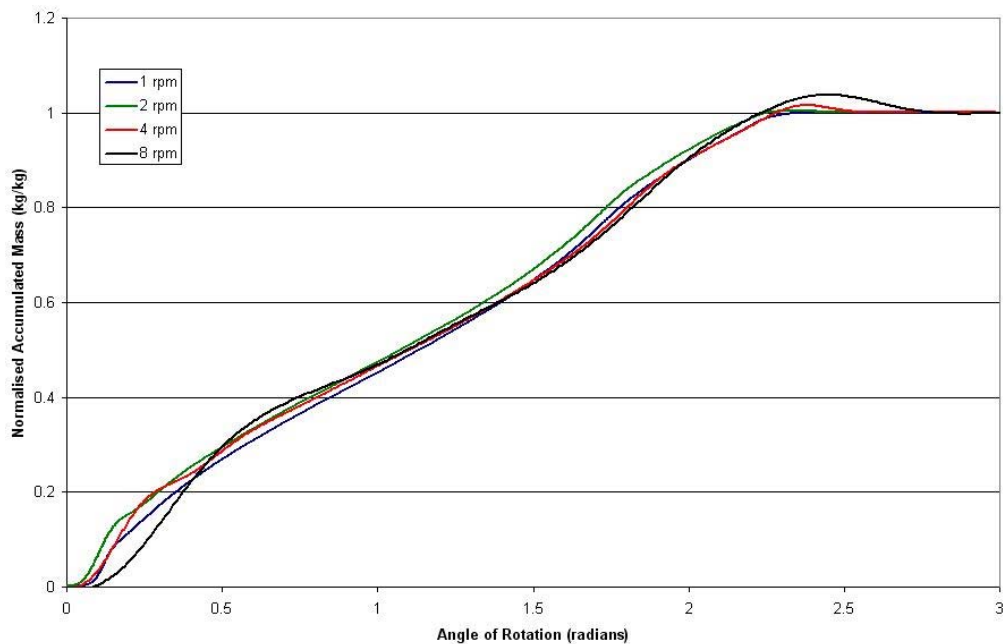


Figure 5.44. Normalised accumulated mass profiles at different rotational speeds (Alternate Flight, Filter Sand).

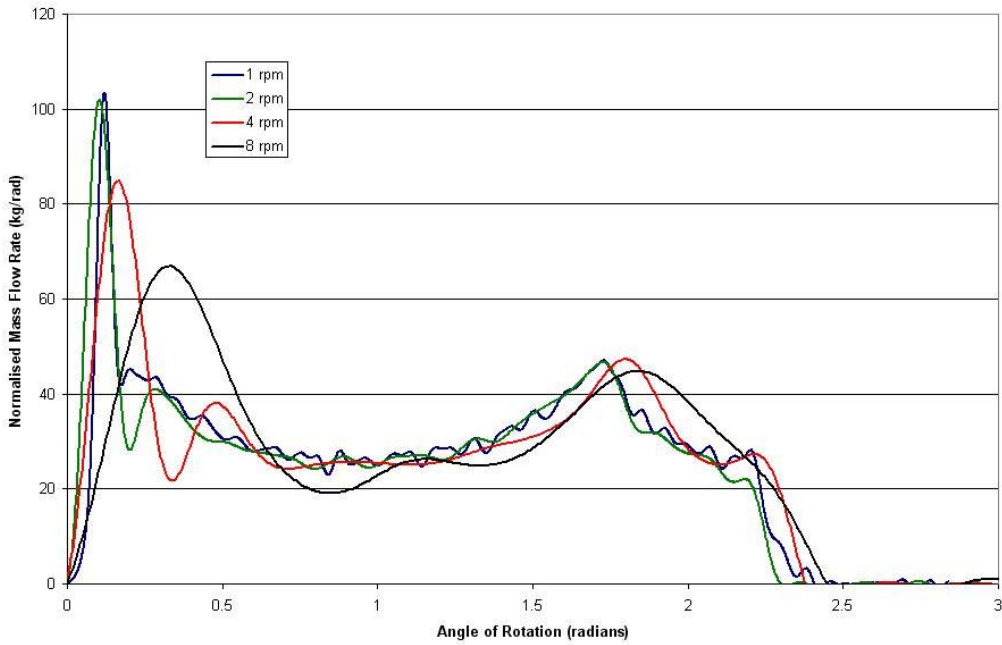


Figure 5.45. Normalised mass flow rate profiles at different rotational speeds (Alternate Flight, Filter Sand).

Figure 5.45 also shows that there appears to be greater variability in the results at higher rotational speeds (higher deviations from the predictions). It can be seen in the 8 rpm experiment that whilst there are fewer waves in the data, they have a far greater amplitude than in slower experiments. Some of this will be due to the faster speed of the experiment, which results in an effectively higher frequency in the results. That is, in a slow experiment, variations in the flow rate will occur slower than in faster experiments. As the experimental data is filtered to remove high frequency signals (noise), the filter will begin to remove these variations in faster experiments, smoothing the curve. Thus, the small variations within the slower experiments will be averaged out in the faster experiments, resulting in a smoother curve with fewer, but larger, features.

5.5.4. Validation with Different Flight Geometries

The next set of parameters to be tested was the geometry of the flight, to ensure that the model could accurately predict the unloading profile for various shapes of flights. Two different flight designs (Full and $\frac{1}{2}$ Scale designs) were tested using the same solid material (filter sand) at two different rotational velocities (2 and 8 rpm) to test the accuracy of the model for different flight geometries. The results of these experiments can be seen in Figures 5.46 to 5.53.

As can be seen from Figures 5.46 to 5.53, the experimental data falls within the 95% confidence interval for all experiments, demonstrating that the model is capable of predicting the unloading profile of the different flight geometries. However, a number of features can be observed in some of these experiments, which were not observed in the previous experiments. In Figure 5.48 it can be seen that the experimental results for the accumulated mass do not follow the same trend as the model predictions. It can be observed that the experimental curve initially approaches the outer limit of the 95% confidence interval, before levelling out and eventually matching the average model prediction. The experimental curve then diverges again due to the dynamic effects. A similar, although far less pronounced, effect can be observed in Figure 5.46, which shows the results for the same flight geometry and material at a lower rotational velocity. Here it can be seen that the experimental data initial increases to match the 95% confidence interval curve, before gradually diverging from this towards the average model prediction. This would tend to suggest, that although the experimental data falls within the 95% confidence interval, there is some deviation between the observed unloading behaviour and that predicted by the geometric unloading model. This may be due to the assumption of a constant dynamic angle of repose through out the experiment, which is not the case as discussed in Chapter 5.5.2. Other sources of this variation could be errors in measuring the flight geometry, especially the flight tip angle of the flight (α_2), which was measured using a protractor, or the radius of curvature of the back of the flight (taken to be the curvature specified in the original design).

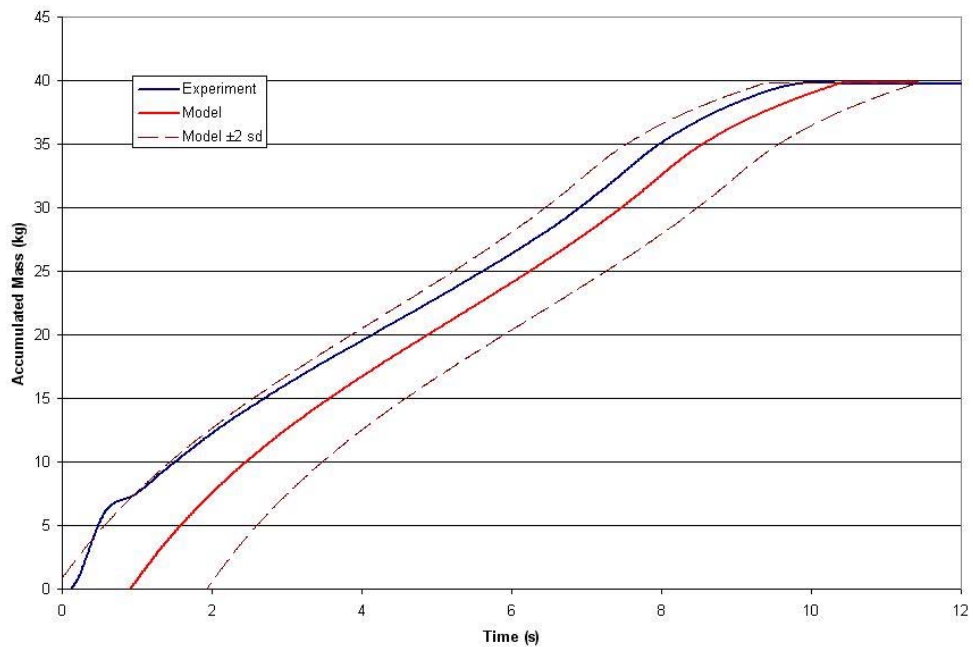


Figure 5.46. Accumulated mass data (1/2 Scale Flight, Filter Sand, 2 rpm).

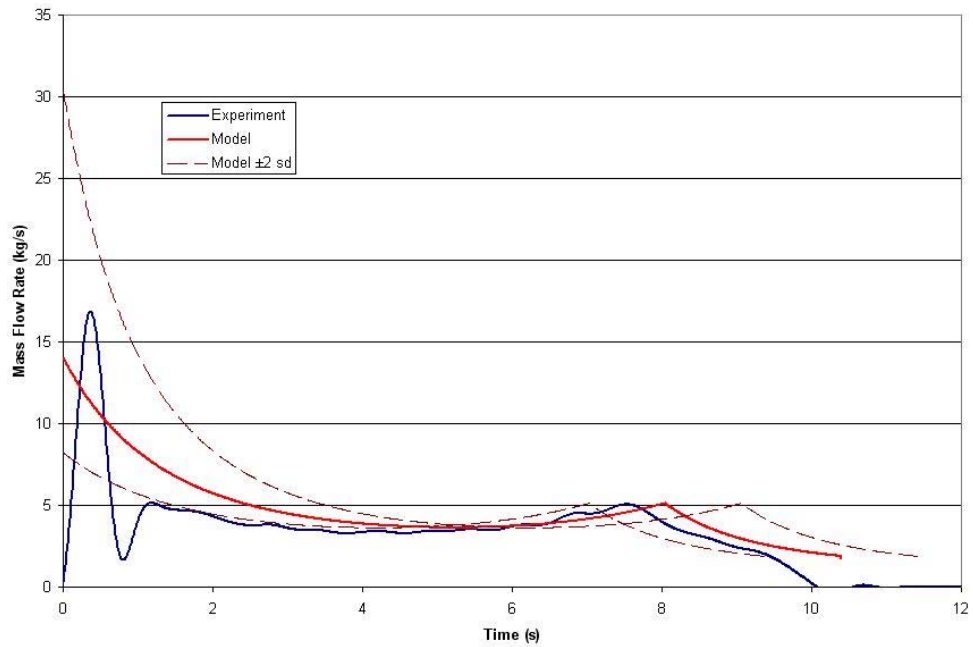


Figure 5.47. Mass flow rate data (1/2 Scale Flight, Filter Sand, 2 rpm).

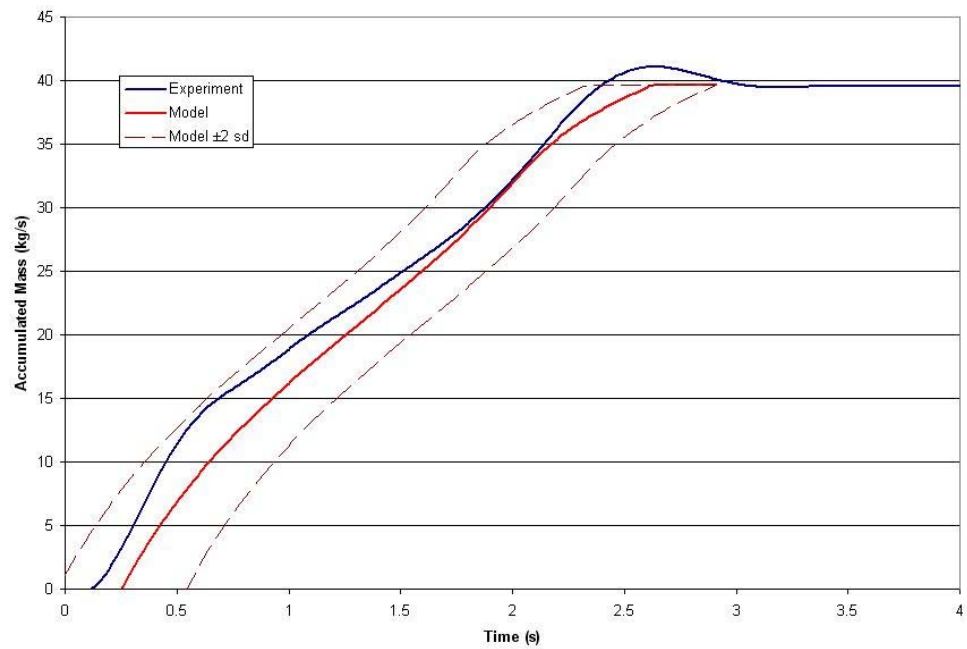


Figure 5.48. Accumulated mass data (1/2 Scale Flight, Filter Sand, 8 rpm).

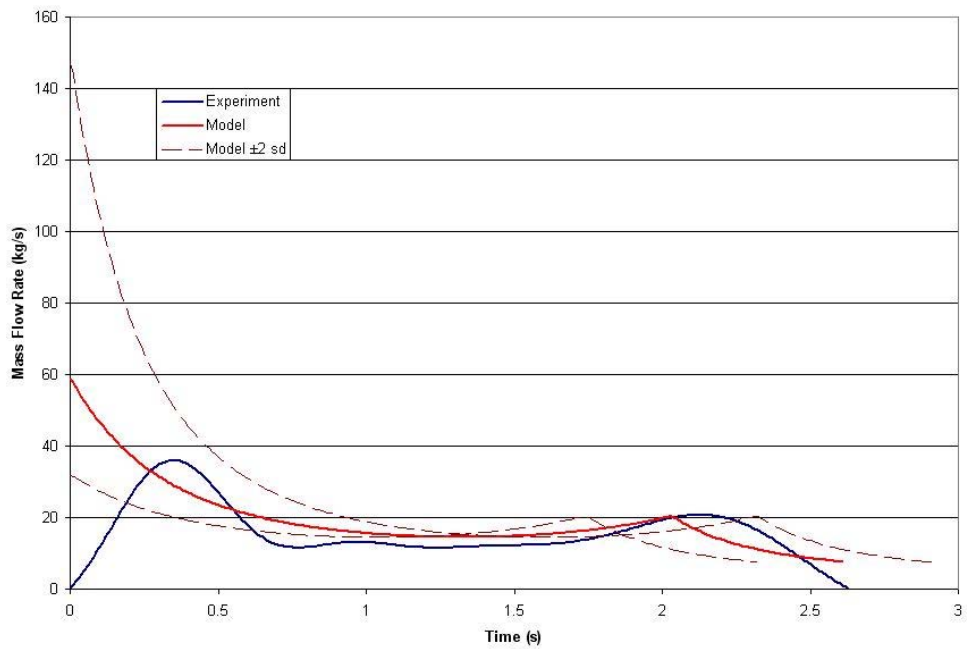


Figure 5.49. Mass flow rate data (1/2 Scale Flight, Filter Sand, 8 rpm).

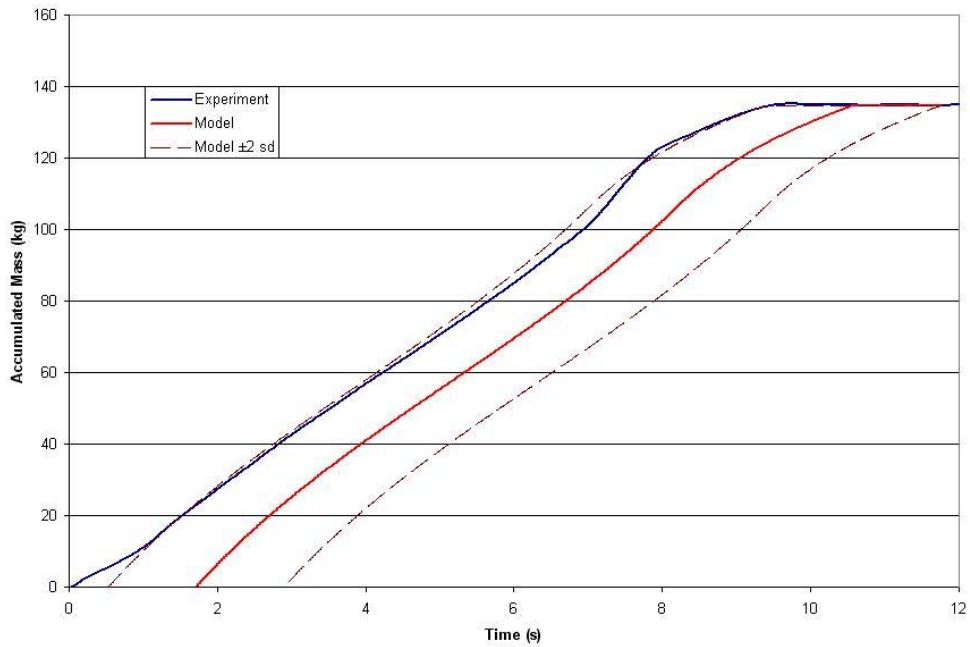


Figure 5.50. Accumulated mass data (Full scale Flight, Filter Sand, 2 rpm).

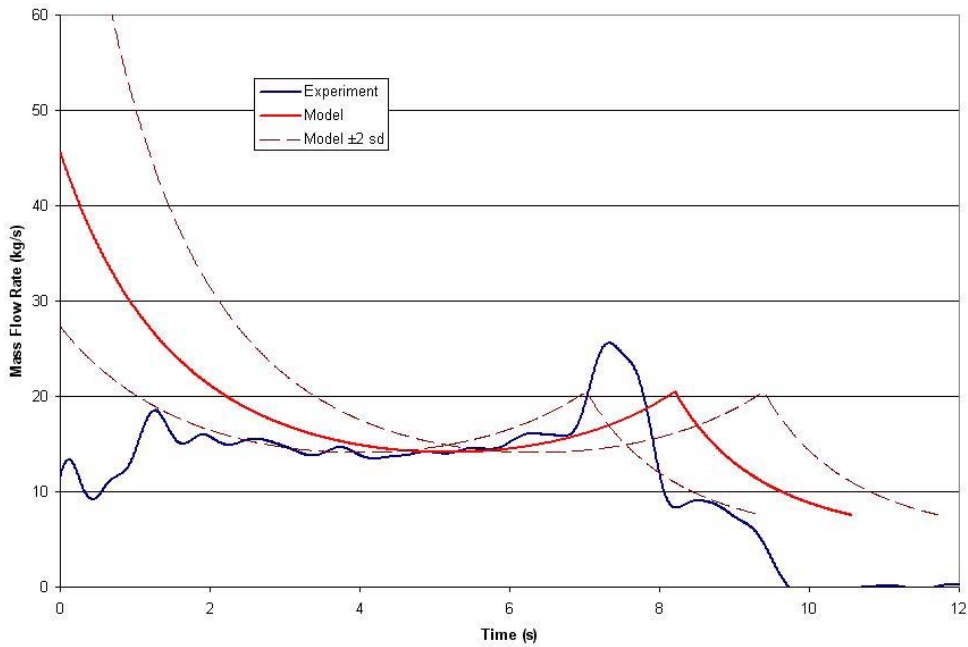


Figure 5.51. Mass flow rate data (Full Scale Flight, Filter Sand, 2 rpm).

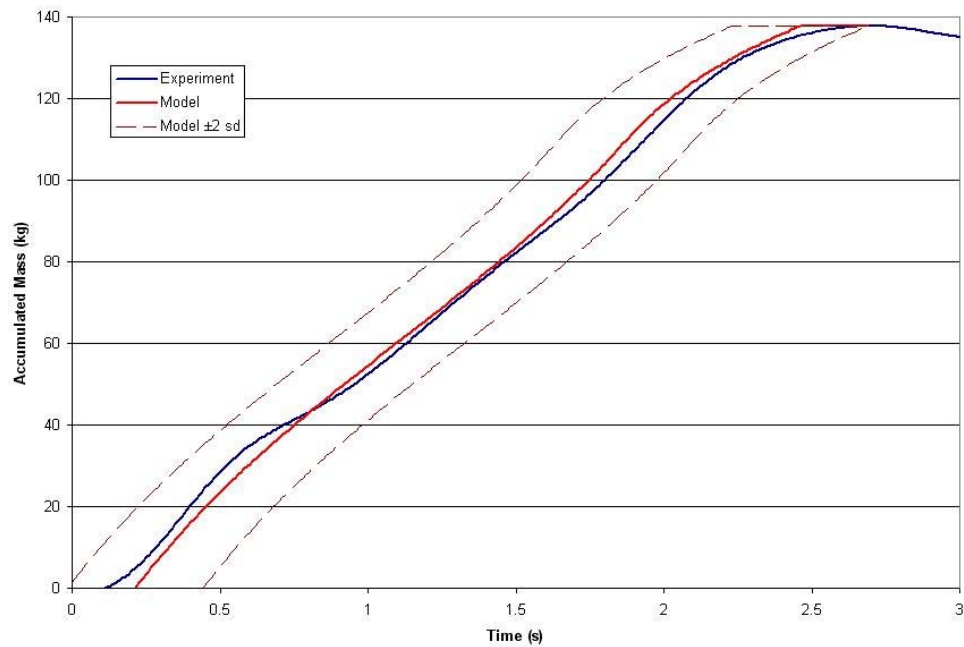


Figure 5.52. Accumulated mass data (Full Scale Flight, Filter Sand, 8 rpm).

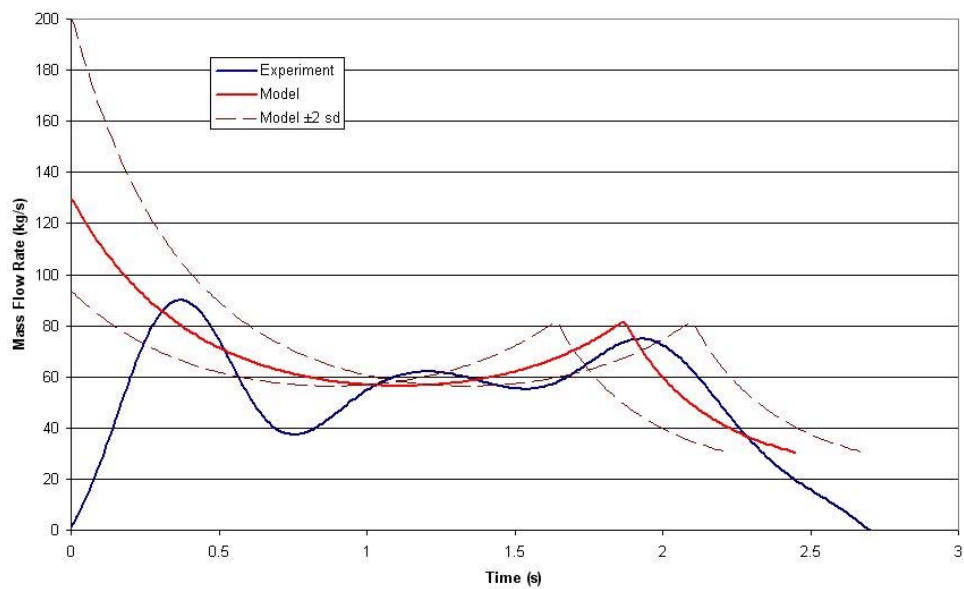


Figure 5.53. Mass flow rate data (Full Scale Flight, Filter Sand, 8 rpm).

It can be seen from Figure 5.51 that the increase in the mass flow rate in the later stages of unloading appears somewhat larger and broader than that observed in other experiments. This corresponds to the unexpected increase in accumulated mass apparent in the later stages of Figure 5.50, where the experimental curve rises to meet the 95% confidence interval curve. This effect is similar to that observed in the experiments conducted without the abrasive surface applied to the flight tip, as discussed in Chapter 5.2.5, suggesting that there may be a bulk movement of solids occurring in the later stages of unloading in this flight. This could be possible due to the increase in the size of the flight, and thus mass of solids, resulting in greater shear forces being applied at the flight tip surface. However, this phenomenon is not observed in Figures 5.52 and 5.53, which show the results for the same flight and material at a higher rotational velocity (8 rpm). This may be due to increased centripetal forces due to the higher rotational speed holding the material within the flight. This theory is supported by the observed increase in the solids dynamic angle of repose at higher rotational speeds discussed in Chapter 5.5.2, which suggests greater centripetal forces are present.

5.5.5. Validation with Different Solid Materials

Finally, it is necessary to ensure that the model is capable of predicting the unloading profile for a range of solid properties. To achieve this, a further set of experiments was conducted using the river sand and zeolite materials in the Alternative flight design at two different rotational velocities (2 and 8 rpm). The results of these experiments are shown in Figures 5.54 to 5.61.

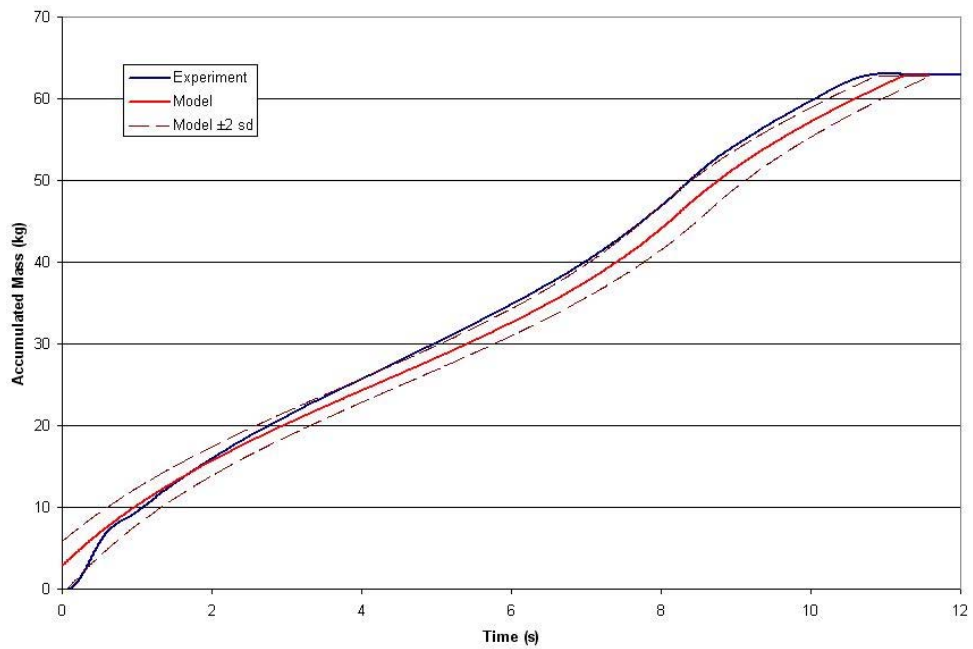


Figure 5.54. Accumulated mass data (Alternative Flight, Zeolite, 2 rpm).

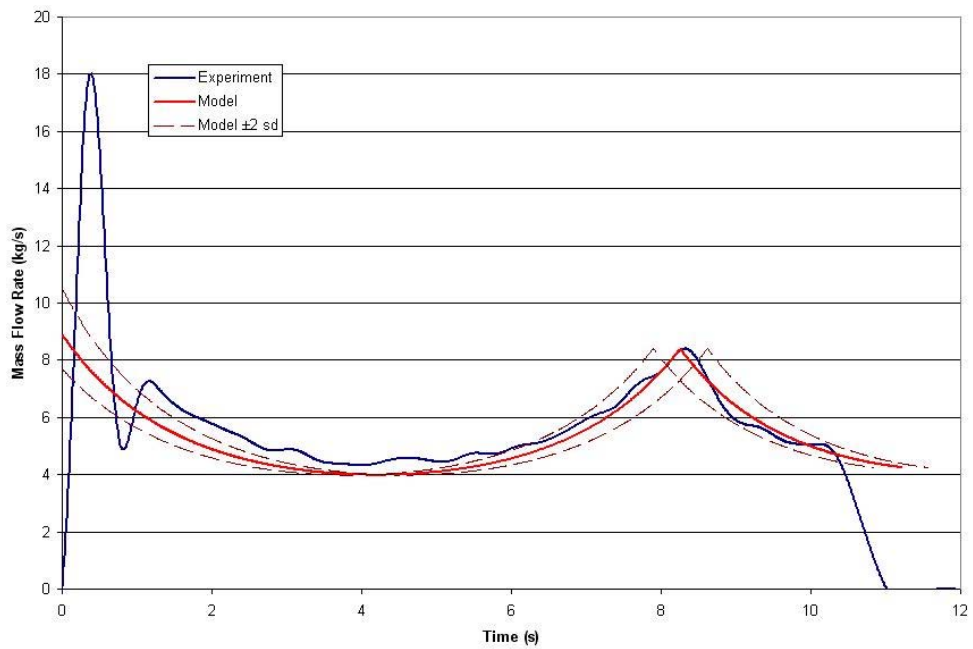


Figure 5.55. Mass flow rate data (Alternative Flight, Zeolite, 2 rpm).

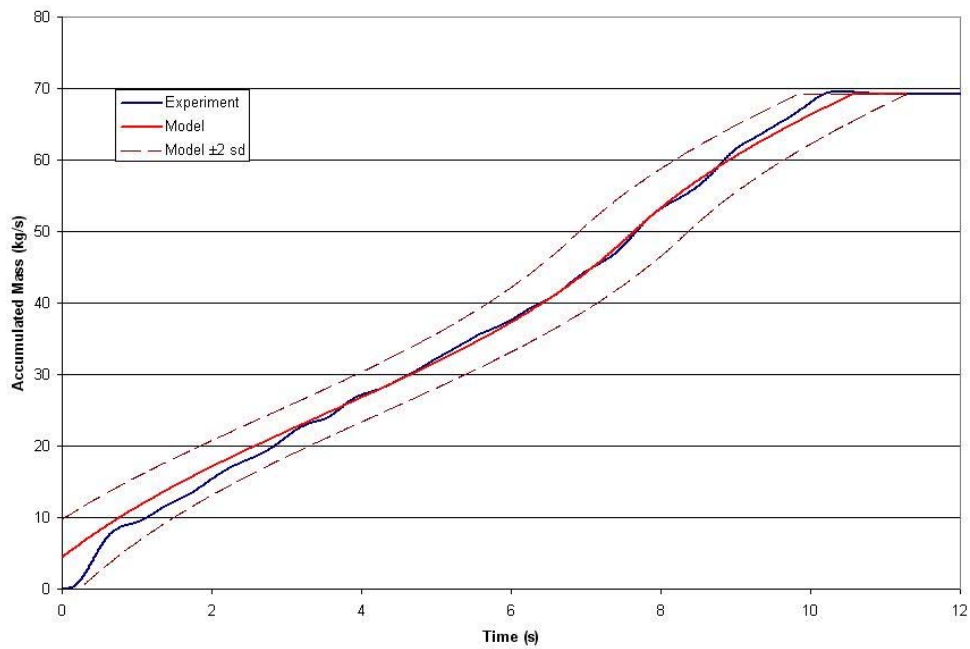


Figure 5.56. Accumulated mass data (Alternative Flight, River Sand, 2 rpm).

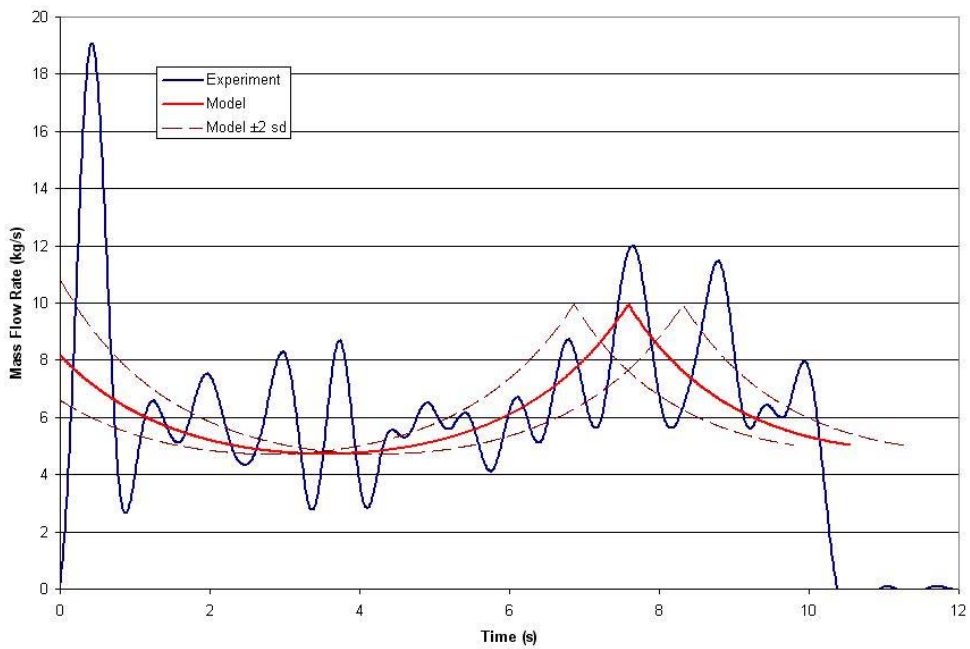


Figure 5.57. Mass flow rate data (Alternative Flight, River Sand, 2 rpm).

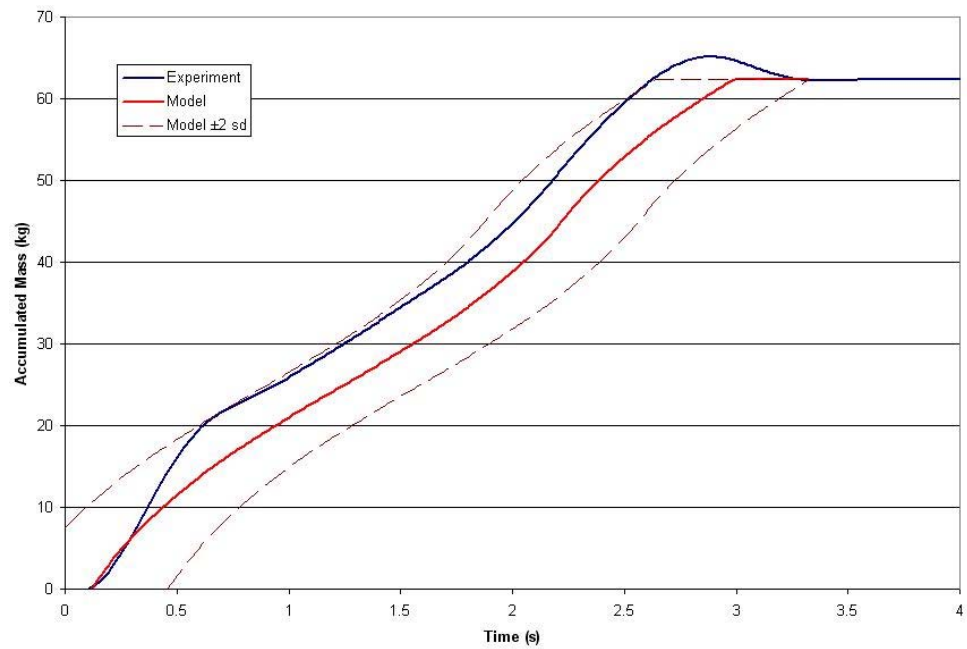


Figure 5.58. Accumulated mass data (Alternative Flight, Zeolite, 8 rpm).

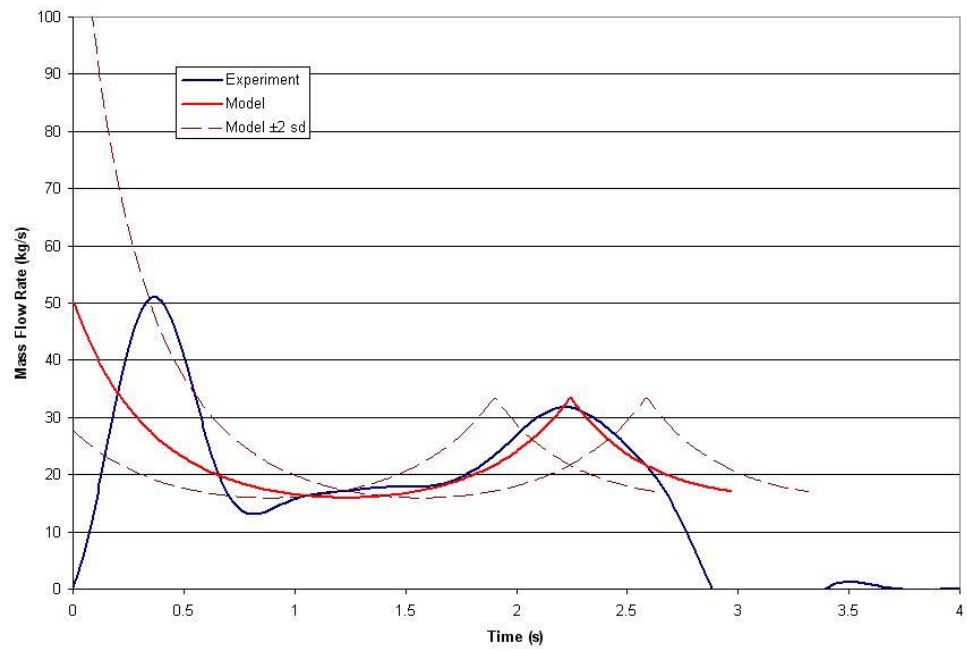


Figure 5.59. Mass flow rate data (Alternative Flight, Zeolite, 8 rpm).

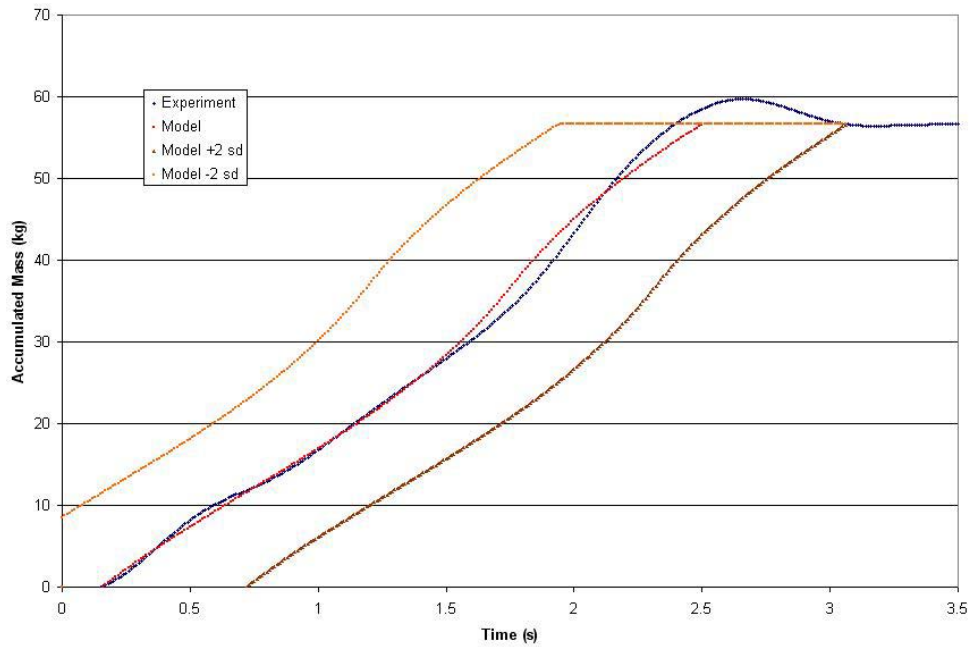


Figure 5.60. Accumulated mass data (Alternative Flight, River Sand, 8 rpm).

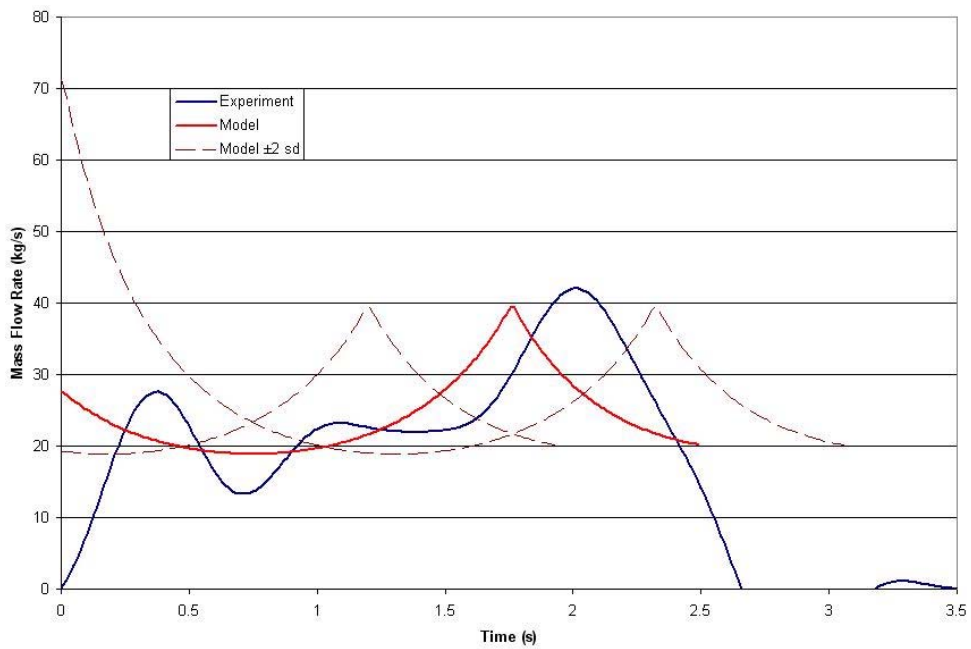


Figure 5.61. Mass flow rate data (Alternative Flight, River Sand, 8 rpm).

As can be seen from Figures 5.54 to 5.61, the experimental results once again fall within the 95% confidence interval on the model predictions. The same general trends that can be observed in the previous experiments are once again present in these results, suggesting that the model predictions are consistent across the full range of conditions tested.

A large amount of noise can be observed in Figures 5.56 and 5.57 that is not present in any other experiment. The reasons for the presence of this noise in only one experiment are unknown, as experiments conducted immediately before and after this experiment show no signs of this noise.

5.5.6. Summary of Model Validation

From the results presented above, it can be seen that the geometric unloading model provides a good match for the experimental data across the range of conditions studied. It is clear that the accuracy of these results is dependent on an accurate measurement of the dynamic angle of repose of the solids material, as this has a significant impact on the shape of the predicted unloading curve. Some variations between the experimental data and the model predictions have been observed, however these variations appear to be isolated to specific experiments, and do not show any visible trends with the variables studied.

It must be noted that the current model assumes a constant dynamic angle of repose for the duration of the flight unloading. However, some of the experimental results suggest that this may not be the case, and this will be discussed below in Chapter 5.6.4 based on observations from the high-speed camera images.

Additionally, it has been noted that the geometric flight unloading model assumes that the solids material flows continuously off the flight tip, and that bulk motion of solids does not occur. As had been demonstrated in Chapter 5.2.5, this assumption does not accurately represent the behaviour of the solids, and some of the experimental results reinforce this. However, the advantages of a more comprehensive model, accounting for these effects, must be weighted against the added complexity of such a model. The

geometric unloading model as it stands is relatively simple, involving only a few easily measurable parameters. A more complex model would require additional parameters and more computational power to implement, thus the added costs may outweigh the advantages of such a model.

In summary, the results presented above demonstrate that the geometric flight unloading model developed in this thesis provides a good representation of the actual unloading characteristics of a flight across a range of conditions. Whilst the model does not fully reproduce the details of the flight unloading behaviour (i.e. dynamic oscillations), it still provides an accurate prediction of the flight unloading profile, given accurate parameter values.

5.6. Analysis of Photographic Data

In addition to the data acquired by the load cells attached to the collection tray, a significant amount of data was also collected using the high-speed camera attached to the drive shaft of the apparatus. This data was primarily used to calculate the dynamic angle of repose of the solids material as discussed in Chapter 5.5.2, however measurement of the thickness and velocity of the unloading solids curtain were also taken for experiments 5-16 (no measurements were taken for those experiments without the abrasive surface). Whilst these variables have no bearing on the unloading of the flight, they are important in studying the gas-solid interactions that occur within the active phase, and will be discussed in Chapter 6.

5.6.1. Curtain Thickness

One of the key assumptions in the geometric flight unloading model is that the amount of mass contained within the flight is defined by the geometry of the flight and the material surface, which joins the flight tip to some point on the flight geometry. As such, it assumes that the thickness of the solids curtain passing the flight tip is zero, and that material is instantaneously discharged from the flight. This is clearly not true, as the solid material must flow over the flight tip in order to be discharged. Thus, there will be a moving layer of solids on top of the material

contained within the flight, which is not accounted for in the geometric unloading model.

The high-speed camera images allow for the thickness of this moving layer of solids to be measured as it passes the flight tip, giving an indication of the amount of mass in this moving layer as well as the initial thickness of the falling curtain of solids. Figures 5.62 to 5.64 show the measured thickness of the moving layer of solids in millimetres compared to the experimental and modelled unloading profiles of the flight for three of the experiments. As can be seen in Figure 5.62, the thickness of the moving layer of solids shows a very similar trend to the experimental unloading profile of the flight. Unlike the unloading profile however, after the minima the thickness continues to increase until the flight finishes unloading, resulting in a broad, but dispersed layer of solids in the later stages of unloading. This trend can be observed in all of the experiments conducted.

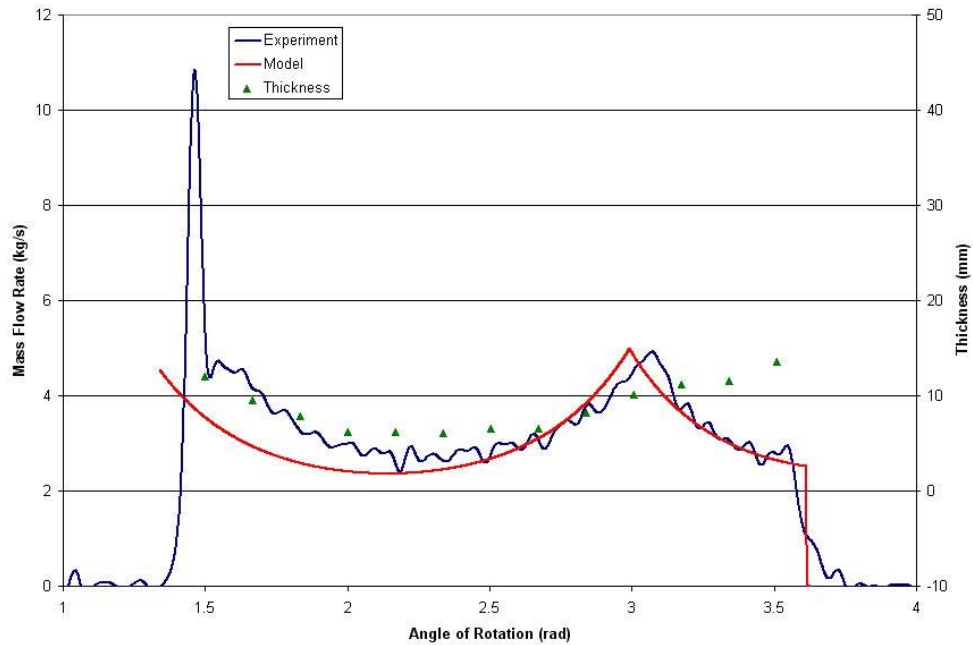


Figure 5.62. Comparison of the thickness of the moving layer of solids compared to the unloading profile of the flight (Alternate Flight, Filter Sand, 1 rpm).

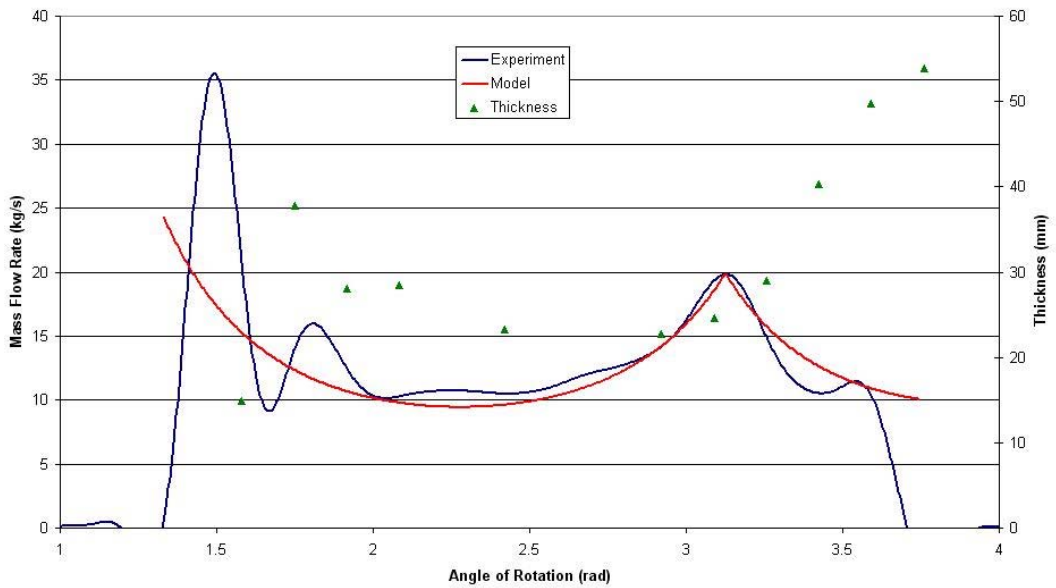


Figure 5.63. Comparison of the thickness of the moving layer of solids compared to the unloading profile of the flight (Alternative Flight, Filter Sand, 4 rpm).

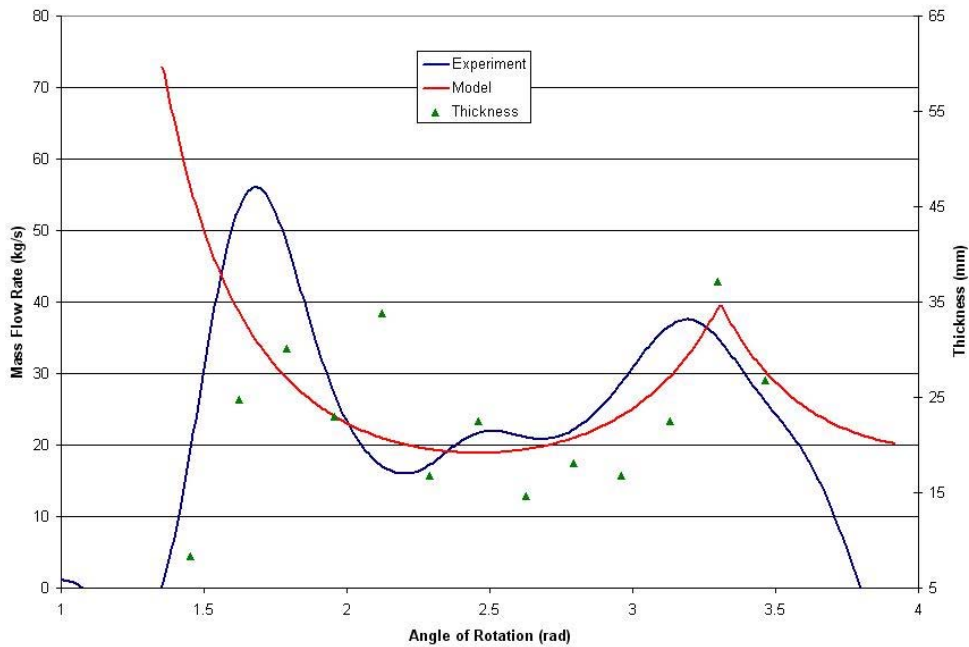


Figure 5.64. Comparison of the thickness of the moving layer of solids compared to the unloading profile of the flight (Alternative Flight, Filter Sand, 8 rpm).

Figure 5.65 shows the thickness profile for the Alternative flight design and filter sand at increasing rotational speeds. This shows that the thickness increases approximately

linearly with rotational speed. This is illustrated by Figure 5.66 which shows the average curtain thickness at different rotational speeds. As higher rotational speeds require material to be discharged at a greater rate, it is logical that the thickness of the moving layer of solids should increase in order to accommodate this, suggesting that curtain thickness should be proportional to the mass flow rate leaving the flight. Given this, it should be possible to predict the thickness profile at any rotational speed based on two experiments at different rotational speeds, thus reducing the number of experiments necessary to characterise the flight unloading. More experiments are needed however to confirm this observation.

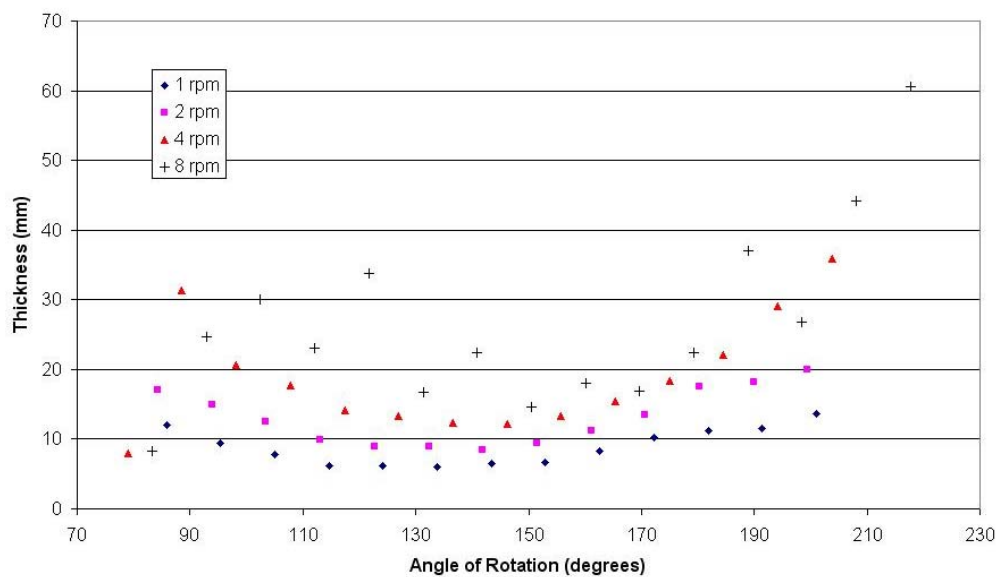


Figure 5.65. Thickness profile at increasing rotational speeds (Alternative Flight, Filter Sand).

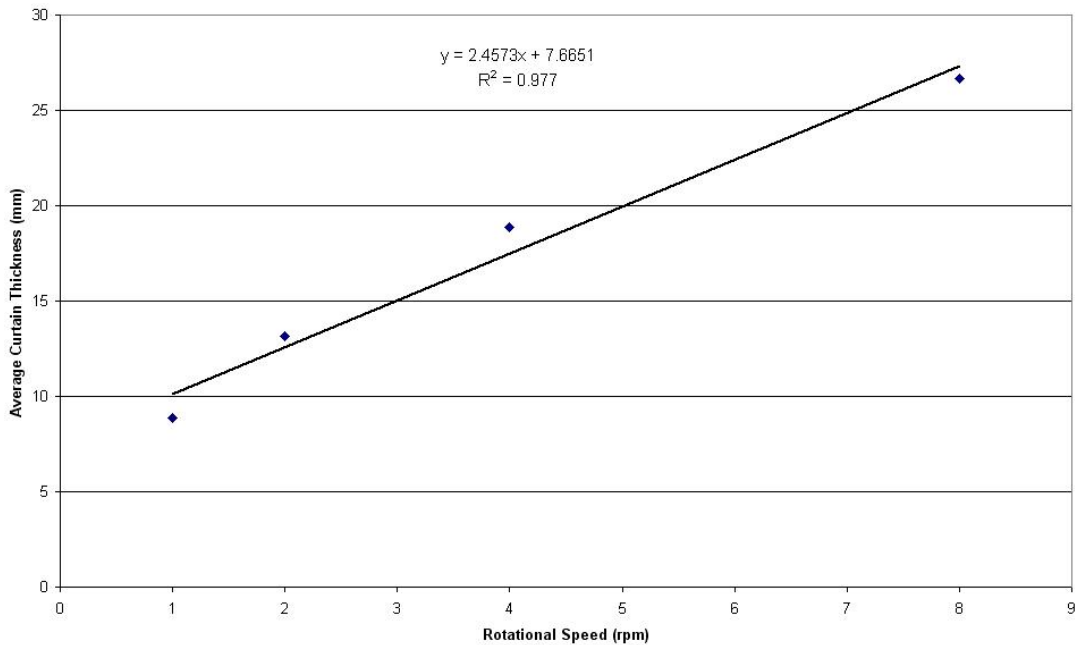


Figure 5.66. Average curtain thickness at increasing rotational speeds (Alternative Flight, Filter Sand).

5.6.2. Particle Velocity

Another factor that has a significant effect upon the path taken by a particle within the falling curtain of solids is the velocity of the solid particles as they leave the tip of the flight. In many cases of models of the solids transport in rotary dryers, this velocity has been assumed to be negligible or zero. The use of high-speed photography to film an unloading flight provides an opportunity to measure the velocity of the solid particles as they leave the flight using particle tracking methods, as discussed in Chapter 5.4.1. Figures 5.67 to 5.69 show the comparison between the measured particle velocities for the same three experiments shown in Figures 5.62 to 5.64.

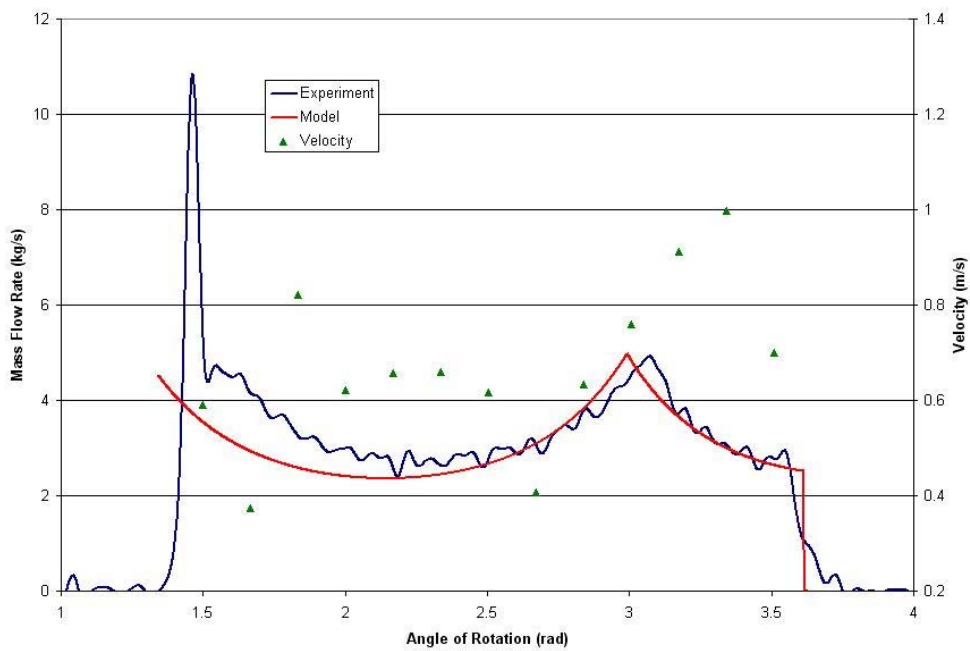


Figure 5.67. Comparison of the velocity of the moving layer of solids compared to the unloading profile of the flight (Alternative Flight, Filter Sand, 1 rpm).

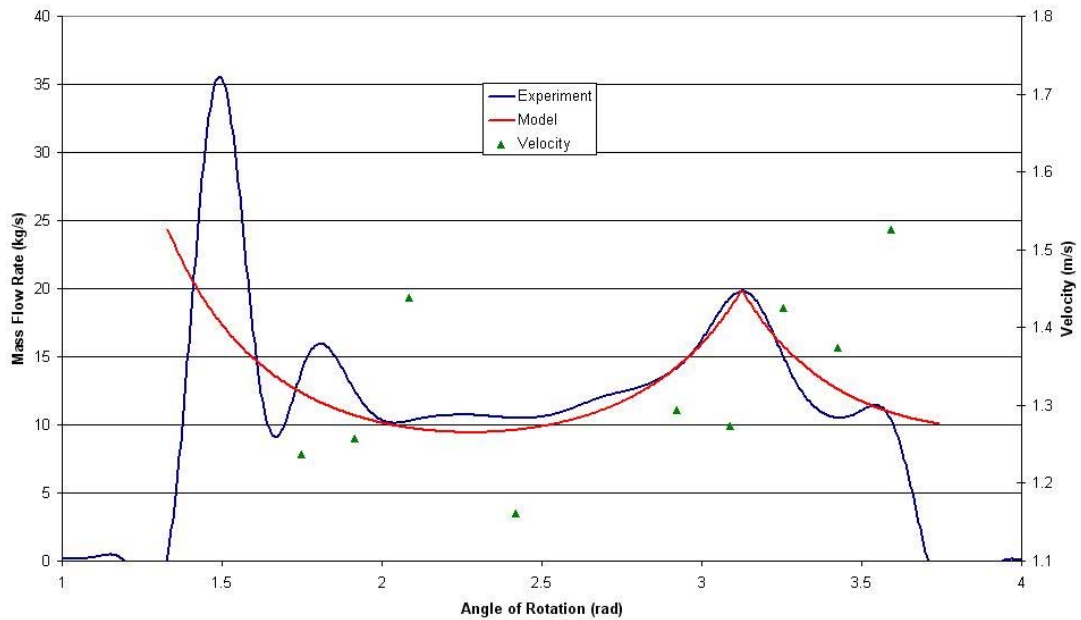


Figure 5.68. Comparison of the velocity of the moving layer of solids compared to the unloading profile of the flight (Alternative Flight, Filter Sand, 4 rpm).

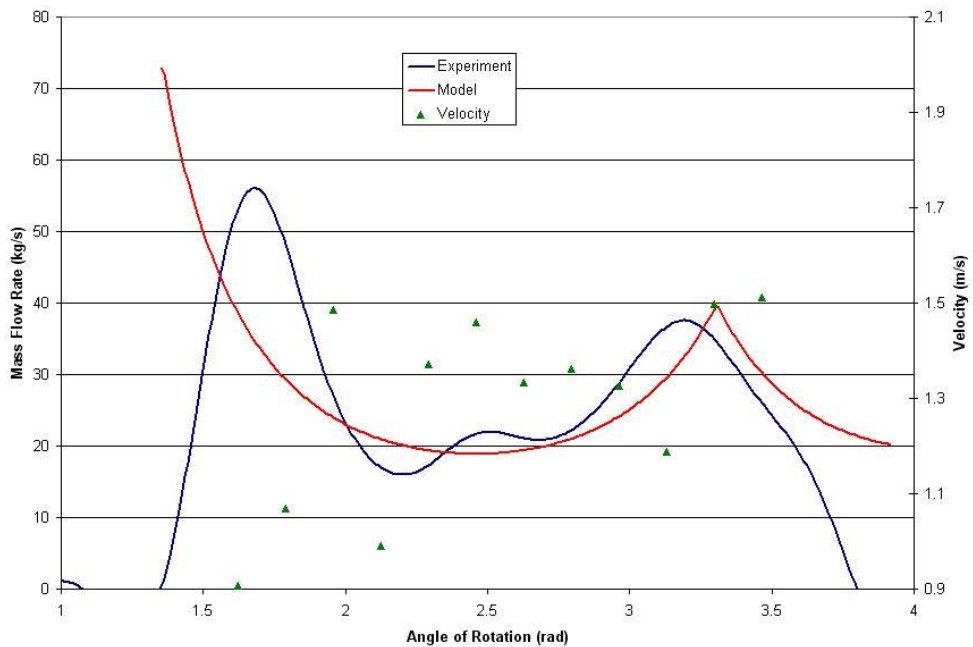


Figure 5.69. Comparison of the velocity of the moving layer of solids compared to the unloading profile of the flight (Alternative Flight, Filter Sand, 8 rpm).

It is immediately apparent from Figures 5.67 to 5.69 that there is a lot of variability in the measured particle velocities. This variability is possibly due in part to the location of the tracked particle within the moving layer of solids. As would be expected, there appears to be a velocity profile within the moving layer of solids, with particles on the top of the moving surface travelling faster than those near the bottom of the moving layer. As particle tracking is dependent upon finding an obvious particle to follow, it is difficult to find particles at a consistent depth within the layer. Where possible, the tracked particles were as close to the surface of the solids as possible, however it was often necessary to choose a particle deeper in the moving layer, thus accounting for much of the variation in the velocity measurements. It was also observed in some experiments that the velocity of the moving layer appeared to vary considerably throughout the experiment, with the layer often appearing to pulsate. This will be discussed further in Chapter 5.6.4.

Whilst it is difficult to observe any significant trends due to the variability in these results, the data does suggest that the particle velocity profile is also linked to the flight unloading profile. This however is a very tenuous suggestion and needs further study to confirm or deny. It can be seen in all experiments that the velocity of the

particles tends to increase slightly towards the end of the unloading of the flight. The results shown, as well as a number of other results, would suggest that the velocity follows a similar trend to the thickness of the curtain in following the shape of the unloading profile until near the end of the unloading, where the velocity continues to increase.

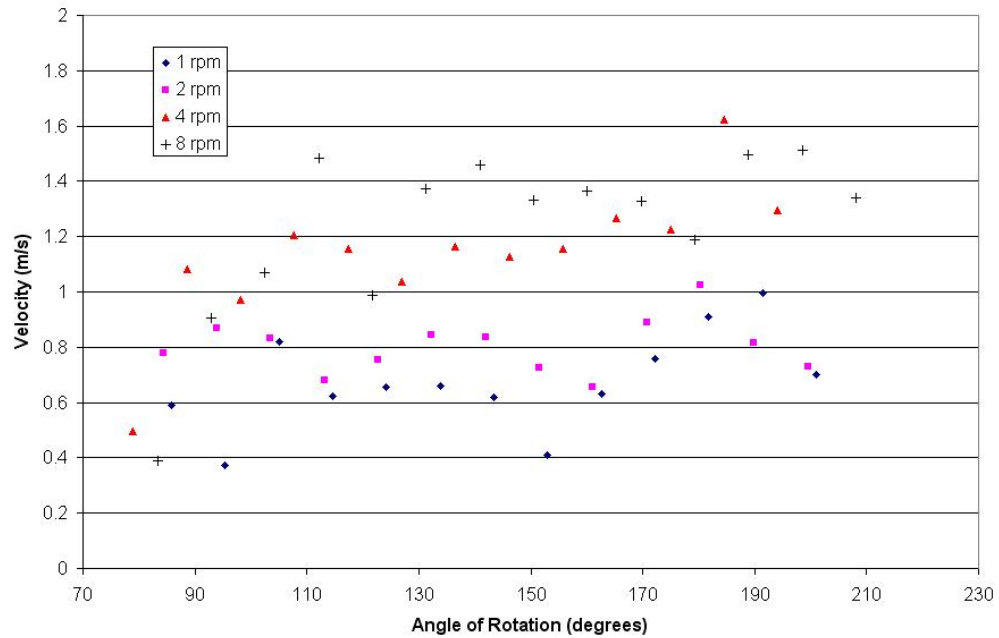


Figure 5.70. Particle velocity profile at increasing rotational speeds (Alternative Flight, Filter Sand).

Figure 5.70 shows the particle velocity profiles for the Alternative flight and filter sand at increasing rotational speeds. As before, it can be seen that the curves do show similar trends, with the curves showing peaks and troughs at similar locations. This suggest that some of the features in these curves may be real effects rather than noise, however there is insufficient data at present to study this in more detail.

Experiment	Mean Particle Velocity (m/s)	St. Dev. of Particle Velocity (m/s)
5	0.67	0.17
6	0.80	0.10
6 repeat	0.77	0.12
7	1.06	0.39
8	1.23	0.31
8 repeat	1.08	0.33
9	0.81	0.09
10	1.02	0.29
11	1.04	0.17
12	1.67	0.25
13	0.87	0.18
14	1.26	0.25
15	0.79	0.08
16	0.92	0.31

Table 5.6. Measured particle velocities (experiment numbers correspond with Table 5.4).

Table 5.6 shows the mean measured particle velocity and the standard deviation of the results for all the experiments where particle velocity was measured. As can be seen, there is a large amount of variation between the results, and in many case there is also significant variability in the results. From comparing the conditions of each experiment with the measured particle velocity, it can be seen that higher rotational speeds result in higher particle velocities. Higher rotational speeds require the flight to discharge mass faster, thus higher particle velocities are to be expected. Also, the larger full scale flight (Experiments 11 and 12), show higher particle velocities than the smaller flights for the same rotational velocity. This is probably due to the longer material surface, requiring more solids to be discharged, and allowing a longer surface for particles to accelerate down before leaving the flight.

5.6.3. Bulk Density of Moving Layer of Solids

Another parameter that has a significant effect on the transport of solids in the falling curtain is the voidage (r) of the curtain as it leaves the flight. The voidage of the curtain is related directly to the bulk density of the moving layer of solids as the flight discharges, and this can be calculated using the variables measured using the flight unloading apparatus and the high-speed camera. The volumetric flow rate of solids from the flight is $\dot{V} = h \times L \times v$, where h is the thickness of the curtain, L is the length of the flight and v is the velocity of the moving layer of solids. The volumetric flow rate can be related to the mass flow (\dot{M}) rate via the bulk density of the solid layer, ρ_{bl} , as shown in Equation 5.4.

$$\dot{M} = \rho_{bl} \dot{V} = \rho_{bl} h L v$$

Equation 5.4. Relating mass flow rate to moving layer dimensions.

From the experiments conducted using the flight unloading apparatus with the high-speed camera, the curtain thickness, length and velocity can all be calculated, as well as the mass flow rate from the load cells. Thus, the bulk density of the solid layer can be calculated using Equation 5.4 as the flight unloads. The results for the calculated bulk density of the moving solids layer for the experiments using the alternative flight design and filter sand at different rotational velocities are shown in Figure 5.71. The mass flow rate predicted by the geometric unloading model is also shown for comparison.

Given the significant error present in the values calculated from the high-speed camera data, there will be even greater errors present in the calculated bulk density of the moving layer. Thus, it is surprising that the calculated bulk density is as consistent as shown in Figure 5.71. With the significant variation observed in the values measured from the photographic data, especially the particle velocities, it would be expected that even more variation would be present in the calculated bulk density. Instead, the calculated bulk density is very similar across the entire period of unloading for the four experiments shown.

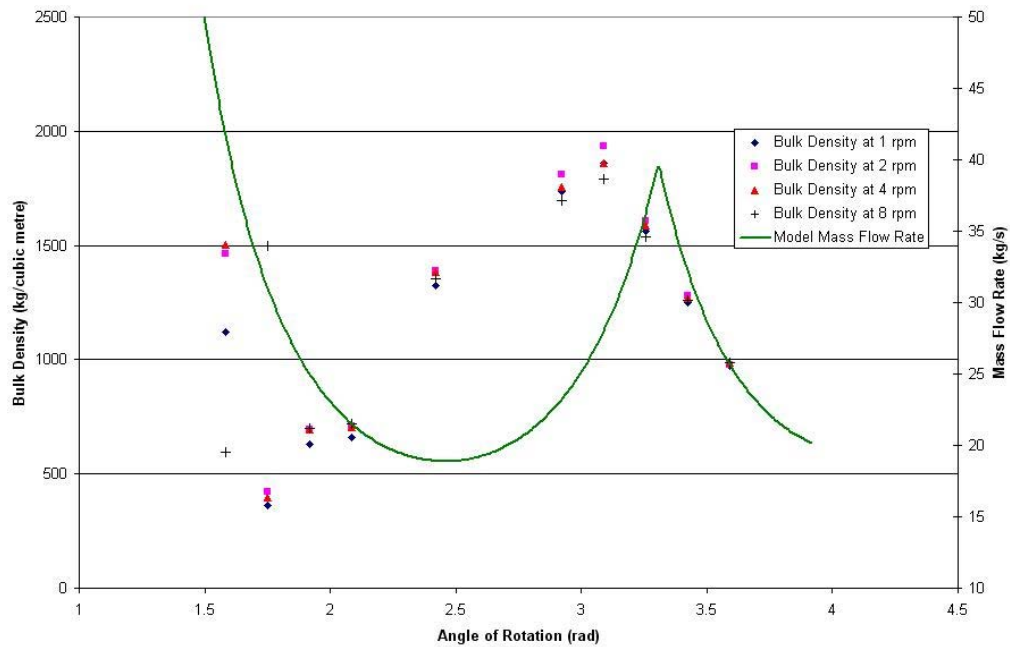


**Figure 5.71. Bulk density of the moving layer of solids at different rotational velocities
(Alternative Flight, Filter Sand).**

The results shown in Figure 5.71 suggest that the bulk density of the moving layer of solids leaving the flight varies throughout the unloading period, and follows a trend similar to that of the mass flow rate of solids leaving the flight. The results also suggest that the bulk density of the moving layer is unaffected by the rotational velocity of the flight. However, more data is needed before a conclusion can be drawn from this.

Comparing the trend of the calculated bulk density to the predicted mass flow rate, it can be seen that there are some similarities. Both curves start high before decreasing to a minimum, then increase again to a peak before falling away once more. However, the location of maxima and minima are offset somewhat, and the curves have slightly different shapes.

5.6.4. Further Observations

In addition to measuring the dynamic angle of repose, thickness and velocity of the moving layer of solids, a number of other observations were made from the high-speed camera images obtained from the experiments. It was observed that the flow of material leaving the flight fluctuated during unloading, with this effect being most pronounced at higher rotational velocities. Figure 5.72 shows one such fluctuation observed during an experiment. The images in Figure 5.72 show a flight in the process of unloading at intervals of 0.016 seconds (2 frames) over a period of 0.08 seconds in total. The development of a wave in the moving layer of solids can be clearly seen as the frames progress.

The existence of these fluctuations has a number of implications on the results of these experiments. Firstly, they provide an explanation for some of the variation observed in the measured thickness and velocities of the moving layer of solids, as it can be seen that these are affected by the fluctuations. Also, these fluctuations can make the measurement of the dynamic angle of repose difficult, as there is not a straight material surface to measure. In these situations, the angle of repose was measured to a line drawn from peak to peak of the waveform. In fact, these variations show that there is not always straight material surface, characterised by the dynamic angle of repose, as is assumed in the geometric unloading model. In order to fully determine the behaviour and effects of these fluctuations, further study and experiments will be required. For the purposes of this thesis, these effects will be assumed to have a negligible effect on the overall behaviour of the system.

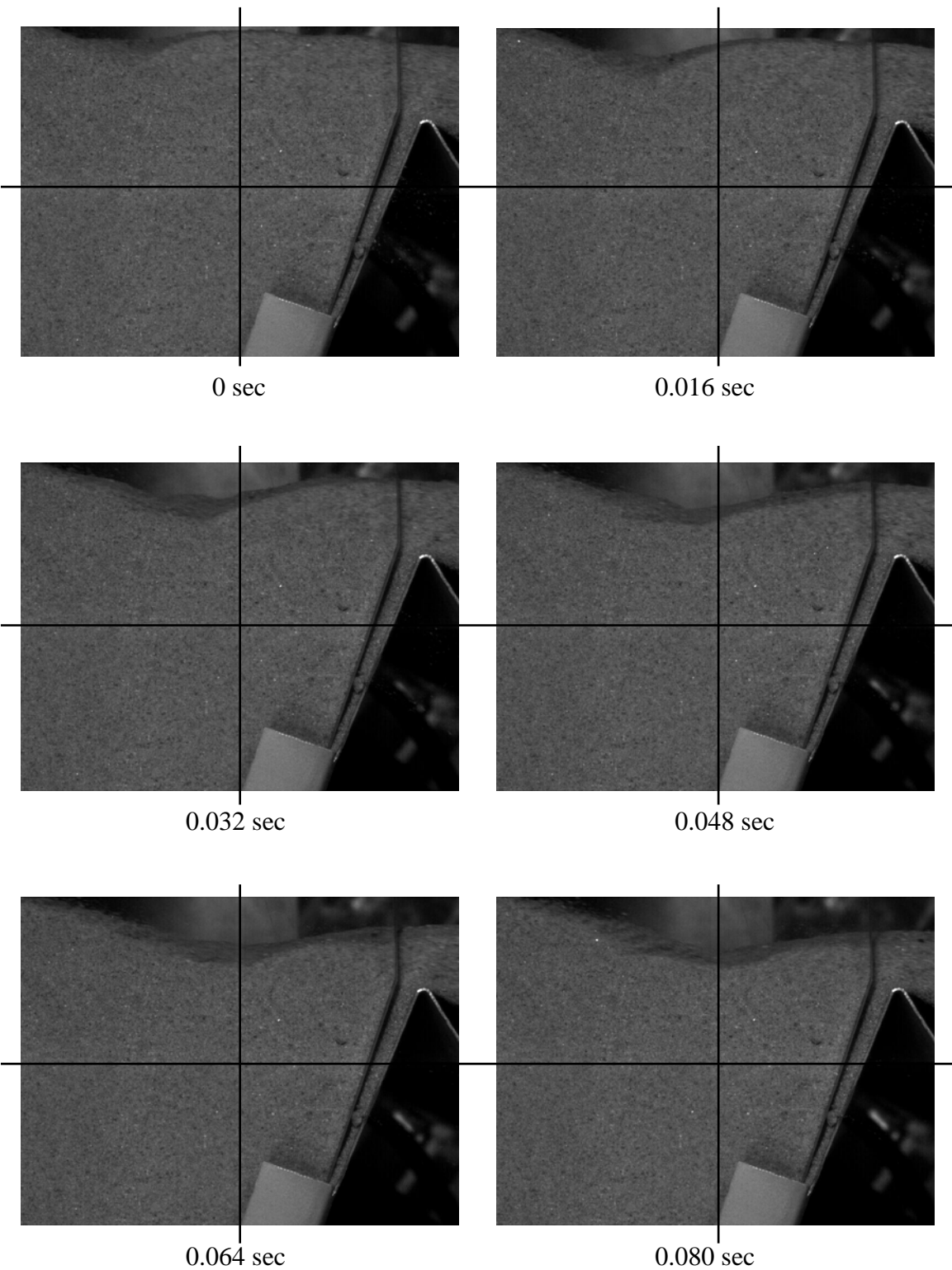


**Figure 5.72. High-speed camera images of a flight during unloading at intervals of 0.016 seconds
(Alternative Flight, River Sand, 8 rpm).**

Chapter 6

6. Modelling Gas-Solid Interactions in Rotary Dryers

The gas-solid interactions are an important aspect in terms of dryer operations, as most of the heat and mass transfer phenomena occur within the falling curtain of solids. However, the gas-solid interactions do not affect only the heat and mass transfer that occur in the dryer. Drag forces acting on the falling solid particles due to the moving gas also contribute to the transportation of solids within the dryer. Thus, a model of the solids transport within a rotary dryer is not complete without considering the effects of the gas-solid interactions.

6.1. The Axial Partitioning Coefficients

As discussed in Chapter 3, the distribution of solids leaving the active phase can be modelled using three partitioning coefficients; C_F , C_R and C_B . As these represent how the falling solids are distributed axially along the dryer, the partitioning coefficients must be dependent on the gas-solids interactions. In order to describe the axial partitioning coefficients, the axial displacement of the solid particles within the moving gas stream must be understood. This requires an understanding of both the drag coefficient of a single particle, and drag on a curtain of particles.

6.2. Experimental Measurement of Single Particle Drag Coefficients

In most industrial dryers, the solid particles will not be spherical, and in many cases may have irregular shapes. Correlations are available to estimate the drag forces acting on a wide range of common shapes, such as rectangles, spheres and other simple shapes⁴³. However correlations for more complicated geometries, such as hexagonally cross-sectioned raw sugar crystals (see Figure 6.1), are generally nonexistent. In order to determine the drag forces acting on a particle of complex geometry a number of approaches can be taken. The simplest approach, and one that has been commonly used in models of dryers (see for example Sherritt *et al.*²⁷) is to

assume that the particle can be adequately represented as a sphere. While this approach may prove adequate in many circumstances, it may be possible to achieve better results by using a more suitable correlation for determining the drag coefficient.

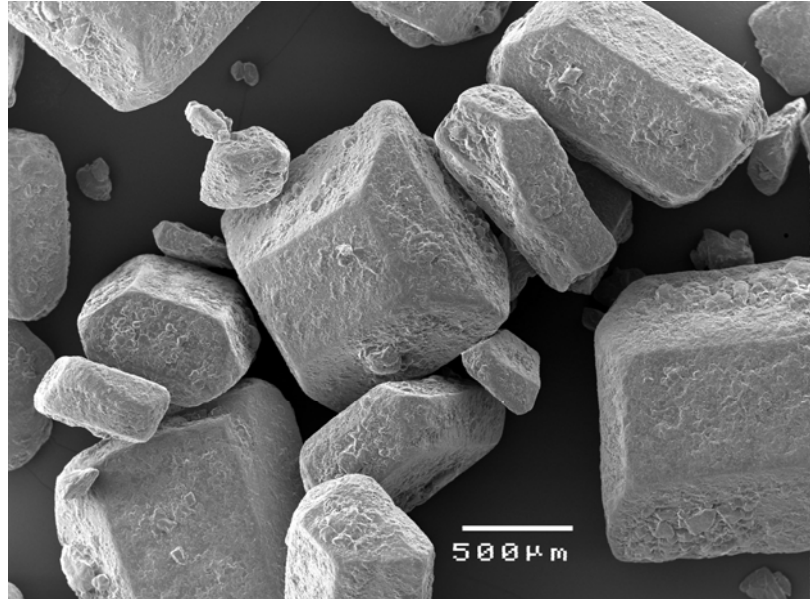


Figure 6.1. Electron microscope image of raw sugar crystals.

One method for achieving this is to develop a composite model for the particle, using a number of simple shapes to develop an approximation to the particle (see Munson *et al.*⁴³ for a more detailed description). This method can provide an approximation to the drag coefficient for fairly simple particle geometries.

Haider and Levenspiel⁵⁶ developed a generalized model (shown in Equation 6.1) for particles of any geometry based on the sphericity of the particle ($\phi = \frac{s}{S}$) where s is the surface area of a sphere with the same volume as the particle, and S is the actual surface area of the particle. Haider and Levenspiel reported that Equation 6.1 provided a reasonable fit to a range of experimental data for both spherical and non-spherical particles⁵⁶.

$$C_D = \frac{24}{Re} \times \frac{1 + e^{2.3288 - 6.4581\phi + 2.4486\phi^2} \cdot Re^{0.0964 + 0.5565\phi} + Re \cdot e^{4.905 - 13.8944\phi + 18.4222\phi^2 - 10.2599\phi^3}}{Re + e^{1.4681 + 12.5284\phi - 20.7322\phi^2 + 15.8855\phi^3}}$$

Equation 6.1. Haider and Levenspiel correlation⁵⁶.

The final option available for calculating the drag coefficient for a particle of complex geometry is to experimentally measure the drag force acting on a particle and to develop an empirical correlation for the drag coefficient.

6.2.1. Theory

The drag force acting on a particle can be calculated based on the acceleration of the particle as it falls through a fluid medium. Using a simple force balance of the gravitational, buoyant and drag forces acting on a particle falling vertically, Equation 6.2 can be developed, where m is the particle mass, a is the acceleration of the particle, g is the acceleration due to gravity, γ is the specific weight of the fluid medium, ∇ is the volume of the particle and F_D is the drag force acting on the particle.

$$ma = mg - \gamma\nabla - F_D$$

Equation 6.2. Force balance on a falling particle.

The drag force acting on a particle can also be expressed in terms of a drag coefficient, C_D , as shown in Equation 6.3. Here ρ is the density of the fluid medium, A is the cross sectional area of the particle perpendicular to the flow direction and v is the velocity of the particle.

$$F_D = \frac{1}{2} \rho C_D A v^2$$

Equation 6.3. Calculation of drag forces based on a drag coefficient.

Equations 6.2 and 6.3 can be rearranged to solve for the drag coefficient as shown in Equation 6.4. As can be seen, the drag coefficient is a function of the particle geometry (m , A and ∇), the fluid properties (γ and ρ) and the velocity and acceleration of the particle (a and v).

$$C_D = \frac{2(mg - \gamma\nabla - ma)}{\rho Av^2}$$

Equation 6.4. Equation for determining the drag coefficient.

The drag coefficient is often expressed as a function of Reynolds number ($\text{Re} = \frac{vd}{\nu}$) where v is the velocity of the particle, d is the particle diameter or characteristic length and ν is the kinematic viscosity of the fluid), and generally takes the form shown in Equation 6.5, where a , b and n are all coefficients determined from experiments.

$$C_D = \frac{a}{\text{Re}} (1 + b \text{Re}^n)$$

Equation 6.5. General form of drag coefficient correlation.

6.2.2. Experimental Method

In order to determine the drag coefficient for a falling particle using Equation 6.4 it is necessary to determine the velocity and acceleration of the particle as it travels through a fluid medium. In order to achieve this, raw sugar crystals were dropped into a 300x100x100 mm glass column filled with ethanol at 25°, and the particles filmed using a high-speed camera (Redlake HG-100K) to determine their displacement over time. Displacement-time data were integrated using a first order approximation to obtain the velocity and acceleration of the particle over time. Ethanol was selected as the fluid medium due to the low solubility of sucrose in ethanol (insoluble in ethanol at 20°C⁵⁷) and the well-tabulated fluid properties⁴³. Given that the drag coefficient is generally a function of the Reynolds number, which takes into account fluid properties, drag coefficients determined using one fluid are should be applicable to any fluid within the same range of Reynolds numbers.

Each crystal was weighed and its dimensions measured using vernier callipers prior to being dropped. Twenty crystals were dropped with the camera set at two different

heights (10 crystals for each height) in the column. Particle sizes ranged between 1.40mm and 2.66mm (longest dimension). The falling particle was filmed at intervals of 3/80 seconds to allow sufficient displacement of the particle between images. A steel ruler was included as a backdrop in all images to provide a scale for measuring distances. The images were then analysed by measuring the number of pixels displaced by the particle in each interval. This distance was then converted to metres and used to calculate the velocity and acceleration of the particle. Figure 6.2 shows an example of an image of a falling crystal.

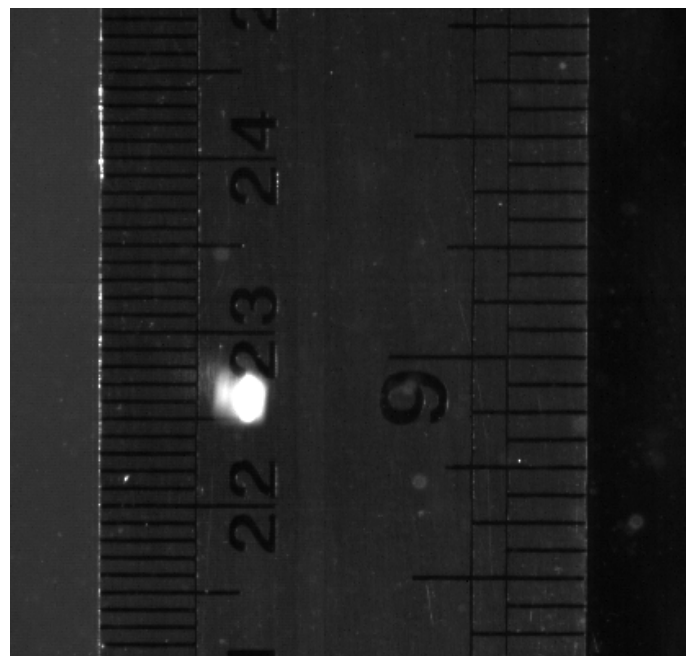


Figure 6.2. Image of a falling sugar crystal.

6.2.3. Results

Figure 6.3 shows the calculated values for the drag coefficient across a range of Reynolds numbers, compared to the predictions of the Schiller-Naumann equation⁴⁴ and the correlation of Haider and Levenspiel⁵⁶ for a particle of sphericity (ϕ) 0.846. Based on observation of the falling crystal, the characteristic length (d) of the crystal was taken as the length between the two points of the hexagonal cross section shown in Figure 6.2, and the cross-sectional area, A , as a rectangle perpendicular to this length. Due to the complex shape of a sugar crystal and the large amounts of variation in the shape of individual crystals, it was assumed that the crystals could be approximated as rectangular prisms. The sphericity of the crystals was approximated using the average particle dimensions for all the crystals studied in the experiment.

As can be seen from Figure 6.3, the data shows an obvious trend with the drag coefficient decreasing with increasing Reynolds number, as is expected. A correlation is also shown on Figure 6.3, using the form shown in Equation 6.5, derived in this work. This curve was fitted to the experimental data using Engineering Equation Solver[®] (EES). This curve provides a good fit to the experimental data (Root Mean Squared Error (rms) = 0.14), as is shown in Equation 6.6. When this is compared to the errors for the Schiller-Naumann equation (rms = 0.26) and the equation of Haider and Levenspiel (rms = 0.51), it can also be seen that the experimental results are noticeably lower than the prediction of both correlations, implying that both correlations over predict the drag forces acting on a sugar crystal.

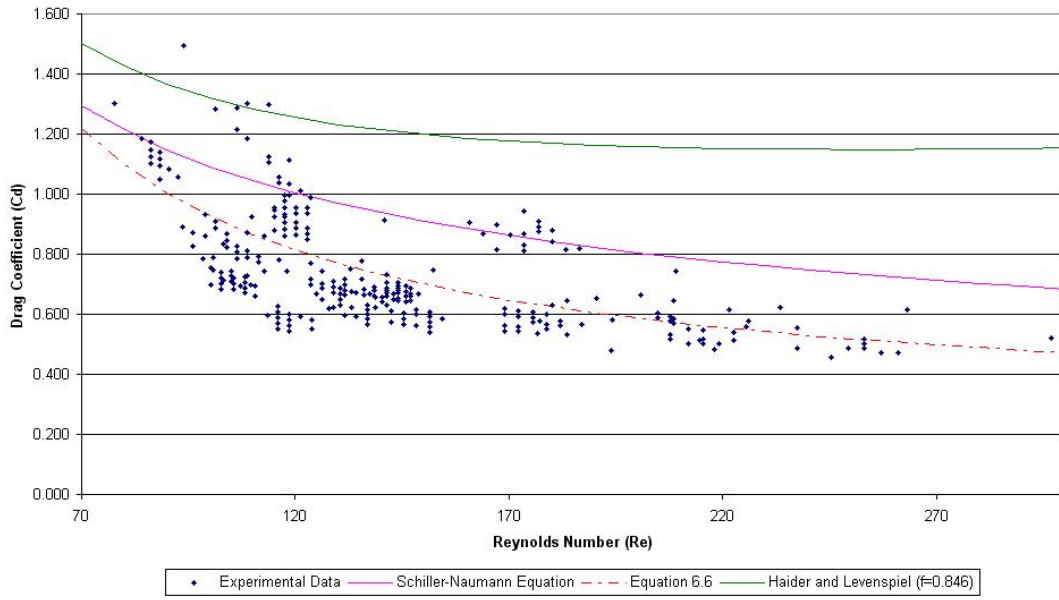


Figure 6.3. Drag coefficient of a falling sugar crystal.

$$C_D = \frac{68}{Re} \left(1 + 0.004 Re^{0.99} \right)$$

Equation 6.6. Modified Schiller-Naumann equation.

6.2.4. Discussion

It was observed that at low velocities, the particles were seen to tumble and drift as they fell. This made measurement of the drag forces acting on the particle difficult as the displacement of the particle was difficult to measure accurately and the alignment of the particle was uncertain. As the particle accelerated however, it was observed that they reached a steady-state, with the particle presenting its most streamlined face to the flow, as shown in Figure 6.2. Here the profile of the falling crystal can be clearly seen, with the pointed end facing the flow, and the long faces parallel to the flow. This streamlined alignment may contribute to the observation of drag coefficients lower than that for a volume-equivalent sphere. Looking at Figure 6.3, it can be seen that the experimental data shows a steep gradient at low Reynolds numbers, with the trend indicating that the drag coefficient for a sugar crystal will be greater than that for a sphere at low Reynolds numbers. This agrees with the observation for the

tumbling crystals, which would have a significantly higher drag coefficient than the particles falling in streamline.

EES was used to find a value for the sphericity of a crystal in the equation of Haider and Levenspiel⁵⁶ that best fitted the experimental data. This gave a sphericity of $\phi \approx 0.4$, whilst using the average dimensions of the crystals used in the experiment, and assuming that the crystal is rectangular, gives a sphericity of $\phi=0.78$. This value is approximately twice that of the value suggested by the Haider and Levenspiel equation. This will be in part due to the assumption the crystal is rectangular, as this underestimates the surface area of the crystal by ignoring bevelled edges and minor faces, and over predicts the volume of the crystal. However, these errors are unlikely to produce the halving in the sphericity that is observed.

Comparing the observed drag coefficients to tabulated values for a range of shapes⁴³ suggests that the orientation of the falling crystal is of most importance when determining the drag forces acting on the crystal. Tabulated results show that ellipses and airfoils have lower drag coefficients than spheres with similar dimensions⁴³. Whilst a sugar crystal is not an ellipse or an airfoil, it does have similar geometry, with an elongated body, which may result in the lower drag coefficients observed.

The range of Reynolds numbers achieved in these experiments ($Re = 70 \rightarrow 300$) compares well to the range of Reynolds numbers that occur within a typical industrial rotary sugar dryer ($Re \approx 100 \rightarrow 500$). Thus, the correlation derived in this work should be useful in estimating the drag forces acting on sugar crystals within these dryers. It must be noted however, that the correlation derived in this paper studied an isolated crystal, thus the actual drag forces within a dryer may be significantly different due to the presence of other particles in close proximity. Further study would be required to assess the effects of multiple crystals falling together.

6.2.5. Summary

The drag coefficient for a falling raw sugar crystal was measured experimentally using high-speed photography. It was found that the drag coefficient for a falling sugar crystal could be described using the equation $C_D = \frac{68}{Re} (1 + 0.004 Re^{0.99})$ where Re is based on the characteristic length of the crystal. Other correlations commonly used to approximate the drag coefficient for irregularly shaped objects provided a poor fit in this situation. The crystal was observed to tumble and drift during the initial period of the fall, but reached a steady-state presenting its most streamlined profile to the flow.

6.3. Methods for Modelling the Gas-Solids Interactions for the Falling Curtain

Whilst knowing the drag coefficient of a single particle falling in isolation is important, it has been shown that this alone is insufficient to model the gas-solids interactions within the falling curtain. Baker⁴⁵ has shown that simple models for the gas-solids interactions (isolated spheres and flat plate assumptions) cannot accurately characterise the behaviour observed within a falling curtain. However, with modern computers and numerical techniques, it is now possible to develop more sophisticated models for fluid systems, using techniques such as computational fluid dynamics (CFD).

6.4. Computational Fluid Dynamics (CFD) Modelling

The unsteady-state Navier-Stokes equations have long been known to provide a complete mathematical description of the flow of incompressible Newtonian fluids⁴³. Due to the complexity of these equations, there are no known general analytical solutions, although there are a very few situations where analytical solutions are possible^{43, 58}. However, the equations can be discretised and solved numerically, and this is referred to as computational fluid dynamics, or CFD. By combining equations describing other phenomena, such as drag, buoyancy and turbulence, with the Navier-

Stokes equations, it is possible to develop accurate models of a wide range of fluid systems.

CFD can be used to model systems involving multiple phases, such as immiscible liquids, or even gas-solid systems. In these situations, the larger phase is referred to as the continuous phase, whilst the other phase(s) are referred to as dispersed phases. A range of different approaches are available for modelling the dispersed phase of multi-phase systems of varying degrees of complexity⁵⁹. The two most commonly used approaches are the Lagrangian and Eulerian approaches.

The Lagrangian approach treats the dispersed phase as consisting of individual elements or particles which do not interact with each other^{58, 59}. Each element is individually tracked as it moves through the continuous phase, allowing particle trajectories to be monitored. As the Lagrangian method assumes that there are no interactions between elements of the dispersed phase, it is only applicable in situations where this is the case. Also, as the Lagrangian method calculates the forces acting on each element of the dispersed phase individually, the calculations required become prohibitive when dealing with large numbers of elements.

The Eulerian approach treats the dispersed phase as an interpenetrating continuum within the continuous phase, and solves a full set of governing equations for each phase (continuous and dispersed phases)^{58, 59}. This reduces the number of equations required when dealing with large numbers of particles, but individual particles can no longer be tracked and studied. Thus, the Eulerian approach is generally more useful for systems involving large numbers of dispersed elements.

An extension of the Eulerian approach for modelling systems involving granular solid is the Eulerian-Granular approach. In this approach, an additional transport equation for the granular temperature is solved⁵⁹. The granular temperature represents the fluctuation of energy in the solids due to random motion and collision of particles. In the Eulerian approach, all fluids in the system share the same pressure field, whilst in the Eulerian-Granular approach, each solid phase has an individual solid pressure field. The Eulerian-Granular approach is appropriate for modelling fluidized beds, and

particle laden flows where the phases mix or separate, and have solid volume fractions between 0 and ~60%⁵⁹.

CFD has successfully been used to model a wide range of gas-solids systems, such as fluidized beds (for example Cooper and Coronella⁶⁰, Du *et al.*⁶¹ and Nakamura and Watano⁶²), downer reactors (for example Ropelato⁶³) and pneumatic conveying (for example Hidayat and Rasmussen⁶⁴). The approach used (Lagrangian, Eulerian, Eulerian-Granular, etc.) depends mainly on the type of system being modelled, and more specifically, the density of particles within the system.

Due to the large number of particles present within the falling solids curtain, a Lagrangian approach was not considered for modelling the gas-solids interactions. Given relatively low particle densities present in the falling solids curtain and the lack of random motion of particles, particle-particle interactions were believed to be minimal, thus an Eulerian-Eulerian model was chosen for this thesis.

6.5. CFD Modelling of Turbulent Flows

CFD uses the Navier-Stokes equations to describe the flow behaviour of fluid systems. In principle, these equations are capable of describing both turbulent and laminar flow without the need for additional equations. However, turbulent flows generally occur at lengths and time scales much smaller than those used in CFD simulations⁵⁸. Direct numerical simulation of turbulent phenomena would require extremely small mesh sizes and computing power significantly greater than that currently available⁵⁸.

In order to predict the behaviour of turbulent flows, a number of different turbulence models have been developed. These models seek to predict the behaviour of turbulent flows without the need for prohibitively fine mesh sizes. Most turbulence models are statistical models and use the Reynolds Averaged Navier-Stokes (RANS) equations⁵⁸. These equations seek to represent the mean flow characteristics, while modelling the turbulence effects without needing small meshes⁵⁸.

The RANS approach breaks flow characteristics into averaged and fluctuating components⁵⁸. For example, velocity, U , may be divided into an averaged component, \bar{U} , and a fluctuating component, u , such that $U = \bar{U} + u$. The averaged component is given by $\bar{U} = \frac{1}{\Delta t} \int_t^{t+\Delta t} U dt$, where Δt is a time scale that is large relative to the time scale of the turbulent fluctuations, but small in comparison to the time scale at which the Navier-Stokes equations are solved⁵⁸.

6.5.1. RANS Equations

Substituting the averaged flow quantities into the Navier-Stokes equations gives the RANS equations, which are given below in Equation 6.7 and Equation 6.8. Here, the bar representing averaged flow quantities has been dropped, except for products of fluctuating quantities. The RANS Energy equation is not discussed here, as it is not required for the simulations in this thesis.

$$\frac{\partial \rho}{\partial t} + \nabla \cdot (\rho U) = 0$$

Equation 6.7. RANS Continuity Equation.

$$\frac{\partial(\rho U)}{\partial t} + \nabla \cdot (\rho U \otimes U) = \nabla \cdot (\tau - \rho \overline{u \otimes u}) + S_M$$

Equation 6.8. RANS Momentum Equation.

Here, ρ is the density of the fluid phase, U is the averaged fluid velocity, u is the fluctuating component of the fluid velocity due to turbulent flow, τ is the molecular stress tensor and S_M represents any external momentum sources (buoyancy, drag, etc. see Chapter 6.5.3). The $\rho \overline{u \otimes u}$ term is referred to as the Reynolds stress⁵⁸.

6.5.2. Eddy Viscosity Turbulence Models

One of the methods used to model turbulent flow assumes that turbulence consists of small eddies that are constantly forming and dissipating, and in which Reynolds stresses are assumed to be proportional to mean velocity gradients⁵⁸. These methods of modelling turbulence are referred to as eddy viscosity turbulence models. The eddy viscosity model assumes that the Reynolds stresses can be related to the mean velocity gradients and Eddy (Turbulence) Viscosity (μ_t), as shown in Equation 6.9⁵⁸.

Here T is the temperature of the fluid, k is the turbulence energy per unit mass,

$$-\rho \overline{u \otimes u} = \mu_t \left(\nabla U + (\nabla U)^T \right) - \frac{2}{3} \delta (\rho k + \mu_t \nabla \cdot U)$$

Equation 6.9. Eddy viscosity model for Reynolds stresses.

In order to apply this model, it is first necessary to determine the turbulent viscosity, μ_t . A number of models exist for this purpose of varying complexity⁶⁵. The most commonly used model is the $k-\varepsilon$ model⁶⁵, a two-equation model for turbulence. The $k-\varepsilon$ is popular as the equation for the turbulence dissipation rate, ε , is easily derived and appears as an unknown in the equation for k ⁶⁵. It is also popular as it is easily realised in practice, and has been used extensively in modelling two-phase gas-solid systems^{61, 66}.

Applying these hypotheses, the RANS momentum equation for the $k-\varepsilon$ model becomes that shown in Equation 6.10. Here $\mu_{eff} = \mu + \mu_t$ and $p' = p + \frac{2}{3} \rho k + \frac{2}{3} \mu_t \bar{\nabla} \cdot U$ (p is the pressure of the fluid). Using Ansys CFX®, the solver generally assumes that $p' = p$. B represents any body forces acting on the fluid.

$$\frac{\partial(\rho U)}{\partial t} + \nabla \cdot (\rho U \otimes U) - \nabla \cdot (\mu_{eff} \nabla U) = -\nabla p' + \nabla \cdot (\mu_{eff} \nabla U)^T + B$$

Equation 6.10. Modified RANS Momentum equation.

The $k - \varepsilon$ assumes that the turbulence viscosity is related to turbulence kinetic energy and turbulence dissipation, as shown in Equation 6.11^{58, 65}.

$$\mu_t = 0.09 \rho \frac{k^2}{\varepsilon}$$

Equation 6.11. $k - \varepsilon$ model for turbulence viscosity.

The equations for k and ε come directly from the differential transport equations for turbulence kinetic energy and turbulence dissipation rate^{58, 65}, and are given in Equation 6.12 and Equation 6.13. The variables $C_{\varepsilon 1}=1.44$, $C_{\varepsilon 2}=1.92$, $\sigma_k=1.0$ and $\sigma_\varepsilon=1.3$ are constants^{58, 65}.

$$\frac{\partial(\rho k)}{\partial t} + \nabla \cdot (\rho U k) = \nabla \cdot \left[\left(\mu + \frac{\mu_t}{\sigma_k} \right) \nabla k \right] + P_k - \rho \varepsilon$$

Equation 6.12. Turbulence kinetic energy equation.

$$\frac{\partial(\rho \varepsilon)}{\partial t} + \nabla \cdot (\rho U \varepsilon) = \nabla \cdot \left[\left(\mu + \frac{\mu_t}{\sigma_\varepsilon} \right) \nabla \varepsilon \right] + \frac{\varepsilon}{k} (C_{\varepsilon 1} P_k - C_{\varepsilon 2} \rho \varepsilon)$$

Equation 6.13. Turbulence dissipation rate equation.

The term P_{kb} in Equation 6.12 is the turbulence production due to viscous and buoyant forces, and is modelled using Equation 6.14^{58, 65}. In situations where a full buoyancy model is being used $P_{kb} = -\frac{\mu_t}{\rho \Pr_t} g \cdot \nabla \rho$ ⁵⁸.

$$P_k = \mu_t \nabla U \cdot (\nabla U + \nabla U^T) - \frac{2}{3} \nabla \cdot U (3\mu_t \nabla \cdot U + \rho k) + P_{kb}$$

Equation 6.14. Turbulence production due to viscous and buoyant forces.

6.5.3. Interphase Momentum Transfer

In addition to buoyant forces, momentum can be transferred between phases due to a number of effects, such as interphase drag forces and lift forces⁶⁷. These are represented in the RANS equations by the term S_M . Each of these can be represented by a suitable physical model.

In the case of a falling curtain of solids, the most important interphase momentum transfer is due to interphase drag forces. The interphase drag force acting on phase α due to phase β are represented by the general equation $S_{M,\text{drag}} = c_{\alpha\beta}^{(d)} (U_\beta - U_\alpha)$ where $c_{\alpha\beta}^{(d)}$ is a coefficient calculated from the dimensionless drag coefficient and U is the velocity of a given phase. For spherical particles, $c_{\alpha\beta}^{(d)}$ can be determined analytically using Equation 6.15⁶⁷ where $A_{\alpha\beta}$ is the cross-sectional area of a particle projected in the flow direction. For this thesis, the Schiller-Naumann equation was used to calculate C_D , as this provides a reasonable approximation to the drag coefficient and was available in the software used.

$$c_{\alpha\beta}^{(d)} = \frac{C_D}{8} A_{\alpha\beta} \rho_\alpha |U_\beta - U_\alpha|$$

Equation 6.15. Interphase momentum transfer coefficient⁶⁷.

6.6. Verification and Validation of CFD Techniques

Whilst CFD has been successfully used to model a wide range of multiphase systems, it was still necessary to verify and validate the techniques used in this thesis. To achieve this, work was conducted in conjunction with researchers at Monash University to use CFD to simulate a number of experiments conducted in a wind

tunnel and to compare the results. The experiments and simulations were conducted separately and then compared to determine the accuracy of the CFD model.

6.6.1. Comparing CFD Simulations to Wind Tunnel Experiments

A number of experiments were conducted in a laboratory scale wind tunnel at Monash University to study the behaviour of a broad curtain of falling solids in a moving gas stream using the apparatus shown in Figure 6.4. The experimental apparatus consisted of a 2.4 metre long tunnel with a 0.15 metre wide, 0.6 metre high cross-section^{47, 68}. Solids were fed under controlled conditions across the entire width of the tunnel and allowed to fall through a moving air stream, before being removed through the floor of the tunnel. The falling curtain was filmed using high-speed photography, and temperature and pressure readings were taken in situ (see Wardjiman *et al.*⁶⁸ for details).

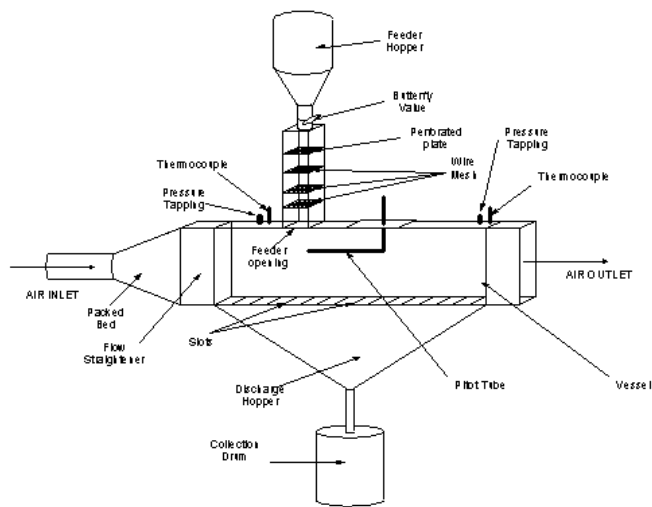


Figure 6.4. Wind tunnel apparatus used by Wardjiman *et al.*⁶⁸

6.6.1.1. Model Structure and Conditions

The CFD model was constructed to the same dimensions as the physical apparatus using CFX 5.7.1. The numerical domain was discretised with a 9mm tetrahedral mesh applied to the region in which the particle curtain existed and extending for a minimum of 50mm beyond the expected curtain boundaries. The remainder of the tunnel was discretised using a maximum mesh size of 35mm, resulting in a total mesh

of 136,000 nodes. The system was solved using the inbuilt Automatic Timescale calculator in CFX 5.7.1⁶⁹ until all residuals were less than 10^{-4} , or 100 iterations had been performed.

The gas velocity at the inlet to the duct was specified at the experimental conditions and at the solids inlet, the mass flow rate, velocity and initial solids volume fraction were specified. The inlet solids volume fraction of solids was calculated based on

experimental data using the following equation $r_{p0} = \frac{\dot{M}_p}{\rho_p U_0 A}$, where \dot{M}_p is the mass

flow rate of solids entering the system, U_{p0} is the initial velocity of the solids entering the duct, and A is the cross-sectional area of the solids inlet.

At the downstream end of the duct, the boundary was defined as an outlet boundary, such that material can only exit the system through this boundary. In the absence of experimental data, the gas and solids inlets were given a turbulence intensity of 5%⁶⁹. The remaining boundary conditions were governed by the no-slip condition.

6.6.1.2. Comparison of Results

The results of the simulations were analysed using the CFX 5.7.1 post-processor. The edges of the curtain were defined using a contour of constant solids volume fraction in the simulated results. The solids volume fraction was plotted using a contour plot and compared to the experimental data, where it was found that the lowest contour, with a solids volume fraction of 5.6×10^{-4} , corresponded well with the experimentally measured results. Measurements of other variables in the system were taken at the same location as the physical measurements in the experiments.

Experiments with Air Flow

Figures 6.5 to 6.9 show the comparison between the simulated 5.6×10^{-4} volume fraction contour and the experimental results for a range of experimental conditions. As the experimental results were measured using photographic means, the measured

curtain boundaries show the maximum and minimum limits of curtain displacement. Thus, the simulated trailing edge contour is measured at the centreline of the tunnel, where displacement is greatest, whilst the leading edge is measured next to the tunnel wall, where the displacement is a minimum.

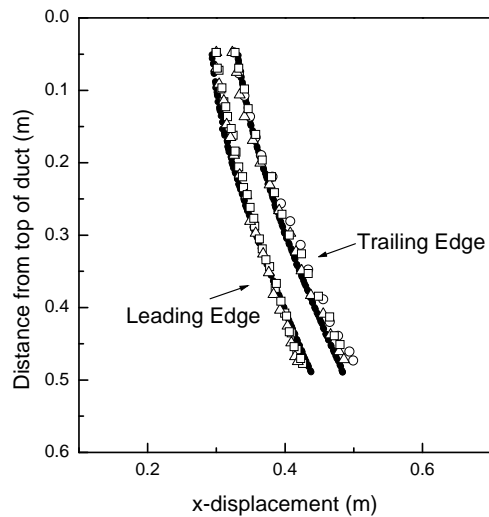


Figure 6.5. Particle curtain trajectories for particle curtain with inlet thickness of 2 cm, solid mass flow rate of 0.040 kg/s, and mean gas velocity of 0.9 m/s (\circ Run 1, \square Run 2, Δ Run 3, \bullet CFD model)⁶⁸.

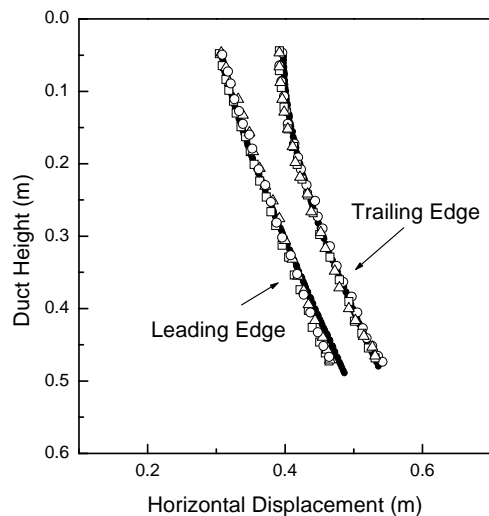


Figure 6.6. Particle curtain trajectories for particle curtain with inlet thickness of 10 cm, solid mass flow rate of 0.040 kg/s, and mean gas velocity of 0.9 m/s (\circ Run 1, \square Run 2, Δ Run 3, \bullet CFD model)⁶⁸.

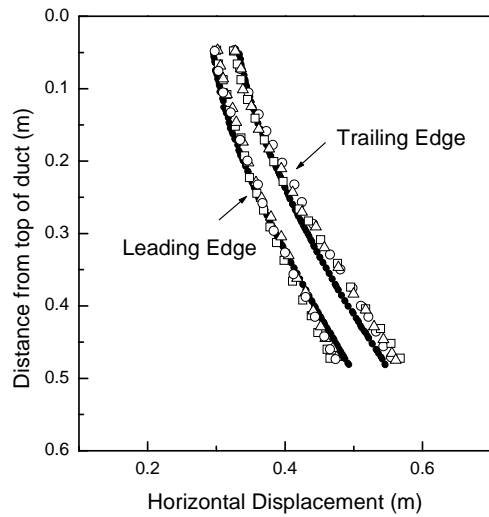


Figure 6.7. Particle curtain trajectories for particle curtain with inlet thickness of 2 cm, solid mass flow rate of 0.040 kg/s, and mean gas velocity of 1.2 m/s (\circ Run 1, \square Run 2, Δ Run 3, \bullet CFD model)⁶⁸.

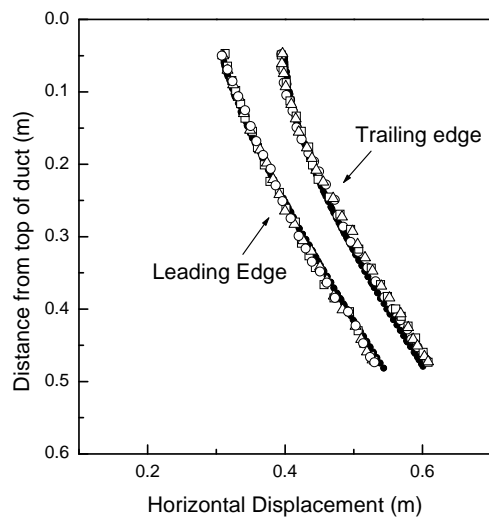


Figure 6.8. Particle curtain trajectories for particle curtain with inlet thickness of 10 cm, solid mass flow rate of 0.040 kg/s, and mean gas velocity of 1.2 m/s (\circ Run 1, \square Run 2, Δ Run 3, \bullet CFD model)⁶⁸.

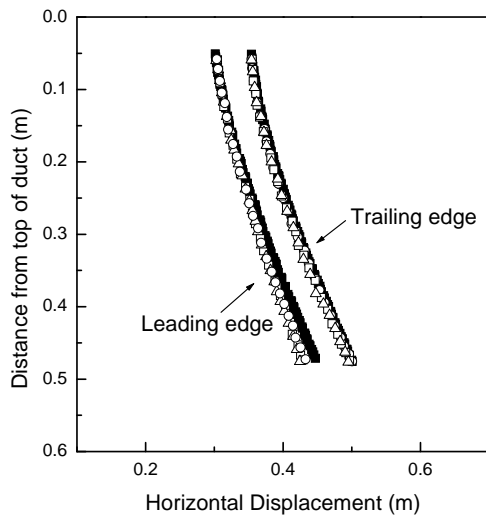


Figure 6.9. Particle curtain trajectories for particle curtain with inlet thickness of 5 cm, solid mass flow rate of 0.047 kg/s, and mean gas velocity of 0.9 m/s (\circ Run 1, \square Run 2, Δ Run 3, \bullet CFD model)⁶⁸.

As can be seen from Figures 6.5 to 6.9, the simulated results compare very well with the experimental results. This demonstrates that CFD is capable of accurately simulating the gas-solids interactions that occur within the falling curtain, allowing predictions of curtain displacement. Figures 6.10 to 6.15 show the comparison between the experimentally measured gas velocity profiles and the model predictions. The match between these results is not as good as for the curtain profiles, however this may be due to errors in the experimental readings. The gas velocity was measured experimentally using a pitot tube located approximately 5 cm beyond the trailing edge of the curtain. Due to the errors involved in locating the trailing edge and accurately positioning the pitot tube at the correct location, it is difficult to determine the accuracy of the gas velocity measurements.

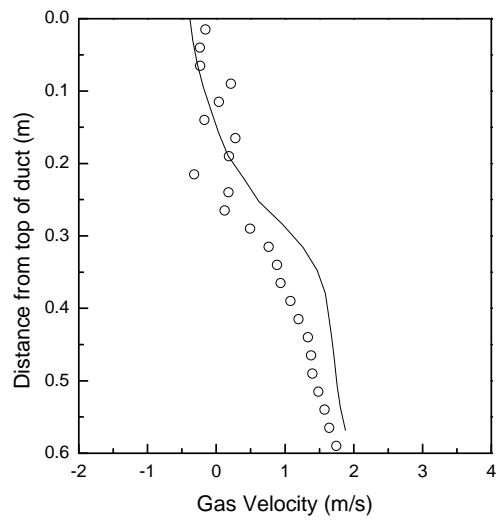


Figure 6.10. Gas velocity profile at the trailing edge for particle curtain with inlet thickness of 2 cm, solid mass flow rate of 0.040 kg/s, and mean gas velocity of 0.9 m/s (○ measured, — CFD model)⁶⁸.

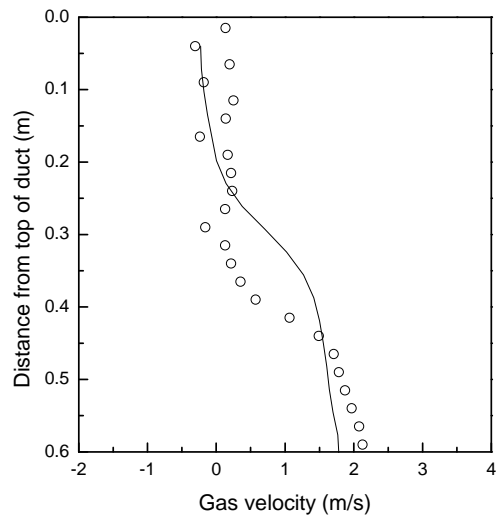


Figure 6.11. Gas velocity profile at the trailing edge for particle curtain with inlet thickness of 10 cm, solid mass flow rate of 0.040 kg/s, and mean gas velocity of 0.9 m/s (○ measured, — CFD model)⁶⁸.

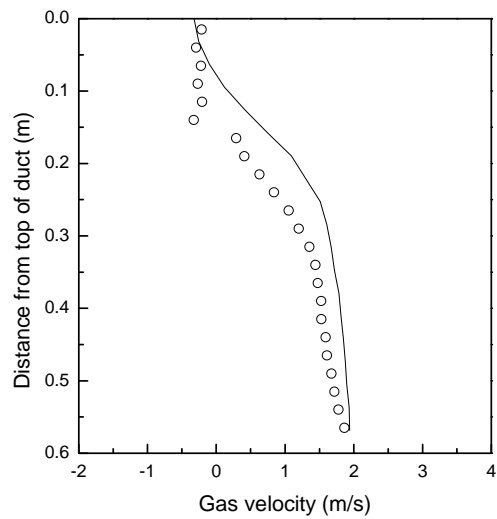


Figure 6.12. Gas velocity profile at the trailing edge for particle curtain with inlet thickness of 2 cm, solid mass flow rate of 0.040 kg/s, and mean gas velocity of 1.2 m/s (○ measured, — CFD model)⁶⁸.

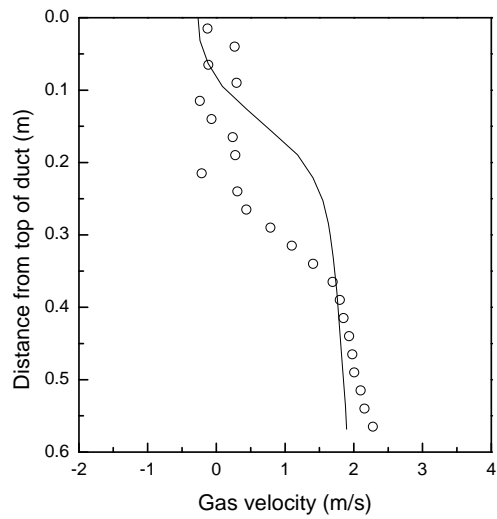


Figure 6.13. Gas velocity profile at the trailing edge for particle curtain with inlet thickness of 10 cm, solid mass flow rate of 0.040 kg/s, and mean gas velocity of 1.2 m/s (○ measured, — CFD model)⁶⁸.

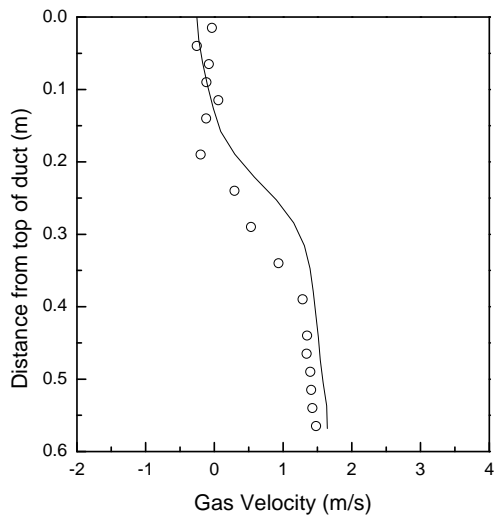


Figure 6.14. Gas velocity profile at the trailing edge for particle curtain with inlet thickness of 5 cm, solid mass flow rate of 0.031 kg/s, and mean gas velocity of 0.9 m/s (○ measured, — CFD model)⁶⁸.

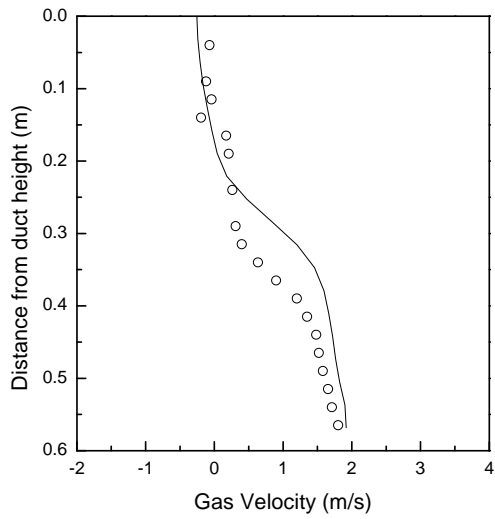


Figure 6.15. Gas velocity profile at the trailing edge for particle curtain with inlet thickness of 5 cm, solid mass flow rate of 0.047 kg/s, and mean gas velocity of 0.9 m/s (○ measured, — CFD model)⁶⁸.

Figure 6.16 shows a colour map profile of the gas velocity along the centreline of the tunnel, showing the entrainment of the gas in the falling curtain. It can be seen that the gas velocity changes very rapidly near the trailing edge of the curtain, thus a small

error in locating the pitot tube could result in a significant change in the measured gas velocity. Given this large potential for error in the experimental results, it is difficult to compare these with the simulated results.

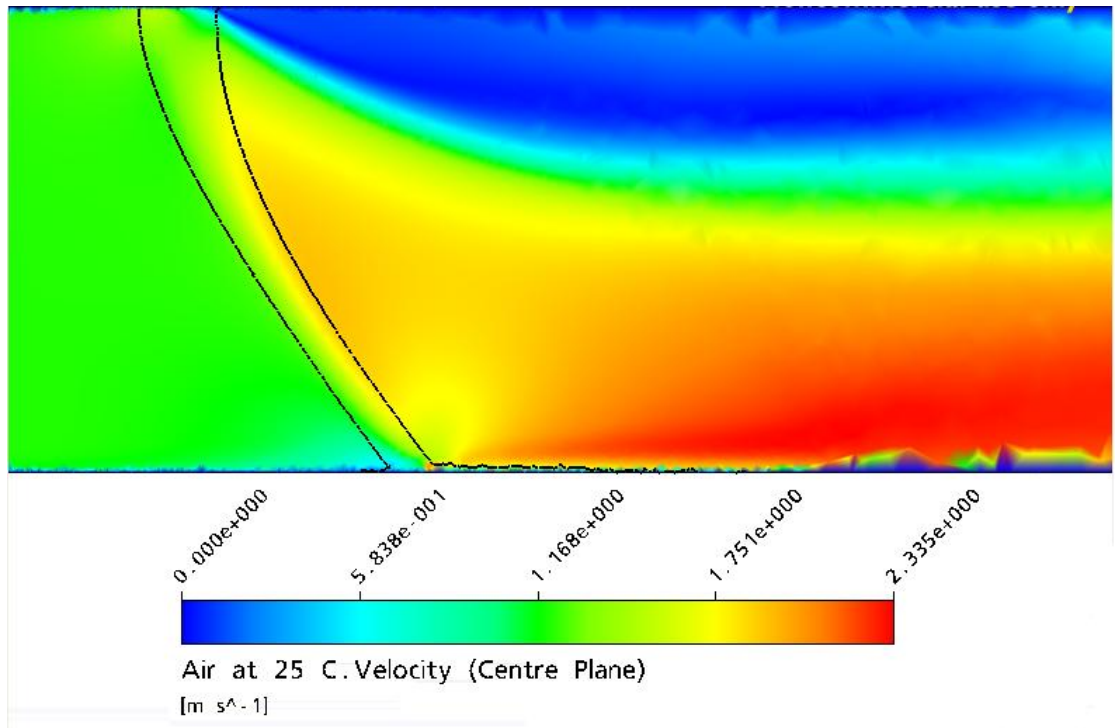


Figure 6.16. Simulated gas velocity profile along the centreline of the tunnel (solids inlet 10cm, 0.070 kg/s and inlet gas velocity 1.2 m/s) with curtain boundaries shown.

Experiments with No Air flow

In addition to studying the displacement of the curtain at different gas velocities, a series of experiments were also conducted without gas flow (see Wardjiman *et al.*⁷⁰ for more details). Figures 6.17 and 6.18 show the results for the experiments and simulation for a solids feed rate of 0.04 kg/s using a 2cm and a 10 cm inlet. It can be seen that with an initial thickness of 2 cm, the solid curtain expands to a thickness of approximately 5 cm, whilst the 10 cm curtain contracts to a similar size. Wardjiman *et al.*⁷⁰ proposed that the shape of the particle curtain was determined by the balance between the particle pressure generated by collisions amongst particles and the pressure difference between the inside and outside of the curtain caused by air pressure reduction within the accelerating suspension

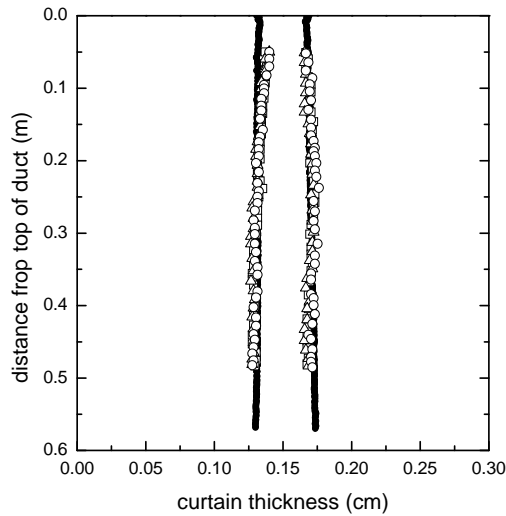


Figure 6.17. Curtain Structure with inlet thickness of 2cm and mass flowrates of 0.040 kg/s (.... CFD, \circ run 1, \square run 2, Δ run 3)⁷⁰.

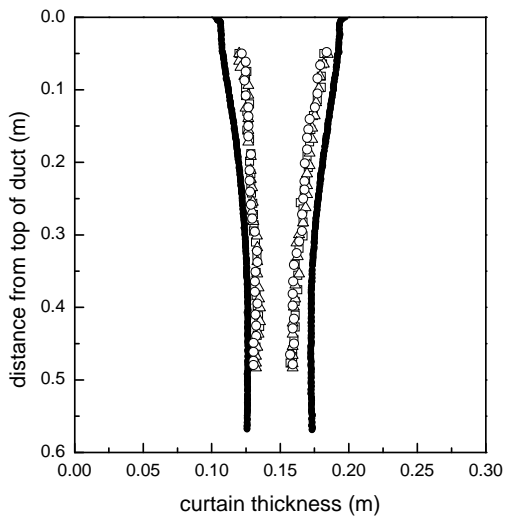


Figure 6.18. Curtain Structure with inlet thickness of 8cm and mass flowrates of 0.040 kg/s (.... CFD, \circ run 1, \square run 2, Δ run 3)⁷⁰.

6.6.1.3. Conclusions

The results discussed above demonstrate that the CFD techniques used to simulate the wind tunnel experiments profile good predictions of the profile of the falling solids curtain. Thus, CFD can be used to give an indication of the displacement of the falling curtain of solids, and thus can be used to determine the axial displacement coefficients.

6.7. CFD Simulation of the Falling Curtain of Solids

The system of gas-solids interactions occurring within a full rotary dryer is extremely complicated, with multiple flights unloading solids at different locations. Each of these individual curtains will have different mass flow rates, particle velocities and solids volume fractions, and the presence of the curtains will affect the flow of gas through the dryer.

To actually model a rotary dryer in operation, complete with moving flights and changing initial curtain conditions, is a difficult task, and one that would require significant computing power. As the aim of the simulations was to gain an approximate value for the axial partitioning coefficients, a series of simpler simulations were conducted rather than simulating the full dryer.

The first series of simulations studied a single curtain of solids falling parallel to a moving gas stream (i.e. a single curtain in isolation). Simulations were conducted to determine the effects of the four most significant factors affecting the displacement of the falling solids; gas velocity, fall height, solids volume fraction and length of curtain. Details of these simulations are given in Chapter 6.7.1. Another series of simulations were conducted using multiple parallel curtains to study how the curtains interacted and affected the displacement of solids, and these are discussed in Chapter 6.7.2.

6.7.1. Single Curtain Studies

In order to achieve meaningful results from the single curtain simulations, it was necessary to determine a set of initial conditions that would represent the average gas-solids interactions for the falling curtain. The curtain conditions for the average fall path of a particle were used, based on the experimental measurements from the flight unloading apparatus and predictions of the geometric unloading model. The experimental results gave an initial curtain width of 18 mm (taken to be the thickness of the moving layer of solids leaving the flight), with an initial particle velocity of 1

m/s. The geometric unloading model predicted a mass flow rate per metre of flight length of 5.18 kg/m·s.

The single curtain studies were simulated in a tunnel 0.8 m long, 0.52 m wide and 2 m tall. Solids were introduced through an 18 mm wide variable length inlet along the centreline of the tunnel, allowing a 0.1 m entry zone for the gas stream. Turbulence was modelled using the k- ε model and a full buoyancy model was used. Drag forces were modelled using the Schiller-Naumann⁴⁴ equation using assuming a particle size of 850 μm (the average particle size of a sugar crystal). Boundary conditions were similar to those used in Chapter 6.6.

Simulations were conducted at a number of different conditions, given in Table 6.1. In order to test the influence of gas velocity on the curtain displacement, simulations were conducted at gas velocities of 0.5 m/s (slow), 1 m/s (normal gas velocity for rotary dryers) and 2 m/s (fast). The effects of changing the mass flow rate (and hence the solids volume fraction) were also tested using mass flow rates of 120% and 80% of the predicted mass flow rate. Finally, the simulations were conducted with 5 different curtain lengths to study how far the moving gas stream penetrated the falling curtain, and how solids displacement varied with curtain length.

Simulation	Gas Velocity (m/s)	Inlet Length (m)	Mass Flow Rate (kg/m·s)
1	2	0.5	5.18
2	1	0.5	5.18
3	0.5	0.5	5.18
4	1	0.5	6.22
5	1	0.5	4.14
6	1	0.4	5.18
7	1	0.3	5.18
8	1	0.2	5.18
9	1	0.1	5.18

Table 6.1. Single curtain simulation conditions.

6.7.1.1. Mesh Dependency

A key aspect in CFD modelling is ensuring that the solution is not mesh dependent. In some situations, generally with very coarse meshes, the solution developed is governed by the mesh structure rather than the Navier-Stokes equations, giving incorrect results. Figure 6.19 shows the results of simulations with the same conditions using three different meshes. As can be seen, there are significant differences between the low resolution mesh (coarse mesh) and the finer meshes, indicating that the mesh is influencing the results. Comparing the two finer meshes, it can be seen that there is little difference between the two, thus the coarser of the two meshes was used to reduce computational requirements.

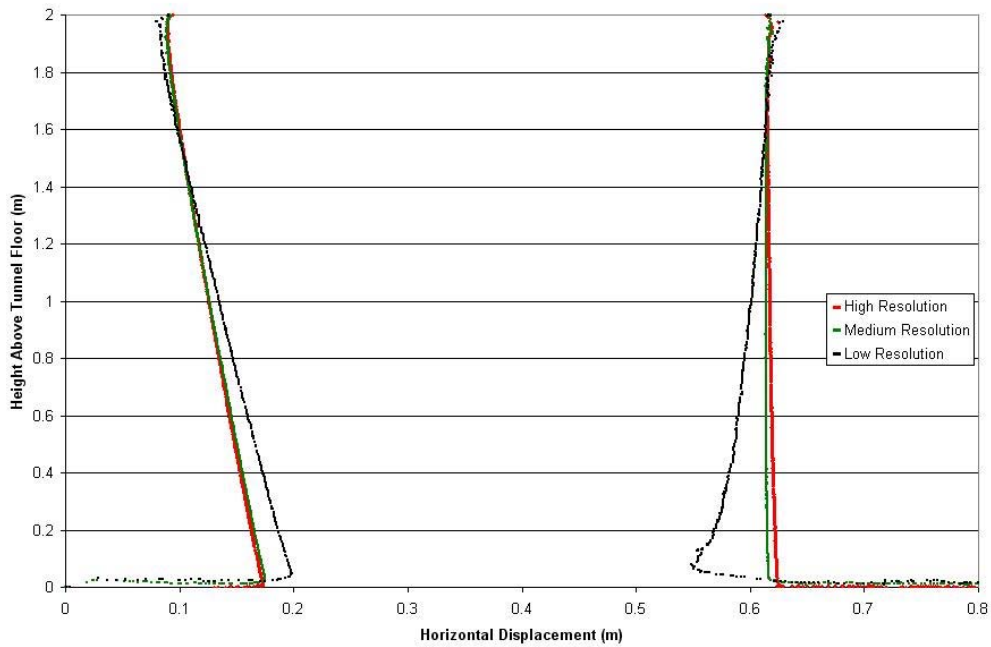


Figure 6.19. Solid curtain profiles using different meshes.

6.7.1.2. Simulation Results

Figure 6.20 shows the simulated results for the curtain profile measured at the centreline of the tunnel, for a 0.5 m long curtain at different gas velocities. It can be clearly seen that the gas velocity has a significant effect on the leading edge of the curtain, with increasing gas velocities causing greater displacement of the solids. At

the trailing edge however, the profile is very similar at both 0.5 m/s and 1 m/s, with the solids falling almost vertically under these conditions. It is only with a gas velocity of 2 m/s that the trailing edge of the curtain is displaced.

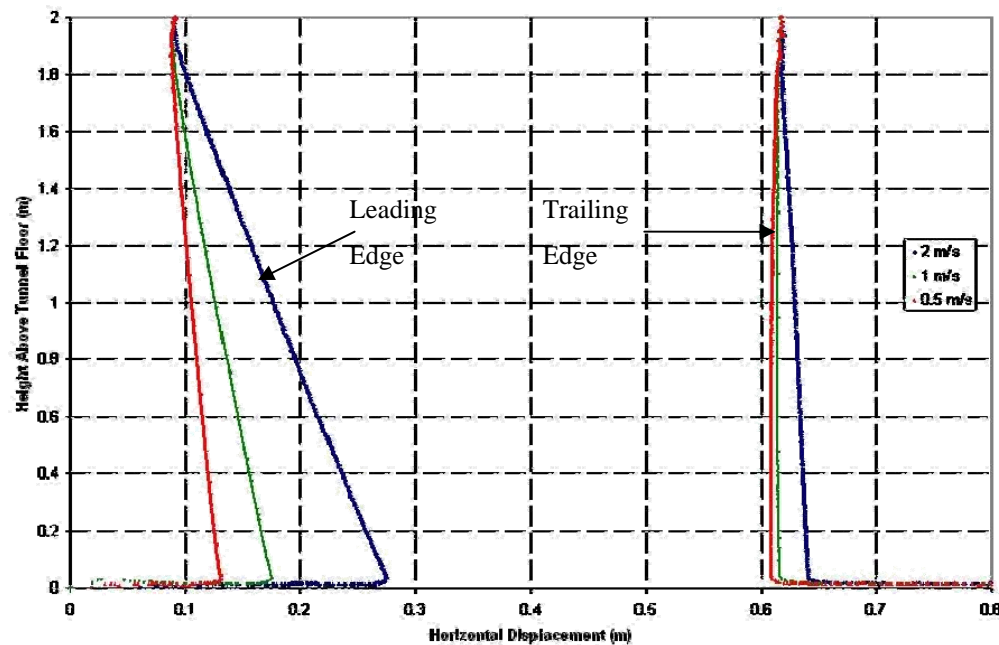


Figure 6.20. Solids curtain profile at different gas velocities.

Figure 6.21 shows a colour map of the horizontal component of the gas velocity for the 1 m/s simulation. These measurements were taken in the horizontal plane at a height of 1 m above the tunnel floor (arbitrarily chosen to illustrate the behaviour of the system), with the gas being introduced from the bottom of the figure. The black line indicates the edge of the particle curtain (defined as a solids volume fraction of 0.43×10^{-3}). Figure 6.21 clearly shows the gas being channelled around the solids curtain, with increases of up to 25% in the gas velocity being observed around the curtain. It can also be seen that the moving gas only penetrating a short distance into the solid curtain, producing an area of negligible horizontal velocity throughout most of the curtain.

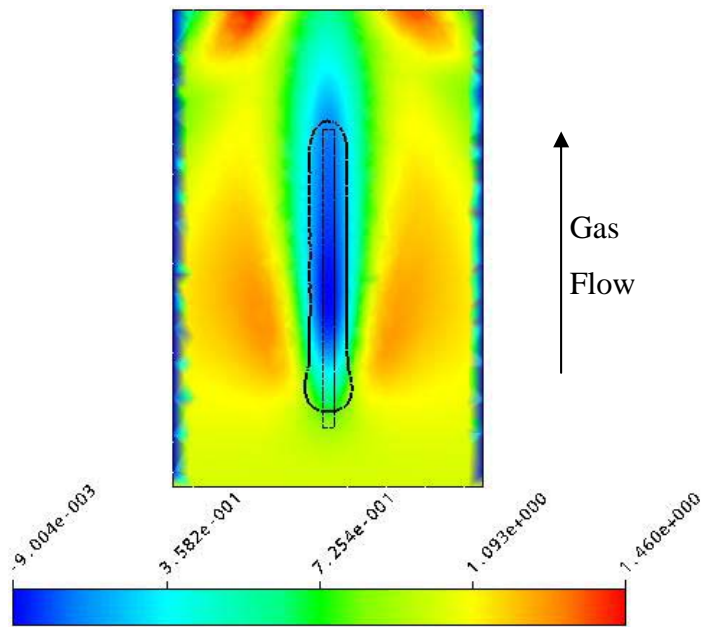


Figure 6.21. Horizontal gas velocity colour map at 1 m above tunnel floor (1 m/s initial gas velocity, 0.5 m inlet, 5.18 kg/m.s solids flow rate). Units are m/s.

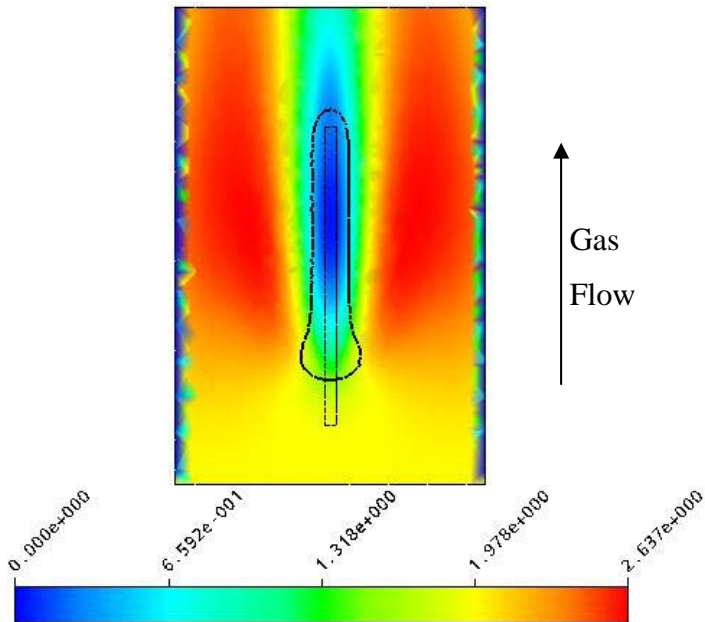


Figure 6.22. Horizontal gas velocity colour map at 1 m above tunnel floor (2 m/s initial gas velocity, 0.5 m inlet, 5.18 kg/m.s solids flow rate). Units are m/s.

Figure 6.22 shows the same measurement as Figure 6.21 for an initial gas velocity of 2 m/s, and again gas velocities up to 25% greater than the initial velocity can be observed. It can be seen that the increased gas velocity has a significant impact on the leading edge of the curtain, causing a noticeable amount of displacement and

compression. It can also be seen that the moving gas penetrates deeper into the curtain than in the 1 m/s simulation, however there is still an area of negligible horizontal gas velocity throughout much of the curtain.

This suggests that the displacement of the solids in a long curtain due to drag would be negligible, as only the first 10-20 cm of the curtain will be displaced. Thus, for long curtains, the gas-solids interactions can be neglected. However, the flights in flighted rotary dryers are generally staggered along the length of the dryer, resulting in a series of offset short curtains. For example, the Invicta Mill dryer number 2 has its flights staggered every 1.133 m along its length. As each curtain is shorter, the effect of the gas-solids interactions is more significant. Additionally, due to the channelling of the gas around the curtains, the next set of curtains will be exposed to a greater initial gas velocity, further increasing the gas-solids interactions.

Figure 6.23 shows the curtain profiles for a 1 m/s gas velocity with different curtain lengths. Looking at the leading edges, it can be seen that they are virtually unaffected by the curtain length, with the exception of the shortest curtain (0.1 m) where the displacement is slightly greater. Similarly, the trailing edges of all simulations except for the 0.1 m inlet experiment show no displacement. In the 0.1 m inlet simulation however, it can be seen that the trailing edge falls vertically for much of the simulation, before being displaced in the lower parts of the curtain. As the trailing edge falls vertically for the first part of the fall whilst the leading edge is displaced, the curtain of solids becomes shorter (in the direction parallel to the gas flow) as it falls. This means that there is less distance for the gas stream to penetrate before it reaches the trailing edge, and eventually, near the bottom of the tunnel, the gas stream penetrates the entire curtain. This results in the displacement of the trailing edge in the lower section of the tunnel. Meanwhile, the longer curtains remain unaffected.

This is illustrated in Figure 6.24 which shows the colour map of the horizontal component of the gas velocity for the 0.1 m inlet experiment, taken at a height of 0.5 m above the floor of the tunnel. In this case, it can be seen that the moving gas stream penetrates all the way through the curtain of solids, resulting in the deflection in the trailing edge. It can be seen, however, that the moving gas stream only just makes it through the solids curtain, thus in the simulations with longer curtains, the gas will not

be able to fully penetrate the curtain, and thus the trailing edge of the curtain will not be displaced.

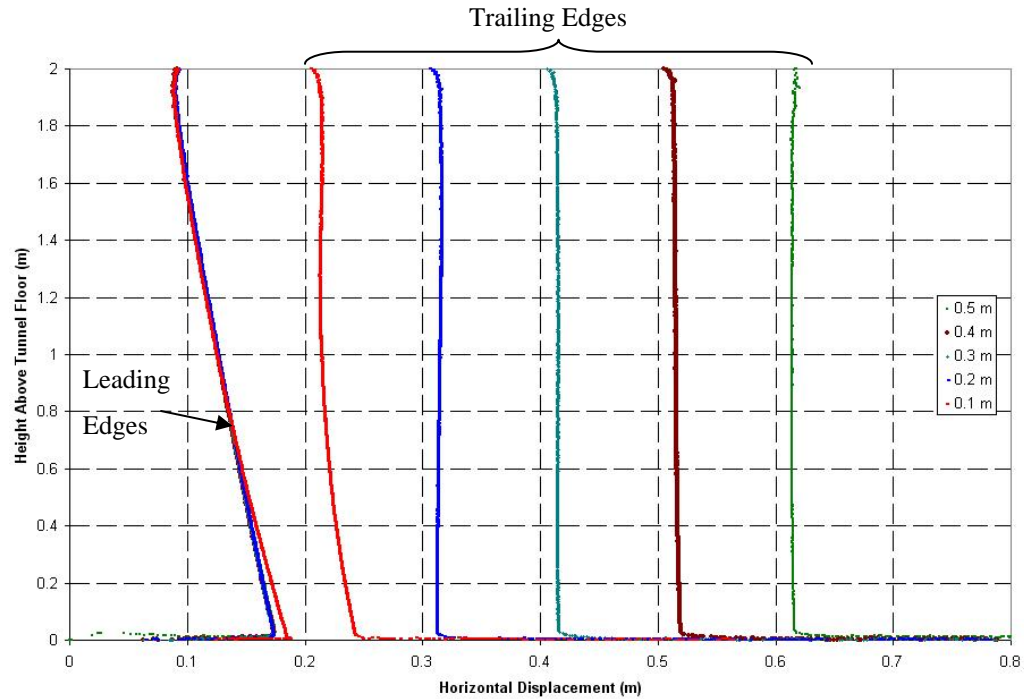


Figure 6.23. Solids Curtain profile at different curtain lengths.

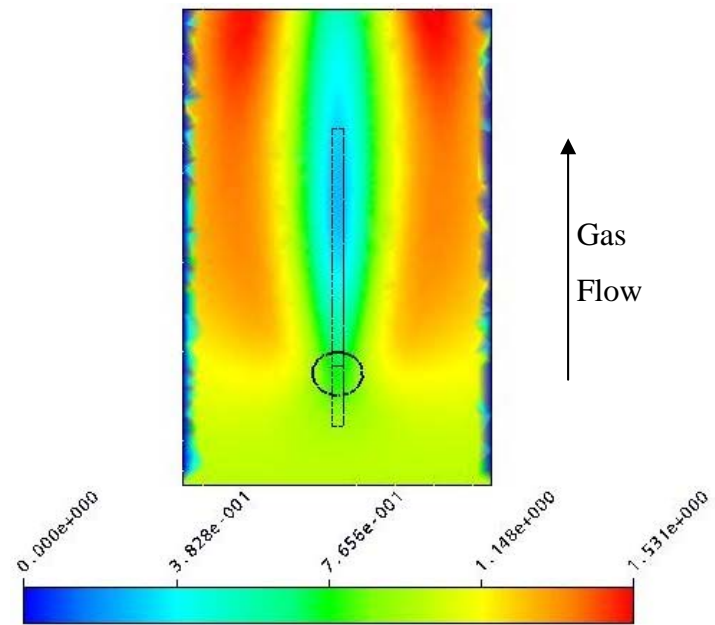


Figure 6.24. Horizontal gas velocity colour map at 0.5 m above tunnel floor (1 m/s initial gas velocity, 0.1 m inlet, 5.18 kg/m.s solids flow rate). Units are m/s.

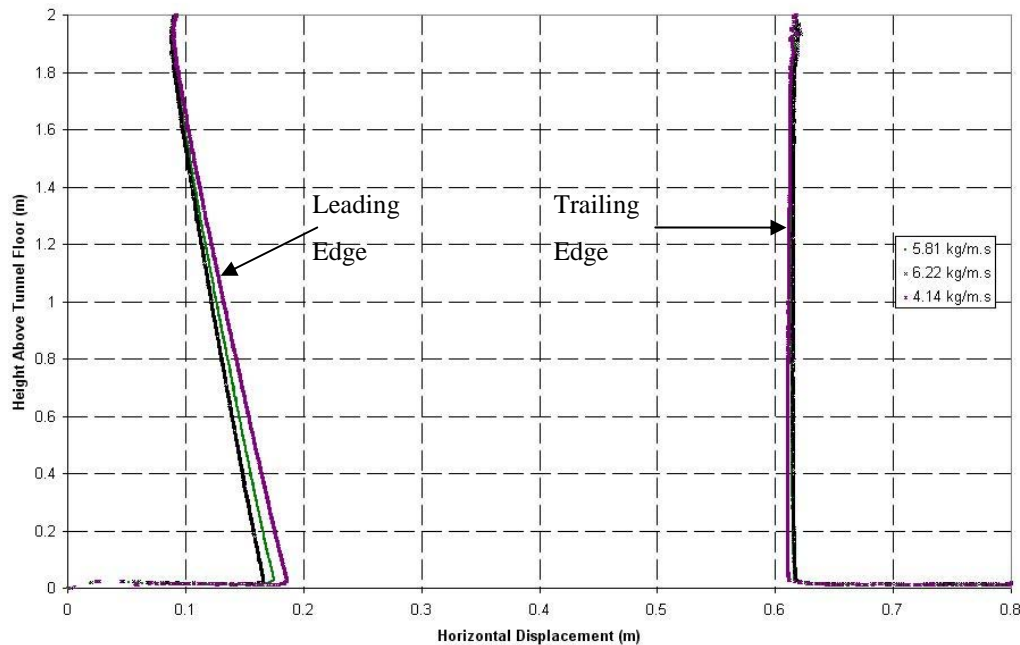


Figure 6.25. Solids curtain profile at different mass flow rates.

Figure 6.25 shows the simulated results of a 0.5 m long curtain in a 1 m/s gas stream with different solid mass flow rates. As decreasing the solids mass flow rate decreases the solids volume fraction in the curtain, it would be expected that this would also result in greater gas-solids interactions. Looking at Figure 6.25, it can be seen that this is indeed the case, with the leading edge of the curtain showing greater displacement with lower solids flow rates. However, the trailing edge appears to be unaffected by the changes in mass flow rate. This indicates that, although the curtain is less dense, the gas stream is still unable to penetrate deeply into the solids curtain.

From the results of these simulations, it is possible to study the trends of the curtain displacement to changes in the gas velocity, curtain thickness and mass flow rate. Figure 6.26 shows the trend in the displacement over a fall of 2 metres of the leading edge of the solids curtain at the gas velocities studied. It can be seen that the curtain displacement is well represented by a second order polynomial, which agrees well with the known fact that drag is proportional to velocity squared. However the small number of points studied makes drawing a solid conclusion impossible. Figure 6.27 shows the trend in the displacement over a fall of 2 metres of the leading edge of the solids curtain for the different solids flow rates studied. It can be seen that the trend in

the displacing does not appear to be linear, however with only three data points it is not possible to determine a more accurate fit to the trend. Looking at Figure 6.23, it can be seen that the curtain thickness has little to no impact on the displacement of the leading edge of the curtain.

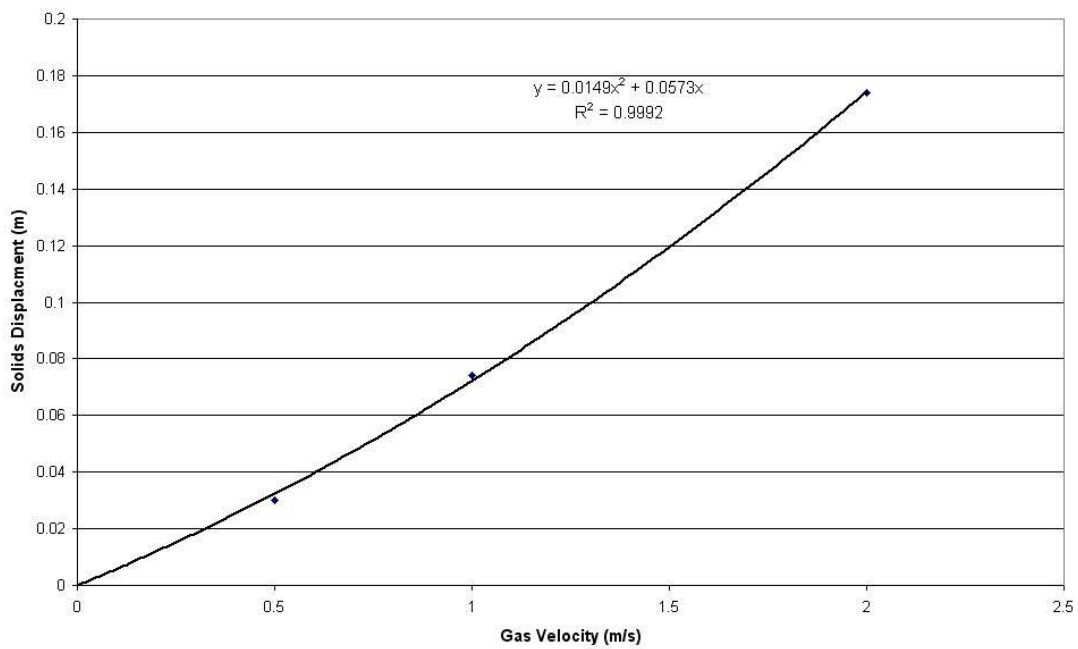


Figure 6.26. Simulated curtain displacement over 2 metres at different gas velocities.

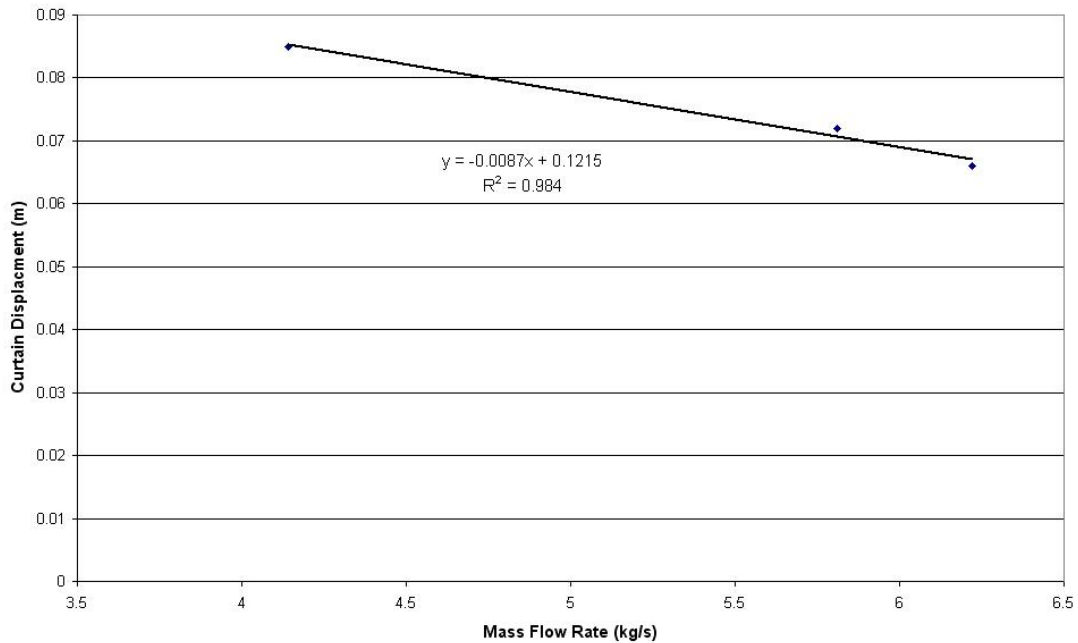


Figure 6.27. Simulated curtain displacement over 2 metres at different mass flow rates.

6.7.1.3. Summary of Single Curtain Simulations

From the results of the simulations discussed above, it is apparent that the most significant factors affecting the displacement of solids in the falling curtain is the gas velocity and the distance the material falls. These two factors show the most significant change in curtain displacement, however these effects are primarily restricted to the leading edge of the curtain. The simulated results suggest that the trailing edge of any curtain longer than 0.5 m will be unaffected by any of the changes studied here.

These observations would suggest that the gas-solids interactions have a negligible effect on the solids transport that occurs within the dryer, with drag forces only having an impact at the very beginning of the curtain. However, as most flighted rotary dryers use staggered flights, the active phase will consist of many short curtains. Each curtain will be exposed to the moving gas stream, and therefore undergo displacement. Also, as the gas is channelled around each curtain, the curtains within the dryer will be exposed to an increased gas velocity, resulting in greater displacement of solids. Thus, the displacement of solids that occurs within a dryer will be greater than that observed in these simulations.

However, the displacement of the solids due to gas-solids interactions still appears small in comparison to the gas-solids interactions reported in literature⁴⁵. The most probable reason for this is the initial conditions of the curtain. In these simulations, the initial conditions were taken using data from the flight unloading apparatus with an unserrated flight. However, most industrial dryers use serrated flights, which create a broader, but significantly less dense curtain. This reduced density will allow greater gas-solids interaction, as shown in Figure 6.25, and thus greater displacement of solids. Another possible factor affecting the results is the interactions between curtains. As can be seen in Figures 6.21, 6.22 and 6.24, the solid curtain causes the gas to be channelled around the curtain. In a system of multiple curtains however, there will not be as much room available for channelling as in the single curtain experiments, which may cause greater interactions between the gas and solids. This will be studied in the next section.

6.7.2. Multiple Curtain Studies

The phenomenon of channelling of the gas flow around the falling curtains in a rotary dryer was first considered by Baker⁴⁵ as part of his studies into the gas-solids interactions. Given that the falling curtain represents impedance to the gas flow, it is logical that the gas flow would try to bypass the obstacle. This effect was apparent in the single curtain simulations discussed previously, where the gas flow was channelled around the side of the falling curtain, resulting in increases in gas velocities of up to 25%.

In a system of multiple curtains, the gas flow should be channelled between curtains, resulting in channels of high gas velocity which may influence solid particles at the edges of the curtain. In order to study this, a number of simulations were conducted using multiple curtains with different spacings between curtains.

These simulations were conducted using the average particle curtain properties used for the single curtain simulations for all curtains. This does not accurately represent the conditions within an actual rotary dryer, however should be sufficient to examine the interactions of multiple curtains, and suitable for the middle of the unloading profile, where the unloading rate is reasonably constant (see Figure 5.39 for example). The simulations were conducted using a tunnel 500 mm high, 340 mm across and 800 mm long. The smaller system (compared to the single curtain simulations) was used due to the extra width of the tunnel required to accommodate multiple curtains and the greater mesh requirements. Solids were introduced along the top of the tunnel starting 100 mm from the gas inlet, and allowing 200 mm between the end of the inlet and the end of the tunnel. The tunnel was discretised with an 8.4 mm tetrahedral mesh across the entire tunnel, resulting in 368,780 nodes.

Four simulations were run with curtain spacings varying between 50 mm and 80mm. Curtains were equally spaced across the tunnel, with the two outermost curtains extended to reach the wall to prevent gas from being channelled along the wall without affecting the curtain. Due to the fixed size of the tunnel, the constant curtain spacing meant that the number of curtains present in the simulations also varied with

curtain spacing. Table 6.2 shows the curtain spacing and number of curtains present in each simulation.

Simulation	Curtain Spacing	Number of Curtains
1	50 mm	3
2	60 mm	3
3	70 mm	2
4	80 mm	2

Table 6.2. Multiple curtain simulation conditions.

Figures 6.28 to 6.31 show the simulated solids volume fraction at a horizontal cross-section 0.25 m above the floor of the tunnel (halfway through the fall) for the different curtain spacings. The black boxes show the location of the solid inlets. As can be seen, with a curtain spacing of 50 mm, the curtains have merged to form a single broad curtain, and as the curtain spacing increases, individual curtains begin to become apparent.

This agrees well with the results reported by Wardjiman *et al.*⁴⁷ and the wind tunnel experiments conducted with no air flow discuss in Chapter 6.6.1.2. In these experiments, it was observed that falling curtains of solids with high solids volume fractions tended to expand until a stable state was reached. Wardjiman *et al.*⁷⁰ proposed that this was due to the difference in pressure inside the curtain compared to outside, causing the curtain to expand until the pressures equalised. This explains the expansion of the curtains observed in the multiple curtain simulations, resulting in the merging of the curtains into a single curtain if the curtain spacing is small enough.

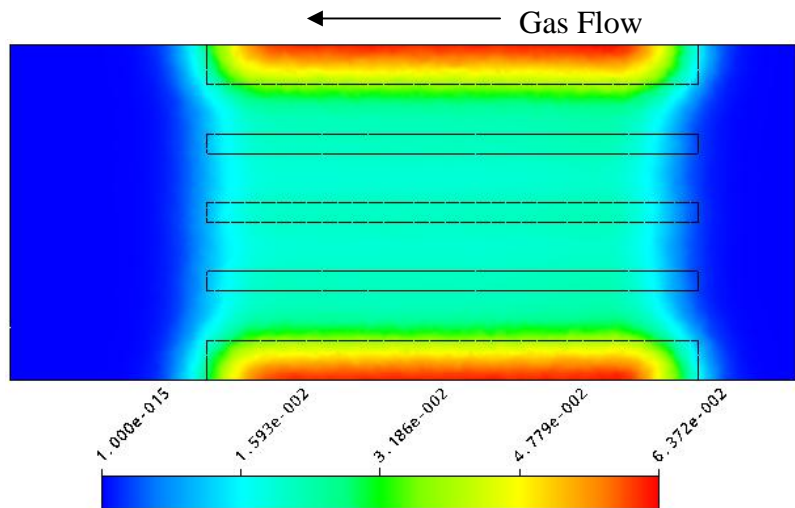


Figure 6.28. Solids volume fraction colour map at 0.25 m above tunnel floor with 50 mm curtain spacing.

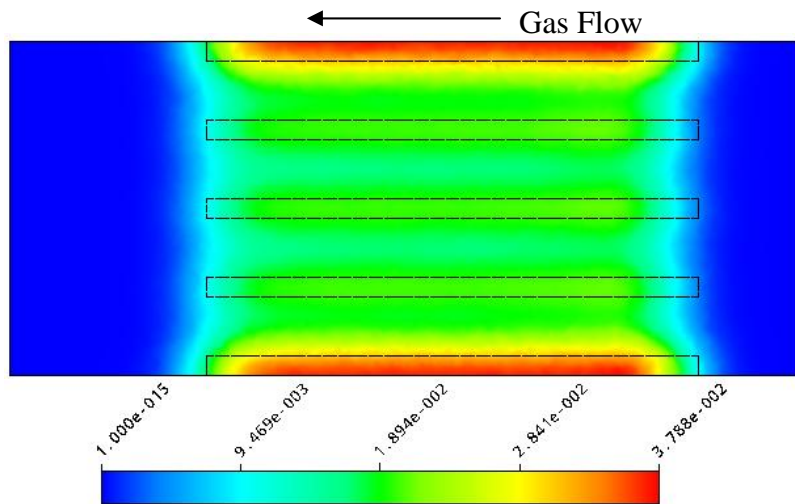


Figure 6.29. Solids volume fraction colour map at 0.25 m above tunnel floor with 60 mm curtain spacing.

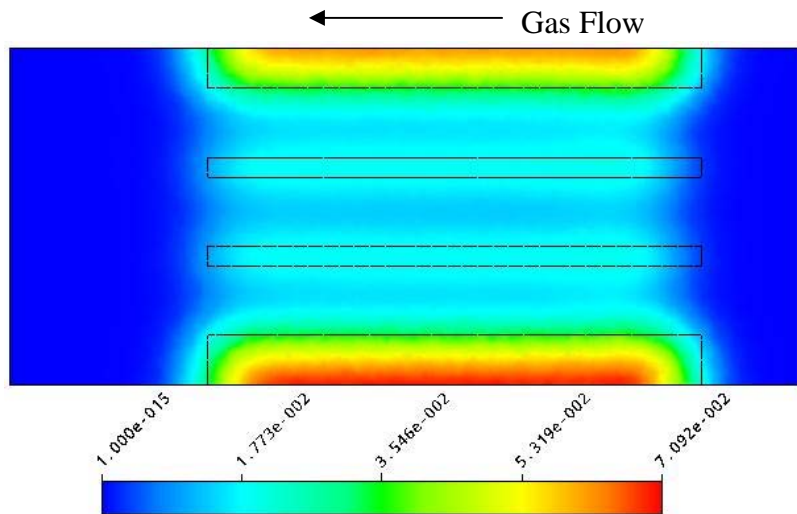


Figure 6.30. Solids volume fraction colour map at 0.25 m above tunnel floor with 70 mm curtain spacing.

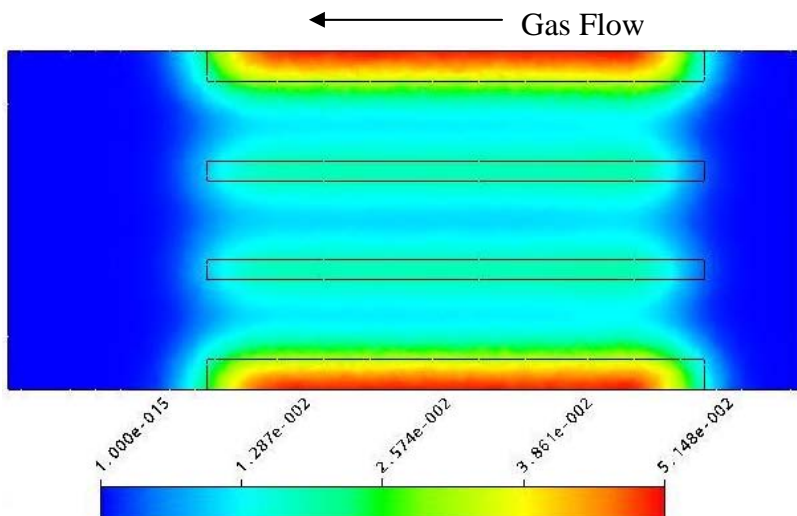


Figure 6.31. Solids volume fraction colour map at 0.25 m above tunnel floor with 80 mm curtain spacing.

This means that at low curtain spacings, where the curtains have merged into a single uniform curtain, that the gas flow through the curtain should be uniform, as there are no regions of lower solids volume fraction for the gas to be channelled through. As the curtain spacing increases, and individual curtains become distinct, the regions of lower solids volume fraction between the curtains will allow for the gas to be channelled through these regions. This effect is seen in Figures 6.32 to 6.35, which show the gas velocity profile at the same cross-section of the tunnel. The thick black line indicates the contour of a solids volume fraction of 4.3×10^{-3} .

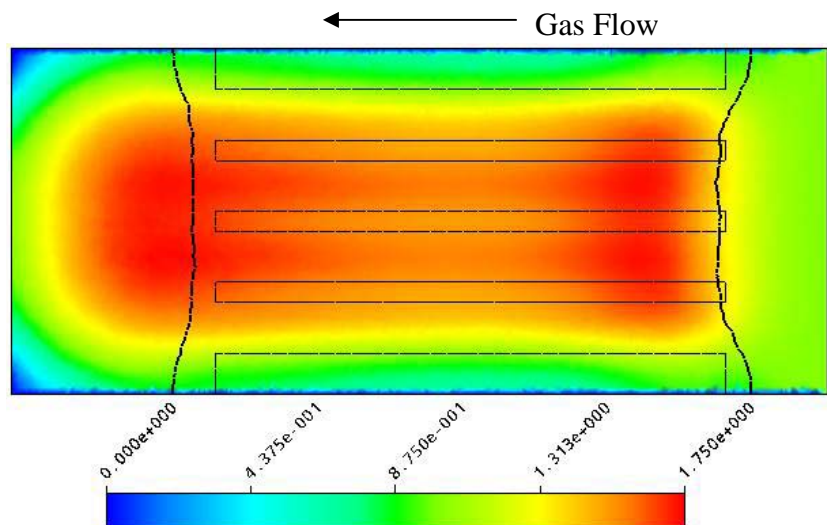


Figure 6.32. Horizontal gas velocity colour map at 0.25 m above tunnel floor with 50 mm curtain spacing. Units are m/s.

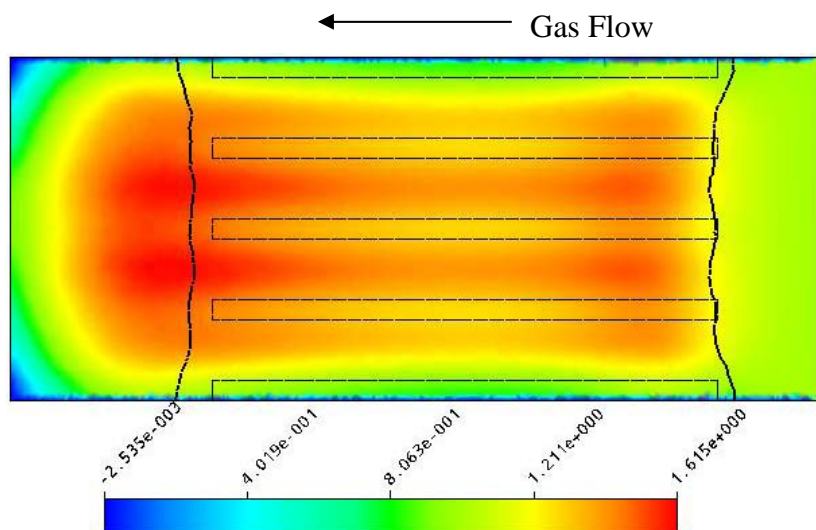


Figure 6.33. Horizontal gas velocity colour map at 0.25 m above tunnel floor with 60 mm curtain spacing. Units are m/s.

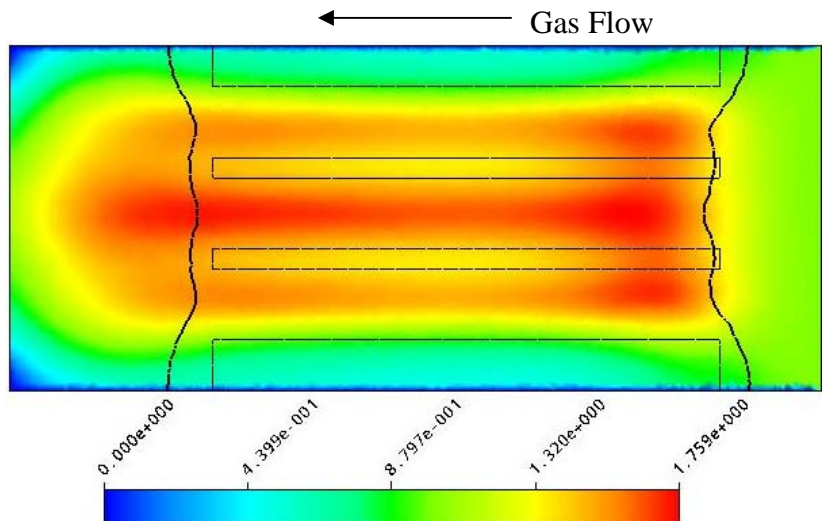


Figure 6.34. Horizontal gas velocity colour map at 0.25 m above tunnel floor with 70 mm curtain spacing. Units are m/s.

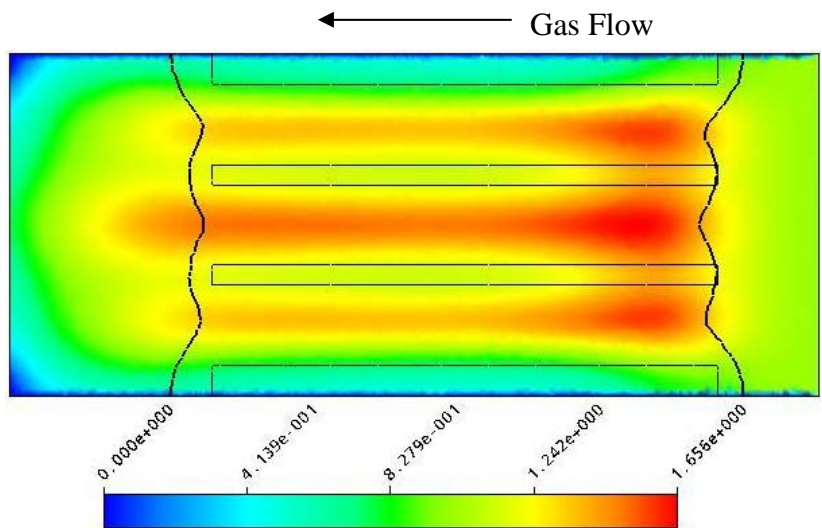


Figure 6.35. Horizontal gas velocity colour map at 0.25 m above tunnel floor with 80 mm curtain spacing. Units are m/s.

As can be seen in Figures 6.32 to 6.35, the amount of channelling of gas flow between the curtains increases with increasing curtain spacing, as was expected. At a curtain spacing of 50 mm and a fall height of 0.25 m, the gas velocity through the combined curtains is close to uniform, whilst at a curtain spacing of 80 mm significant channelling of the gas flow can be seen. In these simulations, it can be seen that there is significant gas velocity within the curtains, unlike the single curtain experiments where the gas velocity within the curtain was negligible.

This increased gas velocity within the falling curtain of solids should result in an increased displacement of the solids compared to the single curtain simulations, as is shown in Figure 6.36. Figure 6.36 shows the profile of the falling curtain, defined by a solids volume fraction of 4.3×10^{-3} , for the different simulations compared to the single curtain simulation with the same initial conditions. The curtain profile was measured along the centreline of one of the solid inlets.

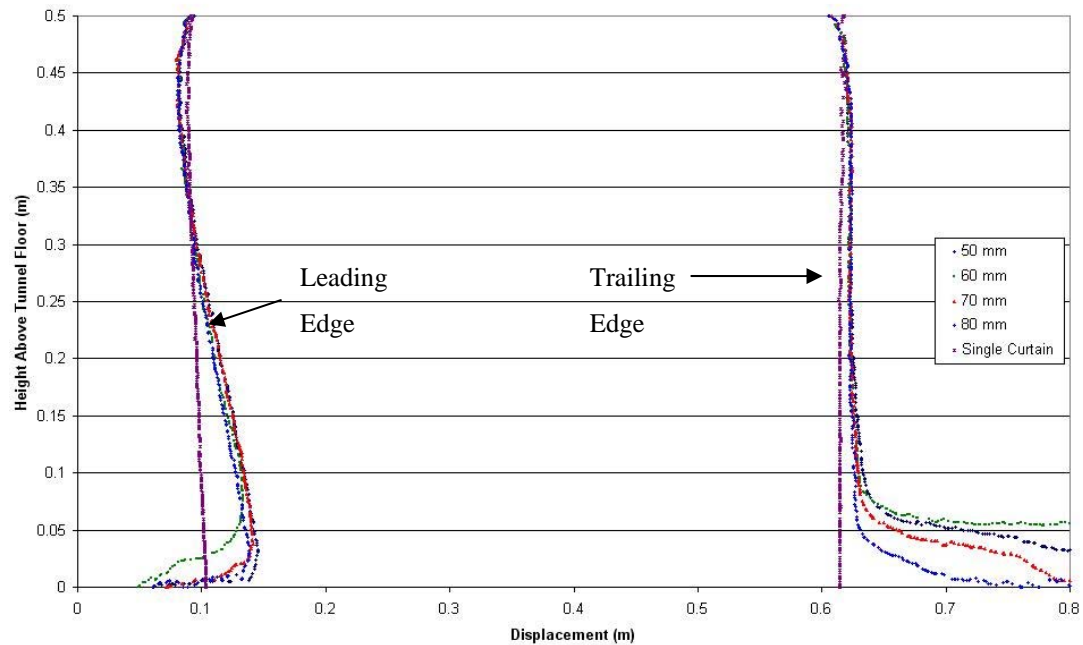


Figure 6.36. Plot of curtain profiles for different curtain spacings.

It can be clearly seen that the single curtain simulation predicts less displacement of the solids curtain, due to the channelling of the gas flow around the curtain. Interestingly, curtain spacing appears to have a minimal impact on the displacement of the solids, despite the different gas flow profiles observed. This is understandable for the leading edge of the curtain, where the solids are exposed to the full gas velocity, however, given the variation of gas velocity within the curtain, one would expect the trailing edges to show different extents of displacement.

More generally, it can be seen that the effects of the gas-solids interactions occur primarily at the leading edge of the curtain, with a significant displacement of solids

being observed. However, the trailing edge shows only a small amount of displacement, indicating that backmixing is negligible.

6.8. Conclusions

Whilst it has been demonstrated that CFD techniques are capable of accurately simulating the behaviour of a falling curtain of solids in a moving gas stream, further work is required before an accurate simulation of the gas-solids interactions within a rotary dryer can be developed. The results of the simulations discussed above suggest that the gas-solids interactions have a negligible effect on the solids transport in a rotary dryer, which is at odds with past research.

It is believed that the main cause of this is due to the effects of serrated flights. Most industrial dryers use serrated flights, which result in more dispersed, and hence less dense, curtains of solids. This in turn allows for greater interaction between gas and solids, and hence greater displacement of the solids. The simulations conducted in this study used data measured from unserrated flights, resulting in thinner, more dense curtains, leading to the under prediction of solids displacement. An experimental study of the unloading behaviour of serrated flights is necessary in order to develop a better model for the gas-solids interactions.

7. Dryer Model Verification and Validation

7.1. Parameter Estimation

The experimental data used to validate the solids transport model came from a tracer experiment conducted by Monro^{10, 14} on CSR's Invicta Mill dryer number 2, a full-scale counter-current industrial sugar dryer. The Invicta Mill dryer processes approximately 100 tons per hour of raw sugar from 0.2 wt% to 0.02 wt% of moisture. The dryer is 12 m long and 5 m in diameter, and the flights are serrated, two-section flights, with the dimensions of these are given in Table 4.1. The normalised tracer concentration curve from this experiment is shown in Figure 7.1.

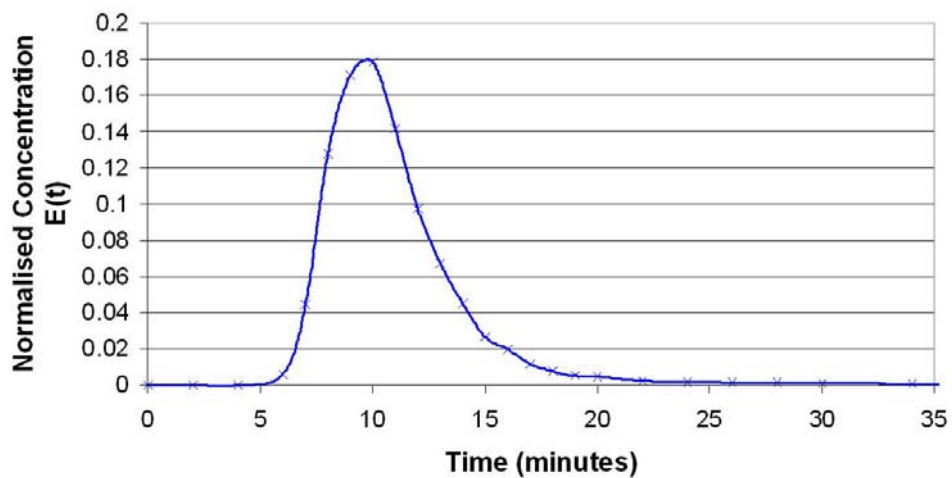


Figure 7.1. Experimental tracer data from Invicta Mill dryer number 2 (Monro¹⁰)

The solids transport model developed in this thesis has four parameters that need to be determined using experimental data. These are;

1. the number of cells, N , used to represent the dryer,
2. the kilning phase residence time, t_{kiln} ,
3. the reduction in the forward step of the solids due to drag, C_F^G , and,
4. the backmixing of solids due to drag, C_B .

Each of these parameters are described in Chapter 3.

Parameter estimation in gPROMS[®] was used to estimate values for the four undetermined parameters using the conditions and tracer data from the experimental results from Monro^{10, 14} (shown in the gPROMS[®] Experiment Entity in Chapter 10.4). Parameter estimation in gPROMS[®] uses a maximum likelihood objective function, which attempts to determine values for the unknown parameters in order to maximise the probability that the mathematical model will predict the values obtained from the experiments. Details of this process are given in the gPROMS[®] Advanced Users Guide⁵¹.

gPROMS[®] also allows the user to specify a variance model for the parameter estimation procedure. As all experimental data will have measurement errors associated with it, it is important to consider this when fitting a model to the data. The variance model describes the experimental error associated with the experimental data, and allows the user to describe the amount of error present. A number of different variance models are available in gPROMS[®], and based on the methods used to obtain the experimental data, it was decided that a constant variance model best described the error in these measurements. For this variance model, a single standard deviation is used to describe the experimental error for each data point. An initial guess and upper and lower limits for the standard deviation are required, and the values used in this thesis were an initial guess of 1 and upper and lower limits of ± 10 . The gPROMS[®] parameter estimation entity for the model is given in Chapter 10.3. Further description of the variance models are given in the gPROMS[®] Advanced Users Guide⁵¹ and details of the gPROMS[®] parameter estimation code used in this thesis are shown in Chapter 10.3.

One important factor with using gPROMS[®] however is the fact that the number of dryer slices used (N) cannot be estimated by gPROMS[®], as it is a structural parameter of the model and cannot be changed during a run. Thus, a series of parameter estimations were conducted using different values of N in order to determine the best fit to the experimental data.

A number of difficulties were encountered with trying to estimate the values for the model parameters using gPROMS[®] due to the complexity of the model. The most significant of these was due to the relationship describing the loading conditions in the dryer (i.e. d_{load} and f_{load}). It is believed that the conditional statements in gPROMS[®] required to limit f_{load} to values between 0 and 1 caused problems with the parameter estimations. Given that the Invicta mill dryer was known to be operating in overloaded conditions, where $f_{load} = 1$, this part of the model was removed to allow the parameters to be estimated. Examination of the simulated data from the fitted model later confirmed that $f_{load} = 1$.

In addition, it was found that the parameter estimation was extremely sensitive to the initial guesses provided for the three parameters. If the initial guesses were not close to the final solution, the estimation procedure would either fail outright, or get caught in a loop. In order to use the parameter estimation process, it was first necessary to manually adjust the model parameters until the simulated results were close to the experimental curve. As a general guideline, the values of the initial guesses used in this thesis were; $t_{kiln} = 8.5$, $C_B = 0.65$ and $C_F^G = 0.33$. This might suggest that these values represent a local minima, rather than the global minima, however using different boundary conditions could not produce a fit to the RTD.

7.1.1. Dryer Geometry and Material Properties

A number of the model parameters are set using the dimensions of the drier and the material properties of the solids (dynamic angle of repose and bulk density). Most of the dimensions of the Invicta drier are well known, however the solids properties within the dryer are not so well known, and need to be discussed here.

7.1.1.1. Flight Serrations

The flights used in the Invicta drier were serrated, thus the flight tip length, s_2 , (see Figure 4.1) is not constant along the flight. This aspect of flight unloading was not studied in this thesis, and previous work, such as Pugh⁷¹, was inconclusive in this

regard. Researchers and industry have generally assumed that the flight tip length can be accurately modelled using an area averaged approach⁵². In this approach, the total area of the serrated flight tip surface is calculated, and used to calculate an effective flight tip length. This is shown in Equation 7.1 for flights with triangular serrations, where $s_{2,eff}$ is the effective flight tip length, s_w and s_d are the width and depth of the triangular serrations respectively and n_s is the number of serrations per metre of flight.

$$s_{2,eff} = s_2 - \frac{1}{2} s_w s_d n_s$$

Equation 7.1. Calculation of effective flight tip length.

7.1.1.2. Solids Density

The material properties of the solids however are less well known, and were not measured during the experimental testing by Monro¹⁰. The bulk density of raw sugar is well tabulated in literature and is generally reported to be approximately 850 kg/m³. This however is the unconsolidated bulk density, whereas the experiments conducted in Chapter 5.4.3.1 show that the operation of a flighted rotary dryer is best characterised using the consolidated bulk density. Thus, a simple laboratory experiment was conducted to measure the consolidated and unconsolidated bulk density of commercial raw sugar using the method outlined in Chapter 5.3.1. The results of this experiment are shown in Table 7.1. As can be seen, the experimentally measured value for the unconsolidated bulk density agrees very well with the tabulated value. The consolidated bulk density of 936 kg/m³ was used in the solids transport model.

Unconsolidated Bulk Density	Consolidated Bulk Density
844.73±0.01 kg/m ³	936.06±0.01 kg/m ³

Table 7.1. Bulk densities of raw sugar.

7.1.1.3. Solids Dynamic Angle of Repose

Implementing an accurate dynamic angle of repose of the solids is somewhat more difficult, as it is known that it varies along the length of the dryer as the material is dried. Physical measurement of the dynamic angle of repose along an industrial sugar drier is extremely difficult due to the size of the driers, and the fact that raw sugar undergoes rapid heat and mass transfer. For the parameter estimations in this thesis, the approach used by Britton *et al.*⁷² was taken. Britton *et al.*⁷² measured the dynamic angle of repose of raw sugar in a trommel at two moisture contents, and assumed that the dynamic angle of repose was linearly related to moisture content. The relationship developed by Britton *et al.* is shown in Equation 7.2⁷², where the dynamic angle of repose is measured in degrees and w is the moisture content measured in kg moisture per kg solids.

$$\phi = 1222.2w + 34.5$$

Equation 7.2. Relationship between dynamic angle of repose and solids moisture content⁷².

7.1.1.4. Solids Moisture Content

In order to use Equation 7.2, it is necessary to know the moisture content profile along the drier. Generally, only the inlet and outlet moisture contents are known, due to the difficulties in measuring the material properties within the drier, as is the case in the experiment conducted by Monro¹⁰. As the moisture content of the solids will change along the length of the dryer due to heat and mass transfer, it is necessary to assume a moisture content profile for the dryer. Britton *et al.*⁷² and others have assumed that the solids moisture content varied exponentially along the length of the dryer, as shown in Equation 7.3, and this was used in this thesis for the parameter estimations. This assumption agrees well with experimental results reported by Pope⁷³ and modelled moisture profiles of Sheehan and Schneider⁷⁴.

$$w_i = w_{inlet} e^{\ln(w_{outlet}/w_{inlet}) \times \frac{i-1}{N-1}}$$

Equation 7.3. Assumed moisture content function.

7.1.2. Estimated Parameter Values

Values of the three non-structural parameters (t_{kiln} , C_B and C_F^G) were estimated for a range of values of N . The fitted RTD curves are shown in Figure 7.2, and it can be seen that the value of N has little effect on the accuracy of the fit. Close inspection of the predictions reveals that higher values of N provide a slightly better fit to the experimental data, however this is a very minor effect and the model can be considered insensitive to N . Table 7.2 shows the estimated values for the model parameters for the different values of N . The range of values for N presented here represent the range across which the model was able to fit the experimental data. For values of N above 35 or below 30, the model was incapable of fitting the experimental RTD.

N	t_{kiln} (s)	C_B	C_F^G
30	9.95	0.41	0.11
31	10.04	0.47	0.34
33	9.28	0.57	0.41
35	8.69	0.68	0.48

Table 7.2. Estimated parameter values.

Whilst increasing N provides a slightly better fit to the experimental RTD, there is a physical limitation on the maximum value of N . As discussed in Chapter 3.1.3, the model structure limits the upper value of N such that the maximum distance material can be transported forwards in one fall does not exceed the length of a single cell. For the Invicta dryer, this limits N to be less than or equal to 35.

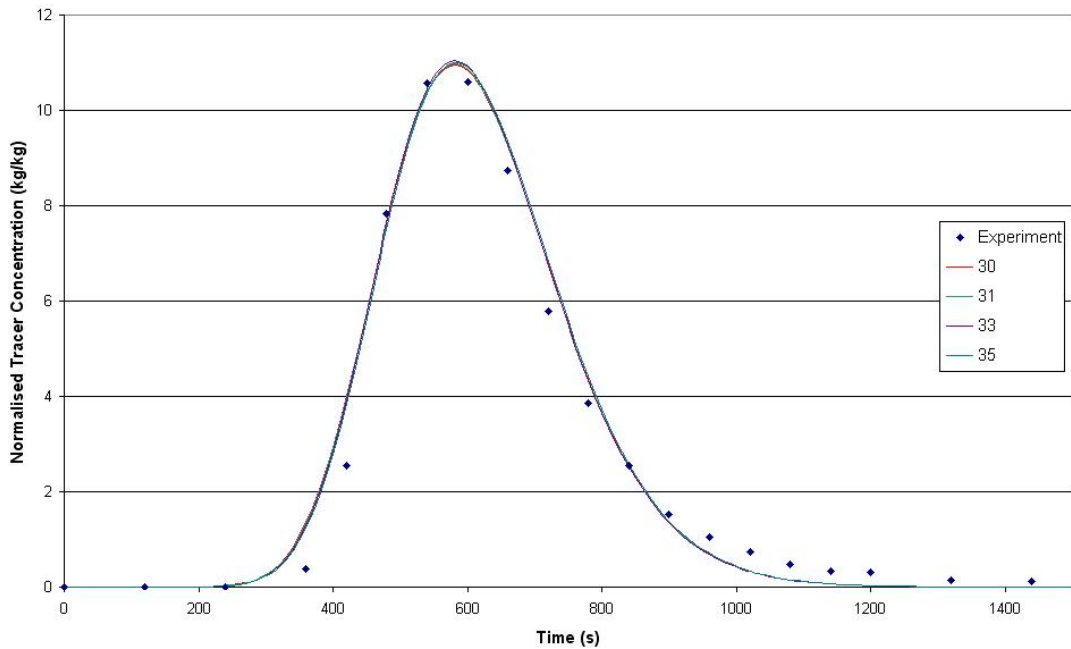


Figure 7.2. Predicted RTD curves at different values of N .

Studying the fit of the model predictions to the experimental data, it can be seen that the fit is generally very good. Overall, the solids transport model closely matches the shape of the experimental curve, however the model can not fully reproduce the initial steep rise of the RTD or the elongated tail. Given that previous researchers have reported that similar models can provide more accurate representations of the experimental data (for example Britton *et al.*⁷²), further investigation of this is necessary.

In order to quantitatively examine the accuracy of the model fit to the experimental data, the mean residence time, standard deviation and skewness of the simulated RTD were calculated for each value of N and compared to those of the experimental curve, as shown in Table 7.3. As can be seen, the simulated values are noticeably different to those of the experimental RTD, with the values calculated from the model parameters being lower than those of the experimental data, especially the standard deviation and skewness. This is primarily due to the extended tail in the experimental results, which is not reproduced by the model. The tail of the RTD serves to increase all three moments of the RTD, thus accounting for the differences observed in Table 7.3.

	Mean Residence Time (min)	Standard Deviation (min)	Skewness (min)
Experiment	11.08	6.73	0.584
$N = 30$	10.28	2.28	0.151
$N = 31$	10.28	2.28	0.151
$N = 33$	10.29	2.27	0.152
$N = 35$	10.32	2.27	0.152

Table 7.3. Comparison of moments of the RTD.

Looking at the trends in the moments of the simulated RTDs shown in Table 7.3, it can be seen that all three moments are insensitive to the value of N . This reinforces the observation that the match between the model and the experimental data is independent of N .

7.2. Physical Realism of Results

Whilst a match to the experimental RTD is an important step in developing a solids transport model, it is possible for the model to provide a good match to the data without having any physical meaning. For example, the model of Lee *et al.*³⁷ provided a good fit to the experimental data used in this thesis, however it was shown by Sheehan *et al.*³⁸ that the turnover of solids predicted by this model was unrealistic. Thus, it is necessary to study the physical realism of the model predictions in addition to the fit to the experimental RTD.

7.2.1. Average Kilning Phase Velocity

Considering the estimated values for the kilning phase residence time, t_{kiln} , it is possible to calculate the average solids velocity in the kilning phase. As an average kilning particle resides in a cell for a period of t_{kiln} , and the length of a cell is L/N ,

the average velocity of a kilning particle is $\bar{v} = \frac{L}{t_{\text{kiln}} N}$. Using this equation, the average kilning phase velocities for different values of N are shown in Table 7.4. These values appear to be very low, however, this is the average of the velocities of all kilning particles. DEM studies performed by Jones *et al.*⁴², and other works on kilning drums, have shown that a kilning bed contains two phases. The bulk of the material exists in a passive phase with negligible axial velocity, whilst most of the axial transport occurs in a thin active layer on the surface. Due to the presence of the large passive phase, the average axial velocity in the kilning phase should be quite low. However, further study into the behaviour of the kilning phase is required to verify this.

N	t_{kiln} (s)	\bar{v} (m/s)
30	9.95	0.040
31	10.04	0.039
33	9.28	0.039
35	8.69	0.039

Table 7.4. Calculated average kilning phase velocity.

The kilning phase residence velocities predicted by the model of Britton *et al.*⁷² are greater than those predicted by the current model by almost an order of magnitude. For a model using 31 slices, the model of Britton *et al.* predicts kilning phase velocities ranging between 0.3 m/s at the inlet to the dryer to 0.2 m/s at the outlet⁷², compared to the estimated kilning phase residence velocity of 0.04 m/s for the current model. It must be noted that the model of Britton *et al.* has not been validated with experimental data⁷².

7.2.2. Trends in Estimated Parameter Values

Looking at Table 7.2, it can be seen that t_{kiln} , C_B and C_F^G show definite trends with changing N . Figures 7.3 to 7.5 show the trends of t_{kiln} , C_B and C_F^G with varying

values of N . As can be seen, C_B shows a linear trend with N , whilst t_{kiln} and C_F^G also show linear trend with the exception of the point at N equal to 30. This is to be expected as the amount of mass contained within each slice of the dryer decreases linearly with increasing N . Given that all mass flowrates are defined by the relationship $F = \frac{m}{t}$, and that the flowrates are independent of N , it follows that t must decrease in inverse proportion to N .

As there is only one set of experimental data available, it is difficult to tell if these parameter values are realistic. In order to properly test the model, more experimental data is necessary so that the model can be studied under different operating conditions. Ideally, RTDs from a range of conditions should be determined, so that the model can be fitted under a range of conditions, and the estimated parameters compared. However, as only one set of data is available, it is difficult to determine the realism of the parameter values.

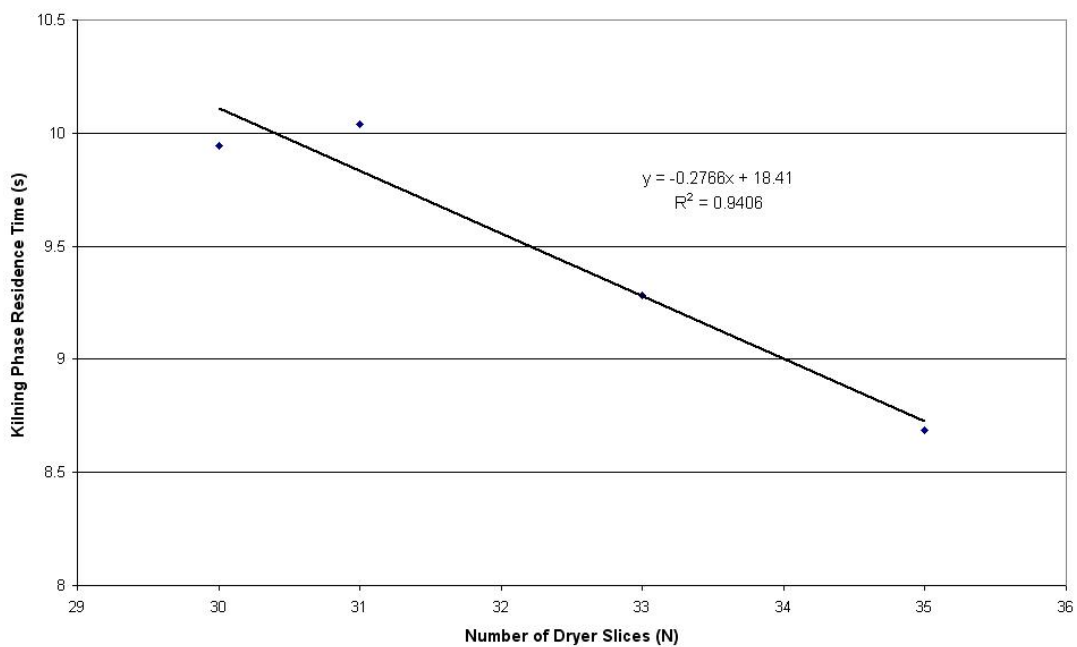


Figure 7.3. Estimated values of t_{kiln} at different values of N .

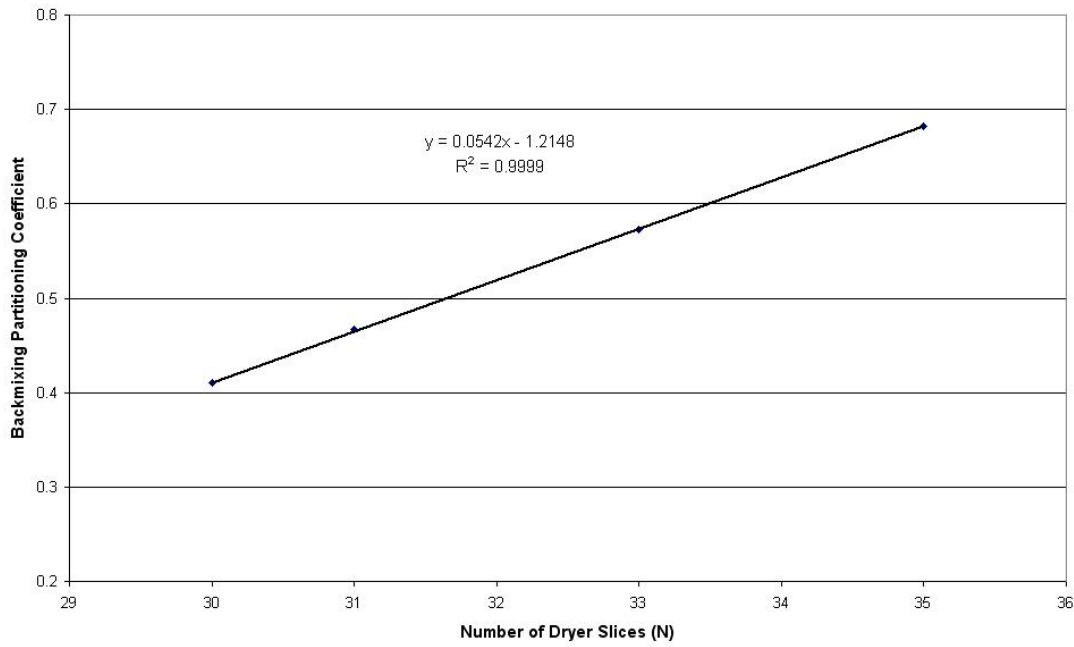


Figure 7.4. Estimated values of C_B at different values of N .

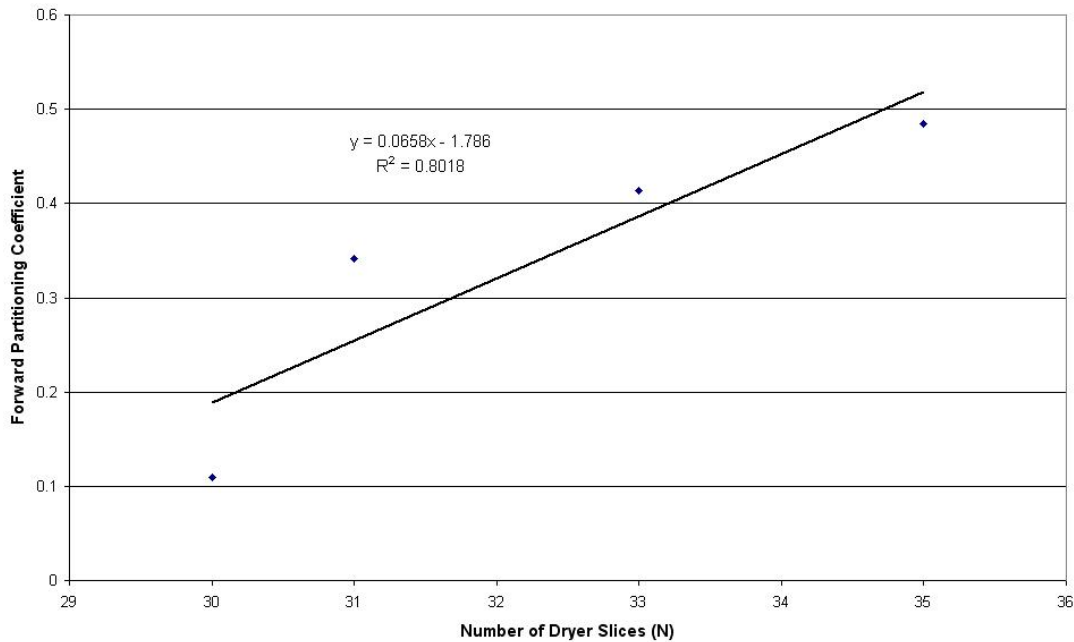


Figure 7.5. Estimated values of C_F^G at different values of N .

However, if the solids transport model is a true physical representation of the dryer, then the predicted conditions within the dryer should be independent of the number of

cells (N) used in the model. Thus, the flux of solids occurring at a given point within the dryer should be independent of N .

This is most easily illustrated by looking at the flowrate of solids moving in the axial direction of the dryer (i.e. the kilning, forward step and backmixing flows). However, as the mass holdup, and thus flowrates, vary along the length of the dryer due to changing solids properties, it is necessary to find a point to study where the mass solids properties will be the same at different values of N . The two most obvious points where the solids properties are independent of N are the first and last cells, where the solids properties are set. For this comparison, the first cell was used, and Table 7.5 shows the value of the kilning, forward and backmixing flowrates for different values of N .

N	Kilning Flowrate	Forward Flowrate	Backmix Flowrate
30	34.36	1.06	8.38
31	32.93	3.33	9.23
33	33.63	4.03	10.65
35	34.22	4.72	11.95

Table 7.5. Dependence of predicted solids flowrates values on N .

Table 7.5 clearly shows that the flowrates of solids are not constant. This means that the solid flowrates within the model (e.g. the rate of kilning flow) is a function of N . This should not be the case, as the flowrates are physical occurrences, and not dependent on the model. This indicates that whilst the solids transport model can accurately reproduce the observed RTD, intuitively the model does not physically represent the system.

7.2.3. Discussion of Model Fit

The results of using parameter estimation to fit the solids transport model to the available experimental data have revealed two issues that need to be considered.

These are the inability of the model to fit the finer details of the experimental RTD, and the dependence of the solids flows on the number of slices used in the model.

The inability of the model to fit the steep initial rise and extended tail of the experimental RTD suggest that alternative model structures need to be considered. As statistical methods were used to fit the model to the experimental data, if it were possible for the model to reproduce these features, the statistical fit should have shown this. However, due to the extreme sensitivity to the initial conditions used in the parameter estimation procedure, it is possible that the solution may not have found the optimal solution.

Thus, it would appear that the model is incapable of reproducing these features as it is. An extended tail on an RTD represents the presence of dead zones or backmixing in the system, so this would suggest that modifications to the solids transport model should increase the amount of backmixing within the model. One possible way of achieving this would be to use a structure similar to that of Britton *et al.*⁷², where the backmixing flow is directed into the previous active phase, rather than the previous active phase. This will be considered in the next section.

The dependence of the solids flowrates on the number of slices used in the model suggests one of two things. Either the entire model does not accurately represent the physical system, or that the result is dependent on the discretization of the system (number of slices, N) rather than the physical equations (akin to the mesh dependency of CFD models discussed in 6.7.1.1). In order to test, and if necessary overcome, the dependence of the result on the discretization of the system, a greater number of slices needs to be used in the model. However, the current model structure limits the number of slices that can be used due to the limitation that material can only be transported a distance of one slice at a time. Thus, in order to use a greater number of slices, the model structure would need to be changed in order to accommodate solids being displaced over multiple slices.

Alternatively, it may be better to abandon the compartment model based approach entirely, and use a different method for representing the dryer, such as a network of zones approach or discrete element modelling. However, these methods are generally

more computationally intensive than compartment based models, thus it is necessary to consider the potential benefits compared to the additional costs.

7.3. Alternative Model Structures

As the results of the parameter estimation showed that the current model structure was unable to reproduce some of the features of the experimental RTD, alternative model structures were considered to improve the model accuracy. Given that Britton *et al.*⁷² reported a good fit to the same set of experimental data, the structure of their model was used in an attempt to achieve a better fit to the RTD.

The model proposed by Britton *et al.*⁷² is very similar to the model developed in this thesis. The key differences between the two models were;

1. In the model of Britton *et al.*⁷², the backmixing of solids occurred between active phases, whereas the current model has backmixing occurring between active and passive phases.
2. Britton *et al.*⁷² used an alternative model for determining the active and passive phase residence times.
3. In the model of Britton *et al.*⁷², the axial partitioning coefficients were such that $C_F^G = 1 - C_B$ and $C_{B,i} = C_{B,\max} \left(\frac{w_{inlet} - w_i}{w_{inlet} - w_{outlet}} \right)$ where w represents the moisture content of the solids and the subscript i represents the i th slice of the dryer. Thus, the axial partitioning coefficients varied along the length of the dryer.
4. Britton *et al.*⁷² developed an equation to describe the turnover of the kilning phase in relation to the mass of the kilning phase and the angular speed of the drum.

5. Britton *et al.*⁷² used Porter's assumption⁵⁴ to determine the design load of the dryer.

The most significant difference between the model of Britton *et al.*⁷² and the current model is the treatment of the backmixing material. As discussed in Chapter 3.1, the methods used in developing the current model suggest that the backmixing material should pass from the current active phase to the previous passive phase as they fall. However, the model of Britton *et al.* assumed that the backmixing solids moved from one active phase to the previous active phase⁷². This should increase the overall amount of backmixing that occurs within the model, as material can pass backwards along the dryer from active phase to active phase.

As the current model appears to require a greater amount of backmixing, the current model was adjusted to be similar to the model of Britton *et al.*⁷². The backmixing flow was changed to flow from active phase to active phase, and the partitioning

$$\text{coefficients were set such that } C_F^G = 1 - C_B \quad \text{and} \quad C_{B,i} = C_{B,\max} \left(\frac{w_{inlet} - w_i}{w_{inlet} - w_{outlet}} \right).$$

However, the altered model retained the geometric flight unloading model and design load model, and the kilning phase residence time was determined using parameter estimation. The comparison between the two models is shown in Figure 7.6.

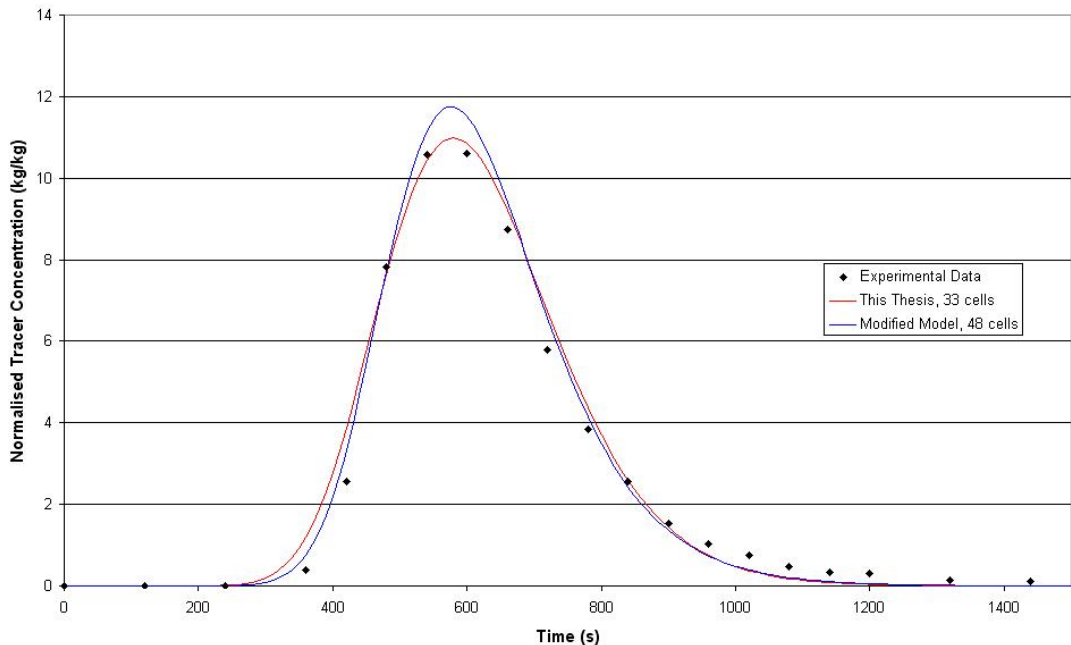


Figure 7.6. Comparison of different model structures.

From Figure 7.6, it can be seen that the results of the new model structure are noticeably different from those of the current model, however the overall match is of a similar quality. The new structure more closely matches the initial steep rise of the RTD, however it overshoots the peak of the curve and is very similar to the current model in the later stages of the RTD. It can be seen that neither model structure is capable of reproducing the extended tail of the RTD, thus other options need to be considered.

It should be noted that Britton *et al.*⁷² reported a much better fit to the experimental RTD in their paper. The differences between the results reported by Britton *et al.*⁷² and those shown above are due to the differences in the models used to determine the active and passive phase residence times (i.e. the geometric flight unloading model).

7.4. Response to Operating Conditions

Another method for studying the physical accuracy of the model is to observe the response of the model predictions to changes in operating conditions. The key operating condition parameters for the model are the solids feedrate to the dryer and

the solids dynamic angle of repose. By changing the value of these parameters, the physical accuracy of the model can be assessed by considering the physical meaning of the observed response in the model.

In order to make studying the model response easier, a constant dynamic angle of repose was used through out the dryer for these studies. This removes the varying conditions along the dryer, meaning all cells should behave identically, and makes changing the dynamic angle of repose in the system easier. Whilst this will not represent a true dryer, it should be sufficient for the purpose of studying the response of the model to changes in operating conditions and removes the complexity of moisture content effects.

7.4.1. Response to Dynamic Angle of Repose

The first operating condition studied was the effect of the dynamic angle of repose of the solids. As this parameter is used to calculate the mass contained within a flight, changing the dynamic angle of repose will affect a number of values within the model. Changing the dynamic angle of repose will affect the design load of the dryer and the active and passive cycle times. These will in turn affect the solids flowrates and holdups within the dryer. Table 7.6 shows the response of these values to changes in the dynamic angle of repose of the solids.

Dynamic Angle of Repose (ϕ)	Average Passive Cycle Time (s)	Average Particle Fall Time (s)	Dryer Design Load (kg)
30	10.685	0.9001	4 400
40	11.365	0.8669	5 508
50	12.316	0.8237	6 784
55	12.816	0.7986	7 495

Table 7.6. Affect of solids dynamic angle of repose on solids transport model.

Table 7.6 shows that the active and passive cycle times and the dryer design load appear to be close to linearly related to the dynamic angle of repose. The changes in

these values will result in changes in the solids flowrates occurring within the model, which are shown in Figure 7.7. As can be seen, as the dynamic angle of repose of the solid increases, so do the flowrates of solids occurring within the dryer. This is because increasing the dynamic angle of repose of the solids increases the amount of solids that can be held within a flight, thus more solids are being cycled through the flights in the same time period.

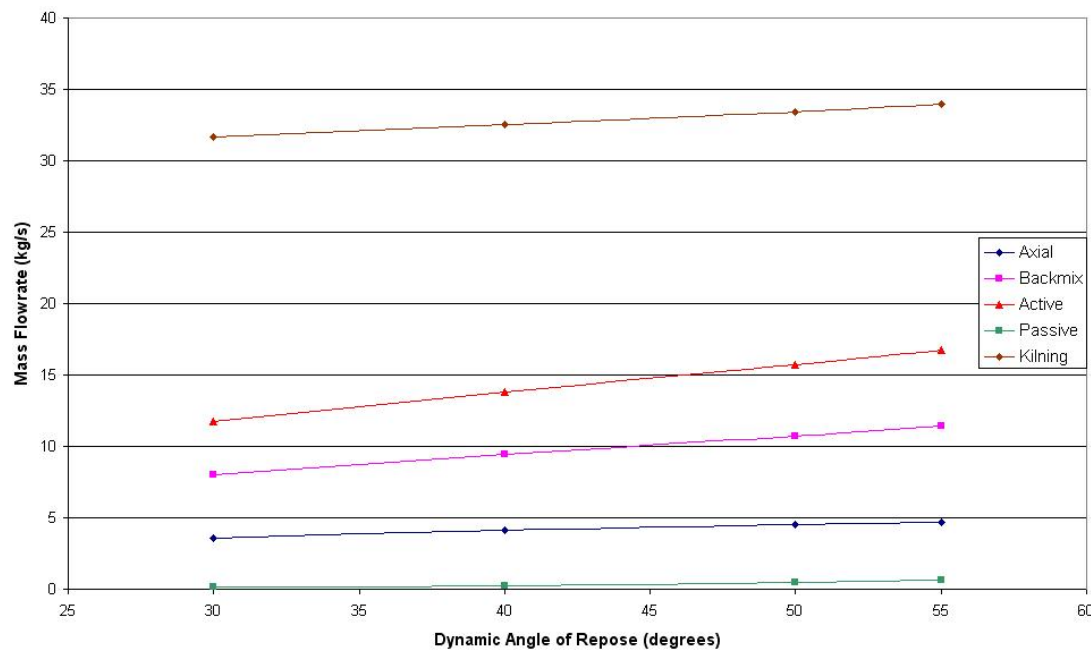


Figure 7.7. Internal solids flowrates versus dynamic angle of repose.

Due to the increase in mass in the flights, there should also be an increase in the mass within the falling curtains. This is shown in Table 7.7, where it can be seen that the active, flighted (mass contained within the flights) and total holdups within the dryer increase with the dynamic angle of repose of the solids. The total passive phase holdups predicted by the model for angles of repose of 30° and 40° are similar to the known holdup of the Invicta Mill dryer number 2, which has a holdup of approximately 14,000 kg. Thus, the overall holdups predicted by the model appear to be reasonable. However, this is due to the requirement that $F = \frac{M}{\tau}$ for the system, rather than the behaviour of the model.

Dynamic Angle of Repose (ϕ)	Active Phase Mass (kg)	Flighted Mass (kg)	Total Passive Phase Mass (kg)
30	370	4 400	14 021
40	420	5 508	15 390
50	453	6 784	16 947
55	467	7 495	17 822

Table 7.7. Dryer holdup at different dynamic angles of repose.

Looking at the values of the flighted mass compared to the total passive mass in Table 7.7, it can be seen that model predicts that the flighted mass forms only a small portion of the total passive holdup within the dryer, ranging from 31% to 42% of the total passive holdup. This suggests that there is a significant kilning bed present within the dryer, however it is generally believed that the Invicta Mill dryer number 2 operates only slightly above its design load. The cause of this discrepancy needs to be determined in order to determine the accuracy of the model. This would required experiments to accurately determine the design load of the dryer.

Dynamic Angle of Repose (ϕ)	Active/Flighted Mass	Active/Passive Mass
30	8.42%	2.64%
40	7.63%	2.73%
50	6.69%	2.68%
55	6.23%	2.62%

Table 7.8. Ratio of active to passive masses for different dynamic angles of repose.

One of the most important characteristics of a flighted rotary dryer is the ratio of mass in the falling curtains to the holdup within the dryer. This ratio represents the fraction of the solid undergoing drying at any point during the dryer's operation. Table 7.8 shows the ratio of the active mass to both the flighted mass and the total passive mass for the different solids dynamic angles of repose. As can be seen, the ratio of active mass to the total passive mass is very low, less than 3%. This would mean that only a very small fraction of the solids within the dryer are undergoing drying at anytime, meaning the dryer is very inefficient. This ratio of active mass to passive mass seems

unusually small, suggesting that the model may not be physically representative of the system (specifically the design load seems to be too small). However, given the lack of experimental data in this area, it is impossible to determine whether or not the dryer actually operates under these conditions.

7.4.2. Response to Dryer Feed Rate

The other key operating condition for a rotary dryer is the dryer feed rate, as this is often the most easily controlled parameter in the system. The response of rotary dryers to changes in dryer feed rate has also been extensively by previous researchers, such as Friedman and Marshall¹¹ and Matchett and Baker²³ to name a few. To study the response of the solids transport model to changing dryer feed rates, a series of simulations were conducted using different feed rates with a solids dynamic angle of repose of 40°, and the results of these are shown in Table 7.9.

Dryer Feed Rate (% Normal)	Total Passive Holdup (kg)	Kilning Flowrate (kg/s)
100%	15 389	32.5
90%	14 561	29.8
80%	13 733	27.1
70%	12 906	24.3
60%	12 078	21.6
50%	11 250	18.9
40%	10 423	16.2
20%	8 767	10.7

Table 7.9. Passive holdup and kilning flowrate at different dryer feed rates.

For a dynamic angle of repose of 40°, the model predicts a dryer passive design load of 5,580 kg. Comparing this to the passive holdups shown in Table 7.9, it can be seen that even at 20% of the normal dryer feed rate, the model still predicts that the dryer is overloaded. This does not seem to be reasonable, as it is unlikely that a dryer would be operated so far beyond its design conditions. This suggests that the design load

predicted by the geometric flight unloading model is too small, and this needs to be investigated further. This will be considered in the next section.

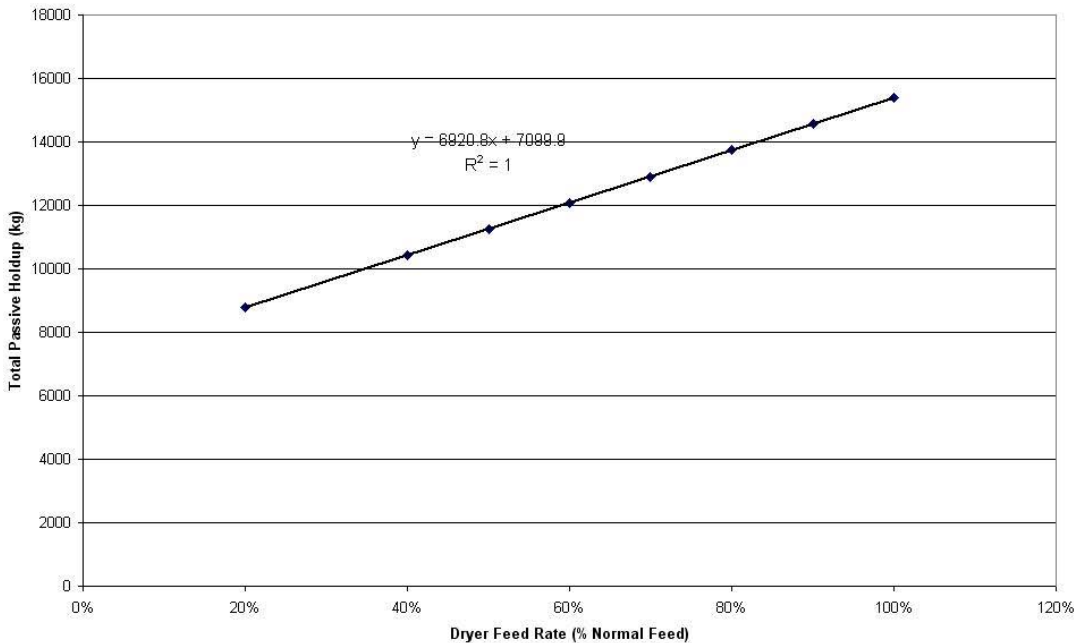


Figure 7.8. Total passive holdup versus dryer feed rate.

Figure 7.8 shows a plot of the predicted passive holdup versus the dryer feed rate, and it can be seen that holdup is linearly related to feed rate. This agrees well with the Friedman and Marshall model¹¹, and the requirement that $F = \frac{M}{\tau}$. However, it can also be seen that the trend of the passive holdup does not go to zero at no feed rate. This is due to the prediction that the dryer is still overloaded at low feed rates, as once the holdup within a dryer exceeds the design load, the response of the holdup to increasing feed rate is decreased. Beneath the design load, the slope of the line should increase, and pass through the origin. This was shown by Matchett and Baker^{12, 23}, whose solid transport model showed two distinct responses to changing feed rate above and below the design load of the dryer. In the case of the current model, when the total passive mass decreases below the predicted design load of the dryer, the slope of the line should increase significantly. As the feed rate decreases further, the passive holdup will decrease rapidly, until it reaches a holdup of 0 kg at zero feed rate.

7.5. Effect of Design Load

As discussed above, the solids transport model appears to underestimate the design load of the dryer, resulting in improbable distribution of mass between active and passive phases. The design load is important in the solids transport model as it defines the point at which the flowrate of solids entering the active phase is limited (see Chapter 3.2.2). Thus, if the design load used in the model is too small, the flowrate of solids entering the active phase will be limited to a smaller value than it should, reducing the mass of solids in the active phase.

As increasing the design load used in the model increases the maximum flowrate of solids entering the active phase, this will also increase the rate at which solids move through the dryer due to the action of the flights. This should then reduce the amount of kilning flow necessary, reducing the mass of solids necessary in the passive phase.

To give an indication of how this would affect the model predictions, a multiplying factor was added to the design load calculation in the solids transport model. Parameter estimation was used to fit the solids transport model with the adjusted design load calculation to the experimental data from Invicta Mill's dryer number 2 for a range of values of this factor, for a constant dynamic angle of repose of 40°. Table 7.10 shows the predicted solids holdups in each phase for these simulations.

	Design Load (kg)	Active Phase Mass (kg)	Total Passive Mass (kg)	Total Dryer Holdup (kg)	Active/Passive Mass
100%	5 508	420	15 389	15 809	2.73%
150%	8 262	630	15 831	16 451	3.98%
200%	11 016	840	15 607	16 447	5.38%

Table 7.10. Effect of increasing the model design load on holdups.

From Table 7.10, it can be seen that as the design load is increased (due to the multiplying factor), the distribution of solids between the phases changes. It can be

seen that the total dryer holdup remains constant relatively constant, due to the requirement that $F = \frac{M}{\tau}$. However, as the design load increases, the ratio of active mass to passive mass increases, indicating that a greater portion of the solids is undergoing drying at a given time. As most rotary dryers are designed to operate with approximately 10% active mass, this indicates that as the design load is increased in the model, the predictions become more reasonable. However, even increasing the predicted design load by 200% only gives 5.4% active mass, which is still unusually low.

This is a significant increase in the predicted design load. Even the previous model for the dryer design load, developed by Porter⁵⁴, only predicts a design mass 35% greater than the model developed in this thesis. This would tend to suggest that the problem lies in the model structure rather than the predictions of the design load, however experimental data is needed to confirm this.

This needs to be investigated further, in order to accurately determine the design load for the dryer. This will make it possible to determine whether the current models give realistic predictions for the design load, or if an alternative model needs to be developed. Until this is done, it is not possible to assess the accuracy of the rest of the model, as it is dependent on the design load predictions to determine the behaviour of the model.

7.6. Discussion

From the results discussed above, it can be seen that while the model provides a good fit to the experimental data, the flowrates and mass holdups predicted seem to be unusual. Most importantly, the design loads predicted by the model appear to be significantly smaller than they should be, resulting reduced amounts of solids in the active phase and an increased presence of kilning flow.

This highlights the importance of understanding the kilning behaviour of flighted rotary dryers, and the need for experimental data to determine the correct design load. However, there is currently very limited data available on this, thus it is not possible

at this point in time to include verified values. The model predictions shown in 7.5 do indicate that, given a larger design load than currently predicted, the solids transport model can predict reasonable values for the mass holdup within the system.

It is also clear that more information is required from experiments regarding the material properties along the length of the dryer, or a mass transfer model needs to be combined with the solids transport model. In order to accurately fit the solids transport model, it is necessary to know the dynamic angle of repose of the solid material along the length of the dryer. However, due to the difficulty in measuring this, most experimental studies of industrial dryers have neglected this. As has been shown above, this forces the assumption of arbitrary profiles of the solids properties along the dryer, which raises questions about the accuracy of the final model. Thus, in order to fit the model accurately, this data needs to be determined as part of the experiment. This could be done either by measuring the solids properties along the length of the dryer during the experiment, or by using a pilot scale dyer where the solids properties are constant. This may raise questions regarding scaling of results to full scale operations, however as the model is based on the geometry of the system, the model should be able to scale up without any difficulties.

Chapter 8

8. Conclusions and Recommendations

8.1. Conclusions

A numerical solids transport model for flighted rotary dryers was developed in this thesis, based on the physical behaviour of a flighted rotary dryer. This model was combined with geometric modelling of the unloading profile of a dryer flight and computational fluid dynamics analysis of the gas-solids interactions that occur within the dryer. The predictions of the solids transport model were compared to experimental data obtained from CSR's Invicta Sugar Mill's dryer number 2.

Experiments using the flight unloading apparatus have shown that a geometric model of flight unloading can accurately predict the unloading profile of a flight. Experiments were conducted using three flight geometries and three solid materials at rotational velocities between 1 and 8 rpm, and the geometric flight unloading model was found to accurately reproduce the observed unloading profile under all experimental conditions. Measurements taken from high-speed camera images of the flight during unloading showed that the velocity and dynamic angle of repose of the solids in the flight was not constant, and that these varied significantly throughout each experiment. Further study of these images revealed that the discharging of solids from a flight was not continuous, and that the material in the flight undergoes bulk failure.

A drag coefficient for sugar crystals falling in isolation was determined based on experimental measurements. The drag coefficient was found to be well represented by the equation $C_D = \frac{68}{Re} (1 + 0.004 Re^{0.99})$. The common assumption that falling particles can be adequately represented as isolated spheres was compared to the experimentally measured drag coefficients. It was found that the assumption of spherical particles predicted drag coefficients up to 40% greater than those measured experimentally.

This thesis has also shown that computational fluid dynamics (CFD) simulations are capable of modelling curtains of falling solids dispersed in a moving gas stream, and show promise in modelling the gas-solids interactions occurring within flighted rotary dryers. An Eulerian-Eulerian model was developed to simulate the interactions between falling solid particles and a moving gas stream. Experimental results from wind tunnel experiments were used to validate the CFD model, and the model was shown to accurately predict the displacement of solids.

The CFD model was then used to simulate conditions similar to those experienced in flighted rotary dryers. Simulations using initial condition obtained from experiments using unserrated flights demonstrated that gas-solids interactions were limited to the first 10-20 cm of the curtain under these conditions. However, serrations have a significant effect on the initial conditions of the curtain and this will lead to different results. It was also shown that the channelling of the gas flow between neighbouring curtains could significantly increase the displacement of the solid curtain. The results of the CFD simulations suggested that a more detailed model is required to model the gas-solids interactions in a full scale dryer, however computational limitations prevented a complete analysis.

Comparison of the completed solids transport model with experimental data from an industrial sugar dryer showed that the model provided a good fit to the experimental residence time distribution (RTD). Statistical parameter estimation procedures were used to fit to the experimental data, and a good match was achieved, however it was found that the model was not capable of reproducing some the extended tail of the RTD. An alternative model structure was proposed to address this, however the fit to the experimental data was not improved.

A study of the solids flowrates predicted by the model was conducted to assess the physical realism of the model. It was found that the flowrates of solids within the dryer were dependent on the number of slices used to discretize the dryer. This indicates that the model is not a physical representation of the system, and that the agreement between the model and the experimental RTD is purely statistical.

A study of the effect of the dynamic angle of repose of the solids on the solids transport model showed that increasing the dynamic angle of repose affected the amount of solids contained within the falling curtain. Additionally, it was observed that the design load for the dryer predicted by the model seemed improbably small, resulting in very low amounts of material being present in the falling curtain. A study of the affect of the predicted design load on the behaviour of the dryer showed that increasing the predicted design load resulted in more reasonable solids distributions being predicted.

8.2. Recommendations

Based on the findings discussed in this thesis, the following recommendations are made in order to further develop and test a model for flighted rotary dryers.

- An experimental study of the loading within flighted rotary driers needs to be undertaken in order to determine the correct approach to determining and modelling the design load point. The work in this thesis has highlighted the importance of the design load on the accurate modelling of the solids transport occurring within flighted rotary dryers. Experiments are needed to test and compare the design loads predicted by the geometric unloading model developed in this thesis and Porter's assumption⁵⁴, and used to determine the dryer design load ($M_{p,des}$).
- A study of the behaviour of the kilning phase within flighted rotary dryers needs to be conducted to determine the correct approach to modelling the solids transport due to kilning. A model for the kilning phase residence time (t_{kiln}) needs to be developed, similar to that developed in this thesis for the active and passive phase residence times.
- An experimental study of the unloading behaviour of serrated flights is needed to allow more realistic modelling of the gas-solids interactions in flighted rotary dryers. Additionally, the curtains produced by serrated flights will be significantly different to those generated by unserrated flights. In order to

accurately model the gas-solids interaction that occur in dryers using serrated flights, the initial conditions of curtains from serrated flights need to be measured experimentally. Using the results of these simulations, it should be possible to develop relationships for the axial partitioning coefficients (C_B and C_F^G).

- More experimental tracer studies are required to allow more comprehensive testing of the model. For this thesis, only one set of experimental results was available, which is not sufficient to accurately assess the performance of the model. Experiments of the RTD and holdup in dryers with constant material properties are required to remove the complications of varying solid properties within the dryer. This information is critical to the predictions of the model, and is necessary for accurate results.
- Once the issues discussed above have been addressed, study into alternate model structures is necessary in the continued development of the solids transport model, especially regarding the kilning phase. The current model has been shown to be unable to reproduce the finer features of the observed RTD, thus changes must be made to the model structure to improve the fit to RTD. Whilst the current model was developed based on the physical flow of material within the drier, other model structures may prove to be better suited to modelling flighted rotary driers.
- As has been discussed in this thesis, and highlighted by other researchers (e.g. Wang¹⁵), the use of averaged parameters (such as the mass averaged fall time) within solids transport models of rotary driers does not fully characterise the complex flow behaviours. Using the average fall path approach neglects the dispersion of solids caused by the action of the flights. Alternatives to the averaged fall path approach may need to be considered. However, the added complexity of these models may outweigh the benefits gained.
- In this thesis, gPROMS[®] has been used to implement the solids transport and geometric unloading models. However, gPROMS[®] is poorly suited to the

iterative nature of the geometric unloading model, thus the geometric unloading model was used to develop simple correlations for the key parameters. However, this introduces a number of inaccuracies when operating at conditions at the extreme ranges of these correlations (for example predicting flight loading factors of less than zero at low dryer loadings). Alternative methods of implementing the solids transport and geometric unloading models need to be considered in order to address these issues.

- A heat and mass transfer model is a necessary part of the model for a flighted rotary drier, in order to predict the changes in solids properties due to moisture content along the drier.

9. References

1. Woodcock, C.R. and Mason, J.S., *Bulk Solids Handling*, 1987, Blackie and Son Ltd., London
2. Tegzes, P., Albert, R., Paskvan, M., Barabasi, A.-L., Vicsek, T. and Schiffer, P., *Liquid-Induced Transitions in Granular Media*, Physical Review E., 1999, 60, 5823-5826
3. Halsey, T.C. and Levine, A.J., *How Sandcastles Fall*, Physical Review Letters, 1998, 80, 3141-3144
4. Schofield, F.R. and Glikin, P.G., *Rotary Driers and Coolers for Granular Fertilizers*, Trans. Instn. Chem. Engrs., 1962, 40, 183-190
5. Kelly, J., *Flight Design in Rotary Dryers*, Drying Technology, 1992, 10, 979-993
6. Levenspiel, O., *Chemical Reaction Engineering*, 1999, John Wiley and Sons, New York
7. Vigh, S.N., Genrich, K., Schneider, P., Sheehan, M. and Turnbull, P., *Factory Measurement of Rotary Dryer Residence Time and Its Implications for Processing Capacity*, CSR Ltd.,
8. Renaud, M., Thibault, J. and Alvarez, P.I., *Influence of Solids Moisture Content on the Average Residence Time in a Rotary Dryer*, Drying Technology, 2001, 19, 2131-2150
9. Sherritt, R.G., Chaouki, J., Mehrotra, A.K. and Behie, L.A., *Axial Dispersion in the Three-Dimensional Mixing of Particles in a Rotating Drum Reactor*, Chemical Engineering Science, 2003, 58, 401-415
10. Monro, A., *Examination and Validation of Rotary Sugar Dryer Models*, Honours Thesis in Chemical Engineering, James Cook University, 2000
11. Friedman, S.J. and Marshall, W.R., *Studies in Rotary Drying. Part 1 - Holdup and Dusting*, Chemical Engineering Progress, 1949, 45, 482-493
12. Matchett, A.J. and Baker, C.G.J., *Particle Residence Times in Cascading Rotary Dryers Part 2 - Application of the Two-Stream Model to Experimental and Industrial Data*, Journal of Separation Process Technology, 1988, 9, 5-13

13. Bazin, C., Hodouin, D., Duchesne, C., Thibault, J. and Trusiak, A.R., *Reconciliation of Mass and Energy Data Measurements: Application to a Rotary Dryer*, Canadian Metallurgical Quarterly, 1998, 37, 333-342
14. Sheehan, M., Schneider, P., Monro, A. and Vigh, S., *Transportation and Axial Dispersion of Sugar in Flighted Rotary Dryers*, Proceedings of the ASSCT, 2002,
15. Wang, F.Y., Cameron, I.T., Litster, J.D. and Rudolph, V., *A Fundamental Study of Particle Transport through Rotary Dryers for Flight Design and System Optimisation*, Drying Technology, 1995, 13, 1261-1278
16. Ding, Y.L., Seville, J.P.K., Forster, R.N. and Parker, D.J., *Solids Motion in Rolling Mode Rotating Drums Operated at Low to Medium Rotational Speeds*, Chemical Engineering Science, 2001, 56, 1769-1780
17. Song, Y., Thibault, J. and Kudra, T., *Dynamic Characteristics of Solids Transportation in Rotary Dryers*, Drying Technology, 2003, 21, 755-773
18. Miller, C.O., Smith, B.A. and Schuette, W.H., *Factors Influencing the Operation of Rotary Dryers. 2 the Rotary Dryer as a Heat Exchanger*, Trans. AIChE, 1942, Boston, Massachusetts
19. Shahhosseini, S., Cameron, I.T. and Wang, F.Y., *A Simple Dynamic Model for Solids Transport in Rotary Dryers*, Drying Technology, 2000, 18, 867-886
20. Alvarez, P.I. and Shene, C., *Experimental Study of Residence Time in a Direct Rotary Dryer*, Drying Technology, 1994, 12, 1629-1651
21. Cao, W.F. and Langrish, T.A.G., *Comparison of Residence Time Models for Cascading Rotary Dryers*, Drying Technology, 1999, 17, 825-836
22. Renaud, M., Thibault, J. and Trusiak, A., *Solids Transportation Model of an Industrial Rotary Dryer*, Drying Technology, 2000, 18, 843-865
23. Matchett, A.J. and Baker, C.G.J., *Particle Residence Times in Cascading Rotary Dryers Part 1 - Derivation of the Two-Stream Model*, Journal of Separation Process Technology, 1987, 8, 11-17
24. Matchett, A.J. and Sheikh, M.S., *An Improved Model of Particle Motion in Cascading Rotary Dryers*, Chemical Engineering Research and Design, 1990, 68, 139-148
25. Sherritt, R.G., Caple, R., Behie, L.A. and Mehrotra, A.K., *The Movement of Solids through Flighted Rotating Drums. Part 1: Model Formulation*, The Canadian Journal of Chemical Engineering, 1993, 71, 337-346

26. Wang, F.Y., Cameron, I.T., Litster, J.D. and Douglas, P.L., *A Distributed Parameter Approach to the Dynamics of Rotary Drying Processes*, Drying Technology, 1993, 11, 1641-1656
27. Sherritt, R.G., Caple, R., Behie, L.A. and Mehrotra, A.K., *The Movement of Solids through Flighted Rotating Drums. Part 2 Solids-Gas Interaction and Model Validation*, The Canadian Journal of Chemical Engineering, 1994, 72, 240-248
28. Martin, A.D., *Interpretation of Residence Time Distribution Data*, Chemical Engineering Science, 2000, 55, 5907-5917
29. Claudel, S., Fonteix, C., Leclerc, J.-P. and Lintz, H.-G., *Application of the Possibility Theory to the Compartment Modelling of Flow Pattern in Industrial Processes*, Chemical Engineering Science, 2003, 58, 4005-4016
30. Kemp, I.C. and Oakley, D.E., *Simulation and Scale-up of Pneumatic Conveying and Cascading Rotary Dryers*, Drying Technology, 1997, 15, 1699-1710
31. Shahhosseini, S., Cameron, I.T. and Wang, F.Y., *A Dynamic Model with on-Line Identification for Rotary Sugar Drying Processes*, Drying Technology, 2001, 19, 2103-2129
32. Didriksen, H., *Model Based Predictive Control of a Rotary Dryer*, Chemical Engineering journal, 2002, 86, 53-60
33. Duchesne, C., Thibault, J. and Bazin, C., *Modelling of the Solids Transportation within an Industrial Rotary Dryer: A Simple Model*, Industrial Engineering Chemistry Research, 1996, 35, 2334-2341
34. Cholette, A. and Cloutier, L., *Mixing Efficiency Determinations for Continuous Flow Systems*, The Canadian Journal of Chemical Engineering, 1959, 105-112
35. Schneider, P.A., Sheehan, M.E. and Vigh, S.N., *A Model for Solids Transport in Rotary Dryers*, unpublished, 2001,
36. Schneider, P., Sheehan, M. and Brown, S., *Modelling the Dynamics of Rotary Sugar Dryers*, 13th European Symposium on Computer Aided Process Engineering (ESCAPE), 2003, Finland
37. Lee, A., Sheehan, M.E. and Schneider, P.A., *Solids Transport in Rotary Sugar Dryers*, Proceedings of the ASSCT, 2004, Brisbane
38. Sheehan, M.E., Britton, P. and Schneider, P.A., *A Model for Solids Transport in Flighted Rotary Dryers Based on Physical Considerations*, Chemical Engineering Science, 2005, 60, 4171-4182

39. Ingram, G.D., Cameron, I.T. and Hangos, K.M., *Classification and Analysis of Integrating Frameworks in Multiscale Modelling*, Chemical Engineering Science, 2004, 59, 2171-2187
40. Cameron, I.T., Wang, F.Y., Immanuel, C.D. and Stepanek, F., *Process Systems Modelling and Applications in Granulation: A Review*, Chemical Engineering Science, 2005, 60, 3723-3750
41. Revol, D., Briens, C.L. and Chabagno, J.M., *The Design of Flights in Rotary Dryers*, Powder Technology, 2001, 121, 230-238
42. Jones, C., Hwan, I.H., Zhang, D.-K., Martella, M. and Wu, H., *Dem Simulations of the Effects of Lifters on Solid Mixing in a Rotating Drum*, Chemeca, 2007, Melbourne
43. Munson, B.R., Young, D.F. and Okiishi, T.H., *Fundamentals of Fluid Mechanics*, 1998, John Wiley and Sons, Brisbane
44. Schiller, L. and Naumann, Z., *A Drag Coefficient Correlation*, Zeitschrift des Vereines Deutscher Ingenieure, 1935, 77, 318-320
45. Baker, C.G.J., *Air-Solids Drag in Cascading Rotary Dryers*, Drying Technology, 1992, 10, 365-393
46. Sherritt, R.G., *Modelling the Movement of Solids through Flighted Rotating Drums*, M.Eng. Thesis in Chemical and Petroleum Engineering, University of Calgary, 1992
47. Wardjiman, C., Wang, S. and Rhodes, M., *Behaviour of a Curtain of Particles Falling through a Horizontal Gas Stream*, Chemeca, 2005, Brisbane, Australia
48. Lee, A., Sheehan, M.E., Britton, P.F. and Schneider, P.A., *A Comparison of Compartment Models for Solids Transport in Flighted Rotary Dryers*, Chemeca, 2005, Brisbane, Australia
49. Lee, A., *Statistical Modelling of the Solids Transport Phenomena Occurring within Rotary Dryers*, Honours Thesis in Chemical Engineering, James Cook University, 2003
50. *Gproms Introductory Users Guide*, 2004, Process Systems Enterprise Ltd., London
51. *Gproms Advanced Users Guide*, 2004, Process Systems Enterprise Ltd., London
52. Sheehan, M., *A Study of the Material Transport in a Flighted Rotary Dryer*, Undergraduate Thesis in Chemical Engineering, University of Queensland, 1993

53. Mellmann, J., *The Transverse Motion of Solids in Rotating Cylinders - Forms of Motion and Transition Behaviour*, Powder Technology, 2001, 118, 251-270
54. Porter, S.J., *The Design of Rotary Driers and Coolers*, Trans. Instn. Chem. Engrs., 1963, 41, 272-280
55. Hodgson, M.C.J. and Keast, W.J., *Rotary Dryer Flight Design*, Proc. ASSCT, 1984, 211-218
56. Haider, A. and Levenspiel, O., *Drag Coefficient and Terminal Velocity of Spherical and Nonspherical Particles*, Powder Technology, 1989, 58, 63-70
57. Kelly, F.H.C. and Mak, F.K., *The Sucrose Crystal and Its Solution*, 1975, Singapore University Press,
58. Ansys Cfx-Solver Theory Guide, 2006, ANSYS, Inc., Canonsberg
59. Bakker, A., *Computational Fluid Dynamics*, 2006, Fluent Inc.,
60. Cooper, S. and Coronella, C.J., *Cfd Simulations of Particle Mixing in a Binary Fluidized Bed*, Powder Technology, 2005, 151, 27-36
61. Du, W., Bao, X., Xu, J. and Wei, W., *Computational Fluid Dynamics (Cfd) Modelling of Spouted Bed: Assessment of Drag Coefficient Correlations*, Chemical Engineering Science, 2006, 61, 1401-1420
62. Nakamura, H. and Watano, S., *Numerical Modelling of Particle Fluidization Behaviour in a Rotating Fluidized Bed*, Powder Technology, 2007, 171, 106-117
63. Ropelato, K., Meier, H.F. and Cremasco, M.A., *Cfd Study of Gas-Solid Behaviour in Downer Reactors: An Eulerian-Eulerian Approach*, Powder Technology, 2005, 154, 179-184
64. Hidayat, M. and Rasmuson, A., *Some Aspects on Gas-Solid Flow in a U-Bend: Numerical Investigation*, Powder Technology, 2005, 153, 1-12
65. Launder, B.E. and Spaulding, D.B., *Lectures in Mathematical Models of Turbulence*, 1972, Academic Press, New York
66. Shah, U., Zhu, J., Zhang, C. and Nother Senior, J.H., *Numerical Investigation of Coarse Powder and Air Flow in an Electrostatic Powder Coating Process*, Powder Technology, 2006, 164, 22-32
67. Ansys Cfx Solver Theory Guide, 2006, Ansys, Inc., Canonsburg
68. Wardjiman, C., Lee, A., Sheehan, M. and Rhodes, M., *Behaviour of a Curtain of Particles Falling through a Horizontal Gas Stream*, Powder Technology, In Press,
69. Ansys Cfx Solver Modelling Guide, 2006, Ansys, Inc., Canonsburg

70. Wardjiman, C., Lee, A., Sheehan, M. and Rhodes, M., *Shape of a Particle Curtain Falling in Stagnant Air* Powder Technology, In Press,
71. Pugh, M., *Investigation of the Effect of Flight Geometry on Flight Unloading Characteristics in Rotary Dryers*, Thesis in Mechanical Engineering, James Cook University, 2007
72. Britton, P.F., Sheehan, M.E. and Schneider, P.A., *A Physical Description of Solids Transport in Flighted Rotary Dryers*, Powder Technology, 2006, 165, 153-160
73. Pope, G., Taske, E., Wieden, T. and Brotherton, G.A., *Aspects of Sugar Drying*, Proceedings of the ASSCT, 1993, 167-173
74. Sheehan, M. and Schneider, P., *Modelling of Rotary Sugar Dryers: Steady State Results*, Proceedings of Chemeca, 2000, Perth

10. Appendix I – gPROMS® Code

10.1. Process Entity

{Dryer Model v4

Jan 14th, 2008}

UNIT

D AS Dryer

PARAMETER

L AS REAL # Drum Length (m)

R AS REAL # Drum Radius (m)

omega AS REAL # Angular Velocity of Drum (RPM)

theta AS REAL # Inclination of Drum (degrees)

Nf AS INTEGER # No. Flights

s1 AS REAL # Flight Length 1

s2 AS REAL # Flight Length 2

alpha1 AS REAL # Flight Angle 1

alpha2 AS REAL # Flight Angle 2

N AS INTEGER # No. Cells

rhob AS REAL # Bulk Density of Solids

MONITOR

D.O.tau;

D.O.x_o;

D.O.normalised;

D.C(1).G.d_load;

D.C(15).G.d_load;

D.C(33).G.d_load;

SET

L :=12;

```

R      :=2.5;
omega   :=3;
theta   :=2.8;

Nf     :=28;
s1     :=0.195;
s2     :=0.183;
alpha1  :=90;
alpha2  :=117;

N      :=48;      # Max = 45?

rhob   :=940;

```

ASSIGN

```

D.C(1).P.F_k_in := 98000/3600;
D.C(1).P.x_k_in := 0;

```

```

D.C(N).P.F_b  := 0;
D.C(N).P.x_b  := 0;

```

```

D.O.x_feed    := 3.683E-004*39.6*98000/3600;  # Total moisture injected - volume fraction *
injection time

```

```

D.t_kiln    := 7.704; #16.75;
D.C_b       := 0.5374; #0.1454;
D.C_x_g     := 0.3649; #0.6573;

```

INITIAL

```

D.O.xtime = 0;
D.O.tau = 0;

```

FOR i:= 1 TO N-1 DO

```

D.C(i).P.m = 400; # From Steady-State data (14000/N);
D.C(i).P.x = 0;

```

```

D.C(i).A.m = 40; # From Steady-State data (1400/N);

```

```
D.C(i).A.x = 0;  
  
END  
  
D.C(N).P.m = 200; # From Steady-State data (14000/N);  
D.C(N).P.x = 0;  
  
D.C(N).A.m = 20; # From Steady-State data (1400/N);  
D.C(N).A.x = 0;
```

SOLUTIONPARAMETERS

```
LA Solver := "MA28"  
DA Solver := "DASOLV"  
REPORTINGINTERVAL      := 10  
gExcelOutput           := ON
```

SCEDULE

SEQUENCE

CONTINUE FOR 3600

RESET

D.C(1).P.x_k_in := 3.683E-004; # IMPORTANT: If you change this you need to change the value in the Dryer Model as well.

END

CONTINUE FOR 39.6 # IMPORTANT: If you change this you need to change the value in the Dryer Model as well.

RESET

D.C(1).P.x_k_in := 0;

END

CONTINUE FOR 7200

END

10.2. Model Entities

10.2.1. Active Phase

{ Active Phase Model v4.0

14-Jan 2008, Andrew Lee}

VARIABLE

m	AS mass	# Mass contained within cell
x	AS moisture	# Moisture content of solids in cell
x_p	AS moisture	# Moisture content of entering solids
F_p	AS mass_flowrate	# Mass flowrate into cell
F_x	AS mass_flowrate	# Mass flowrate undergoing axial advance
F_r	AS mass_flowrate	# Mass flowrate returning to passive cell
F_b	AS mass_flowrate	# Mass flowrate undergoing backmixing
t_act	AS mrt	# Mean residence time of active phase
C_x	AS no_unit	# Forward axial partitioning coefficient
C_b	AS no_unit	# Backwards axial partitioning coefficient

STREAM

Axial	:F_x,x	AS SOLIDFLOW
Return	:F_r,x	AS SOLIDFLOW
Back	:F_b,x	AS SOLIDFLOW
In	:F_p,x_p	AS SOLIDFLOW
Data	:t_act,C_x,C_b	AS DATAA

EQUATION

Active Phase Mass Balance Equations

$$m = F_p - F_x - F_r - F_b;$$

$$(m*x) = (F_p*x_p) - x*(F_x + F_r + F_b);$$

Defining mass flowrates

$$F_x + F_r + F_b = m/t_{act};$$

$$F_x = C_x*m/t_{act};$$

$$F_b = C_b*m/t_{act};$$

10.2.2. Passive Phase

Passive Cell Model v4.0

14-Jan 2008, Andrew Lee

VARIABLE

m	AS mass	# Total mass contained within cell
x	AS moisture	# Moisture content of solids in cell
x_x	AS moisture	# Moisture content of axial flow
x_k_in	AS moisture	# Moisture content of kilning flow in
x_b	AS moisture	# Moisture content of backmixed flow
x_r	AS moisture	# Moisture content of return flow
F_x	AS mass_flowrate	# Axial flow into cell
F_k_in	AS mass_flowrate	# Kilning flow into cell
F_b	AS mass_flowrate	# Backmixed flow into cell
F_r	AS mass_flowrate	# Material returning from active phase
F_a	AS mass_flowrate	# Flow to active phase
F_k_out	AS mass_flowrate	# Kilning flow out of cell
t_pas	AS mrt	# Mean residence time of passive phase
t_kiln	AS mrt	# Mean residence time of kilning phase
m_des	AS mass	# Design load of cell under current conditions
m_pas	AS mass	# Current non-kilning mass in cell
m_kiln	AS mass	# Current kilning mass in cell

STREAM

Axial	:F_x,x_x	AS SOLIDFLOW
Active	:F_a,x	AS SOLIDFLOW
Back	:F_b,x_b	AS SOLIDFLOW
Return	:F_r,x_r	AS SOLIDFLOW
Kiln_in	:F_k_in,x_k_in	AS SOLIDFLOW
Kiln_out	:F_k_out,x	AS SOLIDFLOW
DataOut	:m,x	AS DATAF
DataIn	:t_pas,m_des	AS DATAP

EQUATION

```

# Passive Phase Material Balances

$ m = F_x + F_k_in + F_b + F_r - F_a - F_k_out;

$(x*m) = (F_x*x_x) + (F_k_in*x_k_in) + (F_b*x_b) + (F_r*x_r) - x*(F_a + F_k_out);

# Defining Flow Rates

IF m > m_des THEN

    m_pas = m_des;
    m_kiln = m - m_des;

    F_a = m_pas/t_pas;
    F_k_out = m_kiln/t_kiln;

ELSE

    m_pas = m;
    m_kiln = 0;

    F_a = m_pas/t_pas;
    F_k_out = 0;

END

```

10.2.3. Geometry Model

```

PARAMETER

omega          AS REAL

L              AS REAL
R              AS REAL
theta          AS REAL
s1             AS REAL
s2             AS REAL
alpha1         AS REAL
alpha2         AS REAL

```

Nf AS INTEGER

rhob AS REAL

N AS INTEGER

VARIABLE

s1p AS length

s2p AS length

a1 AS no_unit

a2 AS no_unit

a1p AS angle

a2p AS angle

Rf AS length# Radius of flight tip

psifl AS angle # Angle of rotation between two flights

m_p AS mass # Current passive mass

x_p AS moisture # Moisture content of passive solids

phi AS angle # Dynamic angle of repose of solids

mafa AS angle # Mass averaged fall angle (radians)

mafth AS length # Mass averaged fall height

maft AS mrt # Mass averaged fall time

t_flight AS mrt # Mass averaged flighted time

m_des AS mass # Passive mass at design conditions

d_load AS no_unit # Dryer loading factor

f_load AS no_unit

f_load_c AS no_unit

C_x AS no_unit # Forward partitioning coefficient

C_x_g AS no_unit # Gas effect on forward partitioning coefficient

C_b AS no_unit # Backward partitioning coefficient

pi AS no_unit # Value of pi

STREAM

Active :maft,C_x,C_b AS DATAA

Input	:m_p,x_p	AS DATAF
Passive	:t_flight,m_des	AS DATAP

EQUATION

pi = 3.1415926535897932384626433832795;

Geometric Calculations

a1 = alpha1*pi/180;

a2 = alpha2*pi/180;

a1p = (pi/2) - a1;

a2p = a2 - a1p;

s1p = s1*sin(pi-a2)/sin(a2p);

s2p = s1*sin(a1p)/sin(a2p) + s2;

Rf = sqrt(((R-s1p)^2) + (s2p^2) - (2*(R-s1p)*s2p*cos(pi-a2p)));

psifl = 2*pi/Nf;

Mass Average Calculations

maf_h = 1.80225658814015 + 0.0517970853538827*phi - 0.000629336469614827*(phi^2) +
 6.32035529121722E-08*(phi^3) + 1.22476072594873*f_load + 2.16717025928665*(f_load^2) -
 1.21939160376451*(f_load^3) + 0.010656063519491*phi*f_load -
 0.0301050931666396*phi*(f_load^2) + 0.000647364680432361*(phi^2)*f_load -
 0.00059240889866885*(phi^2)*(f_load^2);

mafa = asin(maf_h/(2*Rf)) + pi/2;

maft = 0.649949441894023 + 0.00467465968739589*phi - 8.34170550900737E-05*(phi^2) +
 1.10469313271619E-07*(phi^3) + 0.401111371313164*f_load - 0.105617246423208*(f_load^2) -
 0.012464783688614*(f_load^3) - 0.00275163282481117*phi*f_load -
 0.00121958102772624*phi*(f_load^2) + 0.000113383344526596*(phi^2)*f_load -
 9.32689258128505E-05*(phi^2)*(f_load^2);

t_flight = 2*(mafa - pi/2)/(omega*2*pi/60);

Design Conditions Calculations

```

m_des = rhob*(L/N)*(-2.31115676858565 + 0.339781159235542*phi - 0.0184202242225151*(phi^2)
+ 0.000536975704927556*(phi^3) - 8.65128896429708E-06*(phi^4) + 7.328805813683E-08*(phi^5)
- 2.54709110347933E-10*(phi^6));

d_load = m_p/m_des;
{f_load_c = -0.0450480367762793 - 0.00099740007061655*phi + 2.72671900427568E-05*(phi^2) -
1.2070957963739E-07*(phi^3) + 1.15296535419475*d_load - 1.83760510849243*(d_load^2) +
1.68000076986581*(d_load^3) + 0.00618147656427936*phi*d_load -
0.00605940458513032*phi*(d_load^2) - 0.000141023308476207*(phi^2)*d_load +
0.000121061698308722*(phi^2)*(d_load^2);

# This IF statement ensures that if the correlation for f_load gives a negative
# results (due to errors in the correlation), that f_load is given a value
# of zero instead.

IF f_load_c < 0 THEN
f_load = 0;
ELSE
IF d_load > 1 THEN
f_load = 1;
ELSE
IF f_load_c > 1 THEN
f_load = 1;
ELSE
f_load = f_load_c;
END
END
END
END}

f_load = 1;
f_load_c = 1;

C_x = C_x_g*maf_h*sin(theta*pi/180)/(L/N);

```

10.2.4. Cell Model

{Cell Model v3.1

14th January, 2008}

UNIT

A AS Active
G AS Geometry
P AS Passive

EQUATION

P.Active IS A.In;

P.Return IS A.Return;

P.DataOut IS G.Input;

P.DataIn IS G.Passive;

A.Data IS G.Active;

10.2.5. Outflow Model

{ Outlet Model v1.2

14 Jan 2008, Andrew Lee

Model Inculdes:

- Combined outflow data
- Tracer study data
- Mean residence time calculation}

VARIABLE

F_a AS mass_flowrate
F_p AS mass_flowrate
F_o AS mass_flowrate

x_a AS moisture
x_p AS moisture
x_o AS moisture

```

x_feed    AS no_unit    # Total moisture fed to system (integral of x_o over time)
xtime     AS no_unit    # Experiment run time
tau       AS no_unit    # Mean residence time

normalised AS no_unit    # Normalised concentration

```

STREAM

```

Active    :F_a,x_a  AS SOLIDFLOW
Passive   :F_p,x_p  AS SOLIDFLOW
Out      :F_o,x_o  AS SOLIDFLOW

```

EQUATION

```

F_o = F_a + F_p;

(x_o * F_o) = (F_a * x_a) + (F_p * x_p);

# RTD Calculations

$xtime = 1;

normalised = x_o*F_o*3600/x_feed;      # Units: kg/kg.hr

$tau = xtime*x_o*F_o/x_feed;

```

10.2.6. Dryer Model

{Dryer Model v4.0

Jan 14th, 2008}

PARAMETER

N AS INTEGER

UNIT

C AS ARRAY(N) OF Cell
O AS Outflow

VARIABLE

```
t_kiln    AS mrt  
C_b       AS no_unit  
C_x_g     AS no_unit
```

EQUATION

FOR i:=1 TO N-1 DO

```
C(i).P.Kiln_out IS C(i+1).P.Kiln_in;  
C(i).A.Axial   IS C(i+1).P.Axial;  
C(i).P.Back    IS C(i+1).A.Back;
```

END

```
C(1).P.Axial  IS C(1).A.Back;  
O.Active      IS C(N).A.Axial;  
O.Passive    IS C(N).P.Kiln_out;
```

Setting global parameters

FOR i:=1 TO N DO

```
C(i).P.t_kiln = t_kiln;  
C(i).G.C_b = C_b;  
C(i).G.C_x_g = C_x_g;
```

```
C(i).G.phi = 1222.2*(0.02*exp(log(0.002/0.02)*(i-1)/(N-1)))+34.5;
```

END

10.3. Parameter Estimation Entity

EXPERIMENTS

tracer_delay

ESTIMATE

```
D.C_b  
0.65 : 0.0 : 1.0  # 0.36
```

ESTIMATE
D.C_x_g
0.33 : 0.0 : 1.0 # 0.64

ESTIMATE
D.t_kiln
8.5 : 0.0 : 1.0E30 # 11

MEASUREMENT_GROUP
CONSTANT_VARIANCE (1 : -10 : 10)
#CONSTANT_RELATIVE_VARIANCE MEASURED_VALUES (1 : 0 : 10)
#HETEROSCEDASTIC MEASURED_VALUES (1 : 0 : 10; 0.7 : 0 : 1)
SENSOR
D.O.Normalised

10.4. Experiment Entity

INTERVALS
3
21600.0
39.6
7200.0

PIECEWISE_CONSTANT
D.C(1).P.x_k_in
0.0
3.683E-4
0.0

MEASURE
D.O.Normalised
0.0 0.0
21560.0 0.0
21680.0 0.0
21800.0 0.0
21920.0 0.378419524
21980.0 2.5514066
22040.0 7.826695328
22100.0 10.56858801
22160.0 10.59807899

22220.0 8.736699422
22280.0 5.784162829
22340.0 3.853816253
22400.0 2.555643718
22460.0 1.526573824
22520.0 1.037884056
22580.0 0.740868695
22640.0 0.479292525
22700.0 0.335205721
22760.0 0.300286679
22880.0 0.151589848
23000.0 0.110785377
23120.0 0.09287547
23240.0 0.087624126
23360.0 0.068322185
23600.0 0.054226527
23840.0 0.035228627
24080.0 0.040232584
24350.0 0.03095849
24560.0 0.03148637
24800.0 0.025620819
25160.0 0.025655561
26060.0 0.017080546

11. Appendix II - Matlab® Code

11.1. Filtering Flight Rig Data

```
% Flight rig data analysis code v1.3
% Andrew Lee, 28th April 2006

% =====
% This section allows the user to enter the directory and file name for the experimental
% data to be used in this analysis.

rpt = 'y';

default = input('Do you wish to use the default path settings (Y/N)? ','s');

if default == 'N'|default == 'n';

    pathline = input('Enter directory path: ','s');

else

    pathline = 'G:\Thesis\Experimental testing results\flight profile testing\Matthew Pugh\Load Cell
CSV Files'; % Default pathline - Change as necessary

end

while rpt == 'y'|rpt == 'Y';

    infile = input('Enter csv data file name: ','s'); % Filename as filename.csv

    path(path,pathline); % Sets pathline as a search path for Matlab
    indata = csvread(infile); % Reads csv file into structure input

    rpm = input('Enter flight speed (in rpm): ');
    srate = 100;

    % =====
    % This section extracts experimental data, filters for noise and differentiates
```

```

filt = fir1(200,0.03); % Constructing data filter

exptt = indata(:,1); % Extracting time data from input

expta = conv((indata(:,2).'),filt); % Extracting raw data from input and filtering

exptd = gradient(expta,(1/srate)); % Differentiating filtered data

% =====

% =====

% Write data to a csv file

dout = [expta; exptd];
dout = dout';

outfile = [pathline,'f,infile];

csvwrite(outfile,dout);

% =====

rpt = input('Do you wish to filter another file in the same directory (Y/N)? ','s');

end

```

11.2. Fitting Model to Flight Rig Data

```

% Geometric analysis code v2.1 Final Working Copy
% Andrew Lee, 7th August 2007

% =====

% This section allows the user to enter the directory and file name for the experimental
% data to be used in this analysis.

```

```

default = input('Do you wish to use the default path settings (Y/N)? ','s');

if default == 'N'|default == 'n';

```

```

pathline = input('Enter directory path: ','s');

else

    pathline = 'c:\thesis\results\flight rig\experiments\final flight rig results\filtered data'; % Default
    pathline - Change as necessary

end

close all

infile = input('Enter csv data file name: ','s'); % Filename as filename.csv

path(path,pathline); % Sets pathline as a search path for Matlab
indata = csvread(infile); % Reads csv file into structure input

% =====

% Geometric data for apparatus

L = 1; % Flight length (m)
R = 2.5; % Radius of curvature for back of flight (m) - maybe removed later
s1 = 0.1; % Length of flight base (m)
s2 = 0.11; % Length of flight tip (m)
a1 = pi/2; % Flight-wall intersection angle (rad)
a2 = 120*pi/180; % Flight tip angle (rad)

omega = input('Enter rpm of experiment: '); % Rotational speed (rpm)
psii = input('Enter initial angle of rotation (rad): '); % Start point of geometric analysis (rad)
phi = input('Enter material angle of repose (rad): '); % Angle of repose of solid material (rad)
sdphi = input('Enter the standard deviation angle of repose (rad): ');
rhob = input('Enter the bulk density of the material: ');

% Calculating the 95.4% confidence interval of angle of repose.
phip = phi+2*sdphi;
phim = phi-2*sdphi;

% Additional geometric calculations

```

```

st = sqrt(s1^2 + s2^2 - 2*s1*s2*cos(a2));
Rf = sqrt((R-s1)^2+(s2^2)-(2*(R-s1)*s2*cos((3*pi/2)-a1-a2)));
psift = asin(s2*sin(pi-a2)/Rf);

% Calculating transition points

% Average phi
psie = 2*pi + phi - a1 - a2; % End point
psit = pi + phi - a1 + asin(s2*sin(a2)/st); % Triangle point

% +2 st.dev.
psiep = 2*pi + phip - a1 - a2; % End point
psitp = pi + phip - a1 + asin(s2*sin(a2)/st); % Triangle point

% -2 st.dev.
psiem = 2*pi + phim - a1 - a2; % End point
psitm = pi + phim - a1 + asin(s2*sin(a2)/st); % Triangle point

% =====
% Geometric code

i = 1; % Counter

% Variable initialisation
A = 0;
Ap = 0;
Am = 0;
m = 0;
mp = 0;
mm = 0;
t = 0;
psiv = 0;

int = 0.01*(omega*2*pi/60); % Step interval for iteration (rad)

psi = psii;
% Iterative geometric analysis (average phi)
while psi <= psie | psi <= psiep | psi <= psiem;

% For average phi

```

```

if psi < psit;      % Quadrangle analysis

A(i) = (((pi/2)+phi-psi-psift-asin((Rf/R)*sin((pi/2)-phi+psi+psift)))+psift)*((R^2)/2)) -
(0.5*R*Rf*sin((pi/2)+phi-psi-psift-asin((Rf/R)*sin((pi/2)-phi+psi+psift)))) - (0.5*R*Rf*sin(psift)) +
(0.5*s1*(s2*sin(a2)));

elseif psi >= psit & psi < psie;    % Triangle analysis

A(i) = 0.5*s2^2 * sin(a1+a2-(pi/2))*sin(phi-a1-a2-psi)/sin((3*pi/2)-phi+psi);

else

A(i) = 0;

end

% For +2 st.dev.

if psi < psitp;      % Quadrangle analysis

Ap(i) = (((pi/2)+phip-psi-psift-asin((Rf/R)*sin((pi/2)-phip+psi+psift)))+psift)*((R^2)/2)) -
(0.5*R*Rf*sin((pi/2)+phip-psi-psift-asin((Rf/R)*sin((pi/2)-phip+psi+psift)))) - (0.5*R*Rf*sin(psift)) +
(0.5*s1*(s2*sin(a2)));

elseif psi >= psitp & psi < psiep;    % Triangle analysis

Ap(i) = 0.5*s2^2 * sin(a1+a2-(pi/2))*sin(phip-a1-a2-psi)/sin((3*pi/2)-phip+psi);

else

Ap(i) = 0;

end

% For +2 st.dev.

if psi < psitm;      % Quadrangle analysis

Am(i) = (((pi/2)+phim-psi-psift-asin((Rf/R)*sin((pi/2)-phim+psi+psift)))+psift)*((R^2)/2)) -
(0.5*R*Rf*sin((pi/2)+phim-psi-psift-asin((Rf/R)*sin((pi/2)-phim+psi+psift)))) - (0.5*R*Rf*sin(psift)) +
(0.5*s1*(s2*sin(a2)));

```

```

elseif psi >= psitm & psi < psem; % Triangle analysis

Am(i) = 0.5*s2^2 * sin(a1+a2-(pi/2))*sin(phim-a1-a2-psi)/sin((3*pi/2)-phim+psi);

else

    Am(i) = 0;

end

% Angle vector

psiv(i) = psi;

% Calculating time from start point (psiv(1))

t(i) = (psi-psiv(1))/(omega*2*pi/60);

i = i + 1; % Increase counter
psi = psi + int; % Increase psi

end

% =====
% Extracting and trimming experiemntal data

expm = indata(:,1); % Extracting mass data from input
expdm = indata(:,2);

expm = expm(300:(end-300)); % Trim ends of data vector
expdm = expdm(300:(end-300));

spts = find(expdm==max(expdm))-100; % Determine number of starting points before
expeimental curve by locating highest point of mass flow rate.

moff0 = mean(expm(1:spts)); % Calculate initial mass offset

expm = expm - moff0; % Remove initial mass offset

fmass = mean(expm((end-200):end)); % Calculate final mass (w/o offset)

```

```

% =====
% Fitting model and experimental data

spoint = max(find(expdm(1:spts+100) <= 0)); % Finding the start point of the experimental data

% Calculating normalized time and angle of rotation at start of experimental data
startt = -spoint*0.01;
startpsi = -spoint*0.01*(omega*2*pi/60);

for j = 1:length(expm);

    expt(j) = startt + (j-1)*0.01; % Calculate normalized experiment time
    exppsi(j) = startpsi + (j-1)*0.01*(omega*2*pi/60);

end

% =====
% Calculating bulk density and model mass.

fpoint = length(A)/2 - mod((length(A)/2),1);

mo = fmass - rhob*A(1);
mop = fmass - rhob*Ap(1);
mom = fmass - rhob*Am(1);

% Converting area to mass
m = A*L*rhob;
mp = Ap*L*rhob;
mm = Am*L*rhob;

% Calculating discharge rate
dm = -gradient(m,t);
dmp = -gradient(mp,t);
dmm = -gradient(mm,t);
am = m(1) - m + mo;
amp = mp(1) - mp + mop;
amm = mm(1) - mm + mom;

% =====
% Write data to csv file

```

```

% Padding data with 0's to match vector lengths
padlength = length(expt) - length(t);
t = [t, zeros(1,padlength)];
psiv = [psiv, zeros(1,padlength)];
am = [am, zeros(1,padlength)];
amp = [amp, zeros(1,padlength)];
amm = [amm, zeros(1,padlength)];
dm = [dm, zeros(1,padlength)];
dmp = [dmp, zeros(1,padlength)];
dmm = [dmm, zeros(1,padlength)];

%Assembling data for output
dout = [expt; expsi; expm; expdm; t; psiv; am; amp; amm; dm; dmp; dmm];
dout = dout';

% Writing csv file
outfile = [pathline,'m',infile];

csvwrite(outfile,dout);

%plot(expt,expm,t(1:i-1),am(1:i-1),t(1:i-1),amp(1:i-1),t(1:i-1),amm(1:i-1))

disp('finished')

% =====

```